The development of a novel technique for characterizing the MICE muon beam and demonstrating its suitability for a muon cooling measurement

Mark Alastair Rayner
Worcester College, Oxford

Thesis submitted in fulfilment of the requirements for the degree of Doctor of Philosophy at the University of Oxford

Trinity Term, 2011

Abstract

The International Muon Ionization Cooling Experiment (MICE) is designed to demonstrate the currently untested technique of ionization cooling. Theoretically, this process can condition the high quality muon beams required to build a neutrino factory or muon collider which will be the next generation of machines for the study of Particle Physics. The beam line to transport muons into the MICE cooling channel lattice cell was installed in December 2009. Step I of the experimental programme, whose goal was to demonstrate that the beam line can generate beams similar to those expected in a neutrino factory cooling channel, was completed in August 2010.

Methods were developed to use time difference measurements in the MICE time of flight counters (TOFs) to obtain a transverse spatial resolution of approximately 10 mm and to track muons through the focusing elements of the beam line, thus allowing the trace space vectors of individual muons to be reconstructed and their integrated path length to be calculated. The TOFs were used to make an absolute measurement of the momentum of muons with zero bias and a systematic error of less than 3 MeV/c.

The measured trace space vectors of single muons were used to estimate the emittances and approximate optical parameters of eighteen muon beams. The results of beam line simulations were compared with the measurements and, once the effects of experimental resolution had had been included, found to be in good agreement.

A sample of individual muons whose phase space vectors had been measured was injected into a simulation of the full MICE cooling channel; the beam was found to be suitable for demonstrating muon cooling, although some fine tuning of the cooling channel optics will eventually be required.

Ad maiorem Dei gloriam

Acknowledgements

First and foremost I would like to thank my supervisor, Dr. John Cobb, for his wisdom and kindness. I enjoyed talking about physics with him immensely and will not forget his frequent admonition (passed down through the generations) that 'Mark, physics is about *numbers*'.

I would also particularly like to thank Marco Apollonio, with whom I had many interesting discussions, and who provided the 'G4Beamline' simulations which are described in section 4.3.1. Indeed I greatly appreciate the support of all the mice in Oxford, and of my new colleagues at the Université de Genève while I finished writing my thesis.

I am especially grateful to the MICE collaboration and the engineers at the Rutherford Appleton Laboratory for their hard work to design, build and operate the experiment. Particular thanks are due to Rob Edgecock, Yordan Karadzhov (who provided the timing calibration; cf. section 3.2) and the authors of the 'G4MICE' analysis code. I would also like to thank Maurizio Bonesini for the opportunity to work with the time of flight detectors at the Università degli Studi di Milano Bicocca in 2007 and 2008. I gratefully acknowledge the support of the British taxpayer through the Science and Technology Facilities Council.

On a personal note I would like to thank my parents, my brother David and my friends at Worcester College, the Oxford University Catholic Chaplaincy, and beyond. Paradoxically, given the subversive nature of the musical and philosophical excursions of some of my friends (you know who you are!) you kept me sane. *Laos Deo semper.*

Contents

Introduction **1**

1 The key to precision in neutrino physics and at the energy frontier **2**

1.1 A brief historical introduction to neutrinos 3

1.2 Neutrino oscillations 4

1.2.1 Atmospheric neutrino oscillations 5

1.2.2 Solar neutrino oscillations 6

1.2.3 Current experimental searches 7

1.3 The advantages of a neutrino factory 8

1.4 Ionization cooling and the muon collider 10

1.5 Conclusion 11

2 The design and status of the MICE ionization cooling demonstration **12**

2.1 Ionization cooling 12

2.1.1 Trace space, emittance and the Twiss parameters 13

2.1.2 Beam correlations for optimal cooling 14

2.1.3 Phase space and normalized transverse emittance 15

2.1.4 Choice of absorber material 17

2.2 The Muon Ionization Cooling Experiment 18

2.2.1 Design of the cooling channel lattice cell 18

2.2.2 Instrumentation of the channel 19

2.2.3 The muon beam 20

2.2.4 Status of the experiment 21
2.3 Step I of the MICE experiment 22
2.3.1 The design of the muon beam line 22
2.3.2 Matching conditions in the upstream spectrometer 24
2.3.3 Emittance inflation in the MICE diffuser 25
2.3.4 Optical configurations of the MICE beam line 27
2.3.5 The Step I data taking campaign 30
2.4 Conclusion 30

3 Measuring time and position with the time of flight detectors 31
3.1 The time of flight detectors TOF0 and TOF1 31
3.2 Timing resolution revisited 33
3.2.1 Reconstructing the time of a particle 33
3.2.2 Timing resolution per pixel during Step I 36
3.3 Measuring transverse position 38
3.3.1 Calibrating the measurement 38
3.3.2 Resolution and beam size 46
3.3.3 Combining the measurements 48
3.4 Conclusion 49

4 Time of flight and transverse position in data and simulation 50
4.1 Particle identification for the Step I data sets 50
4.2 Stability of the electron peak 54
4.2.1 Geometry of the TOF0 and TOF1 detectors 54
4.2.2 Calibration of the absolute time of flight 56
4.2.3 The anomalous electron-positron asymmetry 56
4.3 Simulation of the upstream time of flight system 59
4.3.1 The G4Beamline-G4MICE simulations of the Step I beams 59

4.3.2 Time of flight in data and simulation 61
4.3.3 Transverse position in data and simulation 63
4.4 Conclusion 66

5 Measurement of muon momenta 67

5.1 Phase space reconstruction at the MICE beam line 68
5.1.1 Beam transport in the MICE time of flight system 68
5.1.2 Measuring longitudinal momentum 71
5.1.3 Reconstructing transverse momentum 73
5.2 Iterative reconstruction algorithm 74
5.2.1 Iterative path length correction 75
5.2.2 Monte Carlo study of the reconstruction algorithm 76
5.2.3 Eliminating systematic bias on p_z 77
5.2.4 Momentum resolution and the efficiency of the algorithm 81
5.2.5 Momentum spectra in data and simulation 83
5.3 Measurement of the transverse angles x' and y' 85
5.3.1 The effect of resolution, scattering and nonlinearities 85
5.3.2 Comparison between data and simulation 90
5.4 Conclusion 90

6 Distributions in transverse trace space at TOF1 93

6.1 Resolution bias on optical parameters 95
6.1.1 The effect of detector resolution on emittance measurements 97
6.1.2 The effect of multiple scattering 97
6.1.3 Resolution bias in (β, ϵ)-space 101
6.2 Comparison between data and simulation 102
6.2.1 The trace space distribution of the base line beam 103
6.2.2 The effect of a χ^2 cut on simulated beam measurements 106

6.3 Measurement of the emittance of the Step I beams 107

6.4 Summary 107

7 Simulation of a measured beam in the MICE cooling channel 110

A The Step I data sets 114

A.1 The re-scaled TURTLE data sets 115

A.2 The genetic algorithm data sets 116

B Sketch of a fully constrained calibration 119

C Statistical error on Twiss parameters 122

D Measurements of the Step I data sets 123

Bibliography 127

List of Figures

1.1 The Feynman diagram for muon decay 3

1.2 The International Scoping Study neutrino factory design 9

1.3 A sketch of the principle of ionization cooling 11

2.1 Twiss parameterization of trace space 14

2.2 Ionization cooling of a focused and defocused beam 14

2.3 The MICE lattice cell and the upstream and downstream spectrometers . . . 18

2.4 The MICE schedule 21

2.5 The Step I MICE muon beam line 23

2.6 The momentum spectra of pions and muons at dipole 2 23

2.7 A sketch of the principle of emittance inflation in the diffuser 26

3.1 A schematic of a MICE time of flight detector 32

3.2 The passage of a particle through a TOF scintillator slab 34

3.3 A sketch showing the cabling of TOF0 and TOF1 34

3.4 The pixel coverage of the February and August calibrations 35

3.5 The data set used to calibrate the new position measurement 36

3.6 A measurement of the timing resolution of a pixel 37

3.7 A comparison of the two position measurement techniques 39

3.8 Calibration of the horizontal slabs of TOF0 40

3.9 Calibration of the vertical slabs of TOF0 41

3.10 Calibration of the horizontal slabs of TOF1 42

3.11 Calibration of the vertical slabs of TOF1 43
3.12 Parameters of the new calibration 44
3.13 The efficiency of the new calibration 45
3.14 A comparison of the old and new position measurements 46
3.15 Error distributions of the old and new position measurements 47

4.1 Particle identification with the time of flight system 51
4.2 Time of flight for a base line muon dominated beam 52
4.3 Time of flight distributions of the emittance-momentum matrix beams . . . 53
4.4 Stability of the February and August calibrations 55
4.5 The anomalous electron-positron peak asymmetry 57
4.6 Monte Carlo path length for electrons and positrons 58
4.7 The longitudinal gradient profile of quadrupoles 4 – 9 60
4.8 A comparison between time of flight distributions in data and simulation . . 62
4.9 A comparison between measurements of x in data and simulation 64
4.10 A comparison between measurements of y in data and simulation 65

5.1 The upstream time of flight system 67
5.2 The longitudinal gradient profile of the base line beam 69
5.3 The p_z spectrum of the base line beam 71
5.4 The base line transfer matrix as a function of p_z 72
5.5 The base line angle reconstruction coefficients as a function of p_z 74
5.6 Estimating path length in a top hat quadrupole 75
5.7 Reconstructed muon path lengths between TOF0 and TOF 78
5.8 The systematic error on p_z 79
5.9 The evolution of the mean s and p_z residuals 80
5.10 Reconstructed muon momenta at TOF1 82
5.11 The efficiency of the reconstruction algorithm 83

5.12 A comparison between momentum spectra in data and simulation 84
5.13 Momentum spectra for all the Step I re-scaled TURTLE beams 86
5.14 Reconstructing x' at TOF1 87
5.15 Reconstructing y' at TOF1 87
5.16 The linearity of the reconstruction algorithm 88
5.17 Nonlinearity and the treatment of fringe fields 89
5.18 The effect of measurement error on angle reconstruction 89
5.19 A comparison between x' distributions in data and simulation 91
5.20 A comparison between y' distributions in data and simulation 92

6.1 Simulated trace space of the base line beam 94
6.2 Dispersion in a simulation of the base line μ^- beam 95
6.3 Reconstructed trace space of the base line beam in data 96
6.4 A correction for resolution bias with scattering deactivated 98
6.5 A correction for resolution bias in a full simulation 100
6.6 The effect of resolution bias 101
6.7 A comparison between reconstructed resolution smeared simulation and data 103
6.8 Reconstructed trace space of the base line beam in data and simulation . . . 104
6.9 χ^2 distributions in data and simulation 105
6.10 The effect of resolution bias for reconstructed $\chi^2 < 6$ 107
6.11 A comparison between (β, ϵ) in data and simulation for $\chi^2 < 6$ 108
6.12 Measurements of the Step I beams after a $\chi^2 < 6$ cut 109

7.1 The evolution of measured $\langle E \rangle$, $\langle p_z \rangle$ and $\beta_\perp$ in a simulation of Step VI . . . 111
7.2 The longitudinal magnetic field in Step VI 112
7.3 The evolution of ϵ_{N} of a measured beam in a simulation of Step VI 113

B.1 Diagram of the TOF cable calibration constants 120

D.1 Legend for the emittance-momentum matrix beam plots in Appendix D . . . 123

D.2 ϵ, β and α as a function of p_z for the μ^- beams 125

D.3 ϵ, β and α as a function of p_z for the μ^+ beams 126

List of Tables

1.1 The properties of the Standard Model leptons 4

2.1 A comparison between ionization cooling absorbers 17

2.2 The beam parameters required upstream of the diffuser 26

2.3 Magnet currents for the base line optical designs 29

3.1 The timing resolution per pixel in TOF0 37

3.2 The timing resolution per pixel in TOF1 38

3.3 Cable length corrections for TOF0 45

3.4 Cable length corrections for TOF1 45

3.5 Illustration of the former measurement bias 46

3.6 Time and position resolutions in Step I 48

4.1 Time of flight particle identification cuts 52

4.2 Beam composition of the emittance-momentum matrix data sets 54

4.3 Positions and rotations of TOF0 and TOF1 55

4.4 The uncorrected mean time of flight of the $e^{\pm}$ peak in data 56

4.5 Mean Monte Carlo e^{-} and e^{+} path lengths 57

4.6 The positions of the Step 1 detectors and magnets 59

4.7 The relative numbers of e, μ and π in simulations of the matrix elements . . 61

4.8 Mean and RMS x and y of the emittance-momentum matrix data sets 63

5.1 A Monte Carlo study of the performance of the reconstruction algorithm . . 77

5.2 Bias and error on the reconstruction of path length 77

5.3 Bias and error on the reconstruction of longitudinal momentum 82

5.4 A comparison between mean p_z in data and Monte Carlo 85

5.5 Bias and error on reconstructed x' and y' 88

A.1 Conversions between current and field for the beam line magnets 114

A.2 Data sets for the rescaled TURTLE μ^- beams 115

A.3 Data sets for the rescaled TURTLE μ^+ beams 115

A.4 Data sets for magnet scans around the (6 mm, 200 MeV/c) μ^+ beam 116

A.5 Data sets for magnet scans around the (6 mm, 200 MeV/c) μ^- beam 117

A.6 Data sets for magnet scans around the (3 mm, 240 MeV/c) μ^- beam 117

A.7 Data sets for a scan of the dipole 1 current for a beam of π^+ 118

A.8 Data sets for the genetic algorithm μ^- beams 118

A.9 Data sets for the genetic algorithm μ^+ beams 118

D.1 Measured beam properties of the Step I re-scaled TURTLE beams 124

Introduction

The International Muon Ionization Cooling Experiment (MICE) is designed to demonstrate the principle of ionization cooling for the first time. Chapter 1 explores the scope for Particle Physics discovery of the neutrino factory and the muon collider: two facilities for which ionization cooling is an indispensible technology. Chapter 2 describes the Accelerator Physics of ionization cooling in the context of the MICE experiment and the design of the new muon beam line at the Rutherford Appleton Laboratory.

The subject of this thesis is the characterization of the muon beams generated by the new beam line. The crux of the analysis is the development of an innovative technique to measure the phase space beam distributions using the MICE timing detectors. Chapter 5 describes an algorithm which reconstructs the longitudinal and transverse momentum of individual muons. Chapter 6 focuses on parameterizing the properties of the beams in transverse phase space. Both chapters feature comparisons of the measured momentum spectra, emittances and optical parameters with Monte Carlo simulations.

The purpose of the prior two chapters is to lay the groundwork for these measurements. Chapter 3 measures the resolution of the existing calibration of the MICE time of flight counters and describes the development of a new technique to measure transverse position with them which is optimized for the requirements of phase space reconstruction. Chapter 4 applies these time and position measurements to the data to measure the stability of the calibration and define data sets for the subsequent analysis based on particle identification using the time of flight peaks. The Monte Carlo simulations used throughout the thesis are introduced at this stage and simple comparisons of the time of flight and position are presented.

The final chapter is a brief look to the future. In Chapter 7 a sample of measured muon phase space vectors is inserted into a simulation of the full MICE cooling channel in order to evaluate the suitability of the beams for demonstrating ionization cooling.

Chapter 1

The key to precision in neutrino physics and at the energy frontier

Super beams are currently continuing the historically fruitful search for new neutrino physics, but suffer from systematic uncertainties which may limit their ability to discover CP violation and constrain the neutrino mixing matrix. A neutrino factory based on muon storage rings has a greater scope for discovery but would require beam cooling within the lifetime of the muons. The only proposed solution is the undemonstrated principle of ionization cooling. Muon storage rings could in the future also provide muon collisions at the energy frontier.

Cosmological models predict that three-hundred low energy neutrinos populate every cubic centimetre of the universe today, having fallen out of thermal equilibrium seconds after the Big Bang. Every second, fusion reactions in the sun generate a flux of 7×10^{10} neutrinos per square centimetre at the orbital radius of the earth, with an energy distribution peaked at 0.3 MeV. Slightly higher energy neutrinos are emitted at lower fluxes by radioactive decays in the earth's core, fission in nuclear reactors and supernovae bursts which occur at a rate of about three a century; a still broader distribution which extends to PeV is generated by the interaction of cosmic rays with the atmosphere. The spectrum ends at EeV with very low fluxes from active galactic nuclei, and the decays of pions created by high energy cosmic rays interacting with cosmic microwave background photons at the Δ resonance. As well as offering a plethora of sources, studying neutrinos creates interesting challenges for the experimenter: the mean free path of a 1 GeV neutrino in water is 2×10^8 km.

Neutrinos are created in particle-antiparticle pairs in Z^0 decays, and alongside a charged lepton in $W^\pm$ decays. Evidence suggests that the three observed charged lepton eigenstates are mirrored by three neutrino eigenstates, and that the matrix which connects these bases in charged current interactions is not only non-diagonal, like the matrix which governs the interactions of the W with the $+\frac{2}{3}e$ and $-\frac{1}{3}e$ quarks, but contains large non-diagonal components. The rotation of the basis appears to be approximately tribimaximal, parameterized by Euler angles $\arcsin(1/\sqrt{3})$, $\pi/4$ and 0, and an unknown CP violating phase. The first two angles have been measured using solar and atmospheric neutrinos, and an upper limit has been placed on the third angle using reactor neutrinos [1–3], however recently published evidence from the T2K and MINOS experiments indicates a non-zero value [4,5]. If this is the case, and the phase is also non-zero, leptonic charged current interactions violate CP symmetry, and fulfil the second of Sakharov's three conditions for Baryogenesis: such a model has the potential to explain the matter-antimatter asymmetry in the observed Universe [6,7].

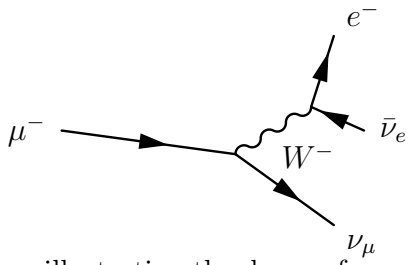

Figure 1.1: A Feynman diagram illustrating the decay of a muon (μ^-). The muon decays into a muon neutrino (ν_μ) and a virtual weak gauge boson, W^-, which decays after a short period governed by the Heisenberg Uncertainty Principle into an electron (e^-) and an anti-electron neutrino ($\bar{\nu}_e$).

The T2K and MINOS experiments use accelerator neutrinos of a few GeV from the decays of pions and kaons. The dominant systematic error in this type of experiment arises from uncertainties on particle production cross-sections when high energy proton beams interact with a nuclear target to generate these particles. This error can be eliminated by instead studying a neutrino beam which originates from muon decays, as illustrated in Figure 1.1. Such a facility is called a neutrino factory, and would produce a well understood neutrino beam with a narrow energy spectrum, ideal for constraining the neutrino mixing matrix. The key technology, however, is the currently undemonstrated principle of ionization cooling, a way to reduce the emittance of a beam in microseconds, which was initially conceived for a muon collider. The Muon Ionization Cooling Experiment (MICE) is designed to demonstrate ionization cooling for the first time.

1.1 A brief historical introduction to neutrinos

In 1930, Wolfgang Pauli hypothesized the emission of a light, electrically neutral spin-$\frac{1}{2}$ particle, as a 'desperate remedy' to preserve the principle of energy-momentum conservation in the theory of nuclear β-decay. It had been observed that the recoil energy of the electron did not account for the mass difference between the neutron and the proton; furthermore it was not a singular value, as expected for a three-body interaction, but a continuum. In 1956, Reines and Cowan made the first direct measurement of the 'neutrino' (ν) by observing the products of the inverse interaction $\bar{\nu}p \rightarrow ne^+$ when reactor anti-neutrinos interacted with the nuclei of water molecules inside their detector.

The years following Pauli's hypothesis saw the discovery of new particles as cosmic rays impinged on magnetized cloud chambers and photographic emulsions. Anderson discovered the positron (e^+) in 1932, following Dirac's prediction of antimatter in 1928, by observing tracks which appeared to be electrons but curved the other way. Seven years later, he and his student observed tracks which curved more sharply than those of electrons, but less sharply than those of protons at the same velocity, suggesting a particle with intermediate mass. This 'mesotron' was initially mistaken for the next particle to be discovered, Yukawa's pion (π^+), observed by Powell, Lattes and Occhialini in 1947. The mesotron is now known as the muon (μ^-), and decays into an electron and two neutrinos. The charged pion distinguished itself by its decay into the muon and only one neutrino.

While the discovery of the pion vindicated Yukawa's prediction of 1935, the discovery of the muon was a surprise. The muon is over two-hundred times more massive than the electron

Lepton	$Q/\|e\|$	Mass	L_e	L_μ	L_τ
e^-	-1	0.5110 MeV	1	0	0
μ^-	-1	105.67 MeV	0	1	0
τ^-	-1	1776.8 MeV	0	0	1
ν_e	0	< 0.7 eV	1	0	0
ν_μ	0		0	1	0
ν_τ	0		0	0	1

Table 1.1: The charge, mass and flavour quantum numbers of the leptons [8]. Cosmic microwave background data from the Wilkinson Microwave Anisotropy Probe have been analysed to give a 95% confidence limit on the sum of the neutrino masses in the absence of direct measurements [9]. The charge and lepton flavour quantum numbers of the corresponding antiparticles have the opposite sign.

and unstable, but apparently identical in other respects. The set of charged 'leptons' was completed in 1975 with the discovery of the still more massive tau lepton (τ^-). In 1990 the picture was shown to be complete, at least in the energy domain currently accessible, by the measurement of the number of neutrino flavours $N_\nu = 3$ via the measurement of the width of the decay of the Z boson. In the Standard Model each charged lepton is partnered by a similarly flavoured neutrino (e^-, ν_e), (μ^-, ν_μ) and (τ^-, ν_τ). The properties of the six leptons are shown in Table 1.1. The lifetimes of the muon and tau lepton are 659 m/c and 8.11 μm/c respectively, where c is the speed of light. The other leptons are stable in the Standard Model.

The leptons are distinguished from quarks by not coupling to the strong force, and by the strict conservation of the flavour quantum numbers L_e, L_μ and L_τ at charged current vertices. This is illustrated by the decay of the muon, shown in Figure 1.1. The muon generates a muon neutrino, and an electron is created alongside an *anti*-electron neutrino. Limits on the rates of lepton flavour non-conserving processes $\mu \to \gamma e$ and $\mu \to 3e$ have been measured to be less than 1.2×10^{-11} and 1.0×10^{-12} respectively. Furthermore, neutrinoless double beta decay $(Z, A) \to (Z + 2, A) + 2e^-$, with $\Delta L_e = 2$, has been shown to have a half life in excess of 1.9×10^{25} years at 90% confidence in ^{76}Ge.

1.2 Neutrino oscillations

Compelling evidence for lepton number non-conservation emerged in 1998, when the Super-Kamiokande experiment reported a zenith angle dependent deficit in the flux of ν_μ from the atmosphere [10]. The collaboration expected to observe ν_e and ν_μ generated by the interactions of cosmic rays with nuclei in the atmosphere in the ratio 1:2, as a result of the decay chain $\pi^+ \to \mu^+\nu_\mu$; $\mu^+ \to e^+\nu_e\bar{\nu}_\mu$. While the total ν_e flux and the flux of 'downward' ν_μ from interactions directly above the location of the detector agreed with their predictions, a statistically significant deficit of 'upward' ν_μ created in the atmosphere on the opposite side of the earth was observed.

This and other observations of neutrino disappearance were interpreted as flavour oscillations according to the theory of Pontecorvo and Maki, Nakagawa and Sakata, in which ν_e, ν_μ and ν_τ are not mass eigenstates [11, 12]. These 'flavour eigenstates' are the mixtures of the

true mass eigenstates ν_1, ν_2 and ν_3 which interact with a W boson to produce each of the charged leptons e, μ and τ. The mixing is parameterized in terms of three Euler angles and a CP-violating phase:

$$\begin{pmatrix} \nu_e \\ \nu_\mu \\ \nu_\tau \end{pmatrix} = \begin{pmatrix} c_{12}c_{13} & s_{12}c_{13} & s_{13}e^{-i\delta} \\ -s_{12}c_{23} - c_{12}s_{13}s_{23}e^{-i\delta} & c_{12}c_{23} - s_{12}s_{13}s_{23}e^{-i\delta} & c_{13}s_{23} \\ s_{12}s_{23} - c_{12}s_{13}c_{23}e^{-i\delta} & -c_{12}s_{23} - s_{12}s_{13}c_{23}e^{-i\delta} & c_{13}c_{23} \end{pmatrix} \begin{pmatrix} \nu_1 \\ \nu_2 \\ \nu_3 \end{pmatrix}, \quad (1.1)$$

where $c_{ij} \equiv \cos\theta_{ij}$, and $s_{ij} \equiv \sin\theta_{ij}$. Each element of the matrix is the amplitude for a particular neutrino mass eigenstate to be created in a charged current interaction with a charged lepton of a particular flavour. The unitarity of the matrix expresses the hypothesis that if other neutrino mass eigenstates exist, they do not mix with the electron, muon or tau lepton.

1.2.1 Atmospheric neutrino oscillations

Long baseline 15 km $\lesssim L \lesssim$ 12,000 km atmospheric ν_μ disappearance may be explained as pseudo two-flavour oscillations, with a single rotation of the neutrino mass basis about the atmospheric mixing angle θ_A. Suppose that two of the neutrino mass eigenvalues are approximately degenerate $m_1 \approx m_2$, and mixed in some superposition $\psi_{12} = -\sin\theta_{12}\nu_1 + \cos\theta_{12}\nu_2$. The mass eigenstates evolve in time according to the Schrödinger equation, by gaining a phase factor e^{-iEt}. Assume that there is no ν_3 component in ν_e: as the ν_1 and ν_2 components must have been created with the same momentum and have degenerate masses, the terms gain the same phase factor, remain in the same proportion, and ν_e retain their flavour, as observed experimentally.

The Super-Kamiokande detector is capable of detecting and distinguishing ν_e and ν_μ in the energy range 0.1 GeV to 10 GeV. Consider the hypothesis that some of the ν_μ 'oscillate' to become ν_τ, and suppose that the ν_μ and ν_τ flavour eigenstates are a rotation $\mathbf{R}(-\theta_\mathrm{A})$ of ψ_{12} and ν_3:

$$\begin{pmatrix} \nu_\mu \\ \nu_\tau \end{pmatrix} = \begin{pmatrix} \cos\theta_\mathrm{A} & \sin\theta_\mathrm{A} \\ -\sin\theta_\mathrm{A} & \cos\theta_\mathrm{A} \end{pmatrix} \begin{pmatrix} \psi_{12} \\ \nu_3 \end{pmatrix}.$$

If a particle is created as a pure ν_μ flavour eigenstate in the atmosphere its wave-function will evolve as $|\Psi(t)\rangle = \cos\theta_\mathrm{A} e^{-iE_{12}t}|\psi_{12}\rangle + \sin\theta_\mathrm{A} e^{-iE_3 t}|\nu_3\rangle$ and a $\nu_\mu \to \nu_\tau$ oscillation amplitude $\langle\nu_\tau|\Psi(t)\rangle = e^{-iE_{12}t}\sin\theta_\mathrm{A}\cos\theta_\mathrm{A}(e^{i(E_{12}-E_3)t} - 1)$ develops after a time t. After some simplification, the oscillation probability is given by

$$\mathrm{Prob}(\nu_\mu \to \nu_\tau) = |\langle\nu_\tau|\Psi(t)\rangle|^2 = \sin^2(2\theta_\mathrm{A})\sin^2\frac{\Delta m^2_\mathrm{A} L}{4E}, \quad (1.2)$$

where $\Delta m^2_\mathrm{A} \equiv m_3^2 - m_1^2$, L is the distance from creation to observation, and $E \approx p$ is the energy of the neutrino. Although mass differences are significant, as Table 1.1 shows they make a negligible difference to the total energy.

The hypothesis that ν_μ oscillate to ν_τ with a probability given by Equation 1.2 was found to fit the Super-Kamiokande data well, and was corroborated by a similar observation of the disappearance of ν_μ in an accelerator neutrino beam by the MINOS experiment [13]. Both data sets were found to be consistent with $\Delta m^2_\mathrm{A} = 2.40 \times 10^{-3}$ eV^2 and $\theta_\mathrm{A} = \pi/4$. Such a mixing angle is called maximal, as the oscillation probability will eventually equal

unity at $L/E = 2\pi/\Delta m^2_{\mathrm{A}}$, and at intervals of $4\pi/\Delta m^2_{\mathrm{A}}$ thereafter. Therefore in the Super-Kamiokande experiment, all 1 GeV atmospheric ν_μ will have oscillated to ν_τ after a distance $L = 330$ km. As this is considerably larger than the distance from the atmosphere to the detector, but considerably smaller than the diameter of the earth, the theory elegantly explains the observation that no downward neutrinos 'disappear', but that $\sim 50\%$ of upward neutrinos do.

1.2.2 Solar neutrino oscillations

The sun is a source of electron neutrinos. Its energy comes from the *pp* chain: $pp \to de^+\nu_e$; $pd \to {}^3\mathrm{He}\ \gamma$; ${}^3\mathrm{He}\ {}^3\mathrm{He} \to {}^4\mathrm{He}\ pp\gamma$, resulting in a flux of 7×10^{10} ν_e cm^{-2} s^{-1} at the orbital radius of the earth. In addition, a number of other reactions create more energetic neutrinos at fluxes which are orders of magnitude weaker, but significant, as detection cross-sections increase with neutrino energy. The *pep* chain, and the creation and decay of ^{7}Be and ^{8}Be take the neutrino spectrum up to 14 MeV [14].

Between the 1960s and the end of the twentieth century, a number of experiments reported a deficit in the flux of neutrinos from the sun. In particular the Homestake, SAGE, GALLEX and Kamiokande detectors all reported varying fluxes accounting for between 30% and 60% of the predicted flux [14].

The solar deficit may be explained by the hypothesis that a small difference $\Delta m^2_\odot = \Delta m^2_{12}$ between the approximately degenerate m_1 and m_2 mass eigenvalues leads to oscillations of ν_e to some superposition $\psi_{\mu\tau}$ of ν_μ and ν_τ. As with atmospheric neutrinos, this mixing may be explained by a single rotation $\mathbf{R}(-\theta_\odot)$:

$$\begin{pmatrix} \nu_e \\ \psi_{\mu\tau} \end{pmatrix} = \begin{pmatrix} \cos\theta_\odot & \sin\theta_\odot \\ -\sin\theta_\odot & \cos\theta_\odot \end{pmatrix} \begin{pmatrix} \nu_1 \\ \nu_2 \end{pmatrix}$$

In a similar manner as in Section 1.2.1, an equation analogous to Equation 1.2 may be derived; however the analysis of solar neutrinos is complicated by the interaction of neutrinos with the electrons in sun. While ν_e and oscillated ν_μ and ν_τ can all recoil from virtual Z bosons emitted by solar electrons, ν_e have an additional amplitude (forbidden for ν_μ and ν_τ by flavour conservation) to interact with solar electrons by exchanging a virtual W boson. This 'matter effect', postulated by Wolfenstein in 1978 and developed by Mikheyev and Smirnov in 1986, alters the oscillation probabilities [15, 16].

Solar neutrino oscillations were confirmed by the SNO experiment, which was capable of detecting both the ν_e flux and the total flux of all flavours [1], and confirmed by the KamLAND experiment, which observed $\bar{\nu}_e$ in the range 2 to 10 MeV from nuclear reactors across Japan at a flux-weighted average travel distance $L = 180$ km [17]. By observing oscillations in the disappearance probability as a function of neutrino energy, KamLAND is the only experiment to have directly observed neutrino oscillations. The solar neutrino data are consistent with $\Delta m^2_\odot = 7.58 \times 10^{-5}$ eV^2 and $\theta_\odot = \arcsin(1/\sqrt{3})$ [8].

1.2.3 Current experimental searches

The neutrino mixing matrix in Equation 1.1 is known as the Pontecorvo-Maki-Nakagawa-Sakata matrix after some of the pioneers of the theory. As the introduction to this chapter observes, it is directly analogous to the Cabibbo-Kobayashi-Maskawa matrix, which contains the amplitudes for each of the $+\frac{2}{3}e$ quarks to couple to each of the $-\frac{1}{3}e$ quarks when interacting with a W boson. One may consider ν_1, ν_2 and ν_3 to be fundamental particles with probabilities to interact with either a e, μ or τ given by the modulus squared of the elements of the PMNS matrix.

The analyses in Section 1.2.1 and Section 1.2.2 only compute the effect of a single rotation, and a single mass splitting in isolation. A better approach is to take into account all three rotations and eigenstates simultaneously [8]. The resulting confidence limits on the mixing angles are quite broad, and depend on the mass hierarchy. As observing neutrino oscillations only provides information on mass differences, the absolute scale of the mass eigenvalues is not known (an upper limit has been derived from cosmological data; see Table 1.1), and it is not yet known whether m_3 is greater than or less than m_1 and m_2.

The hypothesis from Section 1.2.1 that there is no $|\nu_3\rangle$ component in $|\nu_e\rangle$ is equivalent to setting $\theta_{13} = 0$. Note that the value of δ is irrelevant to the mixing in this case. The atmospheric and solar basis rotations may be combined consistently by setting $\theta_{23} = \theta_{\mathrm{A}}$ and $\theta_{12} = \theta_{\odot}$. In the maximal $\theta_{23} = \pi/4$ case, $\psi_{\mu\tau} = (\nu_\mu - \nu_\tau)/\sqrt{2}$, and $\nu_3 = (\nu_\mu + \nu_\tau)/\sqrt{2}$. If $\theta_{13} = \arcsin(1/\sqrt{3})$, the PMNS matrix is tribimaximal, however this particular arrangement should only be considered an *aide-mémoire*, as the angles are predicted to run at different energy scales [18]. There is no known reason for the angles to be so much larger than those in the CKM matrix.

A further peculiarity is that only left-handed neutrinos and right-handed antineutrinos have been observed in nature. Neutrinos are therefore unique in the Standard Model as massless Dirac fermions with one of the spin-substates missing. One might more economically imagine the neutrino to be a single spin-$\frac{1}{2}$ Majorana particle ($\nu \equiv \bar{\nu}$) with two substates ν_{L} and ν_{R}. If neutrinos are Majorana particles one must add two extra CP violating phases to the PMNS matrix, although it is anticipated that these would not be observable.

In addition, two unexpected signals have been observed in recent years. The LSND experiment challenged the unitarity of the PMNS matrix, with inconclusive evidence for a sterile flavour [19], and the CPT invariance of the Standard Model has been challenged by the MINOS atmospheric neutrino data, as the 90% confidence measurements of $(\theta_{23}, \Delta m^2_{23})$ differ for the $\bar{\nu}_\mu \to \bar{\nu}_e$ and $\nu_\mu \to \nu_e$ data sets [20].

A number of 'super beams' (T2K and MINOS, and in the future CNGS and NOνA) are designed to measure θ_{13}. These neutrino beams, predominantly composed of muon neutrinos, are generated by colliding protons with a stationary target and allowing the resulting pions and kaons to decay. The beam is directed towards a detector which searches for electron neutrino appearance. For small θ_{13} the measurement is complicated by intrinsic electron neutrinos in the beam, flavour mis-identification and significant uncertainties on the cross-sections to produce pions and kaons, which result in uncertainty on the initial ratios $\nu_\mu : \bar{\nu}_\mu : \nu_e : \bar{\nu}_e$. If θ_{13} is large, as recently indicated by T2K and MINOS [4,5], the reactor experiments Double Chooz, Daya Bay and RENO should be able to confirm the result [21–23]. While matter effects do not affect the rate of ν_e disappearance in reactor experiments due to the low

neutrino energy, they are significant for super beams, potentially allowing the determination of the neutrino mass hierarchy, through comparison of the rate of ν_e and $\bar{\nu}_e$ appearance.

Remarkably the OPERA experiment, which reported the first ν_τ appearance candidate in 2010 [24], recently released evidence that neutrinos in their beam travel faster than the speed of light [25]. The result will now be independently checked at the T2K and MINOS super beams. If confirmed, the result would contradict Einstein's theory of relativity [26].

1.3 The advantages of a neutrino factory

The proposed neutrino factory is designed to measure θ_{13} and search for evidence of CP violation in leptonic charged current interactions. The latest International Scoping Study base line design is shown in Figure 1.2 [27]. The key features are the final race-track shaped muon storage rings, within which bunches of either μ^- or μ^+ circulate until they decay, as illustrated in Figure 1.1. The energy of the storage ring will have a well defined energy, yet to be finally determined, of several tens of GeV. As $E \gg m_\mu$, when the μ^- (μ^+) decay, the ν_μ and $\bar{\nu}_e$ ($\bar{\nu}_\mu$ and ν_e) are emitted within narrow cones aligned with the axis of the long straight edges of the storage rings, allowing neutrino beams to be directed at large detectors at two base lines.

If $\theta_{13} \lesssim 0.01$ it may not be possible for super beams to measure it, due to the uncertainty on the initial flux and the backgrounds [28]. This uncertainty could be eliminated by generating the neutrino beam from muon decays, with the muon and electron flavours created in equal proportion. Neutrino factory detectors would probably be magnetized, and therefore able to distinguish the charge of the lepton produced in neutrino interaction inside the fiducial volume, as well as its flavour. The θ_{13} oscillation signal would then be a 'wrong sign' muon: a $\nu_e \to \nu_\mu$ oscillation yields a μ^- rather than the μ^+ which would be associated with the interaction of an intrinsic $\bar{\nu}_\mu$. This signal gives better precision than $\nu_\mu \to \nu_e$ because charge identification is easier with muons than electrons, as they ionize media over a long track rather than showering.

A great advantage of a neutrino factory is that the signal for CP violation would simply be a difference in the rates of $\nu_\mu \to \nu_e$ and $\bar{\nu}_\mu \to \bar{\nu}_e$. As with the transit of solar neutrinos through the sun, the physics is complicated by matter effects, which nevertheless allow δ to be eliminated from the $\nu_e \to \nu_\mu$ oscillation probability to second order in the small hierarchy parameter $\Delta m^2_{12}/\Delta m^2_{23}$ at a 'magic' base line 7300 km $\lesssim L \lesssim$ 7600 km which depends only on the density of the earth [29]. This disentanglement may allow the two variables to be measured with greater precision. Super beams may be able to measure δ, by observing the oscillation probability as a function of neutrino energy, however this is a difficult measurement which can only be performed for large θ_{13} and δ. This analysis could also be performed at a neutrino factory.

In a neutrino factory the muon beam is generated by the decay of pions created by the interactions of a high energy proton beam with a nuclear target [30]. As the muons are a tertiary beam, they are created with a large distribution of transverse displacements and are highly divergent. The principal difficulty in building a neutrino factory is to transport a high flux of muons into the accelerating part of the lattice, indicated in Figure 1.2 by a combination of linacs, recirculating linacs (RLAs) and fixed field alternating gradient

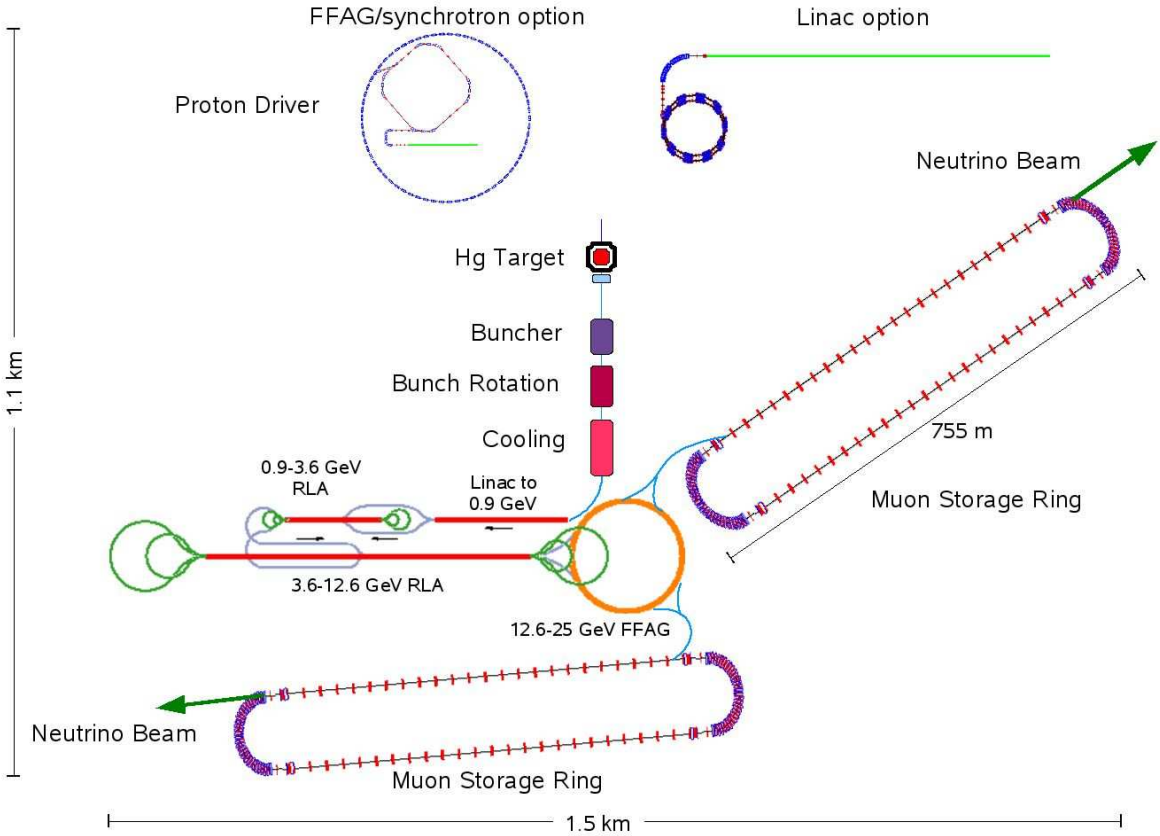

Figure 1.2: The International Scoping Study neutrino factory design [27]. The design may be divided into two sections: the target, front-end and cooling channel, which have solenoidal beam transport; and the acceleration lattice (not finalized) and storage rings. This design has a storage ring energy of 25 GeV.

accelerators (FFAGs). Whichever combination of RLAs and FFAGs is chosen for the final acceleration stages, only muons which can be transported into the finite acceptance of the acceleration lattice can contribute to the final neutrino flux. In order to maximize the flux it is therefore important to maximize the number of particles in the region of transverse phase space within which particles can be accelerated. The measure for the volume of phase space occupied by a beam in a solenoidal focusing lattice is the normalized emittance, described in Chapter 2: the compression of transverse phase space is the subject of this thesis.

1.4 Ionization cooling and the muon collider

The concept of cooling beams using ionization energy loss in media appears to have first been suggested by O'Neill in the 1950s in response to the desire to replace the fixed target accelerators of the time with colliders [31]: such machines have the advantage that the centre of mass energy scales as twice rather than the square root of the beam energy, but they require low emittance beams. O'Neill writes:

> "In order to prevent the beams striking the inflectors on subsequent turns, each ring contains a set of foils, thick at the outer radius but thinning to zero about one inch inside the inflector radius. The injected beam particles lose a few Mev [sic] in ionization in the foils; so their equilibrium orbit radii shrink enough to clear the inflectors after the first turn. After several turns, the beam particles have equilibrium orbits at radii at or less than the inside edge of the foils."

While other cooling techniques have come to be used to cool electron and proton beams, no conventional technique is fast enough to cool the beam before it decays. Interest in ionization cooling has therefore continued since Budker identified it as an indispensible technology for a muon collider in 1969 [32].

The muon collider has enjoyed a surge in interest recently because it would provide finely tuned, high centre of mass energy lepton collisions. Unlike in hadron colliders, the interaction energy would not be convoluted by parton distribution functions, and in contrast to e^+e^- colliders the energy would not be limited by synchrotron radiation losses. In addition to the economy of re-using RF cavities via recirculation in synchrotrons, and the advantage of the machine being relatively small, the muon collider also has the strategic bonus that the front-end could be shared by a neutrino factory. 'Project X' at Fermilab is the first step towards such a facility [33].

The design of a muon collider differs from that of a neutrino factory after the initial cooling lattice because significant further 6D cooling is required to achieve a high luminosity [34]. Although technologically sophisticated, the requisite techniques are based on O'Neill's original foil wedge. The technique proposed for the neutrino factory and the initial muon collider cooling lattice is simpler still, and illustrated in Figure 1.3. Rather than a wedge, a symmetrical absorber is placed directly in the path of the beam to reduce the momentum of each particle; a set of RF cavities immediately replaces the lost longitudinal momentum, and the beam remains bunched at the design momentum of the channel. In a full cooling channel a particle loses enough energy to have been stopped a number of times: by including RF cavities, p_z remains constant, and the net effect is to reduce the transverse momentum.

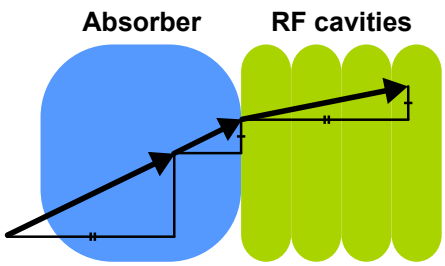

Figure 1.3: A sketch of the principle of ionization cooling. The arrows represent a particle's momentum before and after a liquid hydrogen absorber, and following a set of RF cavities. Ionization energy losses in the absorber reduce the transverse and longitudinal momentum. Electric fields inside the RF cavities replace the lost longitudinal momentum.

1.5 Conclusion

Given the strict conservation of lepton number at interaction vertices, and the approximately diagonal coupling of the three generations of quarks with the W, the observation of large neutrino mixing angles was unexpected. If θ_{13} and δ are both non-zero, CP violation in leptonic charged current interactions could potentially explain the matter-antimatter asymmetry observed in the Universe.

Recently published analyses of data from the T2K and MINOS super beams indicate $\theta_{13} \neq 0$ at $\sim 2.5\sigma$ significance. Whether or not the signals are statistical fluctuations, it may not be possible to answer the remaining questions in the neutrino sector without new experiments. At present it is not known whether the neutrino is a Dirac or Majorana fermion, and no data is available to measure δ, the mass hierarchy, or the absolute mass scale. In addition, the unitarity and CPT invariance of the PMNS matrix has recently been called into question.

If $\theta_{13} \lesssim 0.01$ a neutrino factory is uniquely well placed to measure θ_{13} and δ because it produces well defined beams of high energy electron neutrinos, allowing the study of the golden channel $\nu_e \rightarrow \nu_\mu$. Like a muon collider, which would provide high energy lepton collisions without the expense of the linear acceleration of electrons, it would require fast emittance reduction of the tertiary muon beam. The proposed cooling technology in both cases is the currently undemonstrated principle of ionization cooling.

Chapter 2

The design and status of the MICE ionization cooling demonstration

Ionization cooling is a putative accelerator physics technique designed to reduce the emittance of a neutrino factory muon beam by a factor of six in a microsecond. The Muon Ionization Cooling Experiment is designed to demonstrate the operation of a fully engineered lattice cell of an ionization cooling channel. Step I of the experiment, which was completed in 2010, was devoted to generating and characterizing the muon beams which will be used by MICE.

Ionization cooling is an essential technology for a neutrino factory or muon collider. The Muon Ionization Cooling Experiment (MICE) is designed to demonstrate the operation of a neutrino factory cooling channel for the first time.

A key element of an ionization cooling demonstration, in addition to the assembly and instrumentation of a lattice cell, is the insertion of a range of muon beams with properties like those expected in a neutrino factory. Step I of the MICE experiment, which took place between November 2009 and August 2010, was devoted to generating these beams and measuring their properties. The purpose of this chapter is to describe the design of the cooling channel, the new muon beam line and the Step I data taking campaign.

The chapter begins by using parameterizations of beam distributions in phase space to deal quantitatively with the physics of ionization cooling and describe the expected performance of MICE. The final section explores the physics of Step I in detail, explaining how the beam line is capable of generating muon beams with a range of emittances and momenta which will be matched with the required optical parameters in the cooling channel.

2.1 Ionization cooling

Liouville's theorem states that the '*phase flow preserves volume*': if a surface in the phase space $(\vec{x}, \vec{p})$ of position and momentum evolves according to Hamilton's equations the enclosed volume remains constant [35]. In accelerator physics the independent variable of the phase flow is usually the longitudinal position z, and one studies the horizontal and vertical phase spaces (x, p_x) and (y, p_y), the 4D transverse phase space (x, p_x, y, p_y) or the 6D phase space (x, p_x, y, p_y, t, E).

The purpose of the neutrino factory front-end is to insert muons into the finite acceptance

of the acceleration lattice before a substantial fraction decay: the remaining lifetime in the laboratory frame is then rapidly extended by the time dilation factor $\gamma = E/m_\mu$ as the beam's energy is increased. For muon beams it is necessary to use the undemonstrated principle of ionization cooling, because the techniques conventionally used to cool electron and proton beams require too much time. Ionization cooling uses stochastic forces from matter interactions to disrupt the phase flow, violating Liouville's theorem. Such effects usually tend to cause the beam to expand in phase space, but by carefully choosing the matter in the channel, and by introducing certain phase space correlations using focusing magnets, it is possible to compress the phase flow. This section uses parameterizations to quantify the effect.

2.1.1 Trace space, emittance and the Twiss parameters

The longitudinal momentum p_z is often factorized from the conjugate momentum p_x when considering transverse phase space in beam lines where p_z remains approximately constant. The new 'trace space' of x and the angle to the axis $x' = p_x/p_z \approx \mathrm{d}x/\mathrm{d}z$ is an attractive choice because the matrix to transport (x, x') through drift lengths does not depend on p_z.

The most basic pieces of information about how particles are distributed in trace space are the first and second moments. In both horizontal and vertical trace space, displacement is defined relative to the trajectory of a particle with the design momentum p_z which passes through the centre of the magnets, and so the first moments are typically zero. The second moments are encapsulated by the covariance matrix:

$$\Sigma = \begin{pmatrix} \sigma_{xx} & \sigma_{xx'} \\ \sigma_{xx'} & \sigma_{x'x'} \end{pmatrix}. \tag{2.1}$$

Jaynes has argued that given only this information, if one does not wish to apply any further stipulations it is logical to model the probability distribution as being Gaussian [36]:

$$f(x, x') = \frac{1}{2\pi\epsilon} \exp\left\{ -\frac{(x, x')^{\mathrm{T}} \boldsymbol{\Sigma}^{-1} (x, x')}{2} \right\} = \frac{e^{-A/\langle A \rangle}}{\pi \langle A \rangle}, \tag{2.2}$$

where A is the amplitude or single particle emittance. Defined to be positive, the amplitude follows a chi-square distribution with zero mode. For Equation 2.2, contours of constant A are similar ellipses. The RMS ellipse $\gamma x^2 + 2\alpha x x' + \beta (x')^2 = \epsilon$, illustrated in Figure 2.1, is useful for parameterizing the distribution. The Twiss parameters α, β and $\gamma \equiv (1 + \alpha^2)/\beta$ parameterize the correlations of the distribution and are obtained from the covariance matrix:

$$\Sigma = \begin{pmatrix} \epsilon\beta & -\epsilon\alpha \\ -\epsilon\alpha & \epsilon\gamma \end{pmatrix}. \tag{2.3}$$

As the ellipse follows the phase flow its orientation may change but according to Liouville's theorem the enclosed area $\pi\epsilon$ will remain constant. The emittance $\epsilon = \sqrt{\det \Sigma} = \langle A \rangle / 2$ is the standard measure of the volume of a beam in phase space.

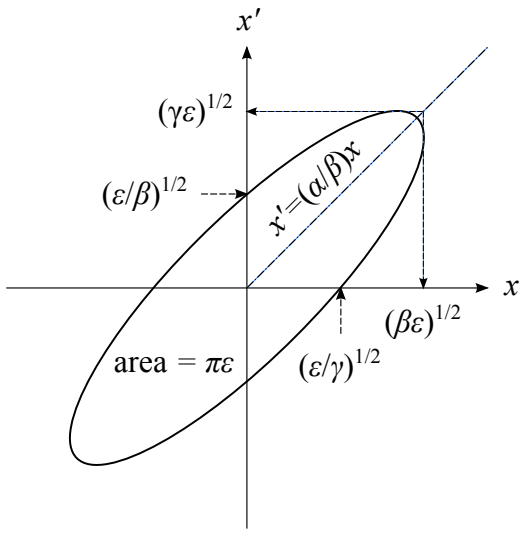

Figure 2.1: The Twiss parameterization of trace space using the RMS ellipse $\gamma x^2 + 2\alpha x x' + \beta(x')^2 = \epsilon$. The Twiss parameters α, β and $\gamma \equiv (1+\alpha^2)/\beta$ define the orientation.

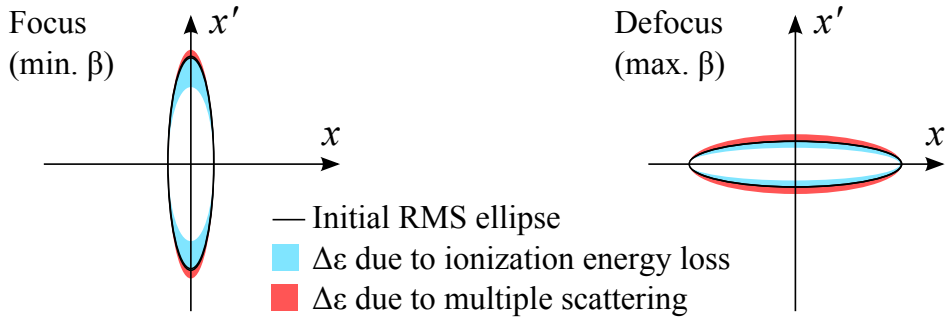

Figure 2.2: In ionization cooling the decrease in emittance can be maximized by focusing the beam. While the decrease in $\sigma_{x'x'}$ due to energy loss is exponential, the increase in emittance due to multiple scattering is minimized for low σ_{xx}.

2.1.2 Beam correlations for optimal cooling

Ionization cooling reduces the emittance by compressing the trace space distribution along the x' axis. As all components of momentum are reduced, cooling is most efficient when the beam is at its most divergent, at a minimum in β. This effect is counteracted by the stochastic effect of multiple scattering off atomic nuclei, as the RMS scattering angle is added in quadrature with the angular divergence $\sigma_{x'x'}$. As sketched in Figure 2.2, the resulting increase in the emittance is minimized when the beam has a narrow distribution in x. Therefore focusing the beam tightly is essential to the success of ionization cooling.

In modern accelerators beams are usually focused using quadrupole magnets. In a typical transfer line such as the MICE muon beam line (described in Section 2.3.1) the betatron function evolves according to the envelope equation:

$$2\beta\beta'' - (\beta')^2 + 4\beta^2 k - 4 = 0, \tag{2.4}$$

where $k(z) = q(\mathrm{d}B_y(z)/\mathrm{d}x)/p_z$ is the focusing strength [37]. The solution to the equation of motion is $x(z) = \sqrt{A\beta(z)}\cos(\phi(z) - \phi_0)$, where A is the amplitude, a constant of the

motion for a particle following the phase flow. This 'betatron oscillation' describes a particle moving around a trace ellipse of constant amplitude. The orientation of the ellipse evolves according to the solution to the envelope equation, with $\alpha = -\beta'/2$ [37].

Identical equations exist in the vertical plane, where each muon has an independent amplitude and oscillation phase. The vertical and horizontal betatron functions are different, but related as $k_y(z) = -k_x(z)$, such that a focus in the horizontal plane is typically accompanied by the beam being defocused in the vertical plane. In the ionization cooling channel of both the neutrino factory and the muon collider the muon beam is transported using superconducting solenoidal focusing coils rather than quadrupoles because the beam can be focused in both the horizontal and vertical plane simultaneously, and because the focusing strength can be bigger, leading to a stronger cooling effect. In solenoidal beam transport particles undergo uncoupled betatron oscillations in the Larmor frame [37]:

$$x_{\mathrm{L}} = \sqrt{A_1\beta_\perp}\cos\left(\Phi - \Phi_1\right) \tag{2.5}$$

$$y_{\mathrm{L}} = \sqrt{A_2\beta_\perp}\cos\left(\Phi - \Phi_2\right), \tag{2.6}$$

where $(x_{\mathrm{L}}, y_{\mathrm{L}}) = \mathbf{R}(\varphi)\cdot(x, y)$, with the Larmor angle advancing at a rate $\mathrm{d}\varphi/\mathrm{d}z = \kappa(z)$ given by the focusing strength $\kappa(z) = \frac{1}{2}qB_z(z)/p_z$. By introducing solenoidal focusing coils one may alter the axial magnetic field $B_z(z)$ and vary the focusing strength $\kappa(z)$, thereby determining the evolution of $\beta_\perp$ according to the solution of the solenoidal envelope equation[1] [39]:

$$2\beta_\perp\beta_\perp'' - (\beta_\perp')^2 + 4\beta_\perp^2\kappa^2 - 4 = 0, \tag{2.7}$$

where the prime again denotes differentiation with respect to distance along the design orbit. $\beta_\perp$ defines the envelope $\sigma_x = \sigma_y = \sqrt{\epsilon_{\mathrm{N}}\beta_\perp m_0 c/p_z}$ within which particles oscillate. A typical coil with an axial field of 4 T has a focusing strength $\kappa = 3\ \mathrm{m}^{-1}$ for a $p_z = 200$ MeV/c beam. By comparison a typical iron core quadrupole with gradient of 1 T/m has focusing strength $\sqrt{k} = 1.5\ \mathrm{m}^{-1}$ at the same momentum.

2.1.3 Phase space and normalized transverse emittance

In order to broaden the discussion to include the consideration of the coupled horizontal and vertical phase space[2] of solenoidal cooling channels as well as quadrupole focusing channels, consider the covariance matrix $\Sigma_\perp$ in the four-dimensional transverse phase space (x, p_x, y, p_y):

$$\Sigma_\perp = \begin{pmatrix} \sigma_{xx} & \sigma_{xp_x} & \sigma_{xy} & \sigma_{xp_y} \\ & \sigma_{p_xp_x} & \sigma_{p_xy} & \sigma_{p_xp_y} \\ & & \sigma_{yy} & \sigma_{yp_y} \\ & & & \sigma_{p_yp_y} \end{pmatrix}.$$

[1] Note that the solenoidal envelope equation contains a term in κ^2, but that Equation 2.4 contains a term in k. Conventions on the definition of focusing strength vary. Wiedemann's definition of the quadrupole focusing strength k is used so as to be consistent with his excellent treatment of wide aperture quadrupoles [38], which inspired the treatment of fringe fields in Chapter 5. Penn's definition of the solenoidal focusing strength κ is used as his work is a valuable reference for Chapter 7 [39].

[2] As the energy loss in ionization cooling is sufficient to stop a muon several times p_z oscillates through cooling channels, as the beam passes through material and RF cavities successively. When $p_z' \neq 0$ the phase flow does not conserve volume in trace space, and one should consider phase space instead.

As before, Twiss parameters are defined using the covariance matrix [39]:

$$\Sigma_\perp = \begin{pmatrix} \epsilon_\mathrm{N}\beta_\perp m_\mu c/p_z & -m_\mu c\epsilon_\mathrm{N}\alpha_\perp & 0 & -m_\mu c\epsilon_\mathrm{N}(\beta_\perp\kappa - \mathcal{L}) \\ & m_\mu c p_z \epsilon_\mathrm{N}\gamma_\perp & m_\mu c\epsilon_\mathrm{N}(\beta_\perp\kappa - \mathcal{L}) & 0 \\ & & \epsilon_\mathrm{N}\beta_\perp m_\mu c/p_z & m_\mu c\epsilon_\mathrm{N}\alpha_\perp \\ & & & m_\mu c p_z \epsilon_\mathrm{N}\gamma_\perp \end{pmatrix}, \tag{2.8}$$

where $\gamma_\perp \equiv (1 + \alpha_\perp^2 + (\beta_\perp\kappa - \mathcal{L})^2)$, and the mean canonical angular momentum enters as $\mathcal{L} = \langle L_\mathrm{can}\rangle / (2m_\mu c\epsilon_\mathrm{N})$. The conserved phase space volume is the normalized emittance:

$$\epsilon_\mathrm{N} = \frac{\sqrt[4]{\det\,\Sigma_\perp}}{m_\mu c}.$$

An elegant proof of the conservation of emittance for linear transformations of the phase space vector which does not make any assumptions about the probability distribution function of the beam may be found in the paper by Dragt, Neri and Ragarajan [40].

In Equations 2.5 and 2.6 A_1 and A_2 are constants of the motion and may be combined to give the transverse amplitude $A = A_1 + A_2$. The mean amplitude yields the normalized beam emittance:

$$\epsilon_\mathrm{N} = (p_z/mc)\,\langle A\rangle\,/4. \tag{2.9}$$

The definition of amplitude is particularly useful when defining the acceptance of a beam line, defined to be the highest amplitude for which a particle will not be lost from the beam by hitting a magnet or cavity aperture. Such a particle is said to have been 'scraped'.

The emittance of a raw tertiary muon beam is ~ 30 mm. Feasibility Study II of a neutrino factory requires the cooling channel to reduce the normalized emittance of the beam from $\epsilon_\mathrm{N} = 12$ mm to 2 mm, the acceptance of the acceleration section being either 9 mm or 15 mm depending on the details of the design [30]. The International Scoping Study [27] subsequently modified the design to replace recirculating linacs with fixed field alternating gradient acceleration (FFAGs), as suggested by Feasibility Study II-a [41]. FFAGs have a greater acceptance ~ 30 mm, and therefore the International Scoping Study design only requires the cooling channel to reduce the normalized emittance of the beam from $\epsilon_\mathrm{N} = 12$ mm to 7 mm. Machida *et al.* have just submitted a paper to Nature Physics describing the successful operation of EMMA, the first model FFAG with dynamics similar to a muon FFAG.

A muon collider requires a significantly lower emittance to get a sufficiently high luminosity. Recent designs with 4 TeV muon beams call for a normalized emittance of 25 μm [42]. Nevertheless the emittances of beams in electron colliders and proton colliders are smaller still. The emittance of the 100 GeV $e^\pm$ beams in LEP was 120 nm in the horizontal plane and 3.5 nm in the vertical plane, and the 7 TeV proton beams in the LHC will have an emittance of 0.5 nm. The 250 GeV $e^\pm$ beams in the ILC design require a further reduction to 0.02 nm and 8×10^{-5} nm respectively [8].

Absorber material	Z	$\epsilon_{\mathrm{N}}^{\infty}$ (mm)	Normalized $(\epsilon_{\mathrm{N}}^{\infty})^{-2}$
Liquid H	1	1.76	1.000
'Real' H		2.36	~ 0.6
Liquid He	2	2.43	0.524
LiH		3.01	0.374
Li	3	3.40	0.268
Be	4	4.27	0.170
C	6	5.85	0.091
Al	13	11.46	0.024

Table 2.1: The minimum emittances $\epsilon_{\mathrm{N}}^{\infty}$ which may be achieved by a Feasibility Study II cooling lattice using absorbers made of various low-Z materials. $(\epsilon_{\mathrm{N}}^{\infty})^{-2}$ is proportional to the central particle density in a muon beam, and is a common figure of merit when designing muon colliders. Material properties are from the Review of Particle Physics [8].

2.1.4 Choice of absorber material

The intended effect of ionization cooling is to reduce the amplitudes of a high flux of muons to be smaller than the acceptance of the acceleration lattice. The decrease in the mean amplitude of the beam can be quantified by the change in the normalized emittance, expressed by the differential equation:

$$\frac{\mathrm{d}\epsilon_{\mathrm{N}}}{\mathrm{d}z} = -\frac{\epsilon_{\mathrm{N}}}{\beta^2 E}\left\langle\frac{\mathrm{d}E}{\mathrm{d}z}\right\rangle + \frac{(13.6\ \mathrm{MeV})^2\beta_{\perp}}{2\beta^3 E m_{\mu} X_0}, \tag{2.10}$$

where $\langle \mathrm{d}E/\mathrm{d}z\rangle$ is the Bethe-Bloch rate of energy loss in matter, X_0 is the radiation length and β is the speed of the muons, not to be confused with the transverse betatron function $\beta_{\perp}$ [43]. The first term causes an exponential decrease in the emittance as a result of the muons losing transverse momentum by ionization; the second term, the effect of multiple scattering, leads to an 'equilibrium emittance' $\epsilon_{\mathrm{N}}^{\infty}$ below which the emittance cannot be reduced:

$$\epsilon_{\mathrm{N}}^{\infty} = \frac{(13.6\ \mathrm{MeV})^2\beta_{\perp}}{2\beta m_{\mu} X_0 \langle \mathrm{d}E/\mathrm{d}z\rangle}. \tag{2.11}$$

As predicted, the phase space compression has the potential to be strongest for a tightly focused beam.

The equilibrium emittance varies for different absorber materials, and is tabulated in Table 2.1. Although a high absorber atomic number Z increases the rate of energy loss, it also increases (by a larger factor) the effect of multiple scattering, leading to a higher equilibrium emittance, which does not give a useful gain for a neutrino factory beam. The ideal material is liquid hydrogen, however a direct calculation using Equation 2.11 is misleading as it must be contained in a vessel with a higher Z. This effect has been taken into account in a direct integration of Equation 2.10 by Cobb using the geometry of the MICE experiment (see Section 2.2.1), and a more realistic value is recorded in Table 2.1 under 'Real H' [44]. Lithium hydride (LiH) is also included as it was proposed in Feasibility Study II-a [41] as a practical solid alternative to liquid hydrogen for the more moderate cooling required to fit the beam into the acceptance of FFAGs, despite being toxic, reacting with water, and being

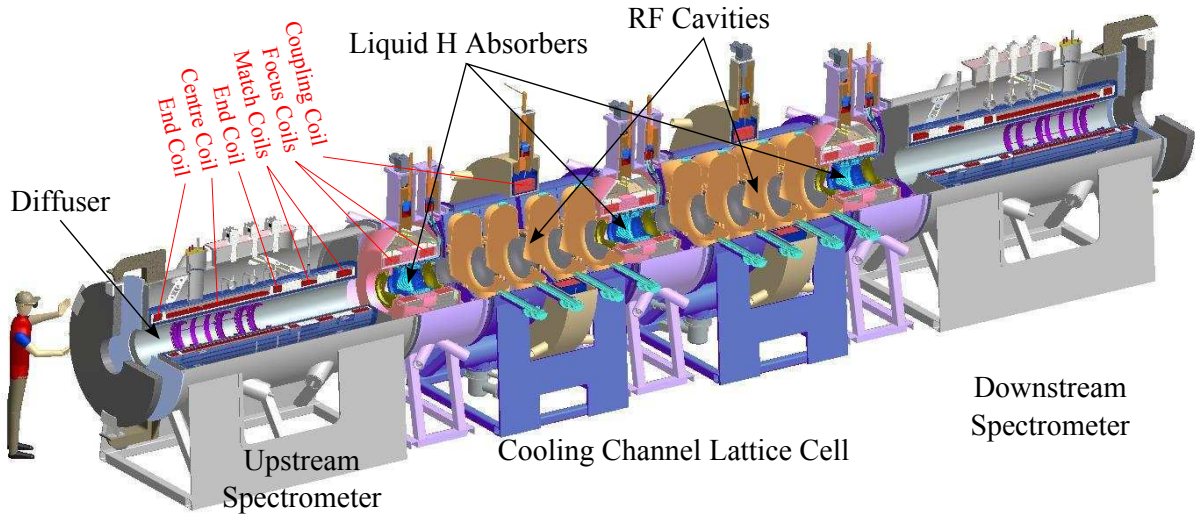

Figure 2.3: The instrumentated MICE cooling channel lattice cell in its final experimental configuration. The spectrometers measure the emittance before and after a beam passes though the experiment.

difficult to obtain as a result of restrictions arising from its capacity to moderate neutrons in nuclear weapons. As it has a mean Z of only 2 the equilibrium emittance is below the 7 mm target required for the International Scoping Study. The values were calculated at $p_z = 200$ MeV/c, not too far below the minimum of ionization energy loss and in line with Feasibility Study II. Although $\langle \mathrm{d}E/\mathrm{d}z \rangle$ is greater at lower energies, and would at first glance appear to lead to a lower equilibrium emittance, the negative slope $\partial \langle \mathrm{d}E/\mathrm{d}z \rangle / \partial E < 0$ in this region would lead to longitudinal instability, and muons being lost from the RF buckets.

2.2 The Muon Ionization Cooling Experiment

The Muon Ionization Cooling Experiment (MICE) is designed to demonstrate the ionization cooling of a muon beam for the first time. Besides refining models of energy loss and scattering, the physical principles are based on electromagnetism and atomic physics and are not in doubt: the experiment is primarily intended to demonstrate the practicality of engineering and operating a single repeatable module of a neutrino factory cooling channel. The design of the lattice is based on Feasibility Study II, which was conducted at Brookhaven in 2001, and proposed a reduction of the transverse emittance from $\epsilon_{\mathrm{N}} = 12$ mm to 2 mm using liquid hydrogen absorbers in a cooling channel with a design momentum of 200 MeV/c [30].

2.2.1 Design of the cooling channel lattice cell

The final configuration of the MICE experiment is illustrated in Figure 2.3. The MICE absorbers are 35 cm long and 30 cm in diameter and hold 21 litres of liquid hydrogen within two sets of 0.18 mm thick aluminium windows separated by vacuum. The distance between absorber centres is 2.75 m. Two sets of four 41 cm long RF cavities replace the 11 MeV lost

in each absorber. The cavities operate at 8 MV/m and 201.25 MHz, and are cooled by water pipes and closed by 0.16 mm thick pre-curved beryllium windows. The full width aperture of the channel varies between 30 cm in the absorbers and 42 cm in the RF cavities.

An element of the lattice design which the cooling channel has in common with the buncher and bunch rotation sections of the neutrino factory (see Figure 1.2) is the solenoidal focusing lattice. The magnetic lattice is designed to transport a high emittance beam with minimal losses, and focus the beam tightly in the absorbers, so as to maximize $|\mathrm{d}\epsilon_{\mathrm{N}}/\mathrm{d}z|$. The focus is achieved by placing a pair of focus coils with opposing currents around each absorber [45]. As $B_z = 0$ midway between adjacent focus coils, boundary conditions exist such that the beam is focused with $\beta'_{\perp} = 0$ and $\beta''_{\perp} > 0$. MICE design currents aim for $\beta_{\perp} = 42$ cm in line with Feasibility Study II. The two matching coils are designed to manipulate the betatron function in the upstream spectrometer such that these boundary conditions are met when the beam enters the cooling channel.

Coupling coils provide the magnetic field to transport the beam between the focus coils. In the base line optical configuration the field in consecutive absorber-focus coil modules is set such that the axial magnetic field in consecutive RF cavities has the opposite sign[3]. For this reason, two absorbers and two sets of four RF cavities is the smallest repeatable element. The lattice cell is therefore 5.5 m long, spanning the distance between the centres of the first and third MICE absorbers.

An important goal of the experiment is to demonstrate that the cooling channel can be built safely. The magnets must be able to withstand forces of ~ 90 tonnes between the coils, and magnetic materials must be bolted down or they may be accelerated to speeds approaching that of a bullet [46]. The stored magnetic energy in the coils is of the order of a few megajoules presenting a danger that the currents induced by a magnet quench could dump this energy into the liquid hydrogen and cause it to boil explosively. Finally, it should also be noted that as there are three absorbers but only two sets of RF cavities, the MICE cooling lattice is one absorber longer than a single lattice cell. It is necessary to begin and end the cooling channel with an absorber so that thermally excited electrons which have been accelerated and ejected from the RF cavities cannot damage the spectrometers.

2.2.2 Instrumentation of the channel

The test of the MICE cooling channel lattice cell will be that it achieves the emittance reduction predicted by Equation 2.10. As the cooling effect of a single lattice cell is only in the region of 10% an emittance measurement with a precision of $\sim 1\%$ is required directly before and after the cooling channel [47]. Therefore independent emittance measurements will be made by the upstream and downstream spectrometers, as illustrated in Figure 2.3. In this manner a fully engineered cooling channel lattice cell will be treated as a 'black box'. Calculations predict that about 10^5 muons will be needed to make a 1% measurement of the fractional emittance reduction of a base line $\epsilon_{\mathrm{N}} = 6$ mm and $p_z = 200$ MeV/c beam passing

[3] The purpose of alternating the polarity of the magnetic field in successive coupling coils is to avoid the growth of the mean canonical angular momentum $\mathcal{L}$ [30]. If the field did not alternate then $B_z \neq 0$ would lead to nonzero kinetic angular momentum $L \neq 0$ in the absorbers. L would then be reduced in magnitude by ionization energy losses and $\mathcal{L}$ would grow incrementally in each successive lattice cell, ultimately leading to a growth in the beam emittance (cf. Equation 2.8).

through the final experimental configuration of MICE [48].

The MICE spectrometers are designed to measure emittance by reconstructing the transverse phase space vectors of individual muons and calculating the covariance matrix in Equation 2.8 element by element. Both spectrometers measure phase space vectors using a scintillating fibre tracker placed in a uniform solenoidal field. The trackers are composed of five planes of scintillating fibres. Each plane will measure transverse position with a resolution of 0.4 mm. The helical trajectory of the muons will then be reconstructed, yielding their transverse momentum with resolution ~ 1 MeV/c [49].

The base line MICE experimental configuration calls for an axial momentum of 200 MeV/c, a uniform spectrometer field of 4 T and constant $\beta_\perp = 33$ cm in the tracker. The field is generated by a long solenoid and trimmed by short coils on either side (the centre coil and end coils in Figure 2.3). As noted in the previous section the two matching coils will then manipulate the betatron function so it is matched at a focus with $\beta_\perp = 42$ cm in the first absorber. The matching conditions for this and other beams are discussed in greater detail in Section 2.3.2.

2.2.3 The muon beam

The phase space distributions of the MICE beams should reproduce some of the features which would develop naturally in neutrino factory lattices. This places requirements on the distribution of the muons in transverse and longitudinal phase space; however creating a beam with the appropriate luminosity would entail building an entire neutrino factory front-end and collective effects have to be modelled separately. MICE was conceived as a 'single particle experiment' [50], where a muon passes though the entire lattice before the next enters.

Neutrino factory beams can be expected to have σ_{p_z} of the order of 10 or 20 MeV/c. This figure varies depending on the preceding lattice design, partly because the beam develops an amplitude-momentum correlation which extends the region of longitudinal stability. Values for various permutations of Feasibility Study II are given in Section 5.2.1 of the report [30]. The effect arises because of the longitudinal-transverse coupling of the equations of motion in solenoidal fields. While the trajectory of a particle on the design orbit is unaffected by a solenoidal focusing coil, a particle with nonzero amplitude gains a transverse momentum kick as it passes through focusing coils[4]. Entering a coil increases the transverse momentum and hence the amplitude, and also the time to traverse a lattice cell, due to the decrease in p_z. In order to remain in the region of longitudinal stability and be accelerated repeatedly, high amplitude particles must therefore have a greater p_z.

As the experiment is a single lattice cell with only two sets of RF cavities the region of longitudinal stability relevant to studies of neutrino factory cooling will not naturally be selected, but must be selected artificially through measurements of the RF phase experienced by each particle in each cavity. As the spectrometers are not capable of precise time measurements two timing detectors (TOF1 and TOF2) will be placed immediately upstream and downstream of the experimental configuration pictured in Figure 2.3.

[4] This effect may be illustrated with reference to the simpler example of a particle passing through the fringe field of a solenoid of field B_0. Busch's theorem dictates that a paraxial particle with charge q and an initial transverse displacement ρ_0 receives momentum kick $p_\phi = -q\rho_0 B_0/2$ [37].

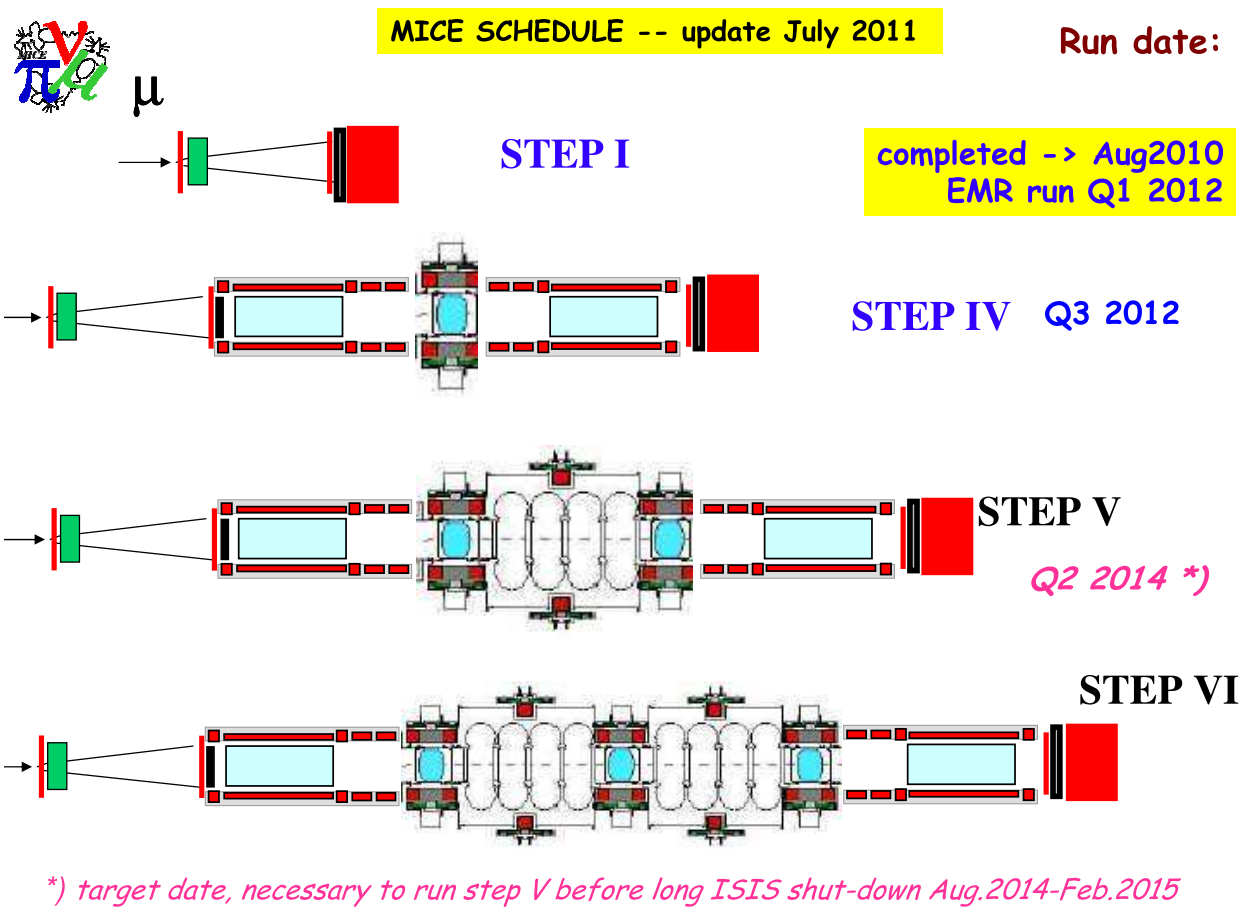

Figure 2.4: The schedule for the installation and testing of the components of the MICE experiment [51]. Step II and Step III have been skipped due to delays in the installation of the spectrometer solenoid.

The beams used to test the performance of MICE will be generated by the MICE beam line, described in Section 2.3.1. The muon component is selected by particle identification detectors upstream and downstream of the channel. The process of particle identification in Step I is described in Chapter 3.

2.2.4 Status of the experiment

As the MICE experiment is primarily an engineering demonstration the elements are being installed incrementally. The schedule is illustrated in Figure 2.4. The dates for Step VI (the final experimental configuration) have not yet been set [51]. Step V, which tests the effect of half a lattice cell, is planned for 2014.

Step I has recently been completed. It was designed to test whether the muon beams which will be used by MICE occupy the required parameter space, and adequately mimic the correlations which would be observed in a neutrino factory. Step I is described in the following section; its analysis is the subject of this thesis.

As a result of delays in the construction of the spectrometer solenoids, the collaboration has decided to proceed directly to Step IV in 2012, with a single absorber and the upstream and

downstream spectrometers. A liquid hydrogen absorber (Feasibility Study II), a lithium hydride absorber block (Feasibility Study II-a) and a lithium hydride absorber wedge (schemes for six-dimensional cooling for a muon collider) will be all tested.

2.3 Step I of the MICE experiment

A neutrino factory would contain ten to twenty of the lattice cells of the type being constructed for the MICE experiment. The intended effect of such a cooling channel is to reduce the transverse normalized emittance from $\epsilon_{\mathrm{N}} = 12$ mm to 2 mm [30]. In order to demonstrate the efficiency of ionization cooling throughout the whole cooling channel the MICE collaboration has decided to measure the effect of the lattice cell on beams with initial $\epsilon_{\mathrm{N}} = 3$ mm, 6 mm and 10 mm [52].

This range of emittances will be generated by increasing σ_{p_x} and σ_{p_y} using multiple scattering in various thicknesses of a high-Z material. Initial designs assumed a $\epsilon_{\mathrm{N}} = 3$ mm beam passing through lead plates ranging from a thickness of zero to 15.2 mm [53]. The design has evolved for engineering reasons since Step I finished, to feature irises made of tungsten petals [54]. In light of the variable nature of the design parameters of the neutrino factory, the initial beams will also have a range of design momenta of 140 MeV/c, 200 MeV/c and 240 MeV/c, generated by tuning the currents in dipoles in the muon beam line [52].

These nine combinations of initial beam parameters are referred to as the *emittance-momentum matrix*. In Step I the MICE collaboration attempted to create a μ^- beam and a μ^+ beam for every element of the matrix. The subject of this thesis is to characterize these beams to test whether they have the required properties.

2.3.1 The design of the muon beam line

The MICE experiment is being installed at a new muon beam line at the ISIS proton synchrotron at the Rutherford Appleton Laboratory in the United Kingdom. The layout of magnets and detectors during Step I is illustrated in Figure 2.5.

The beam line begins with a titanium target which is inserted into the beam of the ISIS proton synchrotron at the end of the cycle, when the protons have an energy of 800 MeV [56, 57]. The resulting beam of scattered protons and pions created in strong interactions with the target is transported into a dipole (dipole 1) by a quadrupole triplet (Q1-Q2-Q3). The current in dipole 1 is chosen to transport pions with a design momentum of order 450 MeV/c, eliminating neutral particles and most protons. Dipole 1 deflects the design pion trajectory by 60 degrees, steering the beam through a vacuum pipe and into the 5 cm radius bore of the decay solenoid.

The muon beams which will be cooled by MICE originate from pion decays in the decay solenoid. The 5 T field helps to capture the emitted muons, and transport them into the acceptance of dipole 2. The momentum spectrum of pions and muons at dipole 2 is illustrated in Figure 2.6. The current in dipole 2 is chosen to transport the design momentum of muons which have been emitted backwards in the frame of the decaying pion in the decay solenoid. These muons have the maximum separation from the peak of pion momenta,

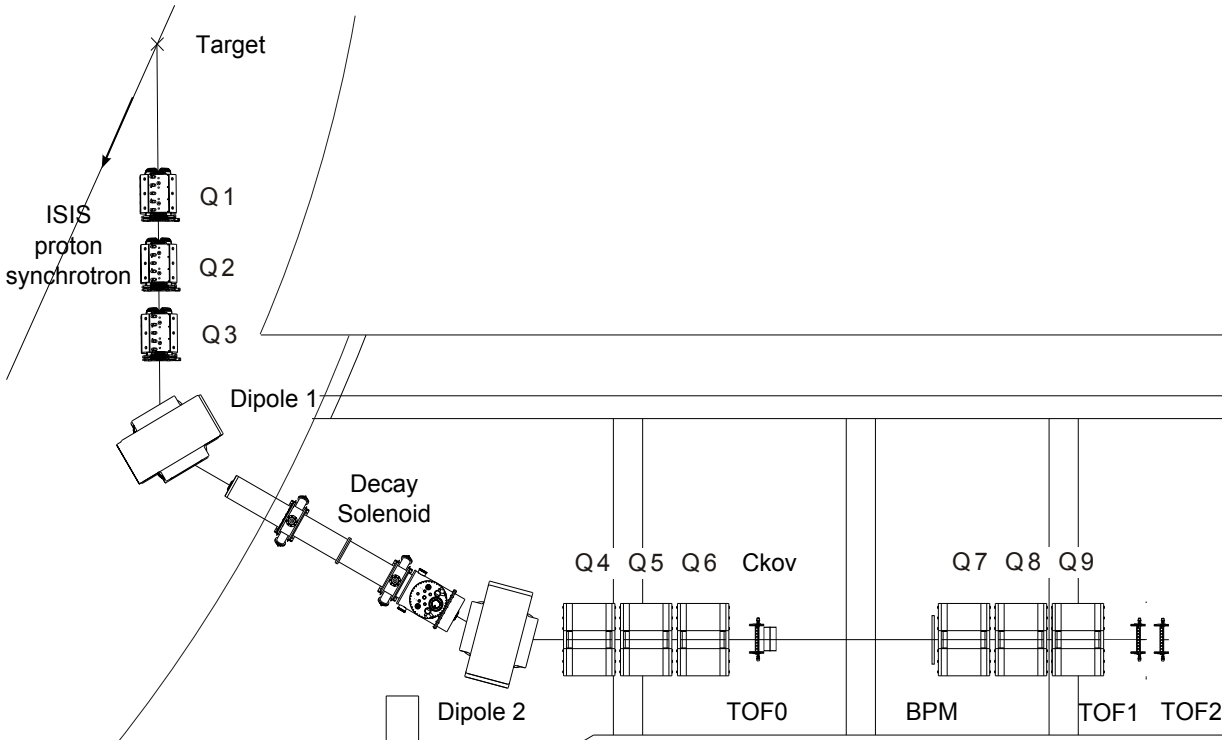

Figure 2.5: A diagram of the MICE muon beam line during Step I. The cooling channel lattice cell and its spectrometers will be incrementally be inserted between TOF1 and TOF2. Figure adapted from MICE note 242 [55].

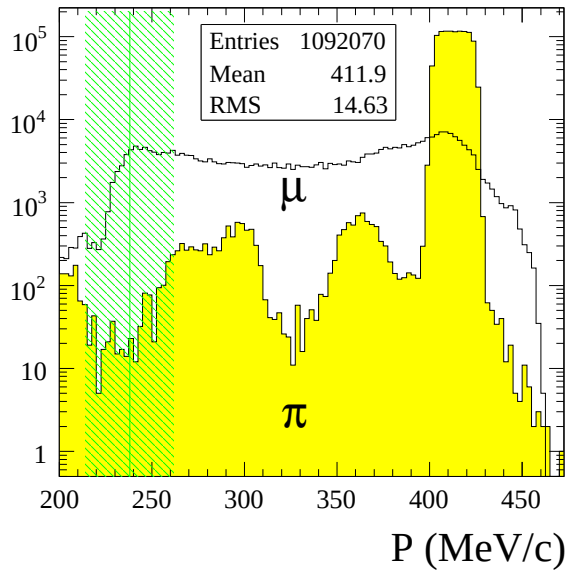

Figure 2.6: The momentum spectra of pions and muons at dipole 2. The current in dipole 2 is chosen to transport the shaded band of backwards decaying muons to maximize the muon flux while minimizing the pion contamination [52].

thereby minimizing the pion contamination in the subsequent beam [52]. The two dipoles can be tuned to transmit backwards decaying muons at any momenta. The particle rate generated by the beam line has been studied by Dobbs [58, 59].

Rather than directly inserting the muon dominated beam from dipole 2 into the MICE cooling channel, the beam first passes through two quadrupole triplets (Q4-Q5-Q6 and Q7-Q8-Q9), three timing detectors (TOF0, TOF1 and TOF2), a Cherenkov detector (Ckov) and a beam profile monitor (BPM). TOF0, TOF1 and the Cherenkov are designed to identify the species of particles before they enter the cooling channel. The Cherenkov has not yet been calibrated, but will eventually help to distinguish muons from pions. TOF0 and TOF1 were calibrated and are described in detail in Chapter 3. TOF2, which will eventually be positioned after the cooling channel, was present in Step I, but not calibrated[5]. The BPM was an *ad hoc* addition to the Step I beam line which was useful for observing the beam in the control room, but is not read out by the DAQ.

In future steps the upstream spectrometer will be installed in its final position directly downstream of TOF1. Each of the beams in the emittance-momentum matrix should have their nominal emittance in the spectrometer, however the beams at the end of the Step I beam line are expected to have approximately the same emittance regardless of the choice of magnet currents, as they originate from the same source. The emittance will be inflated by multiple scattering in the diffuser. The diffuser is a device which will insert a variable thickness of material directly in the path of the beam, in the magnetic field of the first spectrometer solenoid, immediately upstream of the tracker.

For each element of the emittance-momentum matrix the required diffuser thickness t is dictated by the emittance increase to the nominal value. Given t one may calculate the energy loss in the diffuser plate and hence the momentum which the dipoles must be tuned to transmit to get the nominal momentum in the cooling channel. The final question is how to set the currents in the quadrupoles. By setting the current in quadrupoles four to nine one has six handles with which to manipulate the phase space distribution of the tertiary muon beam. In order to understand how to make this choice it is necessary to investigate the matching conditions required in the upstream spectrometer.

2.3.2 Matching conditions in the upstream spectrometer

As the upstream spectrometer will provide the measurement of emittance before the cooling channel 'black box', each of the beams in the emittance-momentum matrix should have their nominal ϵ_{N} and p_z (plus the energy loss in half an absorber[6]) in the uniform field region of the tracker. In addition, the beams must obey certain matching conditions.

For design simplicity and optimal transmission all the beams should obey the matching conditions $\beta'_\perp = 0$ and $\beta''_\perp = 0$ in the uniform field region of the spectrometer. The envelope equation (Equation 2.7) shows that this is only possible at $\beta_\perp = 1/\kappa$. In the base line

[5] The purpose of TOF2, and the secondary purpose of TOF1, is to allow the phases at which individual muons were accelerated to be reconstructed when RF cavities are installed in Step IV.

[6] The MICE cooling channel lattice cell will be installed between timing detectors TOF1 and TOF2 in the following steps of the experiment. Technically the nominal momentum is defined in the centre of the absorbers, and the required momentum in the upstream spectrometer is the nominal value plus the mean momentum loss in half an absorber.

$p_z = 200$ MeV/c cases $B_z = 4$ T and $\beta_\perp = 33$ cm. Currents in the match coils may then be tuned such that the beam is focused with $\beta_\perp = 42$ cm in the centre of the first absorber, as specified in Feasibility Study II [60].

For ease of comparison it is desirable[7] that the 140 MeV/c beams evolve in the cooling channel according to the same betatron function. The envelope equation shows that as the betatron function only depends on initial conditions and the focusing strength $\kappa(z) = \frac{1}{2}qB_z(z)/p_z$. If a beam with $\beta_\perp = 33$ cm is injected into in the uniform field region of the upstream spectrometer the 140 MeV/c beam will evolve with the same betatron function if B_z is reduced in equal proportion to p_z as this yields the same focusing strength. To a good approximation[8] this can be accomplished by scaling the currents in the end, centre, matching, focus and coupling coils (cf. Figure 2.3) by a factor 140/200.

Unfortunately the spectrometer solenoids are not capable of generating a large enough field to achieve $\beta_\perp = 33$ cm for the 240 MeV/c beams. The spectrometer field for these beams will remain at $B_z = 4$ T, yielding a matched betatron function $\beta_\perp = (240/200)\times 33$ cm $= 39.6$ cm. By contrast the currents in the focus coils and coupling coils *will* be scaled, necessitating a separate optimization of the matching coil currents to obtain a focus $\beta_\perp = 42$ cm in the absorbers.

In practice it is necessary to distinguish between the design and measured betatron functions. The design betatron function is the solution to the envelope equation with desirable properties given a particular focusing strength profile and specific boundary conditions. By contrast the measured betatron function is deduced from the covariance matrix. The purpose of the beam line is to insert beams with matched boundary conditions into the upstream spectrometer. The remainder of this chapter is devoted to describing how optical configurations of magnet currents were designed to accomplish this. These design Twiss parameters are compared with measurements in Chapter 6.

2.3.3 Emittance inflation in the MICE diffuser

Simulations predicted that the emittance of the muon beam which emerges from the decay solenoid should be $\epsilon_\mathrm{N} \approx 3$ mm. As emittance is conserved in dipoles, quadrupoles and drifts, it has been assumed that no emittance inflation is required to generate the $\epsilon_\mathrm{N} = 3$ mm matrix elements. The $\epsilon_\mathrm{N} = 6$ mm and 10 mm elements will be generated using increasing thicknesses of a high-Z material.

The principle of emittance inflation in the MICE diffuser is illustrated in Figure 2.7. As the beam passes through the fringe field of the spectrometer solenoid $\beta_\perp$ decreases to a fixed value in the uniform field region. For diffuser thickness $t > 0$ Liouville's theorem is violated by multiple scattering and the emittance increases sharply [53]. As the diffuser plates are thin the beam size $\sigma_x = \sqrt{\epsilon_\mathrm{N}\beta_\perp m_\mu c/p_z}$ remains approximately constant and therefore the betatron function decreases in reciprocal proportion.

[7] This has been disputed.

[8] This is an approximation as $\langle p_z \rangle$ deviates from the nominal values of 200 MeV/c and 140 MeV/c due to energy loss in the absorbers and re-acceleration. Furthermore even in a channel devoid of absorbers and RF, only a zero amplitude muon would maintain the nominal momentum, as particles gain transverse momentum and lose longitudinal momentum as they enter a solenoidal fringe fields. Both effects mean that strictly correct scaling factor will vary slightly from 140/200 in each coil.

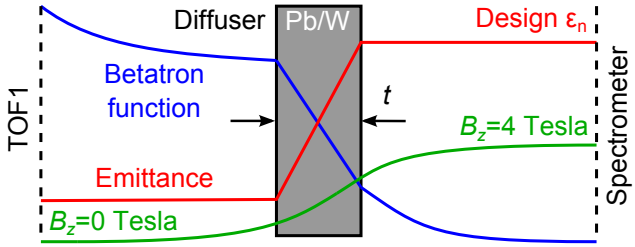

Figure 2.7: A sketch of the principle of emittance inflation in the diffuser showing the interface between a region of quadrupole focusing and a region of solenoidal focusing. Step I was devoted to testing whether the MICE beams will be matched in the spectrometer; in the absence of the spectrometer it was necessary to characterize the beams at TOF1 instead.

			p_z in the absorbers		
			140 MeV/c	200 MeV/c	240 MeV/c
ϵ_N after the diffuser	3 mm	t	0 mm	0 mm	0 mm
		p_z	151 MeV/c	207 MeV/c	245 MeV/c
		$\alpha_\perp$	0.2	0.1	0.1
		$\beta_\perp$	56 cm	36 cm	42 cm
	6 mm	t	5.0 mm	7.5 mm	7.5 mm
		p_z	148 MeV/c	215 MeV/c	256 MeV/c
		$\alpha_\perp$	0.3	0.2	0.2
		$\beta_\perp$	113 cm	78 cm	80 cm
	10 mm	t	10.0 mm	15.5 mm	15.5 mm
		p_z	164 MeV/c	229 MeV/c	267 MeV/c
		$\alpha_\perp$	0.6	0.4	0.3
		$\beta_\perp$	198 cm	131 cm	129 cm

Table 2.2: The lead diffuser thickness t and the momentum p_z and transverse Twiss parameters $\alpha_\perp$ and $\beta_\perp$ which are required immediately upstream of the diffuser to generate the emittance and momentum corresponding to each beam, while fulfilling the matching requirements in Section 2.3.2 [53].

The problem of determining the required boundary conditions before the diffuser has been addressed by Apollonio [52,53]. Table 2.2 shows the diffuser thicknesses, momenta and Twiss parameters on the upstream face of the diffuser to generate the elements of the emittance-momentum matrix, while fulfilling the matching conditions described in Section 2.3.2. These values corresponds to an optimization of the old lead diffuser design. A new tungsten diffuser has been designed to replace this for reasons of engineering practicality, necessitating a re-optimization for the new design if it is adopted. Unfortunately neither the diffuser nor the spectrometer was present in the Step I beam line as the spectrometer solenoid was being repaired. It is therefore necessary to test whether the beam is matched at TOF1, rather than in the uniform region of the spectrometers where the matching conditions are defined.

2.3.4 Optical configurations of the MICE beam line

Previously in Section 2.3 the method of generating a 3×3 emittance-momentum matrix of muon dominated beams has been discussed. The remaining question is: how does one set the currents in the beam line magnets to satisfy the matching conditions in the upstream spectrometer?

Three collections of optical configurations have been designed so far. They are described below, with corresponding currents to be found in Table 2.3.

The base line optical configuration

The first attempt to match a beam was made by Tilley using the TURTLE beam line simulation software to match the base line (6 mm, 200 MeV/c) μ^- matrix element. The quadrupole currents were varied until the matching conditions described in Section 2.3.2 were met [61].

The currents in dipole 1 and dipole 2 were optimized to transmit backwards decaying muons at the required momentum via an optimization using Geant4 by Roberts [62]. Each of the three quadrupole triplets were arranged to focus-defocus-focus in the horizontal plane. The currents are simply reversed for the base line μ^+ optical configuration.

The re-scaled TURTLE 'emittance-momentum matrix' of beams

Apollonio used the principle of magnet re-scaling to obtain optical configurations for the other elements of the emittance-momentum matrix [61]. These new optical configurations are based on Tilley and Roberts' base line optical configuration. They are designed to transport muons to the cooling channel with the nominal emittance and momentum but are *not* optimized to obey the matching conditions.

Magnet re-scaling is a simple technique designed to generate identical betatron functions β_x and β_y for beams at different momenta. The principle is to scale the current in the beam line magnets to the momentum of the new beam so that the focusing strength profile is the same as for the base line beam[9]. In the Step I beam line β_x and β_y evolve according to the envelope

[9] The approach is the same as that described in Section 2.3.2 for the cooling lattice, but applied to the

equation (Equation 2.4) as a function of the focusing strength $k(z) = q(\mathrm{d}B_y(z)/\mathrm{d}x)/p_z$. Working back from the spectrometer, Apollonio calculated p_z at the centre of the each magnet such that energy loss yields the required momentum upstream of the diffuser (cf. Table 2.2) and scaled the currents by the ratio with the momentum at the same position in Tilley's base line configuration.

As noted above, the re-scaling technique simply yield the nominal emittances and momenta and pays no attention to the specific matching requirements on $\beta_\perp$ and $\alpha_\perp$ in Table 2.2. Nevertheless an advantage of re-scaling is that the beams should be *approximately* matched, up to corrections for the effect of the thickness of the diffuser on the Twiss parameters.

The genetic algorithm 'emittance-momentum matrix' of beams

A disadvantage of the base line optical configuration, and therefore also the re-scaled TURTLE optical configurations, is that stochastic effects in the interaction of particles with matter and magnet acceptances were not modelled in detail. Both effects are important as the MICE beams pass through detectors, and simulations predict (cf. Chapter 4) that $\sim 60\%$ of muons are scraped in quadrupole 7. Furthermore, surveys of the geometry of the beam line reveal discrepancies with that assumed by Tilley and Roberts [63].

Apollonio addressed both points by attempting to individually match a beam for each of the emittance-momentum matrix elements using the Geant4 based beam line simulation code G4Beamline, which incorporates a realistic model of interactions in matter [62]. Care was taken to incorporate recent survey results and detailed models of the material of the magnet apertures. A genetic algorithm allowed the current in quadrupoles 4-9 to evolve from the re-scaled TURTLE beam optical configurations according to random mutations. Changes which improved the matching in the uniform field region of the spectrometer were kept, and the evolutionary process resumed with the modified configuration.

With hindsight the configuration space is problematically large for this approach and the algorithm struggled to converge, failing entirely for the $\epsilon_\mathrm{N} = 3$ mm elements of the emittance-momentum matrix. This optical design is not studied in this thesis.

evolution of β_x and β_y in a beam line of quadrupoles rather than $\beta_\perp$ in a solenoidal focusing lattice.

Optical design	Polarity	ϵ_N (mm)	p_z (MeV/c)	Magnet current (Amps) Q1	Q2	Q3	D1	DS	D2	Q4	Q5	Q6	Q7	Q8	Q9
Re-scaled TURTLE	μ^-	3	140	80.3	100.3	69.8	243.1	524.2	73.9	122.5	164.3	108.8	101.3	153.1	130.6
			200	97.7	122.0	84.9	305.0	637.9	91.5	153.4	205.7	136.4	133.9	202.5	172.9
			240	113.7	142.1	98.9	370.1	743.0	104.4	76.2	236.3	156.7	157.0	237.6	203.0
		6	140	81.9	102.3	71.2	248.4	534.6	75.5	125.2	167.9	111.2	104.2	157.6	134.4
			200	*102.4*	*127.9*	*89.0*	*323.2*	*668.6*	*94.2*	*158.1*	*212.0*	*140.6*	*138.7*	*209.8*	*179.2*
			240	118.3	147.8	102.8	390.2	773.0	108.5	183.6	246.2	163.3	164.4	248.8	212.6
		10	140	84.7	105.7	73.6	257.8	552.5	77.8	129.2	173.3	114.8	108.6	164.2	140.1
			200	107.6	134.4	93.5	344.2	703.0	99.1	166.8	223.7	148.3	147.5	223.3	190.7
			240	121.9	152.3	106.0	406.9	797.0	112.0	189.6	254.3	168.7	170.4	258.0	220.4
	μ^+	3	140	80.3	100.3	69.8	243.1	524.0	73.9	122.5	164.3	108.8	101.3	153.1	130.6
			200	97.7	122.0	84.9	305.0	637.9	91.5	153.4	205.7	136.4	133.9	202.5	172.9
			240	113.7	142.1	98.9	370.1	743.0	104.4	176.2	236.3	156.7	157.0	237.6	203.0
		6	140	81.9	102.3	71.2	248.4	534.6	75.5	125.2	167.9	111.2	104.2	157.6	134.4
			200	*102.4*	*127.9*	*89.0*	*323.2*	*668.6*	*94.2*	*158.1*	*212.0*	*140.6*	*138.7*	*209.8*	*179.2*
			240	118.3	147.8	102.8	390.2	772.7	108.6	183.6	246.2	163.3	164.4	248.8	212.6
		10	140	84.7	105.7	73.6	257.8	552.5	77.8	129.2	173.3	114.8	108.6	164.2	140.1
			200	107.6	134.4	93.5	344.2	702.8	99.1	166.8	223.7	148.3	147.5	223.3	190.7
			240	121.9	152.3	106.0	406.9	797.0	112.0	189.6	254.3	168.7	170.4	258.0	220.4
Genetic algorithm	μ^-	6	140	81.9	102.3	71.2	248.4	535.0	75.5	129.2	199.9	105.0	77.8	149.6	117.6
			200	81.9	102.3	71.2	248.4	535.0	75.5	197.3	264.2	159.7	126.4	222.8	185.1
			240	118.3	147.8	102.8	390.2	773.0	108.5	213.9	313.1	198.4	152.7	264.2	224.5
		10	140	84.7	105.7	73.6	257.8	553.0	77.8	111.8	199.6	126.8	80.8	130.1	101.3
			200	107.6	134.4	93.5	344.2	702.8	99.1	168.0	265.4	124.5	109.5	211.7	180.5
	μ^+	6	200	102.4	127.9	89.0	323.2	668.6	94.2	197.3	264.2	159.7	126.4	222.8	185.1
			240	118.3	147.8	102.8	390.2	772.7	108.6	213.9	313.1	198.4	152.7	264.2	224.5
		10	140	84.7	105.7	73.6	257.8	552.5	77.8	111.8	199.5	126.8	80.8	130.1	101.3
			200	107.6	134.4	93.5	344.2	702.8	99.1	168.0	265.4	124.5	109.5	211.7	180.5
			240	121.9	152.3	106.0	406.9	797.0	112.0	138.8	290.5	198.1	155.5	281.3	219.5

Table 2.3: Magnet currents for the re-scaled TURTLE and genetic algorithm optical designs. Tilley and Roberts' (6 mm, 200 MeV/c) base line optical configuration is italicized. The polarity of the currents depends on the charge of the particles the beam line is designed to transport. In all cases each quadrupole triplet is arranged to *focus–defocus–focus* in the horizontal plane.

2.3.5 The Step I data taking campaign

The Step I data taking campaign took place between November 2009 and August 2010. TOF0 and TOF1 were calibrated in February 2010 and August 2010. Quadrupole 2 was broken before the February calibration. All the beam line magnets were operable in the time between the calibrations. This is the period investigated in this thesis.

Data from TOF0 and TOF1 was taken for base line μ^- and μ^+, and indeed all of the re-scaled TURTLE optical configurations with both polarities. These beams are analysed in Chapter 4, Chapter 5 and Chapter 6.

According to the design principles described in the previous section, the polarities of the currents in the dipole and quadrupole magnets was reversed when the polarity of the beam line (set by the polarity of the current in dipole 1) was switched, with the sole exception of the decay solenoid as this was not possible. The only other asymmetry between μ^- and μ^+ beams was the presence of a few centimetres of polyethylene (the proton absorber) inserted directly after the decay solenoid in positive polarity optical configurations to reduce the proton contamination in the beam.

Genetic algorithm data was taken for the selection of matrix elements for which magnet currents are recorded in Table 2.3. These beams are useful components of larger data sets used for the purpose of calibration in Chapter 3 and Chapter 4, but are not characterized in this thesis.

Appendix A lists the experimental runs in the collated data sets of the matrix elements in the re-scaled TURTLE and genetic algorithm optical designs and a number of magnet scans around them.

2.4 Conclusion

The MICE experiment has been devised to demonstrate ionization cooling for the first time, to make building a neutrino factory a realistic short term option. As MICE is primarily an engineering demonstration of a number of sophisticated and potentially hazardous technologies it is being assembled and tested incrementally.

In Step I the collaboration tested an emittance-momentum matrix of μ^- and μ^+ beams designed to be matched with $\epsilon_{\mathrm{N}} = 3$ mm, 6 mm and 10 mm in the upstream spectrometer, and $p_z = 140$ MeV/c, 200 MeV/c and 240 MeV/c in the absorber centres. This selection of beams will allow MICE to demonstrate ionization cooling over the entire design space of a neutrino factory cooling channel in future steps.

The Step I beams were originally to be characterized by the upstream spectrometer, in its final position immediately downstream of TOF1. In the event neither the diffuser or the spectrometer were present in Step I due to a fault in the spectrometer solenoid. In the absence of the spectrometer the beam properties have instead been characterized at TOF1 using the upstream time of flight system. This thesis describes that analysis.

Chapter 3

Measuring time and position with the time of flight detectors

MICE time of flight detectors TOF0 and TOF1 were calibrated to measure time at the University of Sofia. This chapter describes how the calibration has been extended to allow measurements of transverse position by comparing the arrival times of light signals in the photo-multiplier tubes on either side of a detector. The resolution of the detectors is measured to be 51.0 ps and 59.5 ps, and 0.98 cm and 1.14 cm.

The measurement of transverse position is of primary interest to MICE in Step I. It is useful both as a directly measured quantity for comparison with simulation, and as the basis for measurements of transverse momentum, as will be described in Chapter 5.

It was originally intended that the upstream spectrometer would be the final element of the Step I beam line, and measure the transverse phase space vector (x, p_x, y, p_y) of every muon [49]. The measured optical parameters would then have been compared with predictions, and a direct test made as to whether the beam was matched. As a result of a fault with the spectrometer solenoid, the upstream tracker was not available during Step I.

The time of flight detectors TOF0 and TOF1 were used to characterize the transverse phase of the beams instead [64]. They were not designed for this purpose. This chapter describes how a measurement technique was designed and optimized. The detectors are described in the next section.

3.1 The time of flight detectors TOF0 and TOF1

TOF0 and TOF1 are designed to measure the time at which particles pass through them with a resolution of 50 ps [65]. The detectors are both composed of two planes of orthogonally oriented scintillator slabs. TOF0 is made up of two planes of ten scintillator slabs of width 4 cm, length 40 cm and thickness 2.5 cm. The active area of the detector is therefore a square of dimensions 40 cm $\times$ 40 cm, with a thickness of 5 cm. TOF1 has two planes of seven scintillator slabs of width 6 cm, length 42 cm and thickness 2.5 cm. The active area of the detector is therefore a square of dimensions 42 cm $\times$ 42 cm, with a thickness of 5 cm.

TOF1 is illustrated in Figure 3.1. The slabs in both detectors are individually wrapped in aluminized mylar to reflect scintillation light originating within the slabs, and black PVC to prevent light being transmitted between adjacent slabs [66]. The wrapping is thin and

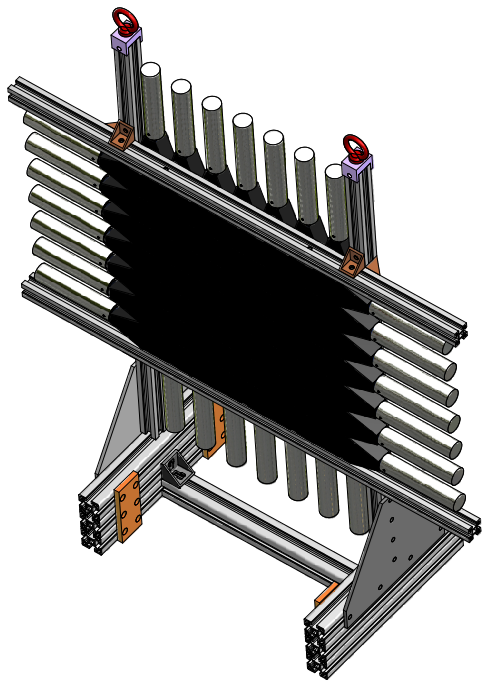

Figure 3.1: The TOF1 detector (illustrated) is composed of two planes of seven 6 cm × 42 cm × 2.5 cm scintillator slabs. TOF0 has a similar design, but is composed of two planes of ten 4 cm × 40 cm × 2.5 cm scintillator slabs.

the slabs were assembled with a tolerance of 1 mm[1]. Each slab has a light-guide and photomultiplier tube (PMT) at either end. TDC and ADC counts are recorded in the DAQ when scintillation light causes a signal in a PMT which triggers its discriminator. The data is then analysed offline by G4MICE [67], the MICE analysis and simulation software package[2]. The measurement technique is described in detail in Section 3.2

A simple position measurement may be made by noting which slab was illuminated in each plane. One may thereby deduce that the muon passed within a square on the face of the detector with the dimensions of the width of a slab. If the position of the muon is estimated to be the centre of this square the measurement will be biased if centre of the beam is on one side.

A complementary position measurement may be made by comparing the time of arrival of light signals in the PMTs at either end of a slab. This measurement is unbiased, and though it has a similar resolution, produces a measurement which is easier to analyse as it is not quantized by slab number. This new position measurement technique is the main subject of this chapter.

Confusingly, the vertically oriented TOF slabs are numbered in the direction of increasing x

[1] The probability of a particle passing through the gap between slabs is negligible, and in the event that a particle does not register a hit in one plane, the reconstruction can nevertheless proceed with information from only the orthogonal slab intersected by the particle's trajectory.

[2] G4MICE is a software package which has been developed by the MICE collaboration for the similation and analysis of the MICE experiment. The code is designed to analyse data and Monte Carlo simulated 'fake data' in the same way. By contrast to traditional beam transport simulations, Geant4 [68] has been used to model the transit of particles, in order to model energy loss and scattering in matter accurately.

in a *left-handed* coordinate system[3]. As a result, a bug in G4MICE version 2.4 returns x_{LH}. This is inconsistent with the right-handed coordinate system which is standard in software based on Geant4. This chapter also describes how to reconstruct x_{LH} using the new timing technique. In later chapters, the transformation $x_{\mathrm{RH}} = -x_{\mathrm{LH}}$ to the right-handed coordinate system of the rest of G4MICE has been made.

The analysis described here shows how the existing TOF timing calibration has been extended for use in characterizing the beam in Step I. The following section describes the time calibration applied automatically in G4MICE by reconstruction software developed at the University of Sofia. The timing resolution of each pixel of TOF0 and TOF1 is also measured. The method for extending the calibration for position measurements (motivated by the unavailability of the spectrometer in Step I) is described in Section 3.3.

If TOF position measurements are required in future steps it would be beneficial to avoid the two phase calibration described in this chapter by fully constraining all degrees of freedom in the initial calibration, and using the measurement of effective propogation speed of light signals recorded in Section 3.3. Appendix B sketches out a possible scheme for such a calibration.

3.2 Timing resolution revisited

The methods by which time and position may be measured using PMT timing measurements are closely related. Timing measurements used in Section 3.2 are obtained using the calibration developed at the University of Sofia. It is necessary to describe the method to understand the technique for extending it described in Section 3.3. In order to put the position measurement in context, the principle behind the time measurement is described here. In addition, as the resolutions of the two measurements are proportional, this section also complements previous treatments by computing the resolution of the TOFs during Step I [69, 70].

3.2.1 Reconstructing the time of a particle

Consider the passage of a particle through a horizontally orientated TOF scintillator slab, as illustrated in Figure 3.2. The particle passes through the slab at time t_x at a displacement x from the mid-plane of the slab. Light signals propagate to both ends of the slab at an effective propagation speed c_{eff}. The arrival times of the signals in the $x < 0$ and $x > 0$ PMTs are given by:

$$t_- = t_x + \frac{l + x}{c_{\mathrm{eff}}} \tag{3.1}$$

$$t_+ = t_x + \frac{l - x}{c_{\mathrm{eff}}}. \tag{3.2}$$

[3] In both left-handed and right-handed MICE coordinate systems, $\hat{z}$ is directed along the design axis, and $\hat{y}$ is directed upwards from the floor of the hall. Therefore $\hat{x}_{\mathrm{LH}}$ points towards the outside of the curve of the particles in the dipole magnets.

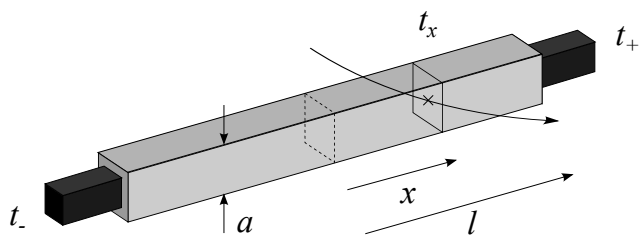

Figure 3.2: A diagram illustrating the passage of a charged particle through a horizontally oriented TOF scintillator slab of length $2l$. The particle passes through the slab at time t_x, at a displacement x from the mid-plane of the slab. The light signal arrives in the $x < 0$ PMT at t_-, and arrives in the $x > 0$ PMT at t_+.

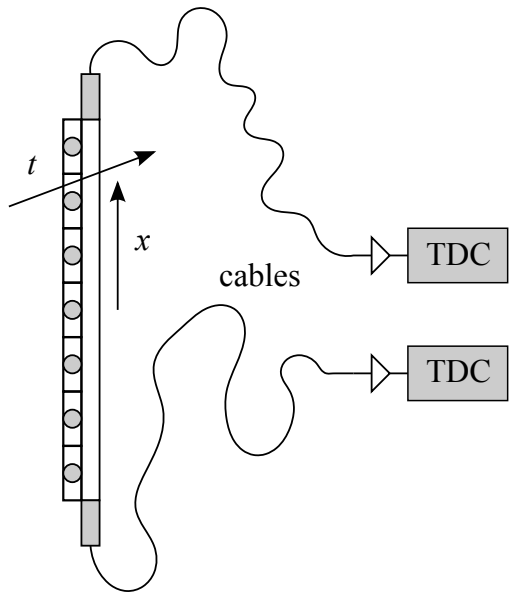

Figure 3.3: A sketch illustrating the readout of the TOF detectors. Cables reading out PMTs on opposite sides of a slab are connected to different TDCs, and the cable lengths may vary.

The $t_\pm$ are obtained using the TOF calibration applied automatically by the G4MICE software [69]. This calibration is adequate for measuring time with the TOF detectors. It is applied to raw TDC and ADC counts in two steps:

1. The first step in the calibration removes a bias and reduces σ_{PMT}. A particle depositing more energy than average in a scintillator slab will tend to trigger the channel's discriminator earlier relative to t_x than a particle which deposits less energy. This effect is cancelled by a *time walk calibration* based on a measurement of the total ADC count in the channel during the passage of the particle.

2. The second step removes the bias on the measurement of $t_\pm$ caused by the variation in the lengths of the cables connecting the PMTs to the data acquisition (DAQ) electronics. The problem is illustrated in Figure 3.3. The *cable length calibration* will be discussed further in Section 3.3.

Two calibrations were performed during the Step I data campaign, in February and August 2010. As the time walk calibration requires a large dataset, it was not possible to calculate a calibration for all the PMTs. Therefore it is not possible to measure the time and position of

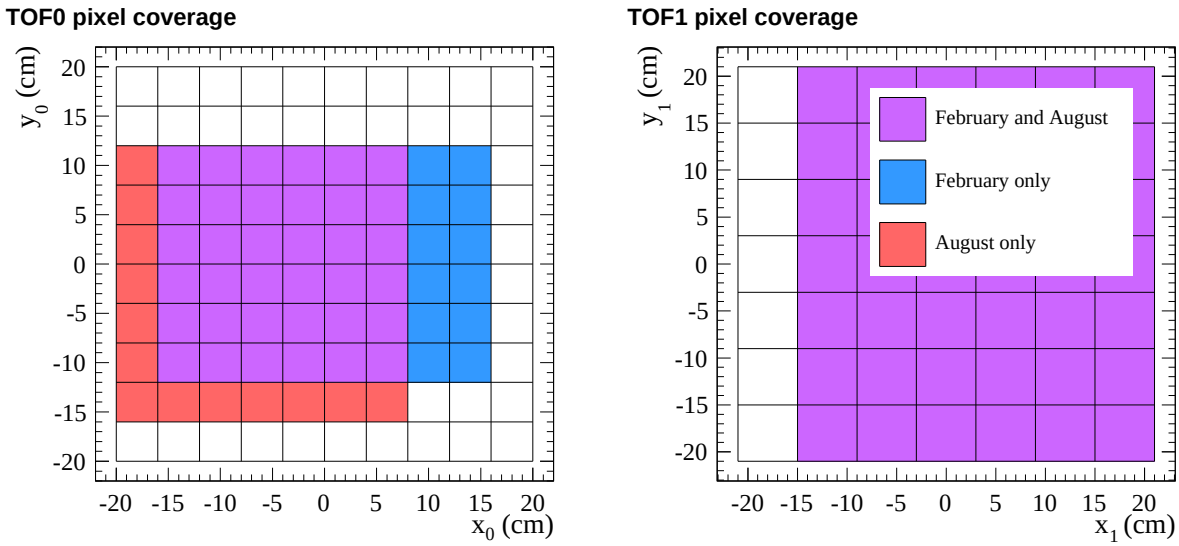

Figure 3.4: The pixel coverages of the calibrations of TOF0 and TOF1 performed in February and August 2010. Insufficient data were available for a time walk calibration in the uncalibrated pixels [69].

particles which traverse some pixels[4] which have very low occupancy. The pixel coverages of the two calibrations are shown in Figure 3.4. The February calibration is used throughout, as it allows for the measurement of more Step I muons.

The time in the horizontal plane of the detector t_x may be reconstructed by cancelling x via the summation of Equation 3.1 and Equation 3.2:

$$t_x = \frac{t_+ + t_-}{2} - \frac{l}{c_{\text{eff}}}. \tag{3.3}$$

The resolution of t_x is $\sigma_{\text{slab}} = \sigma_{\text{PMT}}/\sqrt{2}$, where σ_{PMT} is the RMS deviation of the times t_- and t_+ from the true arrival times of the signals in the PMTs. The propagation speed c_{eff} is not known precisely, but as Section 3.3 demonstrates, it may be assumed to be approximately constant in all slabs. The offset $-l/c_{\text{eff}}$ in Equation 3.3 may be neglected, as the DAQ does not make a precise measurement of the times in TOF0 relative to those TOF1, and the relative lengths of the cables transmitting signals from the PMTs of each detector to the DAQ are not known. Such precision on absolute time of flight is not required for the design purpose of particle identification, but is important when using the detectors to measure momentum. A time of flight calibration based on Monte Carlo simulations which will eliminate this offset is described in Chapter 5.

Both planes of scintillator slabs make independent measurements of the time the particle passes through the detector t. The best measurement may be made by combining the times in the horizontally and vertically oriented planes:

$$t = \frac{t_x + t_y}{2}.$$

[4] A pixel is the square region on a TOF detector defined by the intersection of two slabs in orthogonally oriented planes.

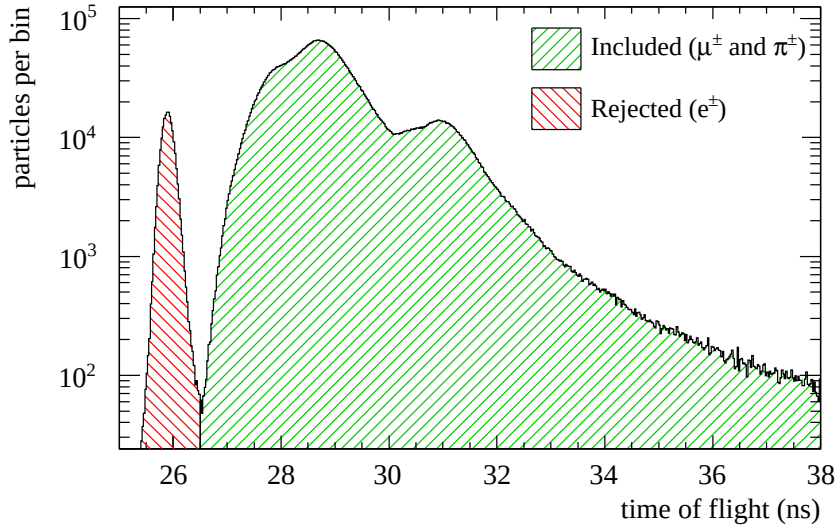

Figure 3.5: The time of flight distribution between TOF0 and TOF1 for every particle recorded during the experimental runs from when quadrupole 3 was fixed until the end of the Step I data taking campaign in December 2010 [72, 73]. Despite variation in the magnet currents in the many experimental runs contributing to this data set, it is nevertheless possible to apply an efficient cut on electrons and positrons, as illustrated. 5.1 million particles pass the cut and have been used for the calculations in this note.

The resolution of the time reconstructed by a TOF detector is therefore:

$$\sigma_t = \sigma_{\text{slab}}/\sqrt{2} = \sigma_{\text{PMT}}/2. \tag{3.4}$$

The detectors have been designed to achieve $\sigma_t = 50$ ps, in order to measure the time of flight between TOF0 and TOF1 with a resolution of 70 ps, and the RF phase at which muons traverse the cavities with a resolution approaching 10 degrees [71]. If the calibration has been performed correctly, t is an unbiased measurement of the true time of passage.

3.2.2 Timing resolution per pixel during Step I

σ_{PMT} will undoubtedly vary from pixel to pixel. Therefore σ_{PMT} in Equation 3.4 should be taken to be the mean variance of the four PMT timing measurements. The unique resolution of each pixel may be estimated by measuring the RMS of the difference of the measurements made by two slabs $\sigma(t_y - t_x) = \sigma_{\text{PMT}} = \sqrt{2}\sigma_{\text{slab}} = 2\sigma_t$.

The timing resolution of every calibrated pixel has been measured using this method. Every muon and pion recorded during the Step I data campaign is included in the calculation. Electrons and positrons are not included as their pattern of energy deposition is different, and we are interested in the performance of the time-walk calibration on the heavier particles which need to be distinguished from their time of flight peaks. The selection cut is illustrated in Figure 3.5. An example of the calculation is shown in Figure 3.6. Note that the distribution of $t_y - t_x$ is approximately Gaussian.

The time resolution σ_t per pixel in TOF0 and TOF1 is shown in Table 3.1 and Table 3.2. In

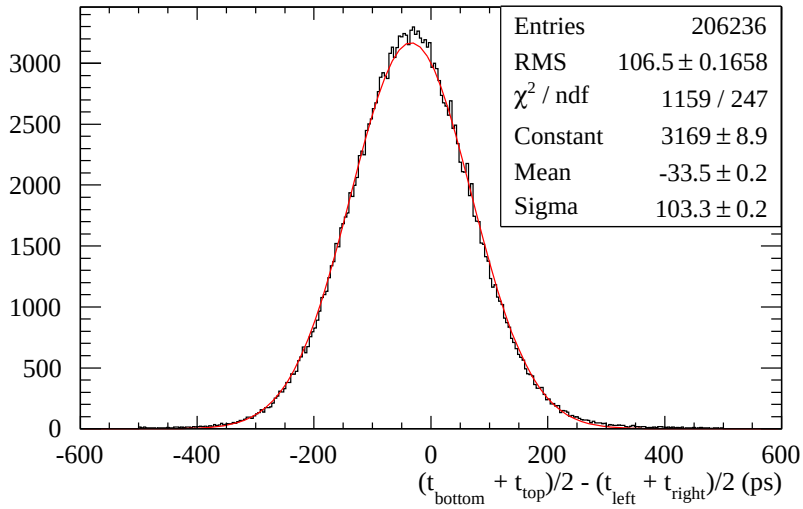

Figure 3.6: The difference in the calibrated times recorded in the two planes of TOF0 for the Figure 3.5 particles which pass through the intersection between slab five in the plane of horizontally oriented slabs and slab five in the plane of vertically oriented slabs. (By convention TOF slab numbering begins at zero and increments in the direction of increasing x and y in the left-handed coordinate system described in the introduction to this chapter [74, 75].) The red curve is a Gaussian fit to the data.

σ_t (ps)		Vertical slab 1	2	3	4	5	6	7	8
Horizontal slab	2	49.0	47.8	59.7	50.8	50.7	50.8	62.1	51.0
	3	48.3	48.0	56.9	47.8	49.0	48.6	57.3	52.7
	4	46.7	47.9	56.3	46.5	47.6	45.9	54.7	49.1
	5	49.6	47.6	57.1	49.0	51.6	50.2	59.3	50.7
	6	47.4	45.6	56.2	48.0	50.0	50.2	59.3	48.1
	7	49.9	48.4	54.8	50.0	50.4	50.3	58.6	51.1

Table 3.1: The resolution σ_t for muons and pions passing through each pixel on TOF0 during Step I, calculated using the data in Figure 3.5.

each case σ_{PMT} was estimated using a Gaussian fit to $t_y - t_x$ in order to eliminate the effect of binning and statistical variation. Typically the error on the estimate of σ_t in the pixel is of the order of 0.5 ps. Values marked with an asterisk are approximate, as fewer than 200 muons and pions hit that pixel during Step I, and there is insufficient data to fit the distribution. In these cases the RMS is recorded instead, with errors of the order of 10 ps.

The performance of the detectors may be summarized by considering the mean and standard deviation of the pixel resolutions. The resolutions of TOF0 and TOF1 are thereby 51.0 ps and 59.5 ps respectively. The pixel resolutions vary with a standard deviation of 4.1 ps in TOF0, and 2.6 ps in TOF1. These calculations have been weighted by the number of muons or pions illuminating each pixel during Step I, and exclude the low occupancy pixels marked with asterisks in Table 3.2.

σ_t (ps)		Vertical slab 1	2	3	4	5	6
Horizontal slab	0	62.0	65.1	62.1	63.0	108*	106*
	1	57.5	60.4	60.4	61.3	56.1	112*
	2	63.0	62.5	60.7	61.0	60.2	59.1
	3	58.7	60.5	56.9	56.2	58.9	59.2
	4	58.4	61.8	58.5	60.1	60.5	57.6
	5	55.1	58.8	58.9	60.0	58.0	57.7
	6	116*	67.9	64.9	67.3	67.4	60.1

Table 3.2: The resolution σ_t for muons and pions passing through each pixel on TOF1 during Step I, calculated using the data in Figure 3.5. Values marked with an asterisk are approximate, and correspond to pixels illuminated by fewer than 200 muons or pions.

3.3 Measuring transverse position

Two independent measurements of the position (x, y) at which a particle passed through a TOF detector can be made. The simpler method takes the position of the pixel traversed by the particle. If a muon passed through horizontal slab i and vertical slab j,

$$x_{\text{pix}} = \left(j - \frac{N-1}{2}\right) a, \qquad \text{and} \qquad y_{\text{pix}} = \left(i - \frac{N-1}{2}\right) a,$$

where a is the slab width, and i and j are numbered in the range 0 to $N-1$, where N is the number of slabs in each plane of the detector [74, 75]. The resolution of this measurement is approximately $a/\sqrt{12}$. As such TOF0 and TOF1 have resolutions of 1.15 cm and 1.73 cm, given that $a = 4$ cm and 6 cm respectively. This technique is already in use in G4MICE [67].

A new method, which it is the subject of this chapter to describe, uses the times recorded by the PMTs. Consider the difference between Equations 3.1 and 3.2:

$$x = \frac{c_{\text{eff}}(t_- - t_+)}{2}. \tag{3.5}$$

The resolution of this measurement is $c_{\text{eff}}\sigma_{\text{PMT}}/\sqrt{2} \sim 1$ cm.

Both measurement techniques are illustrated in Figure 3.7, where vertical slab three of TOF1 has been used as an example. The old and new methods are shown by the black and blue histograms respectively. Although the resolutions of both techniques are comparable, the new measurement is not quantized, is unbiased, and has a Gaussian error distribution. These are considerable advantages if one wishes to remove resolution bias from estimates of beam parameters.

3.3.1 Calibrating the measurement

The difficulty with the measurement of Equation 3.5 is that the effective propagation speed c_{eff} is not well known. Signals might be expected to travel down the slabs at a speed in the range between c/n^2, the speed of a ray being reflected at the critical angle of total

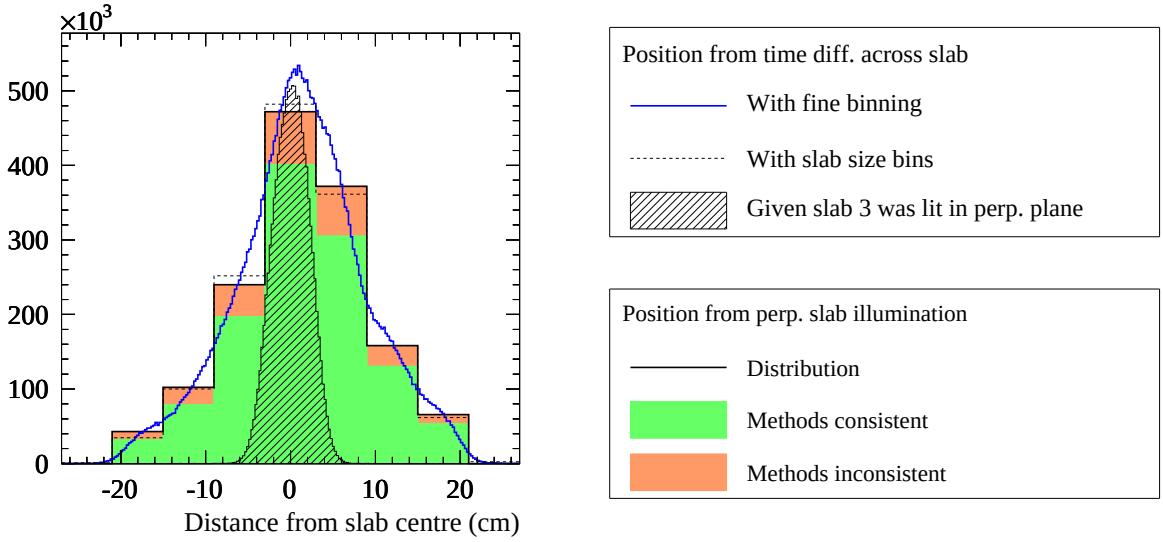

Figure 3.7: A comparison of the two methods of measuring position, using vertical slab three of TOF1 as an example. The y_{pix} distribution (black) may be compared with the measurement of Equation 3.6 (blue, bin weight = 25, optimal c_{eff} and Δ). The green distribution illustrates the fraction of measurements which contribute to the numerator of Equation 3.7. $f = 80.3\%$.

internal reflection, and c/n, the speed of a parallel ray. The scintillators used in TOF0 and TOF1 are Bicron BC-420 and BC-404 respectively [66]. Both materials are based on polyvinyltoluene and have a refractive index $n = 1.58$ [8, 76, 77]. The expected range is therefore 12 cm/ns $< c_{\text{eff}} <$ 19 cm/ns.

The situation is complicated further because the calibration was designed to obtain only the sum, and not the difference, of t_- and t_+. Consider the effect of applying equal and opposite offsets $t_- \to t_- + \Delta/2$ and $t_+ \to t_+ - \Delta/2$ to the times recorded by the PMTs. While the measurement of t_x in Equation 3.3 remains unchanged, the measurement of x in Equation 3.5 is now biased:

$$x = \frac{c_{\text{eff}}(t_- - t_+ + \Delta)}{2}. \tag{3.6}$$

Such offsets have been discovered to remain after the existing calibration has been performed, and vary from slab to slab. While the existing calibration corrects for the combined length of each slab's $x < 0$ and the $x > 0$ cables, the Δ constrain their relative lengths. Naturally, before using Equation 3.6, it is necessary to measure c_{eff}, and to resolve the Δ degree of freedom.

In Figure 3.7, y has been plotted using optimal values for c_{eff} and Δ. These have been derived by varying the parameters and maximizing the variable

$$f(c_{\text{eff}}, \Delta) = \frac{\text{Number of times when } -a/2 < x(t_- - t_+; c_{\text{eff}}, \Delta) - x_{\text{pix}} \leq a/2}{\text{Total number of muons and pions hitting the slab}}. \tag{3.7}$$

While varying Δ translates the distribution along $x(t_- - t_+; \Delta, c_{\text{eff}}) - x_{\text{pix}}$, varying c_{eff} squeezes and stretches it. f is the proportion of muons and pions for which the Equation 3.6 measurement reconstructs the particle in the range delimited by the slab which was illuminated in the other plane of the detector.

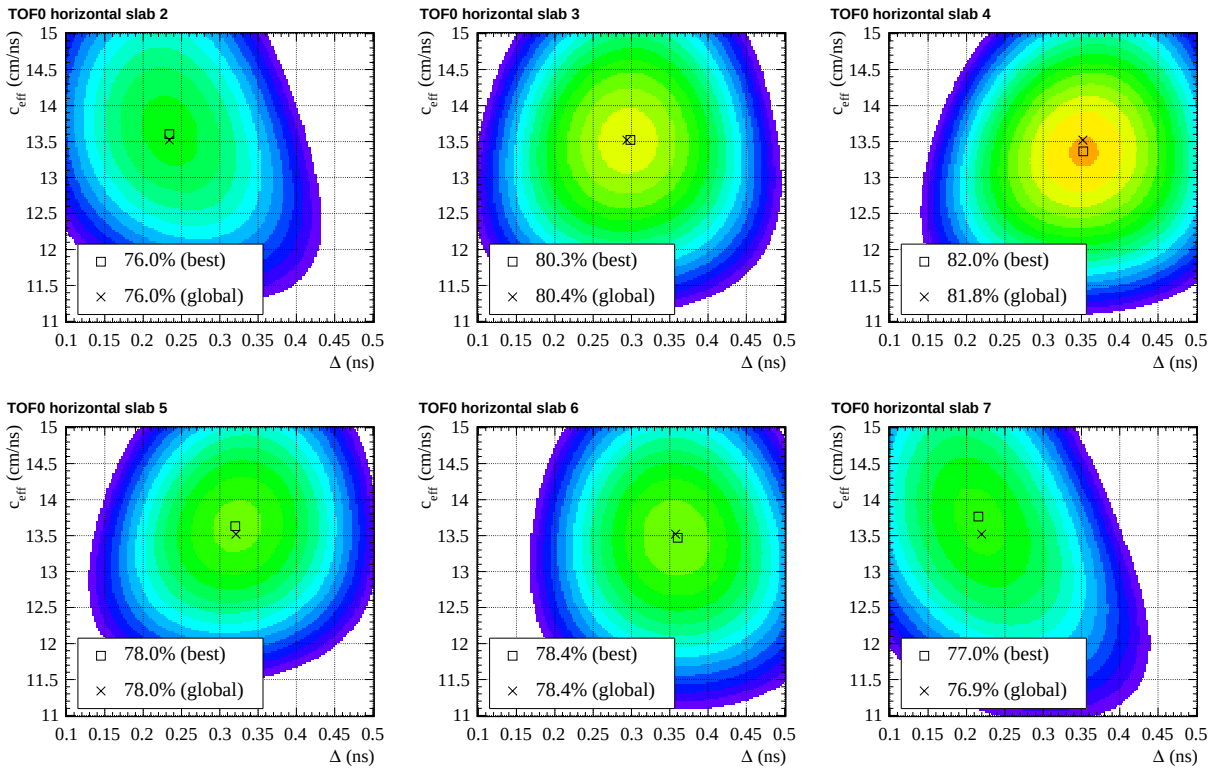

Figure 3.8: $f(\Delta, c_{\text{eff}})$ for the horizontal slabs of TOF0. The colour scale indicates the fraction of Step I muons and pions whose position measured using Equation 3.6 is consistent with the region delimited by the slab which was illuminated in the orthogonal plane of the detector. All the plots in Figures 3.8, 3.9, 3.10, and 3.11 have the same colour scale ranging from 65% (indigo) to 86% (red). The best fit, and the global best fit (with $c_{\text{eff}} = 13.52$ cm/ns) are marked.

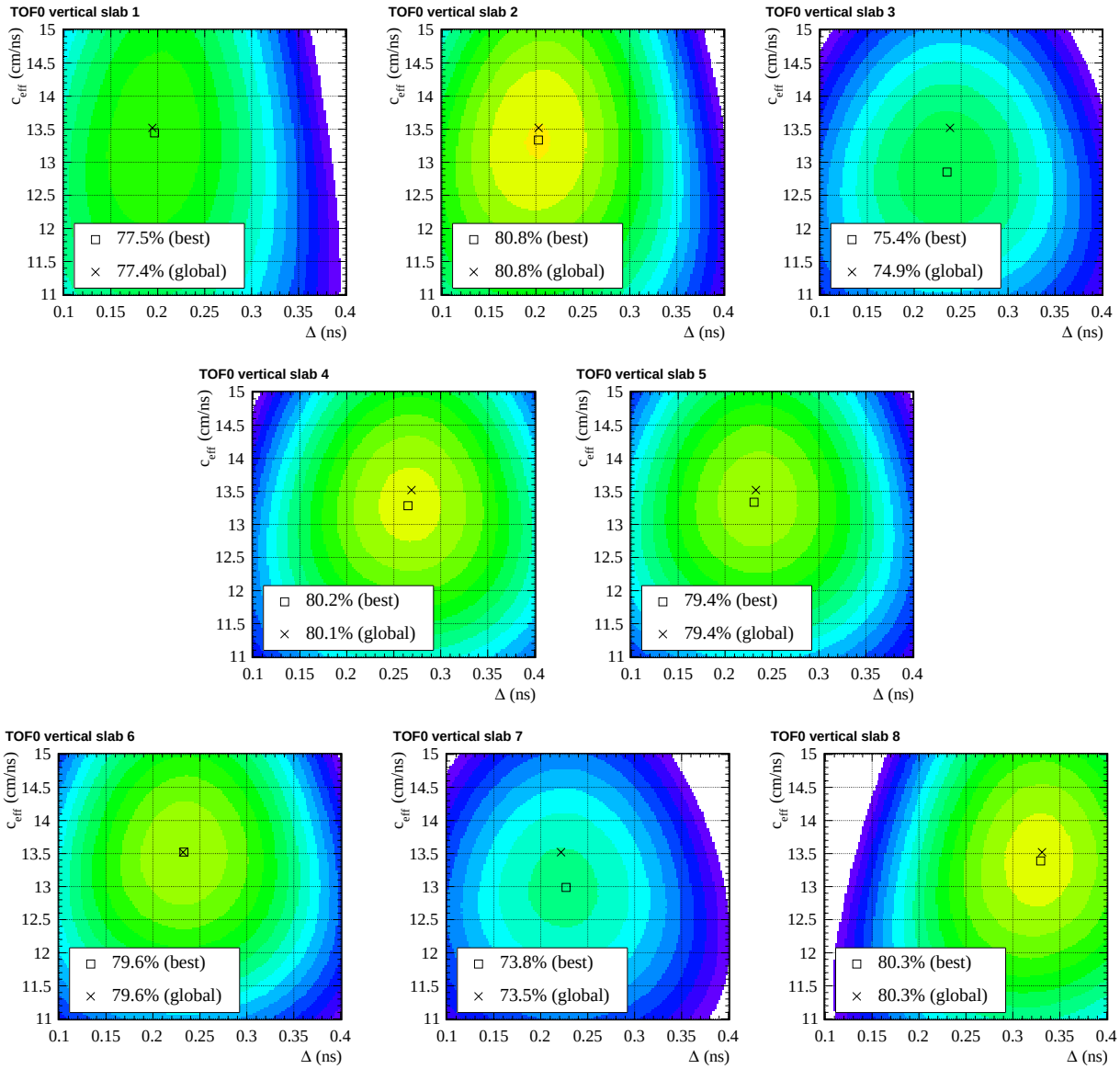

Figure 3.9: $f(\Delta, c_{\text{eff}})$ for the vertical slabs of TOF0. The colour scale indicates the fraction of Step I muons and pions whose position measured using Equation 3.6 is consistent with the region delimited by the slab which was illuminated in the orthogonal plane of the detector. All the plots in Figures 3.8, 3.9, 3.10, and 3.11 have the same colour scale ranging from 65% (indigo) to 86% (red). The best fit, and the global best fit (with $c_{\text{eff}} = 13.52$ cm/ns) are marked.

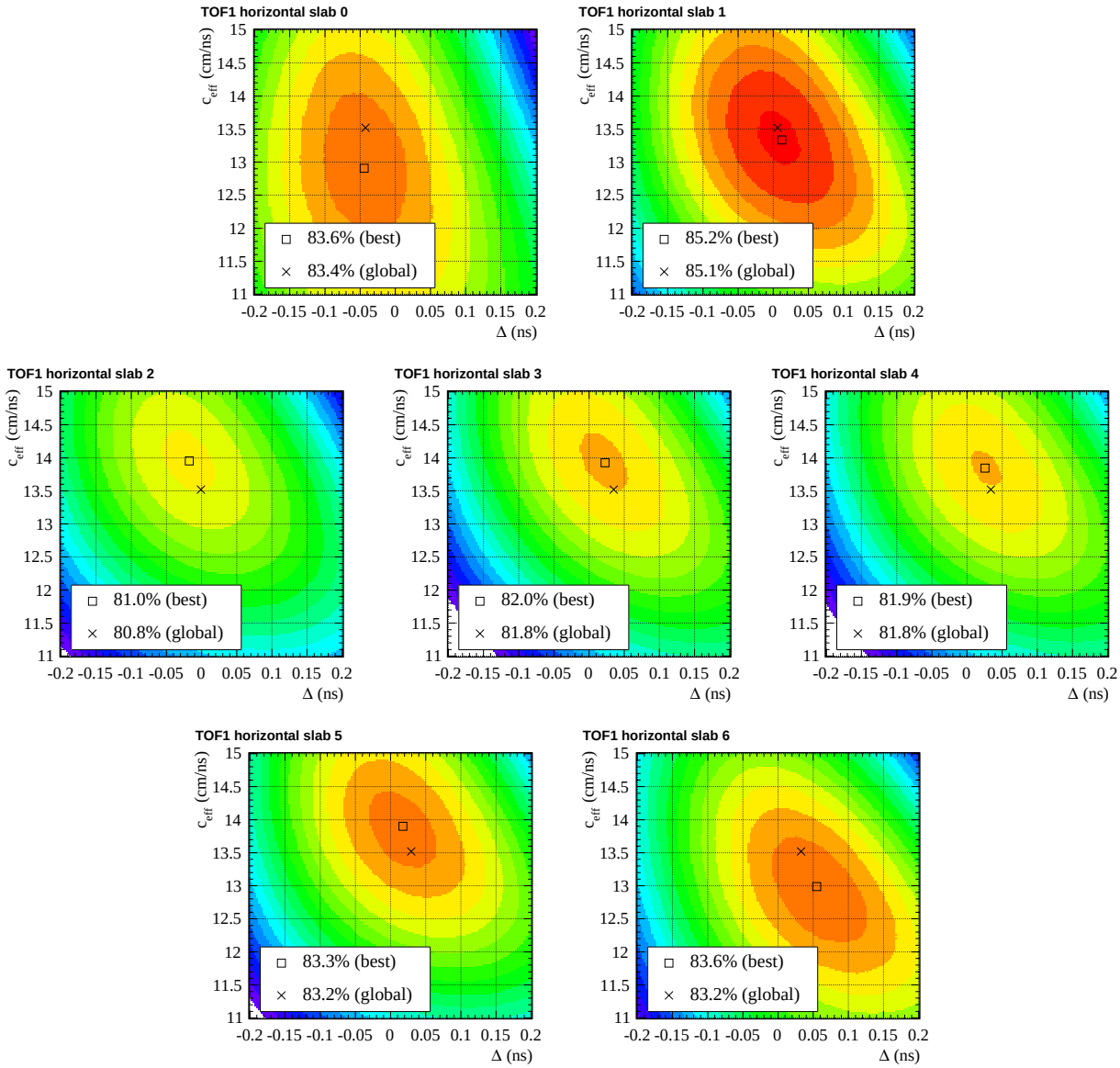

Figure 3.10: $f(\Delta, c_{\text{eff}})$ for the horizontal slabs of TOF1. The colour scale indicates the fraction of Step I muons and pions whose position measured using Equation 3.6 is consistent with the region delimited by the slab which was illuminated in the orthogonal plane of the detector. All the plots in Figures 3.8, 3.9, 3.10, and 3.11 have the same colour scale ranging from 65% (indigo) to 86% (red). The best fit, and the global best fit (with $c_{\text{eff}} = 13.52$ cm/ns) are marked.

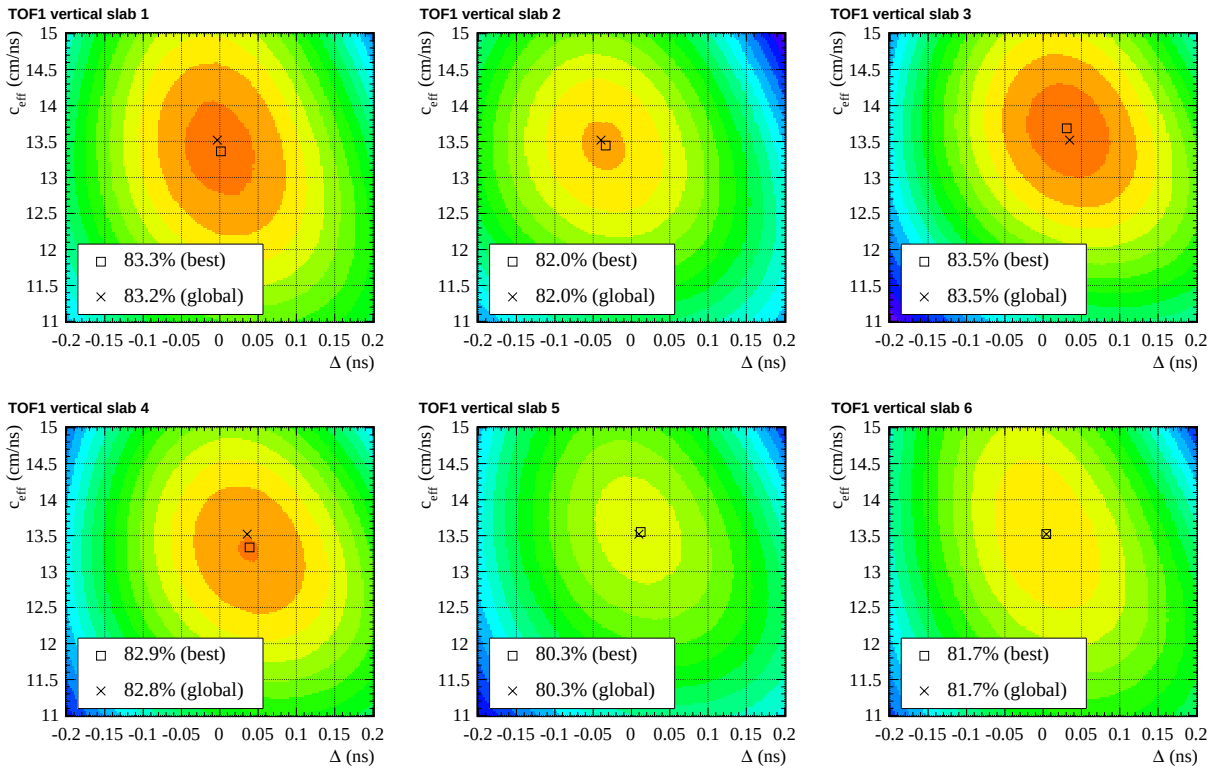

Figure 3.11: $f(\Delta, c_{\text{eff}})$ for the vertical slabs of TOF1. The colour scale indicates the fraction of Step I muons and pions whose position measured using Equation 3.6 is consistent with the region delimited by the slab which was illuminated in the orthogonal plane of the detector. All the plots in Figures 3.8, 3.9, 3.10, and 3.11 have the same colour scale ranging from 65% (indigo) to 86% (red). The best fit, and the global best fit (with $c_{\text{eff}} = 13.52$ cm/ns) are marked.

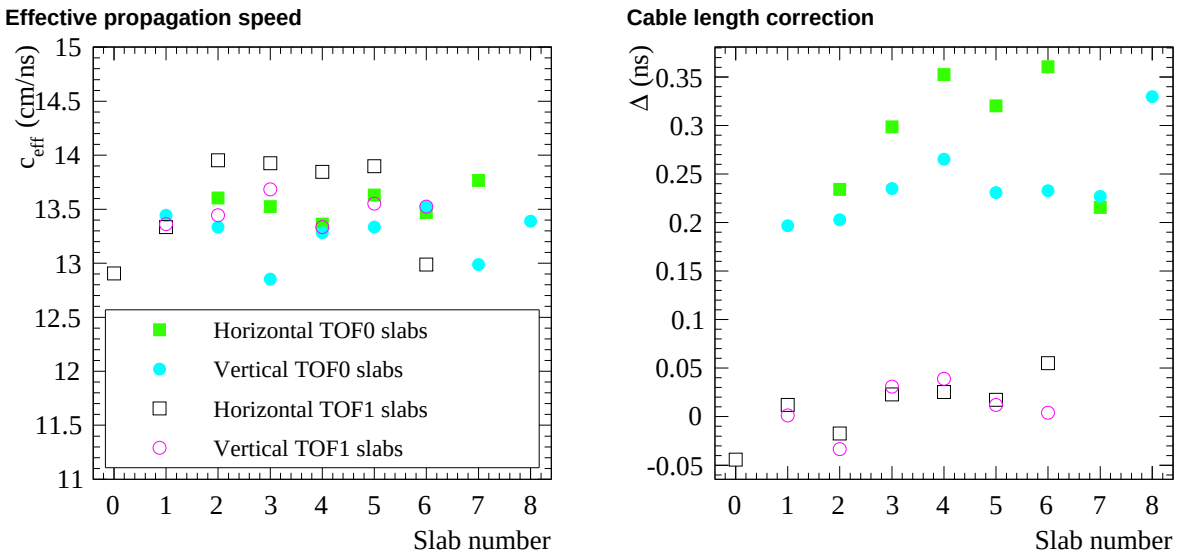

Figure 3.12: The favoured effective propagation speed c_{eff} and cable length correction Δ for each slab of TOF0 and TOF1. The 5.1 million muons and pions in Step I do not provide strong evidence for variation in c_{eff} between TOF0 and TOF1.

Figures 3.8–3.11 show $f(\Delta, c_{\text{eff}})$ maximized for all the horizontal and vertical slabs of TOF0 and T0F1 with calibrated PMTs. The colour scale is the same in all the plots; the summits are marked with a box, and plotted in Figure 3.12. c_{eff} could plausibly vary between TOF0 and TOF1 because the slabs have different dimensions, but there is no evidence for that in these broad peaks. By contrast, the Δ – merely unconstrained degrees of freedom – show significant variation. Neglecting to calculate individual Δ would decrease the agreement between the measurements by a few percent, and bias the measurement by approximately $c_{\text{eff}} \times 0.2$ ns $/2 \sim 1.5$ cm. Note that the correlation between the planes of TOF1 is an artefact of the existing calibration, the result of subtleties in the trigger electronics [69].

The total illumination per slab N, and the quality of the fit f_{max}, are plotted in Figure 3.13. A globally favoured value for the effective propagation speed has been calculated from the mean in the individual slabs, weighted by N:

$$c_{\text{eff}} = 13.52 \pm 0.30 \text{ cm/ns}.$$

The error has been estimated from the variance of the measurements of c_{eff}, weighted in the same manner.

Final measurements of Δ have been made by maximizing f given this globally favoured effective propagation speed. These values are marked with a cross in Figures 3.8-3.11, and are tabulated in Table 3.3 and Table 3.4. They are suitable for analysing data with the February 2010 calibration, but need to be recalculated for subsequent calibrations. Software which may be used for this purpose is described in Appendix A. Appendix B outlines a possible technique for performing a fully constrained cable length calibation in one pass.

The tables also show the corresponding globally favoured fraction of consistent measurements, and how much this has decreased relative to the values of c_{eff} and Δ individually favoured for that slab. The decision to use a global effective propagation speed is justified

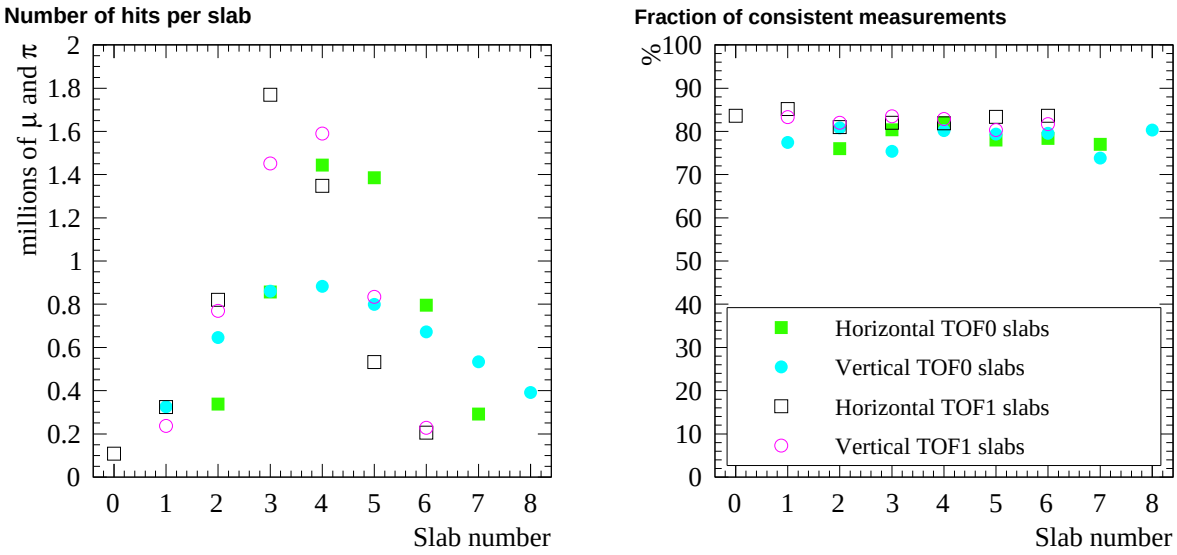

Figure 3.13: The total number of muons and pions illuminating TOF0 and TOF1 slabs during Step I, and the fraction of Equation 3.6 measurements based on the optimal fit in Figure 3.12 which fall in the region delimited by the slab illuminated in the orthogonal plane of the detector.

	Horizontal slabs			Vertical slabs		
Slab	Δ (ps)	f (%)	δf (%)	Δ (ps)	f (%)	δf (%)
1				194.3	77.4	−0.02
2	234.1	76.0	−0.02	202.7	80.8	−0.02
3	294.2	80.4	−0.00	238.1	74.9	−0.46
4	351.9	81.8	−0.12	268.8	80.1	−0.08
5	321.0	78.0	−0.05	232.7	79.4	−0.03
6	357.5	78.4	−0.01	232.1	79.6	−0.00
7	219.7	76.9	−0.06	221.6	73.5	−0.33
8				330.9	80.3	−0.03

Table 3.3: Additional cable length corrections for TOF0 slabs in the February calibration. The global fit, assuming $c_{\text{eff}} = 13.52$ cm/ns. The probability of this global fit, and the reduction from the slab specific best fit is also quoted.

	Horizontal slabs			Vertical slabs		
Slab	Δ (ps)	f (%)	δf (%)	Δ (ps)	f (%)	δf (%)
0	−42.2	83.4	−0.22			
1	6.2	85.1	−0.03	−3.4	83.2	−0.05
2	−1.0	80.8	−0.24	−39.8	82.0	−0.01
3	35.0	81.8	−0.22	34.6	83.5	−0.02
4	33.8	81.8	−0.13	35.8	82.8	−0.06
5	29.4	83.2	−0.18	9.8	80.3	−0.00
6	32.6	83.2	−0.42	4.2	81.7	−0.00

Table 3.4: Additional cable length corrections for TOF1 slabs in the February calibration. The global fit, assuming $c_{\text{eff}} = 13.52$ cm/ns. The probability of this global fit, and the reduction from the slab specific best fit is also quoted.

	Predicted f (centered)	Predicted f ($\frac{1}{3}a$ offset)
TOF0	96.0% ($\|Z\| < 2.05$)	74.3% ($-3.42 < Z < 0.68$)
TOF1	99.2% ($\|Z\| < 2.64$)	77.3% ($-3.74 < Z < 0.75$)

Table 3.5: The area of the normalized error distribution of $x(t_- - t_+; c_{\text{eff}}, \Delta)$ within a region of width a for a centered and offset distribution. The error distribution is modelled as a Gaussian, and the corresponding Z-values are noted.

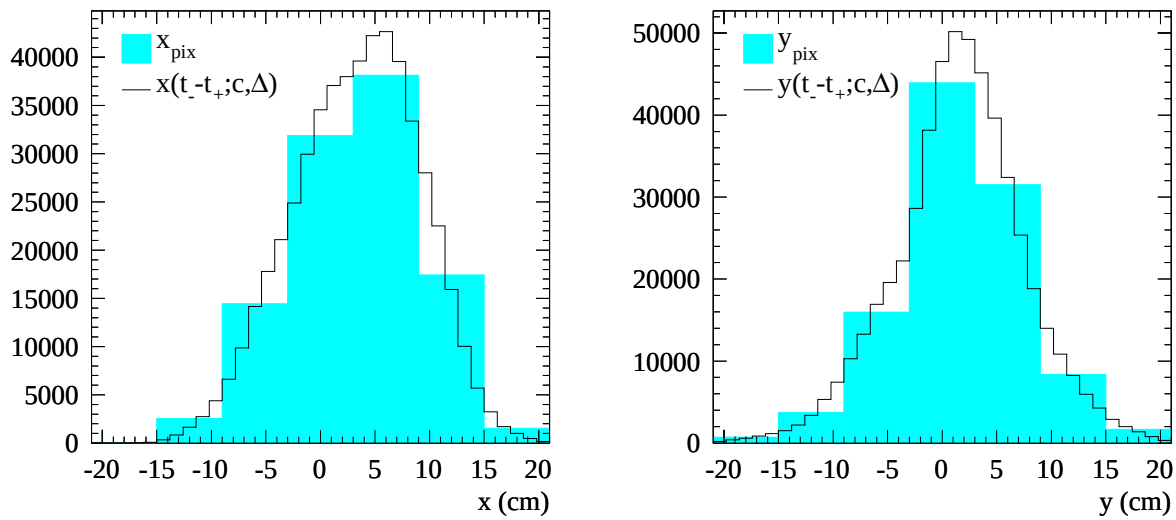

Figure 3.14: An example of a position measurement using real data. These histograms show the position of muons at TOF1 in the baseline (6 mm, 200 MeV/c) μ^+ matrix element dataset [72]. Both the old and new methods are shown.

by the fact that this is a fraction on a percent for all slabs. Nevertheless, at first glance, the values of f appear small. Assuming a Gaussian error distribution, as suggested by Figure 3.6, noting that $\sigma_{\text{PMT}} = 2\sigma_t$, and using the timing resolutions calculated in Section 3.2, f may be predicted given the slab widths of the two detectors. As Table 3.5 shows, the calculations summarized in Table 3.3 and Table 3.4 are not consistent with centered distributions, however we can understand the values if we consider that the distribution of hits on through the slabs will typically be biased towards the side nearest the beam centre. f tends to be greater in TOF1 than TOF0 because the ratio of slab width to resolution is higher, and a greater proportion of the error distribution fits within the region delimited by the slab which was illuminated in the other plane of the detector.

3.3.2 Resolution and beam size

Figure 3.14 shows the distributions at TOF1 which are obtained when the two measurement techniques are applied to the (6 mm, 200 MeV/c) μ^+ matrix element data set[5] [72]. This is the largest ensemble of muons which was recorded during Step I. While both methods lead to measurements of the position of the beam centre which agree within 0.2 mm, the beam sizes are found to differ. The standard deviation is greater when the old method is used.

[5] The method for obtaining this data set is described in Chapter 4.

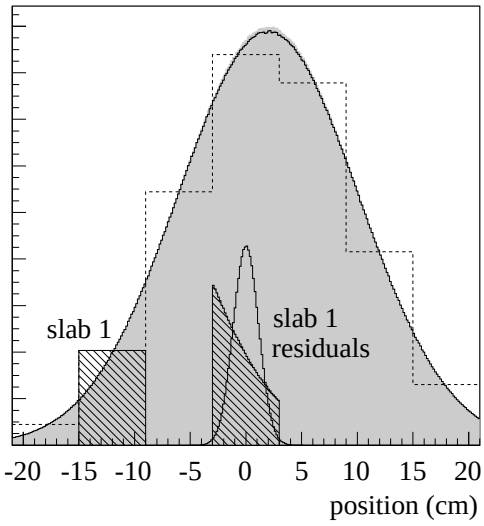

Figure 3.15: A toy Monte Carlo of the effect of the old and new measurement techniques on position measurents. A slightly off-centre beam with and RMS beam size of 10 cm is shown in gray. The old measurement is plotted with a dashed line, and the new measurement is plotted with a solid black line. The residual distributions of $\delta = m - x$ are plotted for both methods, for those particles which pass through slab number one.

In the horizontal plane, 6.23 cm is recorded for the old method and 5.77 mm for the new. Along the vertical axis the difference is smaller, with values of 6.12 cm and 5.91 cm.

The difference in measured beam size is due to the different effects of resolution bias of the two methods. Consider that a particle at true position x is measured to be at a position m:

$$m = x + \delta. \tag{3.8}$$

The deviation δ is sampled from the error distribution of the measurement technique. The error disributions of the two methods are illustrated in the case of TOF1 using a model Monte Carlo in Figure 3.15.

The Step I MICE analysis is concerned with the beam size, emittance, and Twiss parameters at TOF1. When calculated using raw measurements of the phase space variables, each of these statistical parameters will be biased by the effect of measurement resolution. In the case of beam size, the first step towards understanding this effect is to take the variance of Equation 3.8, and rearrange for the square of the true beam size:

$$\sigma_{xx} = \sigma_{mm} - \sigma_{\delta\delta} - 2\sigma_{x\delta}. \tag{3.9}$$

σ_{mm} is the variance of the raw measurements, $\sigma_{\delta\delta}$ is the square of the resolution of the measurement, and $\sigma_{x\delta}$ is the covariance between the true distribution and the error distribution.

In Section 3.3.1, the resolution of the old method was estimated to be $a/\sqrt{12}$, using the approximation that the width of the slab is uniformly populated. Figure 3.15 shows that this is not the case. The distribution is in fact different for each slab. Interestingly, the previous approximation is nevertheless rather good, as a trapezoidal model of the probability density of hits along the range delimited by the slab which was hit in the orthogonal plane

	σ_t	σ_x (old method)	σ_x (new method)	σ_x (combined)
TOF0	51.0 ps	1.15 cm	0.98 cm	0.75 cm
TOF1	59.5 ps	1.73 cm	1.14 cm	1.04 cm

Table 3.6: The time and position resolutions achieved by TOF0 and TOF1 during Step I.

– which appears to be very good approximation in all slabs except the central slab – results in the same expression for the resolution, as the linear term cancels in the integration. The covariance $\sigma_{x\delta}$ also varies in an unpredictable fashion, and can be as large as 5 (mm)^2. Except when measuring highly asymmetric distributions this term can be neglected.

An advantage of the new method is that the error distribution is the same at all points, and entirely uncorrelated with the measurement. The resolution of the new method has already been calculated to be $c_{\text{eff}}\sigma_{\text{PMT}}/\sqrt{2}$. As Table 3.6 shows, this compares favourably with that of the old method.

In the light of Equation 3.9, and with reference to Table 3.6, it may be shown that the standard deviations of the raw measurements plotted in Figure 3.14 differ by an explicable amount when calculated using the two measurement techniques. It should be noted that due to the statistical deviation of measurements of $\sigma_{\delta\delta}$ and $\sigma_{x\delta}$ on finite samples of muons, these corrections are only approximate.

3.3.3 Combining the measurements

The optimal technique for measuring position with the TOF detectors depends on the purpose of the measurement. When measuring statistical parameters such as beam size, the new method may be best, because the procedure for removing resolution bias is transparent, and amounts to subtracting the resolution, which is a constant. As the results are not quantized, it is also useful for visualizing distributions.

If one wishes to know the positions of individual particles, for example in order to track them in simulations of the subsequent steps of the experiment, a combination of the new and old techniques is best. A simple approach would to use a linear combination of the two measurements, weighted according to their errors. This, however, retains the bias of a few centimeters which is typical of the old method.

In certain circumstances, a good compromise may be to employ the new method, except when it reconstructs the particle outside the region delimited by the slab which was illuminated in the orthogonal plane of the detector. In the latter cases, the particle can be recorded as being at the edge of the orthogonal slab.

The new method is used alone for the analyses in this thesis. As the measurement is not quantized and has an unbiased and approximately Gaussian error distribution, this choice simplifies the analysis of reconstructed trace space distributions in Chapter 6 considerably.

3.4 Conclusion

TOF0 and TOF1 are designed to measure time with a resolution of 50 ps at both stations. This chapter describes a method for measuring transverse position using TDC counts in the PMTs. The effective propagation speed of light signals in the scintillator was measured to be 13.52 ± 0.30 cm/ns, with a sample of 5.1 million muons and pions. During Step I the calibration achieved figures of 51.0 ps and 59.5 ps respectively, allowing timing based position measurements to be made with resolutions of 0.98 cm and 1.14 cm respectively.

While this measurement will be useful in the future, the extra corrections for each slab will need to be recalculated for every new calibration. The software used to make the calculations in this note is available as the G4MICE application `XCalibration`. It would be possible to avoid the extra calibration procedure described in this chapter by extending the TOF cable calibration to constrain every degree of freedom. A simplified sketch of how such a calibration might proceed is outlined in Appendix B.

Chapter 4

Time of flight and transverse position in data and simulation

Time of flight distributions are used to perform particle identification and define muon data sets for the Step I emittance-momentum matrix beams, and the stability of the calibration is evaluated using the $e^{\pm}$ peak. Finally, a set of Monte Carlo simulations which are used for comparison with data throughout the thesis are described, and their distributions of time of flight and transverse position are compared with those in the corresponding data sets.

Timing detectors TOF0 and TOF1 are the only calibrated detectors which were operational in Step I. Positioned at the end of the Step I beam line, they have been used to characterize the MICE beams for the analysis in this thesis. In Section 4.1 and Section 4.2 time of flight distributions are used to perform particle identification and to study the stability of the calibration.

In the previous chapter the timing resolution of TOF0 and TOF1 was measured and the calibration was extended to allow the measurement of position. In Section 4.3 the measurements are applied to the Step I data and compared with simulations. The phase space distributions of the muon beams in the simulations and data sets defined in this chapter are then studied in the remainder of the thesis.

4.1 Particle identification for the Step I data sets

The main purpose of the time of flight detectors is to distinguish muons from electrons, pions and protons. TOF0 and TOF1 are separated by $L = 7.71$ m and positioned at the end of the Step I beam line, directly upstream of the future position of the cooling channel. It is possible to examine the particle content of the beam using time of flight peaks because the distributions of each species have approximately the same mean momentum p selected by dipole 2. The mean time of flight of each species varies as $t = (L/c)\sqrt{1 + m^2/p^2}$. Each detector is designed to measure the time of passage of a particle with a resolution of 50 ps [71]. As calculated in Chapter 3, timing resolutions of 51.0 ps and 59.5 ps were achieved in TOF0 and TOF1 during Step 1.

Figure 4.1 shows a typical time of flight distribution with positron, muon and pion peaks labelled. Although not designed to be matched into the cooling channel, the design momentum is near that required to reach the nominal base line momentum of 200 MeV/c

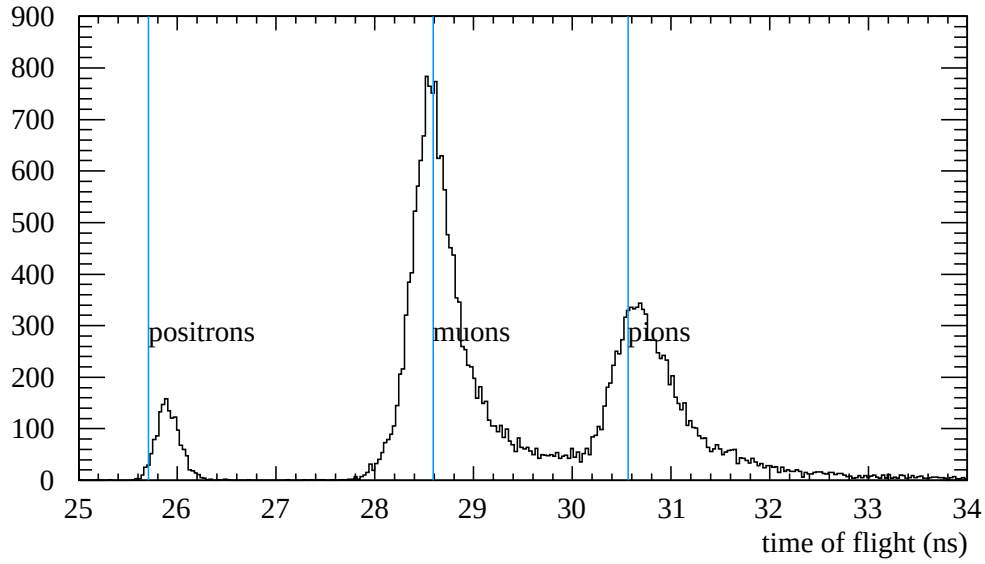

Figure 4.1: The figure shows the time of flight measured by the TOF0 and TOF1 detectors. The lines show the expected positions $t = (L/c)\sqrt{1 + m^2/p^2}$ of the positron, muon and pion peaks, given a momentum of 217 MeV/c. Any proton peak would be trivially distinguishable at > 100 ns. The data is from experimental runs 2730, 2731, 2732 and 2768.

in the absorber centres. It is not possible to distinguish between muons and pions for about 20% of these particles using this method. The time of flight distributions overlap because of the wide momentum acceptance of dipole 2 rather than because of the time of flight resolution $\sigma_t = \sqrt{(51.0 \text{ ps})^2 + (59.5 \text{ ps})^2} = 78.4$ ps, which is of the order of two bin widths. Particle identification is more difficult for high momentum beams, particularly the (10 mm, 240 MeV/c) matrix element which must achieve 240 MeV/c in the absorber centres after energy loss in the maximum thickness diffuser plate (cf. Table 2.2).

The shapes of the time of flight distributions of the emittance-momentum matrix beams are slightly different, due to the specific criteria to select the component of the muon decay spectrum which is created from pions decaying backwards in the decay solenoid. Tuning dipole 2 to accept the momentum of backward decaying muons minimizes the pion contamination as these muons are in the tails of the pion distribution, illustrated in Figure 2.6.

The muon peaks are particularly broad in these time of flight distributions, as shown in the data from the base line (6 mm, 200 MeV/c) μ^+ element of the emittance-momentum matrix in Figure 4.2. There is no evidence of a pion peak. If one exists at the predicted time of flight of 31 ns it is invisible under the declining tails of the broad muon distribution. It is not possible to tell from from the data alone what proportion of the distribution between 30 ns and 32 ns is pions and what is low energy muons. A muon at the time of flight of the predicted pion peak would have $p_z \approx 165$ MeV/c.

Similar distributions are observed for all of the matrix elements except the (3 mm, 140 MeV/c) μ^- beam. The distributions are drawn in Figure 4.3, with logarithmic axes to highlight noise if it exists in the data and to aid the eye in searching for pion peaks and setting cuts. In each case the $e^\pm$ peak is fixed and the broad muon peak is narrower and faster for the higher momentum matrix elements. The tails of the μ^+ distributions are a little longer than the tails of

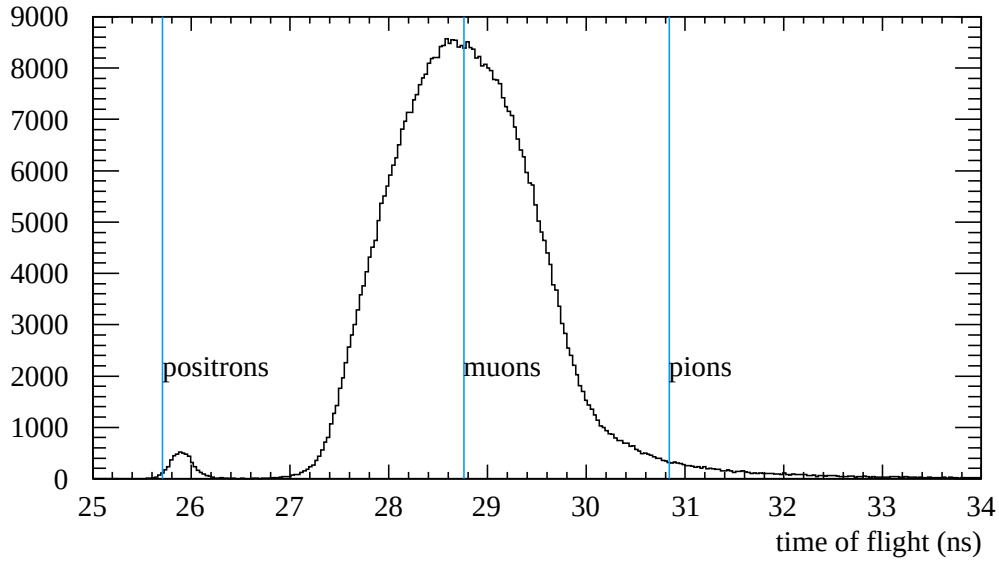

Figure 4.2: The time of flight between TOF0 and TOF1 for the (6 mm, 200 MeV/c) μ^+ matrix element. Dipole 2 is set here to accept a design momentum of 237 MeV/c. After energy loss in various detectors, the mean momentum between TOF0 and TOF1 is expected to be 211 MeV/c [61]. The lines illustrate the expected position of positron, muon and pion peaks, if they exist. The experimental runs which make up this data set are listed in Appendix A.

PID cuts	t^e_{low}	t^e_{high}	$t^{\mu\pi}_{\text{low}}$	$t^{\mu\pi}_{\text{high}}$
140 MeV/c	25.0 ns	27.0 ns	27.0 ns	43.0 ns
200 MeV/c	25.0 ns	26.5 ns	26.5 ns	40.0 ns
240 MeV/c	25.3 ns	26.5 ns	26.5 ns	36.0 ns

Table 4.1: Time of flight particle identification cuts based on the distributions in Figure 4.3. Muons and pions are grouped together as it is not possible to separate them in beams tuned to accept muons emitted backwards in the centre of mass frame of the decaying pions.

the μ^- distributions, and there in a suggestion that low emittance nominal $p_z = 200$ MeV/c beams have broader peaks. The most noticeable feature is the very narrow muon peak of the (3 mm, 140 MeV/c) μ^+ beam. One would expect it to have a similar distribution to its μ^- counterpart in the emittance-momentum matrix and it is believed to be anomalous. This beam will be re-tested in the next data taking period.

In all cases a positron peak is trivially distinguishable, and it is not possible to distinguish muons and pions. Time of flight cuts have been assigned to create $e^\pm$ and μ/π data sets, as recorded in Table 4.1. For simplicity the cuts are identical for both polarities and each emittance, and vary depending only on the momentum of the beam. The boundary between the $e^\pm$ peak and the μ/π peak was taken simply to be the minimum of the distributions between the two prominent neighbouring peaks. The low $e^\pm$ edge and the high μ/π edge have been selected to be the points at which the distributions rise above the noise. The low level noise is attributed to coincidental but independent light signals in the two detectors. The contamination of the data is $< 0.1\%$.

The sizes of the Step I data sets which follow from these cuts are shown in Table 4.2. The

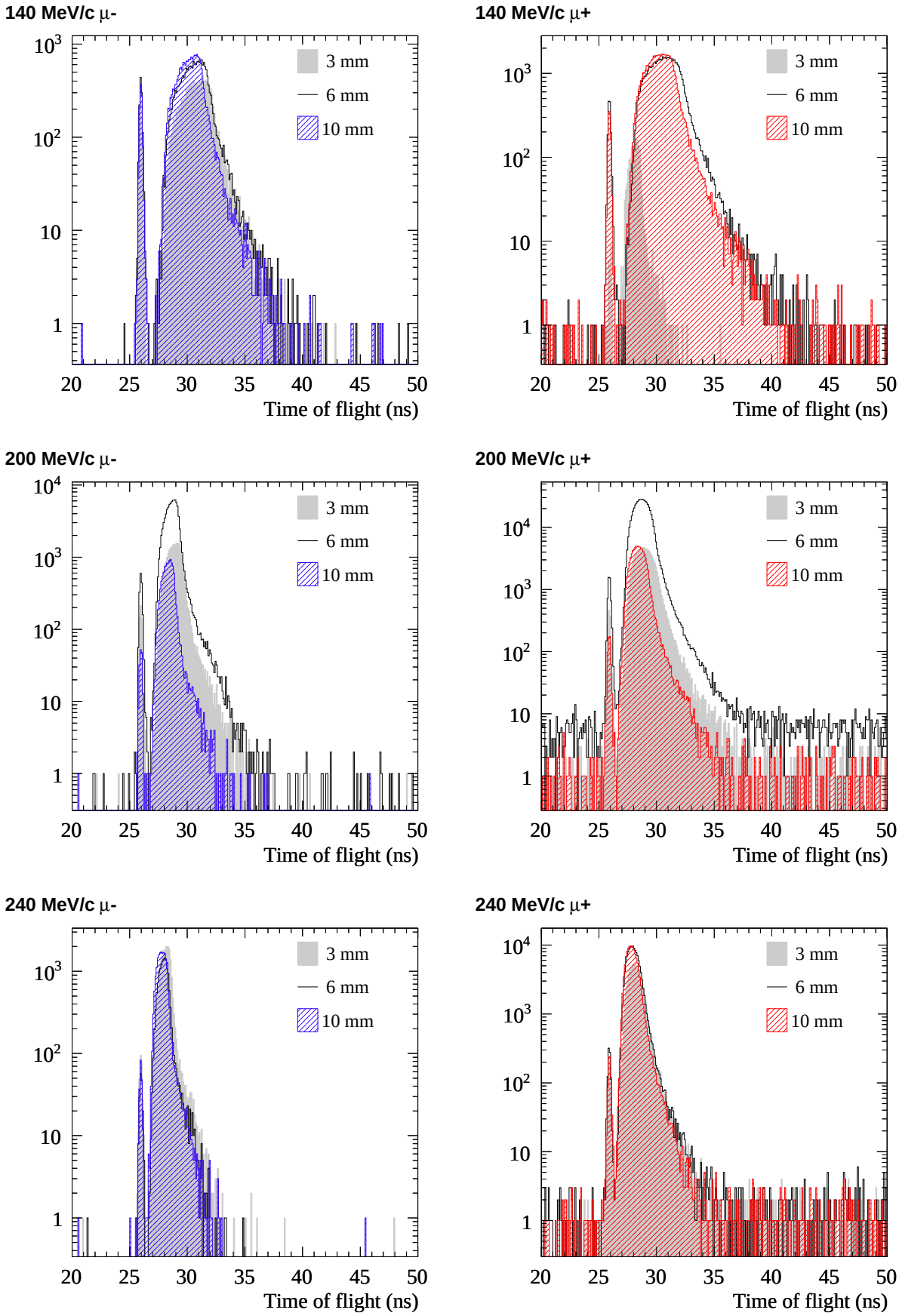

Figure 4.3: Time of flight distributions for the eighteen emittance-momentum matrix beams (cf. Section 2.3). Logarithmic axes have been used to aid the eye in differentiating signal from noise when deciding particle identification cuts.

$N_{\mu\pi}$ ($N_e/N_{\mu\pi}$)		μ^- beams p_z (MeV/c) 140	200	240	μ^+ beams p_z (MeV/c) 140	200	240
ϵ_N (mm)	3	13,215 (7.2%)	26,282 (2.2%)	22,580 (1.2%)	1,771 (1.7%)	101,025 (1.4%)	77,967 (0.8%)
	6	19,502 (6.0%)	87,917 (1.9%)	14,868 (1.1%)	55,942 (2.5%)	531,283 (0.9%)	128,823 (0.7%)
	10	19,707 (5.1%)	11,017 (1.4%)	18,870 (1.0%)	53,148 (2.0%)	80,887 (0.7%)	121,296 (0.6%)

Table 4.2: The number of particles which pass the μ/π cut in Table 4.1 for each element of the emittance-momentum matrix, and the number passing the $e^{\pm}$ cut as a percentage of the μ/π peak.

largest data sets are the base line (6 mm, 200 MeV/c) μ^- and μ^+ elements. The table also shows that the $e^{\pm}$ peak is bigger for low momentum and negative polarity beams.

4.2 Stability of the electron peak

The stability of the $e^{\pm}$ peak is illustrated by Figure 4.4. Its mean and RMS time of flight in each experimental run throughout the whole Step I data taking campaign is plotted. As electrons and positrons are highly relativistic at momenta of the order of hundreds of MeV/c their distribution should be peaked at $\sim L/c$ with width given by the time of flight resolution $\sigma_t = 78.4$ ps.

The figure has three surprising features which a discussed in this section. Firstly the February and August calibrations return different mean flight times for the $e^{\pm}$. Section 4.2.1 analyses a recent survey to predict the correct time of flight and Section 4.2.2 explains the (prosaic) cause of the difference and the method used in this thesis to calibrate the absolute value of the time of flight $t_1 - t_0$.

Secondly there is some evidence of a systematic difference between the positions of the positron and electron peaks, Thirdly the RMS value of the peak is unexpectedly large. These effects are investigated in Section 4.2.3.

4.2.1 Geometry of the TOF0 and TOF1 detectors

In order to calibrate $t_1 - t_0$ it is necessary to know the distance between the detectors. A survey of the experimental hall was conducted at the end of the Step I data taking campaign [63]. The surveyors recorded the positions of the corners of TOF0 and TOF1 relative to the centre of dipole 2, with $\hat{z}$ along the design orbit.

L can be determined from the intersection of the detector centre planes $\hat{n} \cdot (\vec{r} - \vec{r}_0) = 0$ with $\hat{z}$. Let the corners of the downstream face of TOF0 be labelled A, B, C and D, proceeding around the edge in either sense. The normal vector $\hat{n}$ is obtained from $\vec{AC} \times \vec{BD}$ and the centre of the detector $\vec{r}_0$ is deduced from $\vec{AC} + \vec{BD}$. The measurements are recorded in Table 4.3. TOF0 and TOF1 therefore intersect the design orbit at $z = \hat{n} \cdot \vec{r}_0 / \hat{n} \cdot \hat{z} = 5293.7$ mm

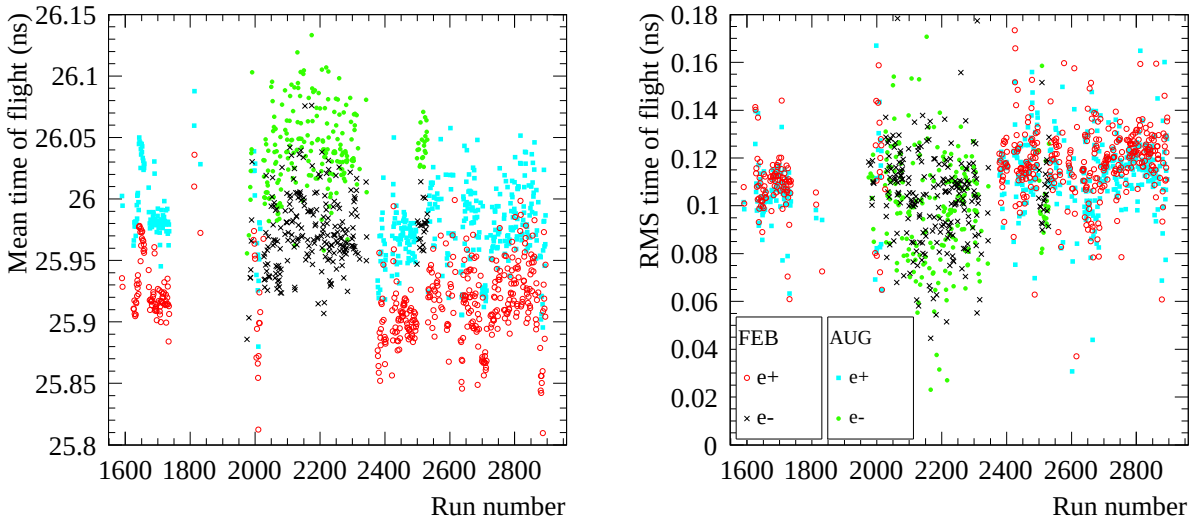

Figure 4.4: The stability of the February and August TOF0 and TOF1 detector calibrations. The mean time of flight $t_1 - t_0$ of the $e^{\pm}$ peak is plotted as a function of the number of the experimental run. The runs span the period from quadrupole 3 being fixed to the end of the Step I data taking campaign: all the runs listed in Appendix A with more than five $e^{\pm}$ are included. The error on the points ranges from 5 ps to 50 ps.

Detector	Detector centre $\vec{r}_0$/mm	Normal vector $100 \times \hat{n}$
TOF0	$(1.8, 2.6, 5293.8)$	$(-0.467, -0.509, 99.998)$
TOF1	$(30.2, -17.6, 12999.0)$	$(-0.927, -1.423, 99.986)$

Table 4.3: Positions and rotations of TOF0 and TOF1 inferred from the survey [63].

$\langle t_1 - t_0 \rangle$ of the $e^{\pm}$ peak	μ^- beams	μ^+ beams
(6 mm, 140 MeV/c)	25.366 ns $\pm$ 3 ps	25.303 ns $\pm$ 3 ps
(6 mm, 200 MeV/c)	25.369 ns $\pm$ 3 ps	25.298 ns $\pm$ 2 ps
(6 mm, 240 MeV/c)	25.370 ns $\pm$ 9 ps	25.289 ns $\pm$ 4 ps

Table 4.4: The mean $e^{\pm}$ time of flight for the $\epsilon_{\mathrm{N}} = 6$ mm matrix element $\mu^{\pm}$ data sets illustrated in Figure 4.5. The values are derived from the raw output of G4MICE using the February 2010 calibration.

and 12999.0 mm respectively and $L = z_1 - z_0 = 7.7053$ m.

The tilt in the detectors is given by the dihedral angle $\cos^{-1}(\hat{n} \cdot \hat{z}) = 0.396°$ and $0.974°$ in the two detectors respectively. Therefore a muon hitting the edge of TOF1 $\sim$ 20 cm from the design axis will travel an extra 3.5 mm. The time of flight will be different by about 10 ps or 0.3%.

4.2.2 Calibration of the absolute time of flight

Although the February 2010 calibration is used in this thesis, the August 2010 calibration is also plotted in Figure 4.4 to illustrate the consistency of the calibration procedure. The mean peak position of the two calibrations follow each other for each experimental run, illustrating that the scatter of the points is not a reflection of instability or noise in the calibration procedure. The distribution of means varies in the same pattern, offset by about 80 ps.

The mean peak positions are different because the calibrations are based on different surveys, with different measurements of L. This effect also accounts for the small offset between the positron peaks in Figure 4.1 and Figure 4.2 and their predicted time of flight. The analysis software of the collaboration (G4MICE [67]) calibrates TOF1 relative to TOF0 using the position of $e^{\pm}$ peaks in data and the assumption $\langle t_1 - t_0 \rangle = L/c$. A dedicated run was performed to perform this calibration and the scatter and correlations in Figure 4.4 were not taken into account. The analysis in this thesis is based on the newer and more complete survey which was described in the previous section.

A second problem is that G4MICE returns times which are too large by a factor 1024/1000 due to a mis-understanding of the precise width of the TDC bins. The supplementary position calibration described in Chapter 3 was performed before this feature was discovered. Therefore this calibration should be applied to TDC hits obtained using the February 2010 calibration without this correction, with no adverse effect on the results as they were cross-calibrated to the physical size of the slabs. The appropriate correction factor has been applied to all other timing measurements in this thesis.

4.2.3 The anomalous electron-positron asymmetry

In both the February and August calibrations a shift of $\sim$ 70 ps is visible between μ^+ and μ^- data sets. The most compelling case is made by the oscillations at the polarity switches near run 2000 and run 2500. One disadvantage of Figure 4.4 is that the runs have a plethora or

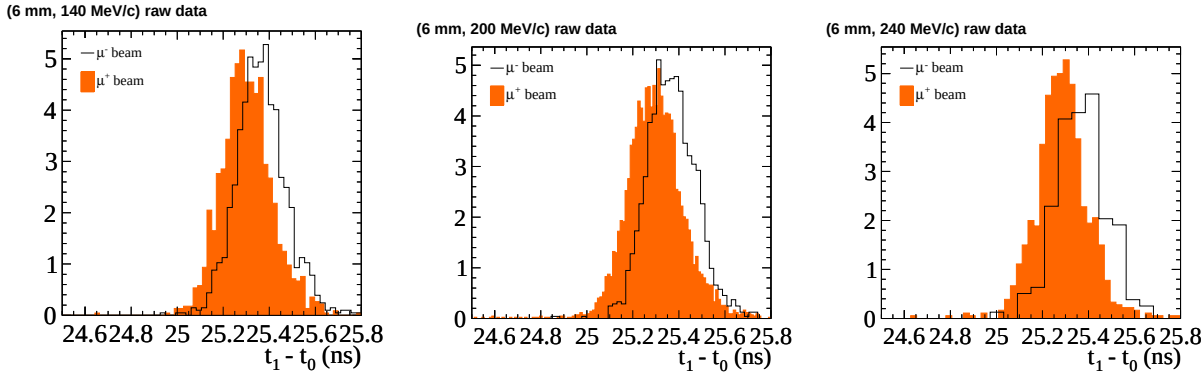

Figure 4.5: Position of the $e^{\pm}$ peaks of the $\epsilon_{\mathrm{N}} = 6$ mm matrix element $\mu^{\pm}$ beams in data. The values are the raw output of G4MICE using the February 2010 calibration. The mean positions of the peaks are recorded in Table 4.4.

$\langle s - L \rangle$ of the $e^{\pm}$ peak	μ^- beams	μ^+ beams
(6 mm, 140 MeV/c)	13.9 ± 0.2 mm	10.9 ± 0.3 mm
(6 mm, 200 MeV/c)	13.8 ± 0.1 mm	11.0 ± 0.1 mm
(6 mm, 240 MeV/c)	14.6 ± 0.2 mm	12.7 ± 0.7 mm

Table 4.5: The mean $e^{\pm}$ excess path length $s - L$ for Monte Carlo simulations of the $\epsilon_{\mathrm{N}} = 6$ mm matrix element $\mu^{\pm}$ data sets illustrated in Figure 4.6. The values are derived from simulations of the re-scaled TURTLE optical designs described in Section /refsec:Simulations.

different optical configurations, however the effect is also visible in the large $\epsilon_{\mathrm{N}} = 6$ mm re-scaled TURTLE emittance-momentum matrix element data sets, as illustrated in Figure 4.5. The mean time of flight of these peaks is recorded in Table 4.4. There is no evidence for a dependence on emittance or momentum.

A number of hypotheses have been proposed to explain the shift. Thermal expansion of the cables or the hall itself does not appear to be large enough effect. 70 ps corresponds to ~ 2 mm and a fractional expansion over L of 0.25%. Given thermal expansion coefficients are of the order of 10^{-5} K^{-1} plausible temperature variations are far too small to cause such an expansion.

A second theory is that the offset is a variation in path length due to the earth's magnetic field. At the surface of the earth the field is ~ 50 μT. 250 MeV/c electrons and positrons travelling perpendicular to this field have a radius of curvature of 17 km, and a relative deflection over $L \approx 8$ m of $L^2/17$ km ≈ 4 mm $= 13$ ps $\times\, c$. This effect is therefore too small to account for the offset. The deflection is also in the transverse rather than longitudinal direction and complicated by the quadrupole magnets, and therefore cannot clearly account for the observed electron-positron time of flight discrepancy.

Another potential cause for the offset is a difference of 70 ps $\times\, c = 21$ mm in the mean path length of the electrons and positrons. As most particles travel along a curved trajectory their integrated path length $s > L$. As the currents in the subsequent dipole 2 and quadrupoles 4-9 were reversed when the beam polarity was switched there should be no difference in the way in which the trace space distributions of e^- and e^+ are transported from the decay solenoid into the upstream time of flight system. However, an asymmetry could arise if the initial distributions are different. There are two possible causes of this. Firstly, the current

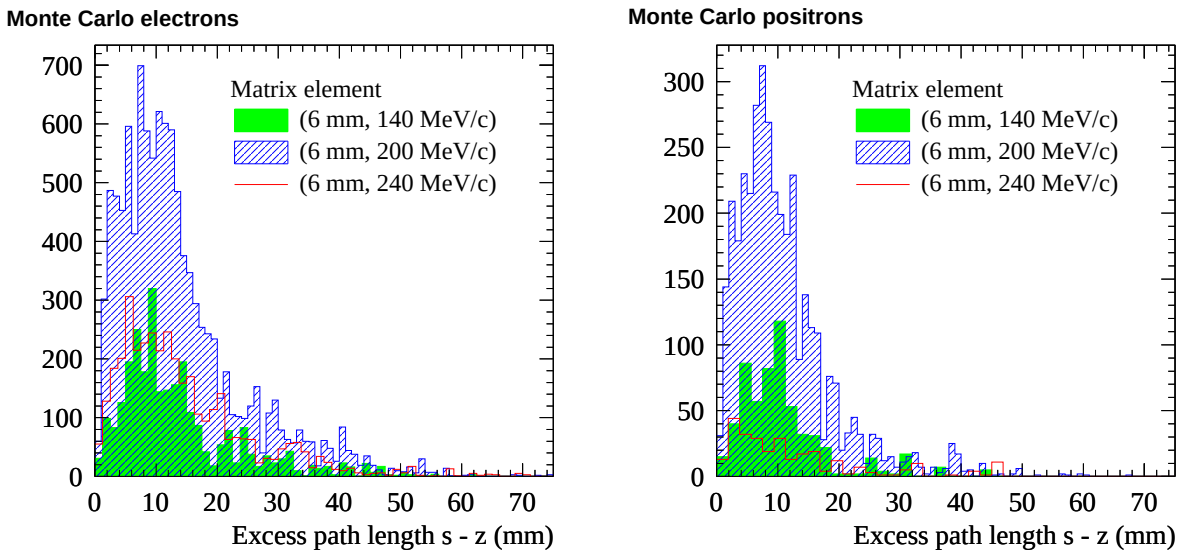

Figure 4.6: The integrated path length s greater than the axial distance L traversed by e^- in μ^- beams and e^+ in μ^+ beams between TOF0 and TOF1 in simulations of the $\epsilon_{\mathrm{N}} = 6$ mm elements of the emittance-momentum matrix. $\langle s - L \rangle$ for these beams is recorded in Table 4.5.

in the decay solenoid was not switched; and secondly, the polyethylene proton absorber was only present for the positive polarity beams. Both effects will alter the distribution of $e^{\pm}$ emerging from the decay solenoid which have the required momentum to be transported through dipole 2, as the beam will not be symmetric in the decay solenoid, as the pion beam inserted into it is not symmetric.

This hypothesis has been tested using simulations of the beam line which are described in the following section. Simulated $s - L$ for the six $\epsilon_{\mathrm{N}} = 6$ mm matrix elements are plotted in Figure 4.6 and the mean values are recorded in Table 4.5. The simulations do show an effect in the required direction, but the difference in the peaks is less than 5 mm.

Non-negligible $e^{\pm}$ excess path length distributions are also the most probable solution to the question of why the $e^{\pm}$ peaks are wider than σ_t. The simulations in Figure 4.6 have an RMS path length RMS of the order of 10 mm = 33 ps $\times$ c. Assuming this spread is independent of the timing resolution in the detectors, this effect increases the predicted $e^{\pm}$ peak width from 78.4 ps to 85 ps, still significantly less than 120 ps observed in the figure.

Both of these effects could be the result of an inadequacies in the simulation of electrons and positrons. $s - L$ distributions with a width of order $c\sigma_t$ would account for the observed $e^{\pm}$ peak width and provide scope for a difference which could account for the asymmetry in mean time of flight. As the spectrometers will eventually make an independent measurement of the phase space distributions of the beams there is no call to improve the simulations to the required degree of precision to resolve this question.

The final hypothesis is that the $e^{\pm}$ peak asymmetry could be due to an instrumental effect caused by fact that the particle rate is higher at TOF0 for positive polarity beams than negative polarity beams [59]. Cobb has suggested that a high rate could lower the photomultiplier tube voltages and thereby increase the transit time in PMTs in the detector [78]. This would cause TOF0 to trigger the discriminator later, resulting in an shorter

Detector	x_0 (mm)	y_0 (mm)	z_0 (mm)	Δz (mm)	Δx (mm)
TOF0	1.8	2.6	−3852.7	50.0	400.0
Cherenkov	0.0	0.0	−3450.0	693.0	450.0
BPM	0.0	−25.0	−354.0	1.6	442.2
Quadrupole 7	0.0	0.0	353.0	658.0	700.0
Quadrupole 8	0.0	0.0	1513.0	658.0	700.0
Quadrupole 9	0.0	0.0	2673.0	658.0	700.0
TOF1	30.2	−17.6	3852.7	50.0	420.0

Table 4.6: The table shows the relative longitudinal positions of the intersections of the detector and magnet centre planes with the design trajectory. The numbers are based on a survey of the MICE hall performed on the 11th and 12th September 2010 [63]. Small changes in the positions of the TOFs may be noted from the previous survey in December 2008, as reported by Rayner and Cobb [79].

measurement of the time of flight. This could also explain the slight decrease in positron time of flight as Step I continued and the target was dipped increasingly deep into the ISIS proton beams [73].

4.3 Simulation of the upstream time of flight system

Before studying the distributions of the MICE beams in trace space this section summarizes the distributions of the data sets defined in Section 4.1 in variables which are directly measured by TOF0 and TOF1. Section 4.3.1 begins by describing how simulations of the beams corresponding to these data sets were produced. Sections 4.3.2 and 4.3.3 compare the data and simulated distributions of time of flight and position respectively.

4.3.1 The G4Beamline-G4MICE simulations of the Step I beams

The evolution of Step I beams in the MICE beam line was first studied using the TURTLE simulation software [71]. Tilley used TURTLE to design the base line (6 mm, 200 MeV/c) optical configuration. This simulation is inadequate for comparison with Step I data from TOF0 and TOF1 as it is based on a prediction of the Step I beam line geometry which is different from the final arrangement of magnets and detectors.

Apollonio made a better model of the beam line based on an up to date survey using the Monte Carlo simulation program G4Beamline [62]. This software has the advantage of detailed magnet field maps and a thorough model of particle interactions in matter provided by Geant4 [68]. This model was developed for the genetic algorithm optical design, but was also used to simulate the re-scaled TURTLE beams [52] (cf. Section 2.3.4).

A more detailed model of the upstream time of flight system has been developed for the analysis in this thesis. Apollonio's G4Beamline simulations have been used as input beams for a simulation of the beam line between TOF0 and TOF1 using G4MICE. G4MICE is also based on Geant4, and benefits from more detailed magnet and detector geometries and material budgets.

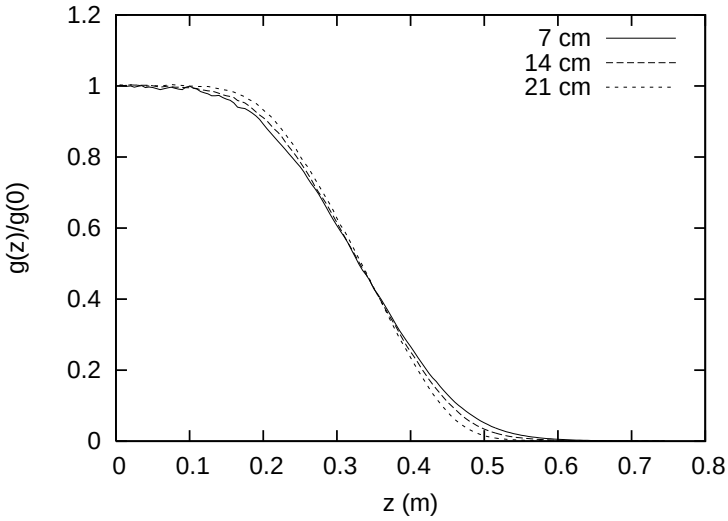

Figure 4.7: The profile of the normalized gradient $g(z) = \mathrm{d}B_y(z)/\mathrm{d}x/g_0$ of quadrupoles 7, 8 and 9 at three axial displacements. The field map was generated using Opera-3d [81]. All three curves have an integral equal to half the effective length of 32.9 cm. Therefore the effective length of the quadrupoles is $l_{\mathrm{eff}} = 65.8$ cm.

The geometry of the simulation is based on the survey of the MICE beam line conducted in September 2010. The location of the TOF detectors was described in Section 4.2.1. The best available information of the components of beam line between these detectors is summarized in Table 4.6. The magnets and detectors were placed at these positions in a Geant4 'world volume' filled with air. Apollonio provided data sets of the phase space vectors of electrons, muons and pions in the G4Beamline simulations of the $\epsilon_{\mathrm{N}} = 6$ mm re-scaled TURTLE optical configurations immediately upstream of TOF0. These ensembles were then simulated in G4MICE from the upstream face of TOF0 to the downstream face of TOF1. The 3 mm and 10 mm elements have not been simulated as there should only be minor differences between the various design emittances in beams with the same nominal momentum, as the Step I re-scaled TURTLE optical configurations have only been adjusted for momentum after the diffuser (cf. Chapter 2 and Appendix A).

The TOF detectors are modelled with the geometry and materials described in Chapter 3. The Cherenkov counter is made of two vessels each of which is modelled with glass, PVC and polyoxymethylene (delrin) windows, a polycarbonate mirror and 23 mm of aerogel [67, 71]. Most energy loss and scattering takes place in the 2 mm of glass and 3.2 mm of PVC in each vessel. The model was adapted (with an improved material budget) from a geometry submitted by detector experts [67]. The beam profile monitor (BPM) is made of two planes of polystyrene fibres with poly(methyl methacrylate) (PMMA) cladding of diameter 1 mm [80]. These have been approximated in the simulation by two polystyrene sheets[1]. The key element of the BPM geometry is a 9.5 mm thick aluminium frame with a displaced square aperture with the width and centre position reported in Table 4.6. The displacement of the frame was not intentional and has a marginal effect on beam transport.

The field map of quadrupoles 7, 8 and 9 was generated using Opera-3d[2]. Their normalized

[1] The radius of pure polystyrene with the same $\rho \mathrm{d}E/\mathrm{d}X$ was calculated and multiplied by $\pi/4$ to give the average thickness traversed per fibre plane. A Rohacell detector covering leads to negligible energy loss.

[2] Opera-3d is a finite element analysis program capable of calculating electromagnetic fields in media [81].

Matrix element	N_e	N_μ	N_π	$N_\pi/(N_\mu + N_\pi)$
(6 mm, 140 MeV/c) μ^-	3,368	35,238	274	0.77%
(6 mm, 200 MeV/c) μ^-	12,516	293,703	2,704	0.91%
(6 mm, 240 MeV/c) μ^-	4,492	310,196	3,274	1.04%
(6 mm, 140 MeV/c) μ^+	595	11,147	349	3.04%
(6 mm, 200 MeV/c) μ^+	3,788	87,006	4,231	4.64%
(6 mm, 240 MeV/c) μ^+	280	12,844	704	5.20%

Table 4.7: The relative numbers of e, μ and π in simulations of the $\epsilon_{\mathrm{N}} = 6$ mm matrix elements.

field gradient profile is shown in Figure 4.7. The central gradient was set according to the conversions in Table A.1 given the currents in Table 2.3. The body of the magnet is made of steel, with a pole tip radius of 35 cm. The pole tip geometry was implemented by Rogers [67]. Scraping in the quadrupole magnets is important as simulations show that $\sim$ 60% of the beam is lost at the aperture of quadrupole 7.

4.3.2 Time of flight in data and simulation

Time of flight distributions for the nominal $\epsilon_{\mathrm{N}} = 6$ mm μ^- and μ^+ beams in data and simulation are shown in Figure 4.8. The February 2010 calibration has been used to produce the data histograms (as throughout this thesis) with the addition of the TDC bin width correction described in Section 4.2.2. The data distributions have then been shifted so that the $e^\pm$ peaks are roughly aligned with those in simulation to aid the eye in comparing the shape of the distributions[3]. The simulated distributions have been smeared by a Gaussian distribution with mean zero and RMS $\sigma_t = 78.4$ ps in order to simulate the effect of time of flight resolution. This has the advantage of matching the shapes of the distributions for comparison and widening the narrow $e^\pm$ peak so that their size may be compared. The simulated distributions have been normalized so that the area of the muon peaks match. The relative numbers of e, μ and π in the simulations are given in Table 4.7.

The agreement is reasonably good at the fast edge of the muon distribution although there is visible disagreement for the slow muons where the tail is longer in data. It is likely that the disagreement arises from the difficulty in modelling high amplitude particles in the simulations. Despite a particular effort having been made to model the material in the quadrupole apertures accurately, the significant scraping at quadrupole 7 makes the transmitted distribution sensitive to its acceptance. As will be demonstrated in Chapter 6 this affects the slow edge most noticeably as most high amplitude particles are found at this side of the distribution as the focusing strength for them is stronger and they were less likely to have been scraped previously.

The pion distributions are of particular interest because, as discussed in Section 4.1, it is not possible to deduce the pion contamination in the broad muon peaks from time of flight data alone. The simulations show that the contamination is only of the order of 1% in μ^- beams and 5% in μ^+ beams. It is not appropriate to make a cut on them as they are distributed throughout the muon peak.

[3] This calibration is treated more carefully when time of flight is used to measure p_z (cf. Section 5.2.3).

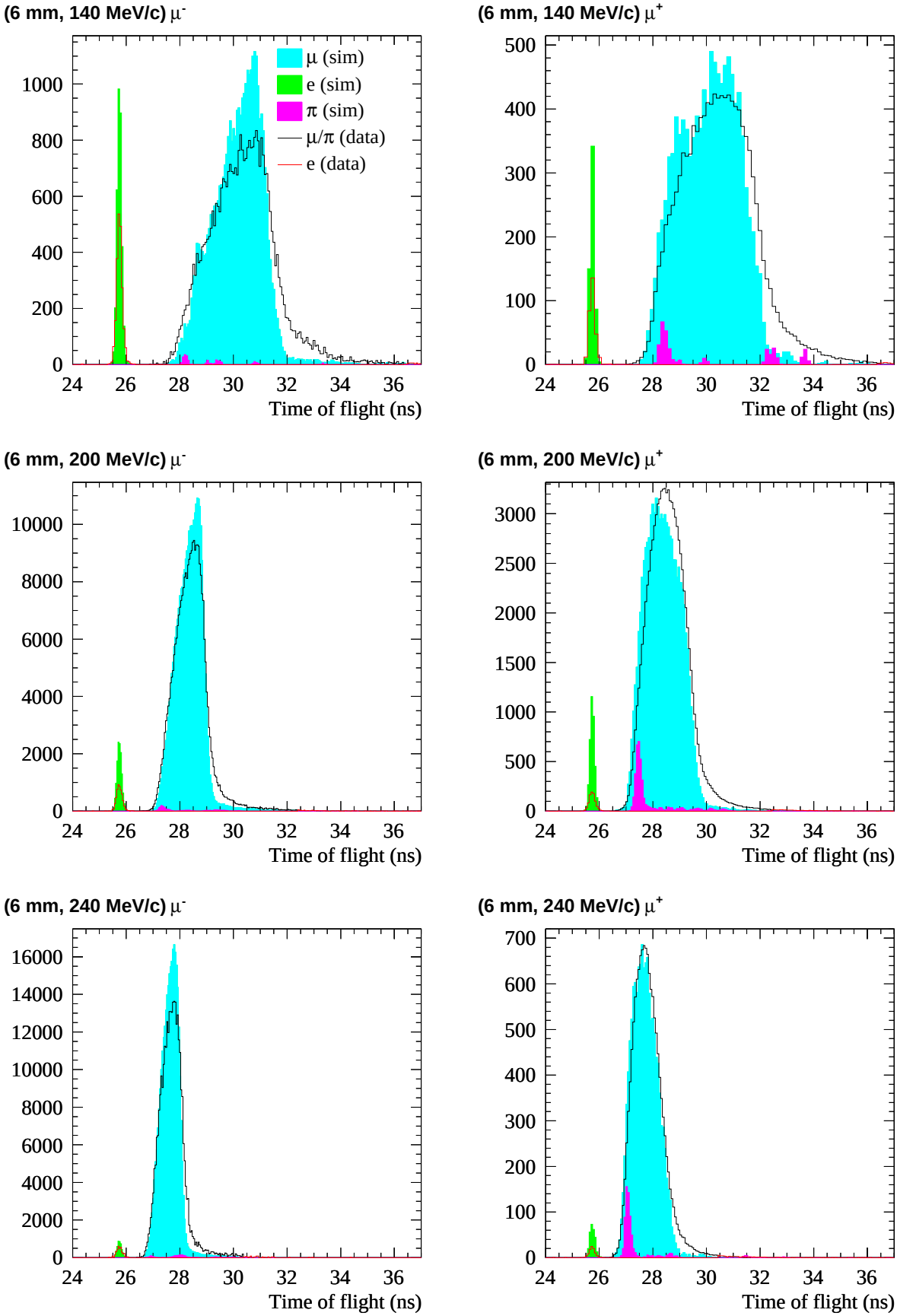

Figure 4.8: A comparison between time of flight distributions in data and simulation for the $\epsilon_N = 6$ mm emittance-momentum matrix beams. The simulation has been normalized so that the sum of the μ and π peaks has the same area as the μ/π peak in data.

Matrix element (cm)	Reconstructed data $\langle x \rangle$	$\langle y \rangle$	σ_x	σ_y	Reconstructed simulation $\langle x \rangle$	$\langle y \rangle$	σ_x	σ_y
(6 mm, 140 MeV/c) μ^-	0.64	−1.03	6.04	6.51	−0.49	0.19	6.39	6.87
(6 mm, 200 MeV/c) μ^-	1.24	−0.90	5.56	6.02	−0.19	0.04	6.18	6.50
(6 mm, 240 MeV/c) μ^-	1.30	−0.88	5.40	5.62	0.14	0.05	6.04	6.25
(6 mm, 140 MeV/c) μ^+	−0.21	−0.39	6.12	6.48	−1.04	0.00	5.82	6.92
(6 mm, 200 MeV/c) μ^+	−0.29	−0.17	5.78	5.88	−1.28	0.12	5.19	6.80
(6 mm, 240 MeV/c) μ^+	−0.28	−0.18	5.70	5.62	−1.30	0.04	4.90	6.52

Table 4.8: Comparison between measurements of x just before TOF1 in data and resolution smeared Monte Carlo truth. The error on the mean and RMS are of the same order, and never greater than 1 mm.

4.3.3 Transverse position in data and simulation

Distributions of transverse position in the horizontal and vertical plane at TOF1 in data and simulation are plotted in Figure 4.9 and Figure 4.10. The simulated distributions are smeared by the position resolution of TOF1 and the data is corrected for the detector offsets measured in the most recent survey and recorded in Table 4.6. The origin of the position distributions is the intersection of TOF1 with the design axis, defined as in the survey to be the line through the centre of quadrupoles 7-9. The simulated distributions have been normalized to the integrated area of the data distributions and the means and standard deviations of the distributions are recorded in Table 4.8.

The shapes of the distributions are remarkably similar irrespective of the nominal momentum or polarity of the beam (as might be expected for re-scaled optical configurations), with vertical distributions being slightly more peaked but having comparable RMS widths to horizontal distributions. None of the means or RMS widths are consistent within measurement error but all are centred within 1.5 cm. A systematic horizontal offset between data and simulation may indicate an error in the correction for the offset of the detector with the design axis. This may be due to the importune removal and replacement of TOF1 from its frame in the days between the end of the data taking campaign and the survey. Nevertheless care has been taken to apply the survey results faithfully.

One may observe a displacement in $\langle x \rangle$ between the μ^- and μ^+ beams which increases with nominal momentum in a fashion mirrored by the simulations. This is likely to reflect the effect of dispersion in dipole 2 of initial phase space distributions which vary slightly as the current in the decay solenoid was not switched when the polarity of the other beam line magnets was switched.

The rough agreement in the magnitude of beam size in data and resolution smeared Monte Carlo is encouraging as a first indication that the transverse phase space of the beams does not differ markedly from expectations. Naturally however, the emittance of the beams is of primary importance, as the design of the diffuser depends on its value, assumed naively to be $\epsilon_{\mathrm{N}} \approx 3$ mm. A full phase space comparison is made in Chapter 6 using the momentum reconstruction technique described in the next chapter.

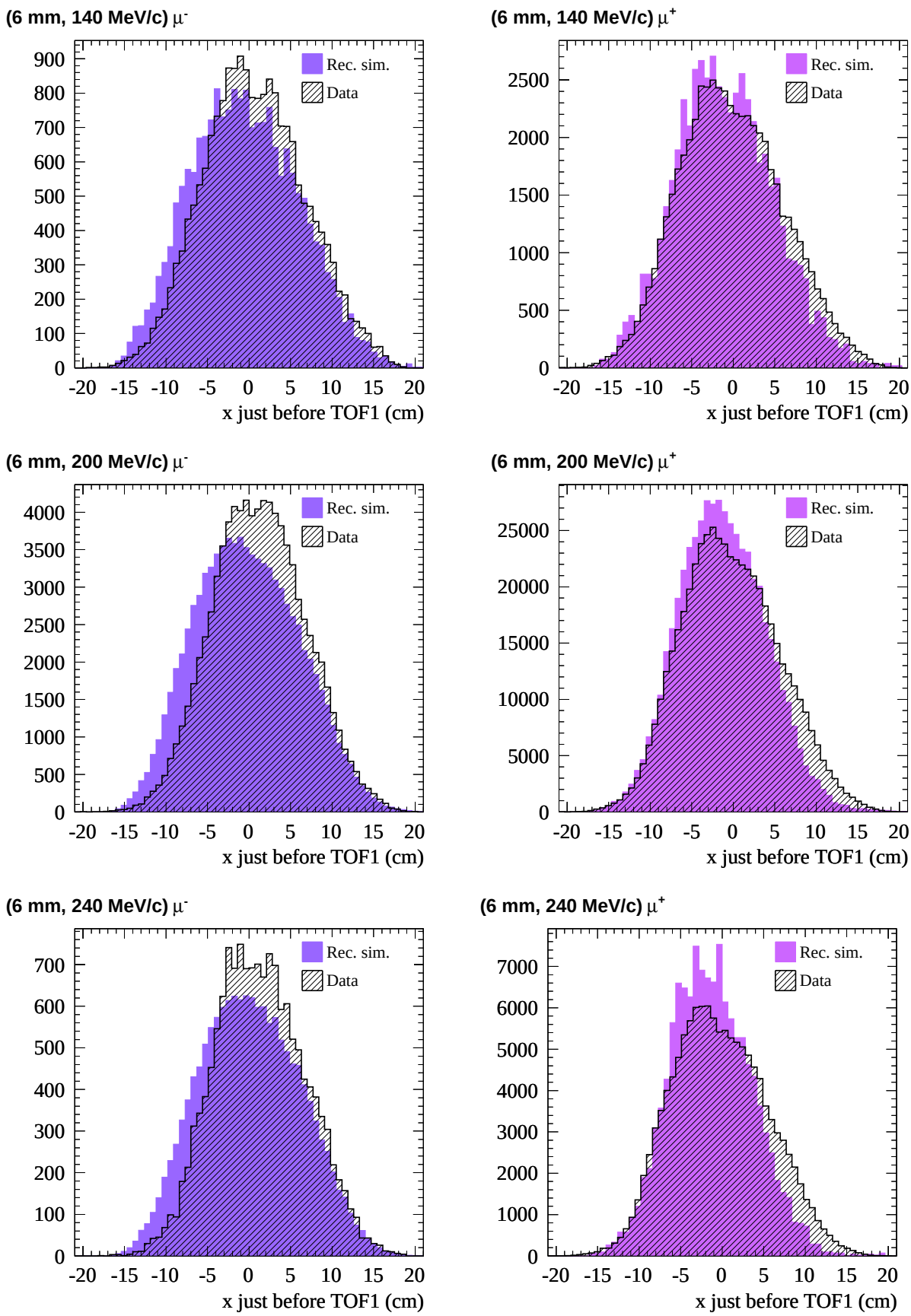

Figure 4.9: A comparison between measurements of x at TOF1 in data and Monte Carlo for the $\epsilon_{\mathrm{N}} = 6$ mm elements of the emittance-momentum matrix for both μ^- and μ^+ beams. The simulated distributions are weighted to the data.

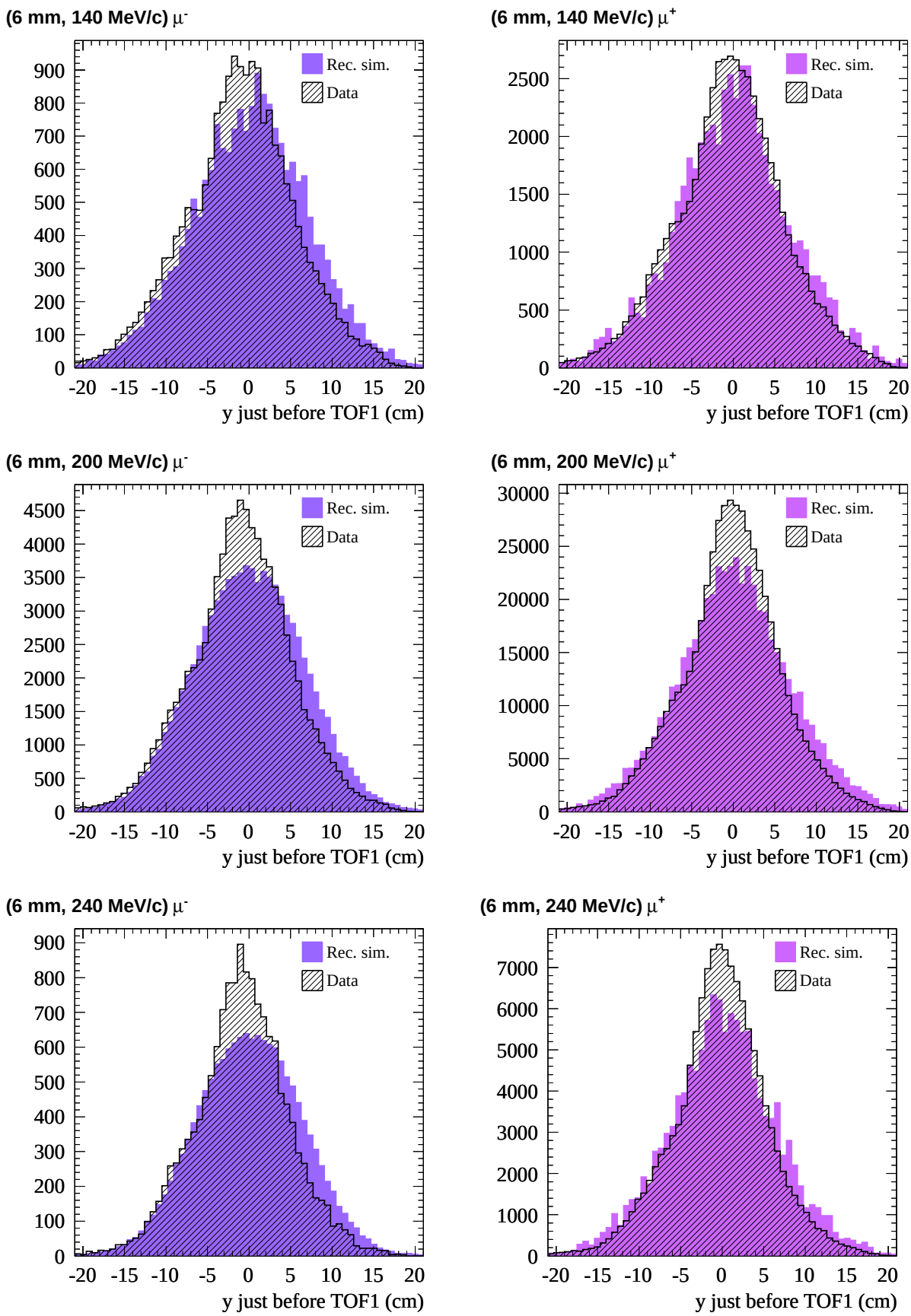

Figure 4.10: A comparison between measurements of y at TOF1 in data and Monte Carlo for the $\epsilon_N = 6$ mm elements of the emittance-momentum matrix for both μ^- and μ^+ beams. The simulated distributions are weighted to the data.

4.4 Conclusion

In this chapter the time and position measurements described in Chapter 3 have been applied to the Step I data. Data sets have been defined for the emittance-momentum matrix of rescaled TURTLE muon beams and compared with Monte Carlo simulations. The size of the Step I data sets is shown in Table 4.2; the size of the Monte Carlo simulations is shown in Table 4.7. These data sets and simulations are analysed further in the following chapters.

The muon beams have been selected using the time of flight cuts in Table 4.1. Electrons and protons may trivially be removed using timing cuts. A pion cut is not necessary as no pion peak is present at the end of the beam line. Some pions do survive, and cannot be removed as they have a broad momentum spectrum, however Monte Carlo simulations show that the contamination of the muon peak is about 1% for μ^- beams and 5% for μ^+ beams. A discrepancy of order 70 ps in the mean time of flight of the electron and positron peaks has not yet been understood.

The comparison between data and simulation in Section 4.3 is encouraging but inconclusive as the simple comparisons of direct measurements of time and position do not provide information about the longitudinal and transverse momenta of the muons: it is not possible to predict the subsequent behaviour of the beams without further analysis. Nevertheless these measurements provide the basis for the reconstruction of particle trajectories in the following chapters. The comparisons here are designed to be a useful reference.

Chapter 5

Measurement of muon momenta

An iterative reconstruction algorithm has been developed to remove a bias of order 5 MeV/c from $\sim$ 3 MeV/c resolution measurements of p_z by the MICE time of flight detectors. The momentum spectra of the Step I beams have been measured and found to be consistent with Monte Carlo simulations. The method also reconstructs the transverse angles x' and y' and encouraging agreement is observed with simulations.

Step I of the MICE experiment was devoted to creating and characterizing each of the beams in the emittance-momentum matrix. In the absence of the upstream spectrometer it was necessary to improvize the measurement using the time of flight system illustrated in Figure 5.1.

This chapter focuses on the reconstruction of individual muon momenta at TOF1, with particular attention to making an unbiased measurement of the longitudinal momentum. The following chapter uses these measurements to characterize the distributions of the beams in transverse phase space. First however, Section 5.1 explains the general principles behind the reconstruction of transverse and longitudinal phase space distributions used in this thesis, and why the traditional method is not appropriate for the MICE beam line.

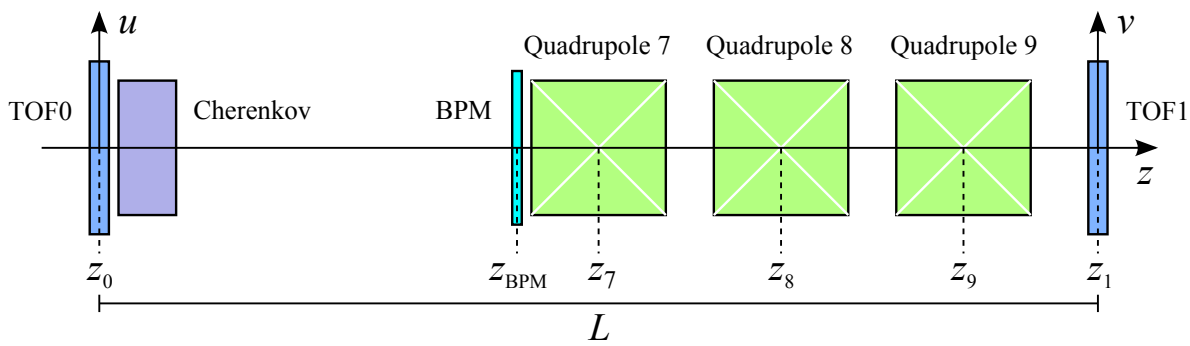

Figure 5.1: The MICE time of flight system [65]. A Cherenkov detector (Ckov), beam profile monitor (BPM), and quadrupole triplet (Q7-Q8-Q9) lie between two high precision timing detectors, TOF0 and TOF1.

5.1 Phase space reconstruction at the MICE beam line

Emittance is traditionally estimated using measurements of a beam's RMS size in three or more profile monitors [38]. The technique relies upon knowledge of the transfer matrices which transport trace space vectors between the detectors. Suppose two of the detectors are TOF0 and TOF1. As demonstrated in Chapter 3 TOF0 and TOF1 are capable of measuring position with resolution ~ 1 cm: consider either the horizontal or vertical plane, and let the measurement of the displacement in that plane be u in TOF0 and v in TOF1, as indicated in Figure 5.1. In the approximation of linear beam transport, a particle's trace space vector (u, u') is then transformed as

$$\begin{pmatrix} v \\ v' \end{pmatrix} = \begin{pmatrix} M_{11} & M_{12} \\ M_{21} & M_{22} \end{pmatrix} \begin{pmatrix} u \\ u' \end{pmatrix} \tag{5.1}$$

where the conjugate variable is the angle of the velocity of the particle with respect to the design axis $u' = \mathrm{d}u/\mathrm{d}z$. Similarly it may be shown that the beam's covariance matrix transforms as:

$$\begin{pmatrix} \sigma_{vv} & \sigma_{vv'} \\ \sigma_{vv'} & \sigma_{v'v'} \end{pmatrix} = \begin{pmatrix} M_{11} & M_{12} \\ M_{21} & M_{22} \end{pmatrix} \begin{pmatrix} \sigma_{uu} & \sigma_{uu'} \\ \sigma_{uu'} & \sigma_{u'u'} \end{pmatrix} \begin{pmatrix} M_{11} & M_{12} \\ M_{21} & M_{22} \end{pmatrix}^{\mathrm{T}}. \tag{5.2}$$

In Step I we wish to measure the emittance at TOF1 $\epsilon = \sqrt{\sigma_{vv}\sigma_{v'v'} - (\sigma_{vv'})^2}$. The transfer matrix can be calculated given knowledge of the magnetic fields in the quadrupoles, and TOF0 and TOF1 provide measurements of σ_{uu} and σ_{vv}, however another measurement is required to fully constrain Equation 5.2 and measure both $\sigma_{v'v'}$ and $\sigma_{vv'}$. This could potentially have been provided by a measurement of the beam size in a third detector such as the beam profile monitor or TOF2. Neither was calibrated and added to the data acquisition in Step I because this traditional method of emittance measurement is not possible in the MICE neam line as the transfer matrices vary significantly over the momentum spectrum of the beams.

A novel method of phase space reconstruction was developed instead which uses the high resolution time of flight measurement made by TOF0 and TOF1. Before this technique is introduced however, it is necessary to discuss beam transport in the time of flight system in more detail.

5.1.1 Beam transport in the MICE time of flight system

The quadrupole gradient of the baseline (6 mm, 200 MeV/c) optical configuration as a function of z in the upstream time of flight system is illustrated in Figure 5.2. The MICE quadrupoles are alternately focusing, defocusing, and focusing in the horizontal plane. As the MICE quadrupoles have relatively wide apertures a thin lens model is inadequate as particles make a significant detour in x and y in the quadrupole fringe fields.

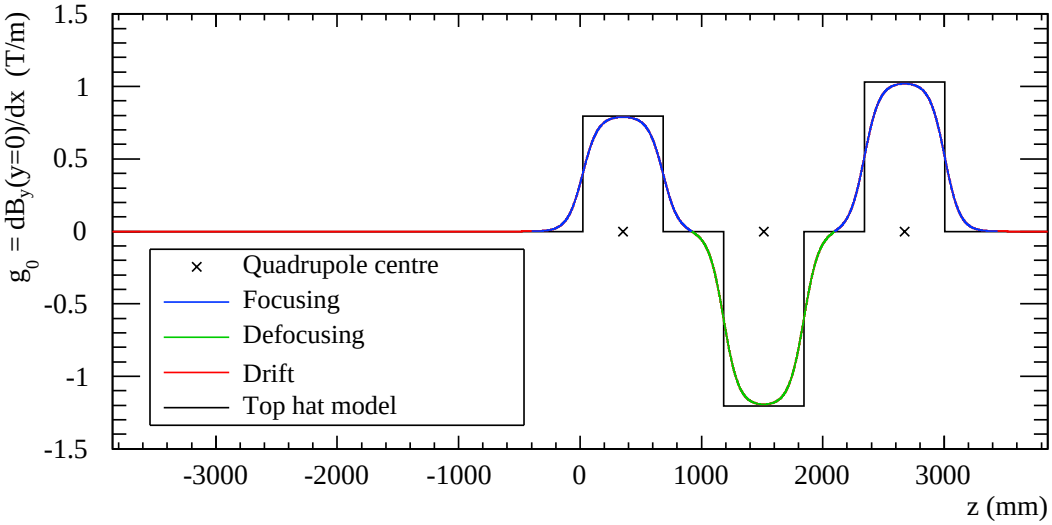

Figure 5.2: The axial quadrupole gradient $g_0 = \mathrm{d}B_y/\mathrm{d}x$ between TOF0 and TOF1. Quadrupole triplet Q7-Q8-Q9 is focus-defocus-focus in the horizontal plane in all Step I optical configurations. The 'top hat' parameterization of the gradient profile which has been used to estimate the path length through the quadrupoles is also illustrated. The width of the top hat functions is the effective length of the quadrupoles $l_{\mathrm{eff}} = 65.8$ cm (cf. Section 4.3.1).

The 'top hat' model of transport through quadrupoles

The quadrupole gradient is often modelled as a top hat of width l_{eff} and height $g_0 = \mathrm{d}B_y(x, 0, z_{\mathrm{quad}})/\mathrm{d}x$, as illustrated in the figure. The transfer matrices across the distance l_{eff} in the focusing and defocusing planes are:

$$\mathbf{F} = \begin{pmatrix} \cos\Omega & k_0^{-\frac{1}{2}}\sin\Omega \\ -k_0^{\frac{1}{2}}\sin\Omega & \cos\Omega \end{pmatrix}, \quad \mathbf{D} = \begin{pmatrix} \cosh\Omega & k_0^{-\frac{1}{2}}\sinh\Omega \\ k_0^{\frac{1}{2}}\sinh\Omega & \cosh\Omega \end{pmatrix},$$

where the central focusing strength is defined as $k_0 = qg_0/p$ and the phase advance $\Omega = \sqrt{|k_0|}l_{\mathrm{eff}}$ [38]. The zero gradient regions may be traversed by the drift matrix:

$$\mathbf{O} = \begin{pmatrix} 1 & l \\ 0 & 1 \end{pmatrix}.$$

where l is the drift length[1]. The transfer matrix between TOF0 and TOF1 is therefore given in the horizontal plane by:

$$\mathbf{M}_x = \mathbf{O}(z_1 - z_9 - \tfrac{1}{2}l_{\mathrm{eff}})\mathbf{F}(g_9)\mathbf{O}(z_9 - z_8 - l_{\mathrm{eff}})\mathbf{D}(g_8)\mathbf{O}(z_8 - z_7 - l_{\mathrm{eff}})\mathbf{F}(g_7)\mathbf{O}(z_7 - \tfrac{1}{2}l_{\mathrm{eff}} - z_0),$$

and in the vertical plane by:

$$\mathbf{M}_y = \mathbf{O}(z_1 - z_9 - \tfrac{1}{2}l_{\mathrm{eff}})\mathbf{D}(g_9)\mathbf{O}(z_9 - z_8 - l_{\mathrm{eff}})\mathbf{F}(g_8)\mathbf{O}(z_8 - z_7 - l_{\mathrm{eff}})\mathbf{D}(g_7)\mathbf{O}(z_7 - \tfrac{1}{2}l_{\mathrm{eff}} - z_0).$$

[1] As noted in Chapter 2 the drift transfer matrix is a function of p_z in phase space but not in trace space. This simplifies the transport of wide p_z spectrum beams in trace space and makes it an attractive parameterization for use in Chapter 5 and Chapter 6.

The slice matrix method

While the top hat transfer matrix method delivers the correct impulse to each particle it neglects the effect of the fringe fields. Alternatively the beam line may be divided into sections of a centimetre or so along $\hat{z}$ with the wide aperture quadrupole fringe fields modelled as ~ 100 adjacent top hat quadrupoles with g_0 given by the magnitude of the fringe field at that point. To this end the gradient profile of the OPERA model in Figure 4.7 was fitted at $x = 7$ cm using a pair of hyperbolic tangent functions:

$$\frac{g_{\text{tanh}}(z)}{g_0} = \frac{\tanh[(a-z)/b] + \tanh[(a+z)/b]}{2}, \tag{5.3}$$

where $a = 33.09 \pm 0.05$ cm and $b = 12.53 \pm 0.08$ cm. This functional form[2] was used in preference to the more widely used Enge parameterization as it was found to be imperceptibly different from the OPERA map and requires fewer parameters. One may integrate it analytically to calculate the effective length:

$$l_{\text{eff}} = \int_{-\infty}^{\infty} \frac{g_{\text{tanh}}(z)}{g_0} \mathrm{d}z = 2a.$$

The parameter b does not affect the effective length but alters the shape of the field. In contrast to $a = l_{\text{eff}}/2$ it's value may be seen in Figure 4.7 to vary slowly as a function of x. This effect is neglected in the analysis in this chapter.

For each optical configuration the central gradient g_0 of quadrupoles 7, 8 and 9 are calculated from the current using the conversion in Appendix A. Three double hyperbolic tangent gradient profiles are scaled by the resulting central gradients and summed with displacements given by their respective positions in the beam line to create profiles like that illustrated for the base line case in Figure 5.2. This procedure has the advantage of correctly modelling the regions where the fringe fields of adjacent magnets overlap. It has been used to create a gradient profile for each of the re-scaled TURTLE optical configurations. The profiles are turned into finely grained step functions by slicing the longitudinal position into 1 cm regions of constant gradient which are modelled as top hat quadrupoles. The total transfer matrix is then calculated in the same was as in the previous section, but with many more matrices.

As the polarity of the magnet currents is switched when the polarity of the beam changes, the quadrupole triplet is always arranged to focus-defocus-focus in the horizontal plane and *vice versa* in the vertical plane. The transfer matrices are therefore the same for μ^- and μ^+ beams with the same nominal emittance and momentum.

The p_z dependence of beam transport in the MICE beam line

It is important to note that the transfer matrices are a function of momentum. The dependency arises both in the focusing strength and the phase advance in the quadrupoles, reflecting the fact that high momentum particles are focused less as they pass through the magnets. This is an important effect as the MICE beam line is designed to have a particularly high p_z acceptance to mimic the front end of a neutrino factory. The momentum distribution just

[2] The double hyperbolic tangent was inspired by Dragt's parameterization of solenoidal fringe fields in his fascinating Lie algebraic treatment of transfer maps through solenoids [82, 83].

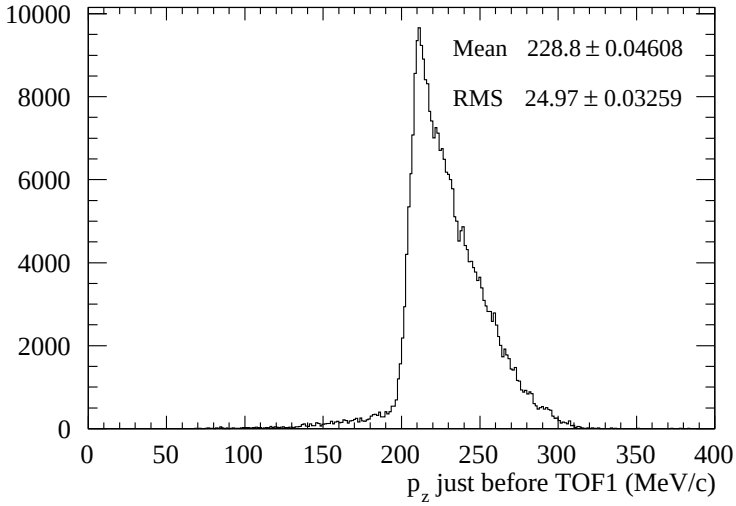

Figure 5.3: The distribution of longitudinal momenta of muons just upstream of TOF1 in a simulated base line (6 mm, 200 MeV/c) μ^- beam. The asymmetrical sharp low momentum edge of the distribution is an artefact of setting dipole 2 to transmit the momentum of muons from pions which decayed backwards in the pion reference frame in the decay solenoid.

upstream of TOF1 in a simulation (cf. Section 4.3) of the base line (6 mm, 200 MeV/c) μ^- beam is shown in Figure 5.3 and the corresponding horizontal and vertical transfer matrices (obtained using the slice matrix method) are shown in Figure 5.4.

The elements of $\mathbf{M}_x$ and $\mathbf{M}_y$ vary quickly at low momenta: at higher momenta relativistic effects mean that the transit speed decreases more slowly as a function of p_z and the oscillations in the transfer map stabilize. As $p_z \to \infty$ the magnets have a negligible effect and the transfer matrices tend to a drift matrix $\mathbf{O}(L)$ in both planes, with $M_{12} \to L = 7.71$ m. This element in particular increases by 100% between 200 MeV/c and 300 MeV/c where most particles are located. As a result of the magnet re-scaling process underpinning the design of the re-scaled TURTLE optical configurations the situation is similar for the other elements of the emittance-momentum matrix. The traditional emittance measurement method therefore cannot be used in the MICE beam line as it requires the transfer matrix to be approximately the same for all particles.

5.1.2 Measuring longitudinal momentum

To characterize the MICE beams it is first necessary to measure their momentum spectra. If a particle's time of flight t and path length s between two planes are known, its momentum p may be calculated via $p/E = s/t$, assuming p to be constant. The average momentum in the air between the TOFs is given by:

$$p(s,t) = \frac{ms/t}{\sqrt{1 - s^2/(ct)^2}},$$

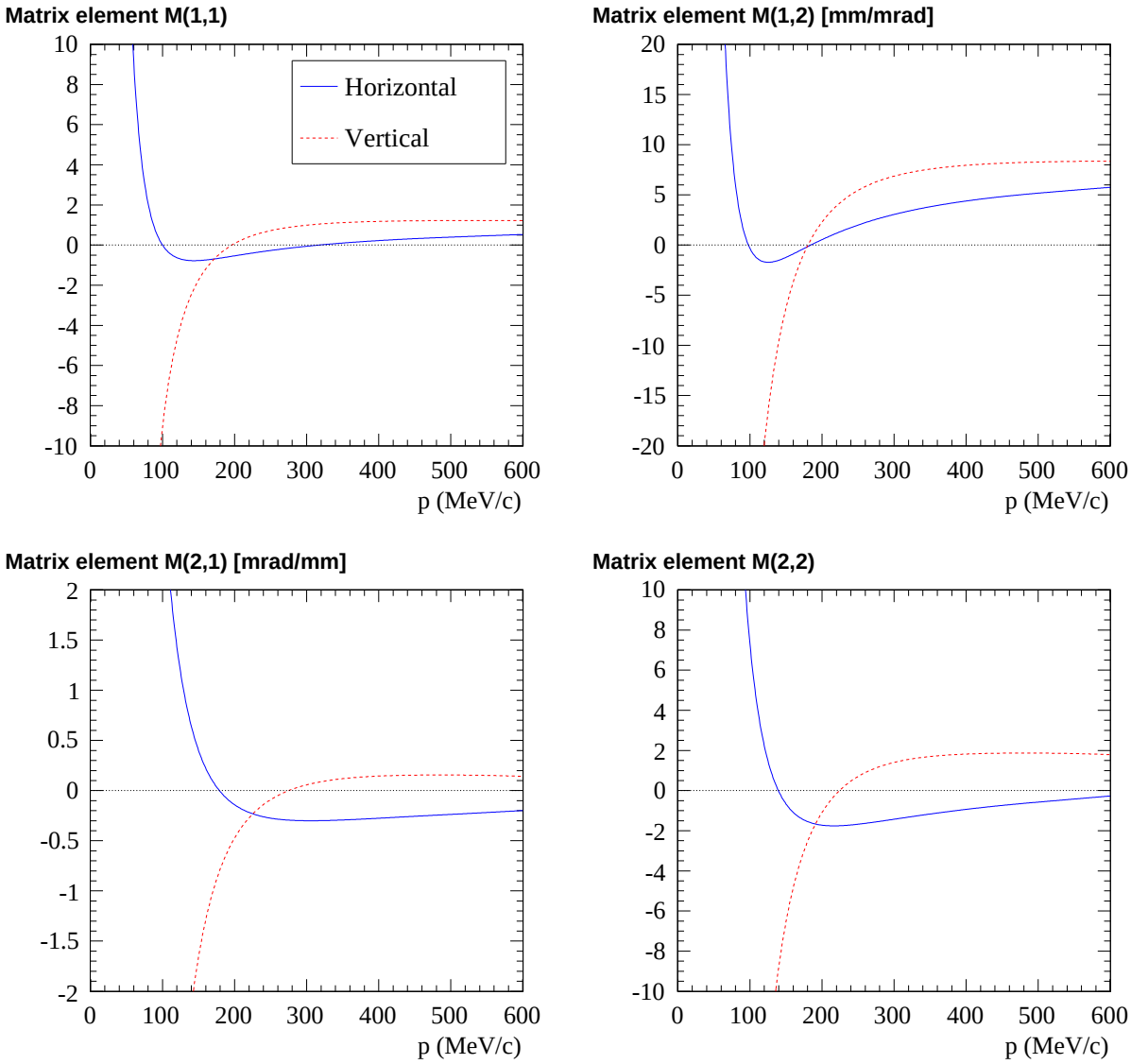

Figure 5.4: The horizontal and vertical trace space transfer matrices between TOF0 and TOF1 as a function of longitudinal momentum for the base line (6 mm, 200 MeV/c) matrix element. $\mathbf{M}_x$ and $\mathbf{M}_y$ have been calculated using the slice matrix technique and include the effect of fringe fields.

with resolution given by:

$$\frac{\sigma_p}{p} = \frac{E^2}{m^2}\sqrt{\left(\frac{\sigma_t}{t}\right)^2 + \left(\frac{\sigma_s}{s}\right)^2}. \tag{5.4}$$

The time of flight resolution was shown in Chapter 2 to be $\sigma_t = 78.4$ ps; the path length resolution σ_s depends on the method of measurement.

Consider first the approximation that the path length is the geometrical distance $L = 7.71$ m between the TOFs. The TOFs will measure the time of flight of a muon with $p = 230$ MeV/c to be $t = 28.3$ ns with a fractional error of $\sigma_t/t = 0.28\%$. The momentum will be measured with $\sigma_p = 3.7$ MeV/c. The error increases with momentum and is smaller for pions than muons. The momentum of electrons and positrons cannot be measured as they are all highly relativistic at this momentum and have no detectable distribution in time of flight.

The approximation $s = L$ leads to an underestimate of p. The measurement bias is given by:

$$\frac{\Delta p}{p} = \frac{E^2}{m^2}\left(\frac{\Delta s}{s} - \frac{\Delta t}{t}\right). \tag{5.5}$$

Therefore, if a 230 MeV/c muon's path length is underestimated by 10 mm the momentum will be underestimated by 1.7 MeV/c. Similarly, if the time of flight is miscalibrated by 30 ps, the momentum measurement will by wrong by 1.4 MeV/c.

Systematic error due to miscalibration of t because of incorrect geometry information and the $e^{\pm}$ peak anomaly reported in the previous chapter are discussed in Section 5.2.3. To correct path length bias one must track the muon between the detectors and integrate its path s. To track the muon one requires the initial transverse and longitudinal momentum at TOF0.

5.1.3 Reconstructing transverse momentum

Taking into account that $\det \mathbf{M} = 1$ for emittance conserving linear transformations Equation 5.1 may be rearranged so that one may deduce the transverse angles at both detectors from the measured positions:

$$\begin{pmatrix} u' \\ v' \end{pmatrix} = \frac{1}{M_{12}} \begin{pmatrix} -M_{11} & 1 \\ -1 & M_{22} \end{pmatrix} \begin{pmatrix} u \\ v \end{pmatrix} \tag{5.6}$$

Measurements of u' in both planes allow the particle to be tracked to TOF1 to make an unbiased measurement of p_z. In addition, and of particular interest in this thesis, this measurement of v' allows the distribution of the muon beams to be reconstructed at TOF1 particle by particle. Using this method one may make a measurement of emittance which is superior to the traditional method as one may directly observe the shape of the beam distribution.

The method is only possible because of the 2% resolution measurement of p_z of individual muons made by the time of flight detectors. Let us define angle reconstruction coefficients such that $v' = A(p)u + B(p)v$. These are plotted in Figure 5.5.

The reconstruction procedure is complicated by the presence of asymptotes in $A(p)$ and $B(p)$ in the low momentum region of the beams. In these parts of the momentum spectrum

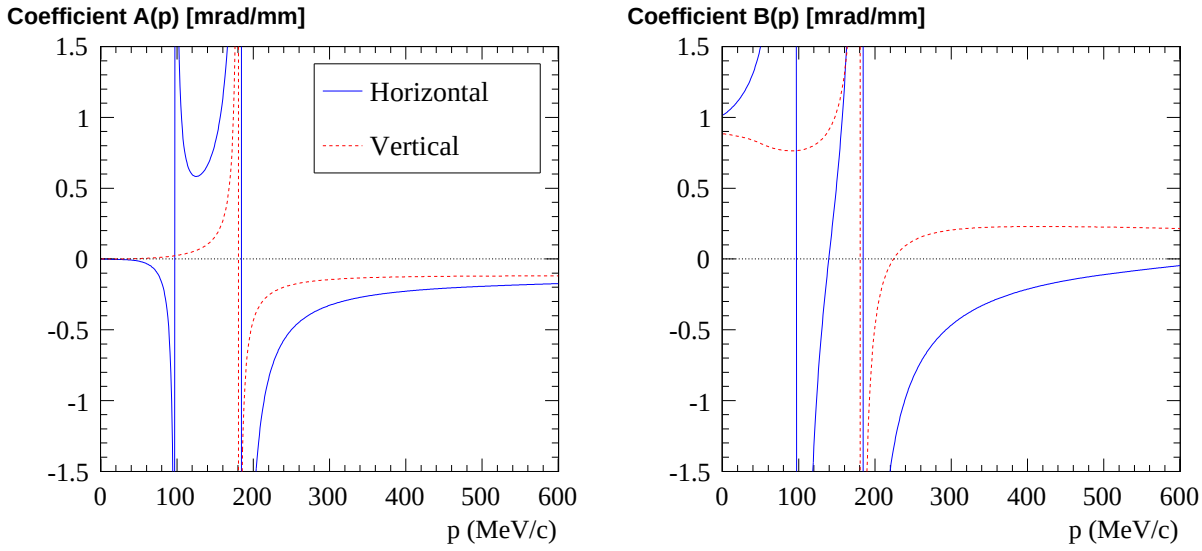

Figure 5.5: The coefficients $A(p) = -1/M_{12}$ and $B(p) = M_{22}/M_{12}$ for the (6 mm, 200 MeV/c) matrix element. Figure 5.3 shows that the region of interest is approximately 200 MeV/c $< p_z <$ 300 MeV/c.

reconstruction of transverse momentum is not always possible, as the coefficients can vary substantially over the error on the p_z measurement. Although the figure is the transfer matrix for the base line (6 mm, 200 MeV/c) beams, the re-scaling design principle of the Step I emittance-momentum matrix data sets ensures that all the beams have similar properties in this at the sharp low momentum edge of their momentum distribution.

Section 5.3 demonstrates that the error on v' is dominated by the position resolution of the detectors and depends on the momentum of the particle: the effect of these errors on emittance measurements is the subject of the next chapter. The reconstruction technique is described in detail in the next section.

5.2 Iterative reconstruction algorithm

In Step I TOF0 and TOF1 have been used to measure the momentum of muons via the solution of the simple equation $p/E = s/t$. In order to make an unbiased measurement of longitudinal momentum it is necessary to estimate the excess path length $\delta = s - L$ travelled by muons between TOF0 and TOF1. Equation 5.6 is used to deduce the initial transverse angles x' and y' at TOF0 so that the particle can be tracked to TOF1 and the path length integrated. As p_z is itself required to solve this equation an iterative tracking algorithm has been designed to eliminate systematic path length bias on p_z. The algorithm is part of the G4MICE reconstruction software and widely accessible as the `Step1Reconstruction` application, written by the author [67].

The algorithm starts with $s = L$. The initial momentum estimate therefore is the solution to the equation $p/E = L/t$. The method then iteratively makes increasingly good estimates of upstream momentum based on increasingly good estimates of path length.

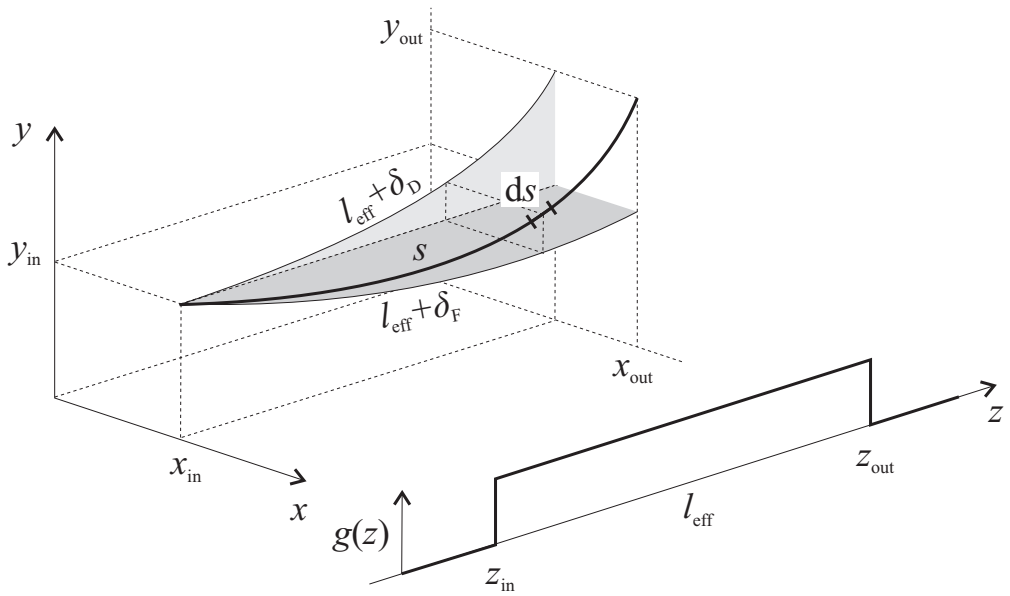

Figure 5.6: The path length of a paraxial particle through a top hat quadrupole $s = l_{\text{eff}} + \delta_{\text{F}} + \delta_{\text{D}}$.

5.2.1 Iterative path length correction

As transfer matrices are linear in the components of the trace space vector the matrices depend only on p_z and are calculated in high precision once at the beginning of the execution of the software application as a function of p_z using the slice matrix method described in Section 5.1.1 so as to model the effect of the fringe fields. The transfer matrix maps are interpolated at the current best estimate of p_z in each iteration in the analysis of each muon trajectory; the values are used to solve Equation 5.6 to obtain x' and y' at TOF0 given x and y in the two detectors. The new transverse position measurement technique described in Chapter 3 is very useful here as the previous slab number based method would have yielded highly quantized results with inferior resolution.

The particle is then propagated in trace space from TOF0 to $z = z_7 - \frac{1}{2}l_{\text{eff}}$, just before quadrupole 7, and its path length in this region is estimated using Pythagoras' theorem:

$$D(z_0, z) \equiv \sqrt{(z - z_0)^2 + (x(z) - x(z_0))^2 + (y(z) - y(z_0))^2},$$

where $x(z)$ and $y(z)$ are calculated by transporting the trace space vector reconstructed at TOF0 using the drift transfer matrix $\mathbf{O}(z - z_0)$. An error is inevitably made at this stage as it is not possible to predict the effect of multiple scattering in the Cherenkov detector, air and beam profile monitor.

By contrast to the calculation of the transfer map, estimating the path length of muons in the quadrupoles depends on initial x, x', y, y' and p_z and must there for be calculated uniquely during every iteration. Using a smooth fringe field model is therefore prohibitively slow as the application is designed to be used online in the control room during future data taking campaigns as well as during the offline Step I analysis presented in this thesis. The top hat model illustrated in Figure 5.2 is used instead.

To obtain the length of the curved path through the quadrupoles $s' \equiv \mathrm{d}s/\mathrm{d}z$ is first expanded

in a Taylor series in the small angles x' and y':

$$s' = \sqrt{1 + x'^2 + y'^2} \approx 1 + \tfrac{1}{2}x'^2 + \tfrac{1}{2}y'^2.$$

The path length $s = L + \delta$ may then be integrated from initial $(x_{\rm in}, x'_{\rm in}, y_{\rm in}, y'_{\rm in}; z_{\rm in})$ at the beginning of the quadrupole field over the entire phase advance $0 < \varphi(z) < \Omega$. The integration is simple as the focusing strength is uniform in this model. Defining $\varphi(z) = \sqrt{|k_0|}(z - z_{\rm in})$, the excess path length is estimated to be:

$$\begin{aligned}\delta^{\rm est} &= \tfrac{1}{2}\int_0^{+\Omega} k_0^{-\frac{1}{2}}\mathrm{d}\varphi\left(\left(-k_0^{\frac{1}{2}}x_{\rm in}\sin\varphi + x'_{\rm in}\cos\varphi\right)^2 + \left(k_0^{\frac{1}{2}}y_{\rm in}\sinh\varphi + y'_{\rm in}\cosh\varphi\right)^2\right)\\ &\equiv \delta_{\rm F}(x_{\rm in}, x'_{\rm in}) + \delta_{\rm D}(y_{\rm in}, y'_{\rm in}),\end{aligned}$$

where the components due to the focusing and defocusing planes are given by:

$$\begin{aligned}\delta_{\rm F}(x_{\rm in}, x'_{\rm in}) &= \tfrac{1}{4}\left(k_0^{\frac{1}{2}}x_{\rm in}^2\left(\Omega - \tfrac{1}{2}\sin 2\Omega\right) - 2x_{\rm in}x'_{\rm in}\sin^2\Omega + k_0^{-\frac{1}{2}}x'^2_{\rm in}\left(\Omega + \tfrac{1}{2}\sin 2\Omega\right)\right)\\ \delta_{\rm D}(y_{\rm in}, y'_{\rm in}) &= \tfrac{1}{4}\left(k_0^{\frac{1}{2}}y_{\rm in}^2\left(\tfrac{1}{2}\sinh 2\Omega - \Omega\right) + 2y_{\rm in}y'_{\rm in}\sinh^2\Omega + k_0^{-\frac{1}{2}}y'^2_{\rm in}\left(\tfrac{1}{2}\sinh 2\Omega + \Omega\right)\right).\end{aligned}$$

At this stage $l_{\rm eff} + \delta^{\rm est}$ is added to the straight line distance calculated between TOF0 and the entrance of quadrupole 7, and a slice matrix interpolation is used to transport the trace space vector of the particle with maximum precision to $z = z_7 + \frac{1}{2}l_{\rm eff}$. The process is repeated in quadrupoles 8 and 9 (and the drifts interspersing them) to estimate the total path length of the muon between TOF0 and TOF1:

$$\begin{aligned}L + \delta^{\rm rec} = \; & D(z_0, z_7 - \tfrac{1}{2}l_{\rm eff}) + (l_{\rm eff} + \delta_7^{\rm est}) + D(z_7 + \tfrac{1}{2}l_{\rm eff}, z_8 - \tfrac{1}{2}l_{\rm eff}) + (l_{\rm eff} + \delta_8^{\rm est})\\ & + D(z_8 + \tfrac{1}{2}l_{\rm eff}, z_9 - \tfrac{1}{2}l_{\rm eff}) + (l_{\rm eff} + \delta_9^{\rm est}) + D(z_9 + \tfrac{1}{2}l_{\rm eff}, z_1).\end{aligned} \tag{5.7}$$

Histograms of the reconstructed path lengths and their residuals are presented in the next section.

5.2.2 Monte Carlo study of the reconstruction algorithm

A Monte Carlo study has been performed to discover the main sources of uncertainty in the reconstruction algorithm: timing resolution, position resolution and multiple scattering. The simulation presented here is a slightly out of date version of the base line (6 mm, 200 MeV/c) μ^- beam Monte Carlo described in Section 4.3. The input ensemble at TOF1 was created with a previous version of G4Beamline and the G4MICE model has its geometry derived from a previous survey and does not contain the beam profile monitor. As this simulation is not compared with data these details do not detract from it illustrating the performance of the reconstruction algorithm.

The study is designed to investigate the performance of the reconstruction algorithm and isolate the effects of timing resolution, position resolution and multiple scattering. Two simulations with multiple scattering on and off were performed using the same initial G4Beamline base line nominal (6 mm, 200 MeV/c) μ^- beam. Five separate reconstructions were subsequently performed on the subset of muons which passed through TOF0 and TOF1 in both simulations in the manner illustrated in Table 5.1. By isolating each effect in this way one

<table>
<tr><th>Simulation</th><th>Scattering</th><th>Time of flight</th><th>(x, y) at TOF0</th><th>(x, y) at TOF1</th></tr>
<tr><td>‘no effects’</td><td>off</td><td rowspan="2">t</td><td rowspan="3">u</td><td rowspan="3">v</td></tr>
<tr><td>‘only M.S.’</td><td>on</td></tr>
<tr><td>‘only t res.’</td><td rowspan="2">off</td><td>$t + \mathrm{N}(0, \sigma_t)$</td></tr>
<tr><td>‘only x res.’</td><td>t</td><td rowspan="2">$u + \mathrm{N}(0, \sigma_u)$</td><td rowspan="2">$v + \mathrm{N}(0, \sigma_v)$</td></tr>
<tr><td>‘all effects’</td><td>on</td><td>$t + \mathrm{N}(0, \sigma_t)$</td></tr>
</table>

Table 5.1: The values of time of flight and transverse position which the reconstruction algorithm was provided with in the Monte Carlo study described in Section 5.2.2. t is the true time of flight and u and v represent the true transverse position in TOF0 and TOF1 in both the horizontal and vertical planes. $\mathrm{N}(\mu, \sigma)$ denotes a random sample from a Gaussian distribution with mean μ and standard deviation σ. The detector resolutions are those measured in Chapter 3: $\sigma_t = 78.4$ ps, $\sigma_u = 0.98$ cm and $\sigma_v = 1.14$ cm.

s (mm)	no effects	only t res.	only x res.	only M.S.	all effects
Mean bias	1.36	1.38	1.63	1.65	1.69
RMS error	2.31	2.46	2.80	3.28	3.59

Table 5.2: A table showing the bias and RMS error of each of the reconstructions of path length s shown in Figure 5.7.

can evaluate their relative importance. The reconstructed distributions are the result of ten iterations of the algorithm.

The path lengths reconstructed by this procedure are compared with the true values in Figure 5.7. The ‘no effect’, ‘only t res.’ and ‘only x res.’ reconstructions should be compared to the true distribution of the simulation with multiple scattering deactivated; the ‘only M.S.’ and ‘all effects’ reconstructions should be compared with the true distribution of the full simulation. As expected multiple scattering increases the mean excess path length of the muon beam from 5.3 mm to 7.5 mm. Both distributions have tails which extend to 25 mm and are narrower than observed for electrons and positrons in Figure 4.6. The distribution of residuals is peaked almost precisely at zero suggesting the algorithm behaves in a consistent manner.

The measurement bias and path length resolution in each case is recorded in Table 5.2. The numbers demonstrate that the resolution is dominated by reconstruction errors due to the stochastic effect of multiple scattering in the Cherenkov detector and in the air between TOF0 and TOF1. Nonlinearities result in the distributions being biased by a millimetre or two: this effect has not been corrected as it is particular to this beam. The zero mode of the residual distribution suggests that the algorithm is designed in a sensible way.

Taking into account all effects, the procedure can remove a bias of order 10 mm to ± 3.6 mm.

5.2.3 Eliminating systematic bias on p_z

Particular care has been taken to eliminate systematic error in the calculation of p_z. The measurement of the excess path length δ in the previous section allows p_z to be estimated

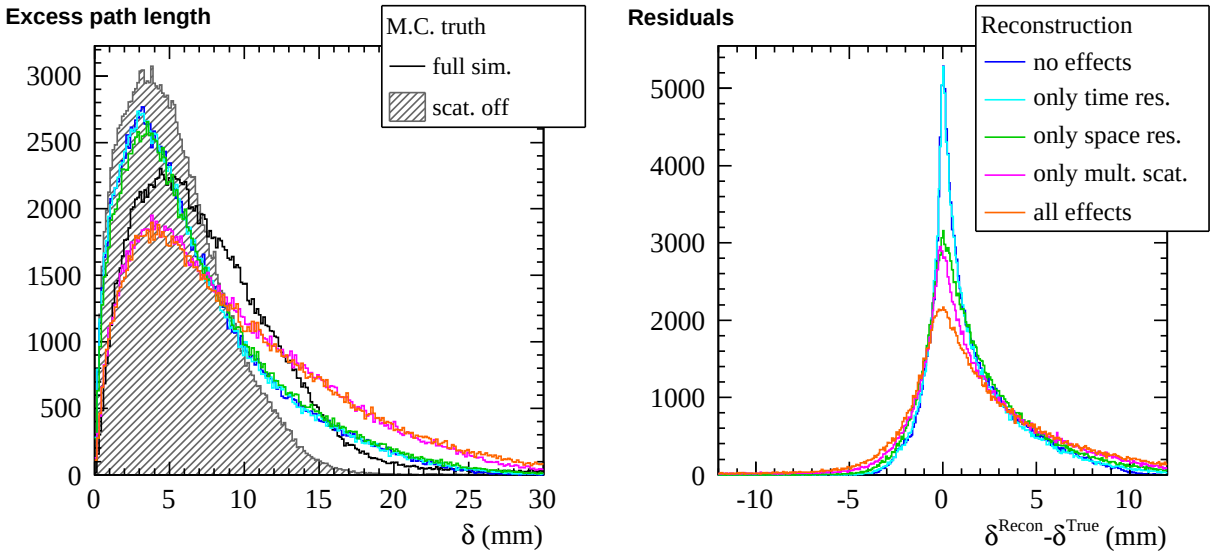

Figure 5.7: A comparison of the reconstructed and true path lengths between TOF0 and TOF1 in the simulations described in Table 5.1. The corresponding measurement biases and resolutions are recorded in Table 5.2. With multiple scattering off, $\langle s \rangle = 5.32$ mm, with an RMS of 3.34 mm. In the full simulation, this increases to, $\langle s \rangle = 7.51$ mm, with an RMS of 4.64 mm.

from the solution of the equation:

$$\frac{p_z c}{E} = \frac{L + \delta}{(L + \langle \delta_e^{\text{sim}} \rangle) + kc\,(t - \langle t_e^{\text{data}} \rangle)}. \tag{5.8}$$

The equation has been derived by subtracting the mean measured $e^{\pm}$ time of flight in data $\langle t_e^{\text{data}} \rangle = (L + \langle \delta_e^{\text{sim}} \rangle)/c$ from the time of flight measured for each muon $t = (L + \delta)/(\beta c)$, where $\beta = pc/E$ and δ is reconstructed by the algorithm.

The advantage of this approach is that it minimizes the systematic error on p_z due to the absolute calibration of the time of flight in data t. As discussed in Section 4.2, the absolute $t_1 - t_0$ calibration of the February 2010 calibration is incorrect as an up to date survey was not available at the time it was performed. Equation 5.8 explicitly discards the absolute calibration provided by G4MICE by initially subtracting the mean $e^{\pm}$ time of flight $\langle t_e^{\text{data}} \rangle$ from the time of flight returned by G4MICE for each muon trajectory t. The measurement therefore only relies of the time taken by muons in excess of the relativistic $e^{\pm}$ component.

In this section the various components of the correction are discussed and a systematic error is assigned to each of them. The total systematic error on p_z is calculated by differentiating Equation 5.8 with respect to the variables and summing the resulting errors [78]. Each individual component and the total systematic error is plotted as a function of p_z in Figure 5.8.

Absolute t calibration using the $e^{\pm}$ peak

As with the particle identification cuts, the properties of the re-scaled TURTLE optical design allow the same value for $\langle t_e^{\text{data}} \rangle$ to be used for all nominal emittances at a particu-

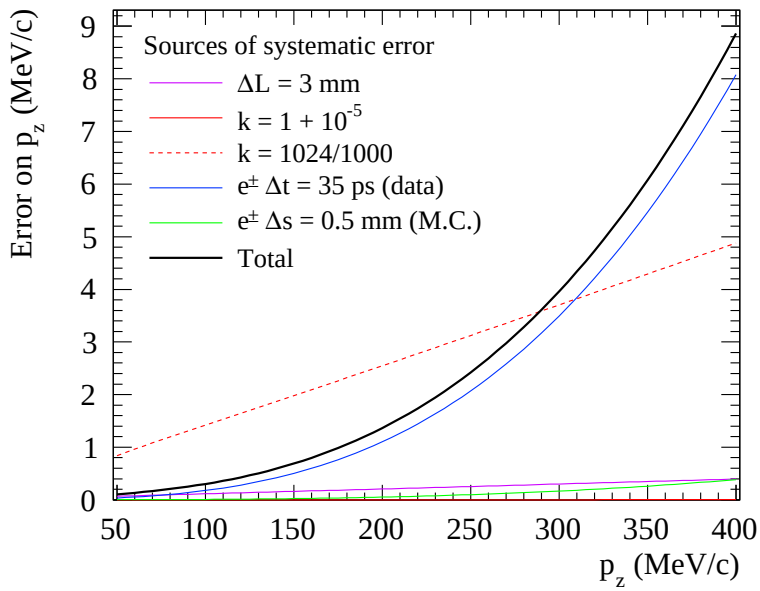

Figure 5.8: Contributions to the systematic error on the longitudinal momentum p_z as a function of p_z. All the components are summed to give the total systematic error except the $k = 1024/1000$ curve which illustrates the error incurred in measurements prior to the discovery that the width of the TDC bins was incorrectly accounted for in G4MICE [84].

lar nominal momentum in the emittance-momentum matrix. In the reconstruction in this thesis the values in Table 4.4 have been used. In the absence of evidence for a kinematic origin for the effect in the Monte Carlo distinct values separated by ~ 70 ps are therefore employed for μ^- and μ^+ beams on the hypothesis that the asymmetry arises from an as yet unknown feature of the calibration. A systematic error of 35 ps is therefore assigned to $\langle t_e^{\text{data}} \rangle$: its contribution to the systematic error on p_z varies as a function of p_z and is plotted in Figure 5.8.

The width of the TDC bins

The factor k accounts for a possible miscalibration of the width of the TDC bins. A systematic error of 10^{-5} is assigned based on information provided by the manufacturers of the TDC electronics [65]. Figure 5.8 shows that this makes a negligible contribution to the total error. As reported in Chapter 4 a factor $k = 1024/1000$ was used prior to July 2010 due to the width of the TDC bins being incorrectly included in G4MICE [84]. This error caused confusion in comparisons between data and Monte Carlo before this date: it is plotted in the figure for reference.

Excess $e^\pm$ path length $s - L$

The denominator of the right hand side of Equation 5.8 is completed by the best estimate of the true $e^\pm$ time of flight $(L + \langle \delta_e^{\text{sim}} \rangle)/c$. This is derived from the sum of the axial separation of TOF0 and TOF1 in the latest survey and the mean Monte Carlo excess $e^\pm$

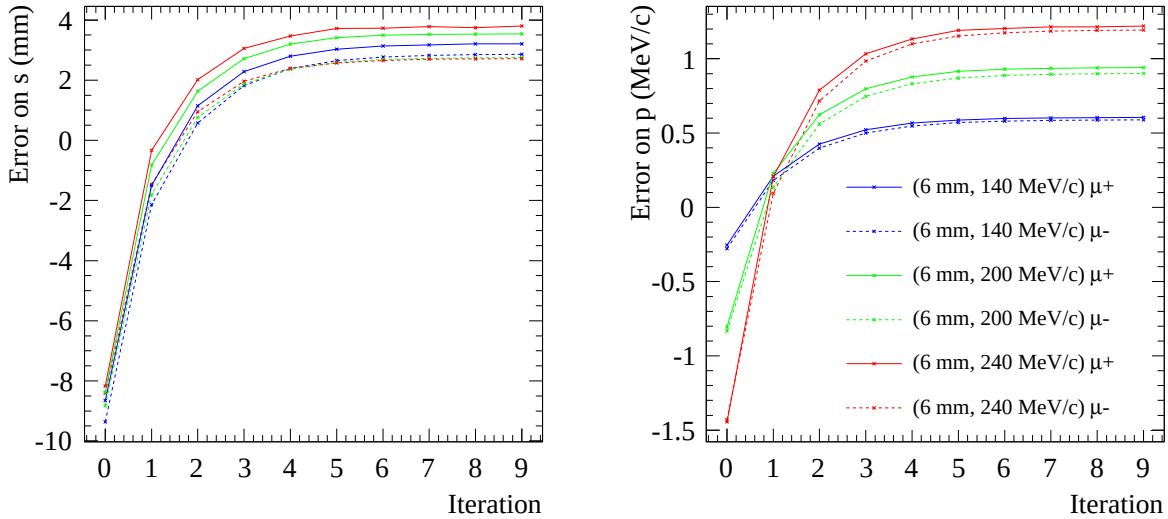

Figure 5.9: The evolution of the mean path length and momentum residuals $\langle s^{\mathrm{Recon}} - s^{\mathrm{True}} \rangle$ and $\langle p_z^{\mathrm{Recon}} - p_z^{\mathrm{True}} \rangle$ as a function of iteration number. The six beams are the six full $\mu^{\pm}$ beams (with pion contamination) simulated using G4Beamline and G4MICE as described in Section 4.3. The damping factor is $f = 0.5$.

path length. The value $L = 7.7053$ m is derived in Section 4.2.1. Although the precision of the survey is better than a millimetre, L is assigned a systematic error of 3 mm as TOF1 was removed from its frame and replaced in the days between the end of the Step I data taking campaign and the survey. The excess $e^{\pm}$ path length $\langle \delta_e^{\mathrm{sim}} \rangle$ is estimated using the Monte Carlo study illustrated in Figure 4.6 using the numbers in Table 4.5 in the same way as with the correction for $\langle t_e^{\mathrm{data}} \rangle$. A systematic error of 0.5 mm is assigned to reflect the reported error on the measurements of mean path length in the simulation. It is possible that the errors assigned to both L and $\langle \delta_e^{\mathrm{sim}} \rangle$ are underestimates: nevertheless Figure 5.8 shows that both contribute less than an MeV/c to the total systematic error and will in any conceivable case be dwarfed by the error due to the anomalous electron-positron asymmetry.

Reconstructed muon path length

The final element of Equation 5.8 to be explained is the path length estimate δ. When the estimate in Equation 5.7 is used in the next iteration the resulting estimates of p_z are found to oscillate in an unpredictable fashion in some low momentum domains. The effect is caused by the fast variation of the elements of the transfer matrices and the presence of asymptotes in the solution to Equation 5.6 in the vicinity of the fast low momentum edge of the momentum spectra. Path length corrections are therefore damped to be a factor f of the difference between the reconstructed value and the value used in the previous iteration δ_{i-1}:

$$\delta_i = \delta_{i-1} + f\left(\delta_{\mathrm{rec}} - \delta_{i-1}\right).$$

With a damping factor $f = 0.5$ the estimates of s and p_z converge smoothly to constant values after five to ten iterations.

The evolution of estimates of s and p_z towards their correct values as a function of iteration

number is illustrated in Figure 5.9. Without damping ($f = 1$) the curves oscillate from positive to negative mean error on each iteration: the damping ensures a smooth progression to stability. Strikingly, the algorithm is seen to generate a stable mean error of a 2 - 4 mm and 0.5 - 1.5 MeV/c in all six cases. This is caused by the asymmetric error distribution observed in Figure 5.7 which was justified by the sharply peaked zero mode of the distribution of path length residuals. It is reproduced in all six cases as each beam is related through the re-scaling of the magnet currents to create the Step I optical configurations. The correlation between error and nominal momentum arises from the dependence of measurement bias on E^2p/m^2 given in Equation 5.5.

Energy loss correction

The final step in the reconstruction of p_z is a small Bethe Bloch correction to account for energy loss in the Cherenkov detector, the beam profile monitor and the ~ 7.5 m of air between TOF0 and TOF1. The reconstruction algorithm described in this section is designed to measure p_z immediately before TOF1, as this is the point at the end of the Step I beam line where all Monte Carlo comparisons and measurements are reported in this thesis.

The momentum just before TOF0, at the end of the drift in air where the majority of t elapses, is given approximately by subtracting half the momentum loss in the air $\Delta p = LE(\mathrm{d}E/\mathrm{d}z)/p$, where $\mathrm{d}E/\mathrm{d}z$

The rate of energy loss is given by the Bethe Bloch equation:

$$\frac{\mathrm{d}E}{\mathrm{d}z} = K\frac{Z}{A}\left[\frac{1}{\beta^2}\ln\left(\frac{2m_ec^2\beta^2\gamma^2}{I}\right) - 1\right],$$

where $K = 0.31$ MeV g^{-1} cm^2 [8]. It is sufficient to model the rate of energy loss as constant in the air and instantaneous in the beam profile monitor. As energy loss affects the momentum measurement by the effect it has on the time of flight energy loss in the Cherenkov may be neglected as it takes place immediately after TOF0 and a negligible fraction of the total time of flight takes place at the higher momentum. The correction therefore gives the momentum immediately upstream of TOF1 to be $p_z = p_{\mathrm{rec}} - \Delta p$ where p_{rec} is the momentum given by the reconstruction algorithm and the correction is:

$$\frac{p_{\mathrm{rec}}\Delta p}{E_{\mathrm{rec}}} = \tfrac{1}{2}L\rho_{\mathrm{air}}\left.\frac{\mathrm{d}E}{\mathrm{d}z}\right|_{\mathrm{air}} + \frac{(z_{\mathrm{BPM}} - z_0)}{L}t_{\mathrm{BPM}}\rho_{\mathrm{BPM}}\left.\frac{\mathrm{d}E}{\mathrm{d}z}\right|_{\mathrm{BPM}}.$$

In line with the model described in Section 4.3.1 thickness of the beam profile monitor is $t_{\mathrm{BPM}} = 1.6$ mm and the densities are taken to be $\rho_{\mathrm{air}} = 1.205 \times 10^{-3}$ g cm^{-3} and $\rho_{\mathrm{BPM}} = 1.06$ g cm^{-3}, with $\langle Z/A\rangle_{\mathrm{air}} = 0.49919$ and $\langle Z/A\rangle_{\mathrm{BPM}} = 0.53768$, and $I_{\mathrm{air}} = 85.7$ eV and $I_{\mathrm{BPM}} = 67.8$ eV [8].

5.2.4 Momentum resolution and the efficiency of the algorithm

The resolution on p_z can be evaluated using the Monte Carlo study introduced in Section 5.2.2. The result of applying the full reconstruction procedure with ten iterations is shown in Figure 5.10. The corresponding bias and error is recorded in Table 5.3. The error

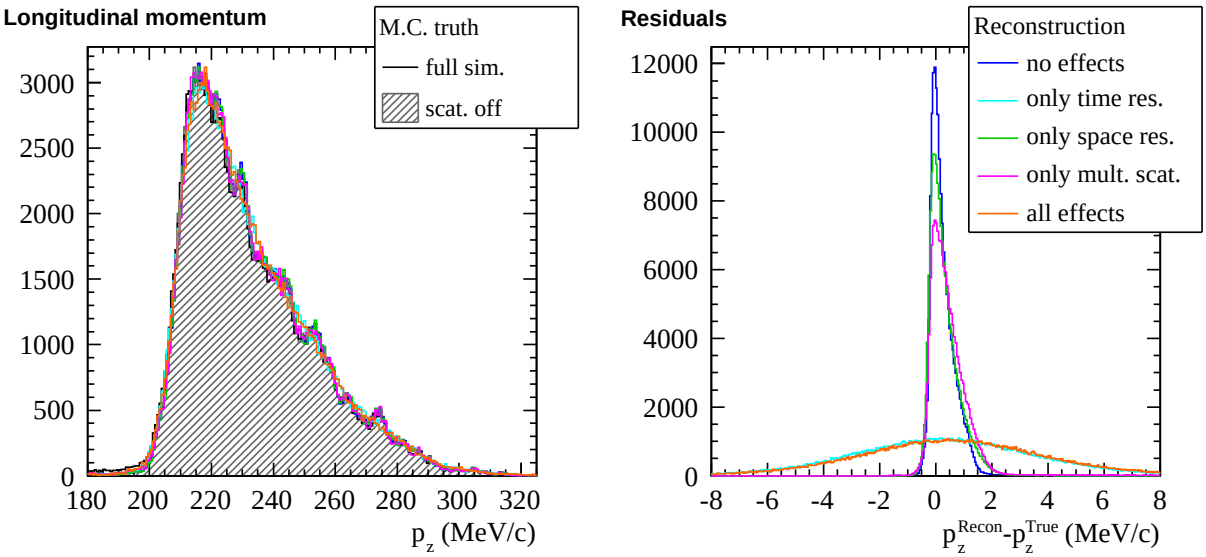

Figure 5.10: A comparison of the reconstructed and true momenta before TOF1 in the simulations described in Table 5.1. The corresponding measurement biases and resolutions are recorded in Table 5.3. With multiple scattering off, $\langle p_z \rangle = 232.52$ MeV/c, with an RMS of 20.28 MeV/c. In the full simulation, $\langle p_z \rangle = 231.97$ MeV/c, with an RMS of 20.49 MeV/c.

p_z (MeV/c)	no effects	only t res.	only x res.	only M.S.	all effects
Mean bias	0.24	0.24	0.30	0.44	0.48
RMS error	0.44 (0.2%)	3.11 (1.3%)	0.53 (0.2%)	0.74 (0.3%)	3.12 (1.3%)

Table 5.3: A table showing the bias and RMS error of each of the reconstructions of longitudinal momentum p_z shown in Figure 5.10.

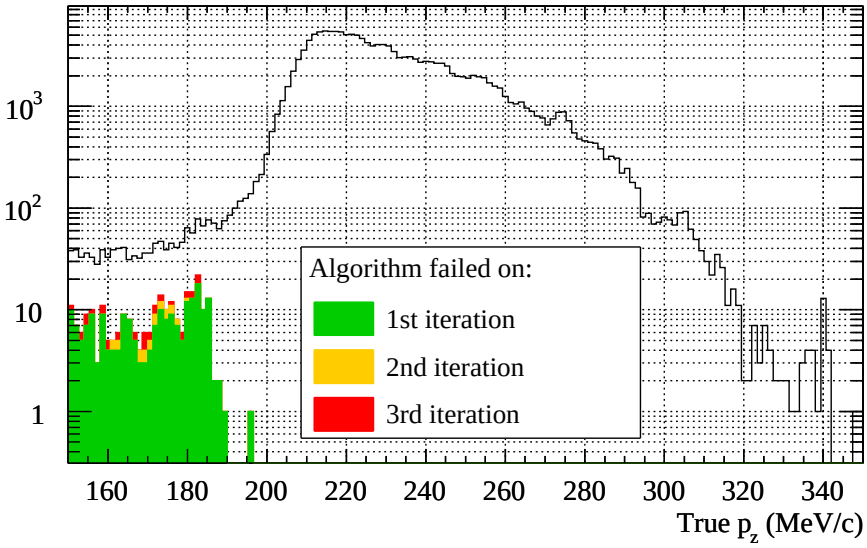

Figure 5.11: Failure of the reconstruction algorithm as a function of p_z.

is dominated by the time of flight resolution. The bias is better than in Figure 5.9 because this simulation was designed to optimize the reconstruction of muons and does not contain any pion contamination. As the pion contamination (between 1% and 5% depending on the element of the emittance-momentum matrix cf. Table 4.7) falls within the muon peak particle identification cuts it is mistaken for muons. These particles are reconstructed with the wrong mass, leading to an extra bias of the order of 0.5 MeV/c on the mean momentum error.

Figure 5.11 shows the efficiency of the algorithm as a function of true p_z. The algorithm has only been found to fail in the low momentum tail of the distribution where about 50% of particles are reconstructed. This region is always observed to be a region of very poor transmission at the base of a sharp edge of the distribution. As the base line case in the figure illustrates this tail is depleted by two orders of magnitude with respect to the adjacent peak. Overall the efficiency is better than 99.5%.

5.2.5 Momentum spectra in data and simulation

The reconstructed p_z spectra of the $\epsilon_N = 6$ mm re-scaled TURTLE Step I beams are compared with the spectra predicted by the Monte Carlo simulations described in Section 4.3 in Figure 5.12. Both unsmeared simulation truth and reconstructed resolution smeared are plotted.

The low-p_z edges of the distributions differ between simulation truth and reconstructed simulation because of the difficulty in reconstructing p_z in the fast changing region of the transfer matrices. Large coefficients in Equation 5.6 lead to larger errors on p_z and instability in the reconstruction algorithm, as shown in Figure 5.11.

Data should therefore be compared with reconstructed simulation, as these effects are reproduced in both cases. Good agreement is observed in the low edge apart from in the case

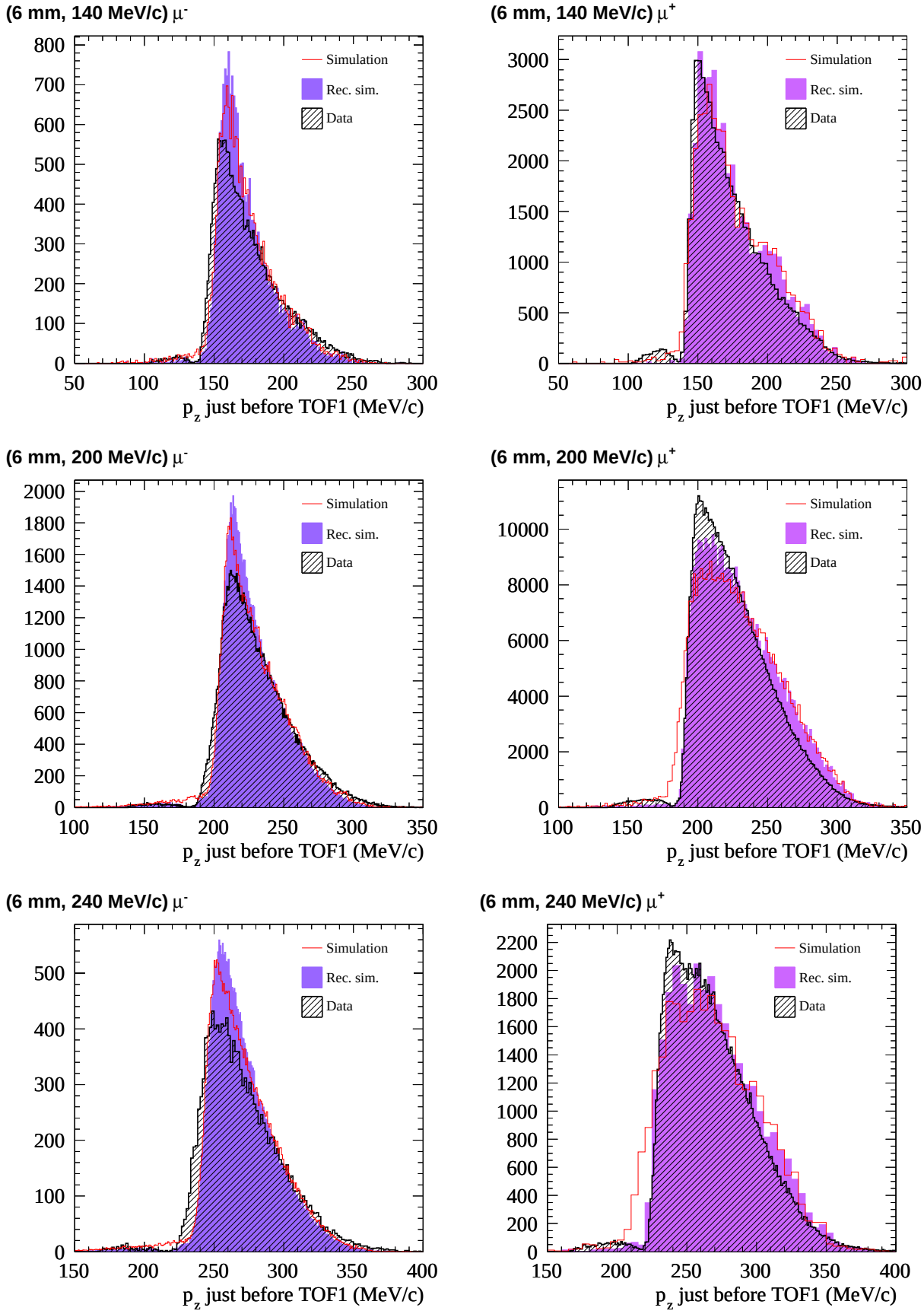

Figure 5.12: A comparison between measurements of p_z just before TOF1 in data and Monte Carlo for the $\epsilon_{\mathrm{N}} = 6$ mm elements of the $\epsilon_{\mathrm{N}} \otimes p_z$ matrix for both μ^- and μ^+ beams. p_z is plotted for Monte Carlo truth, resolution smeared Monte Carlo, and reconstructed data. For statistics and the resolution of each histogram see Table 5.4.

(MeV/c)	Mean p_z		p_z resolution	
	Data	Monte Carlo	Data	Monte Carlo
(6 mm, 140 MeV/c) μ^-	174.8 ± 1.0	173.2 ± 0.0	2.0	2.0
(6 mm, 200 MeV/c) μ^-	230.9 ± 2.0	229.0 ± 0.0	4.1	4.0
(6 mm, 240 MeV/c) μ^-	270.7 ± 3.0	270.8 ± 0.0	6.3	6.3
(6 mm, 140 MeV/c) μ^+	173.9 ± 1.0	177.3 ± 0.0	2.0	2.1
(6 mm, 200 MeV/c) μ^+	227.0 ± 1.9	232.0 ± 0.0	3.9	4.1
(6 mm, 240 MeV/c) μ^+	267.9 ± 2.9	271.3 ± 0.0	6.1	6.3

Table 5.4: Comparison between measurements of p_z just before TOF1 in data and resolution smeared Monte Carlo truth. The statistical error is negligible in all cases. The systematic error is only applicable to data as the Monte Carlo simulation was smeared with detector resolutions and reconstructed in the same manner as the data. The resolution is also given for use in comparing the distributions in Figure 5.12.

of the (6 mm, 240 MeV/c) μ^- beam. Comparisons should be informed by the resolution on p_z, tabulated in Table 5.4. The depleted regions at the base of the low-p_z edges are caused by asymptotes in Equation 5.6, illustrated in Figure 5.5.

The means of the distributions are given in Table 5.4. Statistical errors are negligible for data sets of this size (cf. Chapter 4) and systematic errors on data are as derived previously in the chapter. The means are all consistent, with some evidence for a systematic offset in the μ^+ beams. This is presumably the result of an error in the G4Beamline simulations which were used as input for these Monte Carlo studies..

Plots for all the Step I measurements of elements of the emittance-momentum matrix are shown in Figure 5.13. The cause of the anomalous momentum spectrum of the (3 mm, 140 MeV/c) μ^+ beam is unknown. This optical configuration will be re-tested in the next data taking period and is omitted from study in Chapter 6.

5.3 Measurement of the transverse angles x' and y'

When an unbiased measurement of p_z has been calculated using the iterative algorithm described in the previous section, the final transverse angles x' and y' are calculated at the upstream face of TOF1 using Equation 5.6. These angles can be used to study the distribution of the beam in transverse trace space: this is the subject of Chapter 6. This chapter concludes by studying the contributions of time resolution, position resolution and multiple scattering to the error on the angles, and comparing their distributions in data and Monte Carlo.

5.3.1 The effect of resolution, scattering and nonlinearities

The results of the Monte Carlo study described in Section 5.2.2 are shown for x' and y' at TOF1 in Figure 5.14 and Figure 5.15. The measurement bias and error due to each effect is recorded in Table 5.5.

The first study (illustrated in the figures by the dark blue histograms labelled 'no effects')

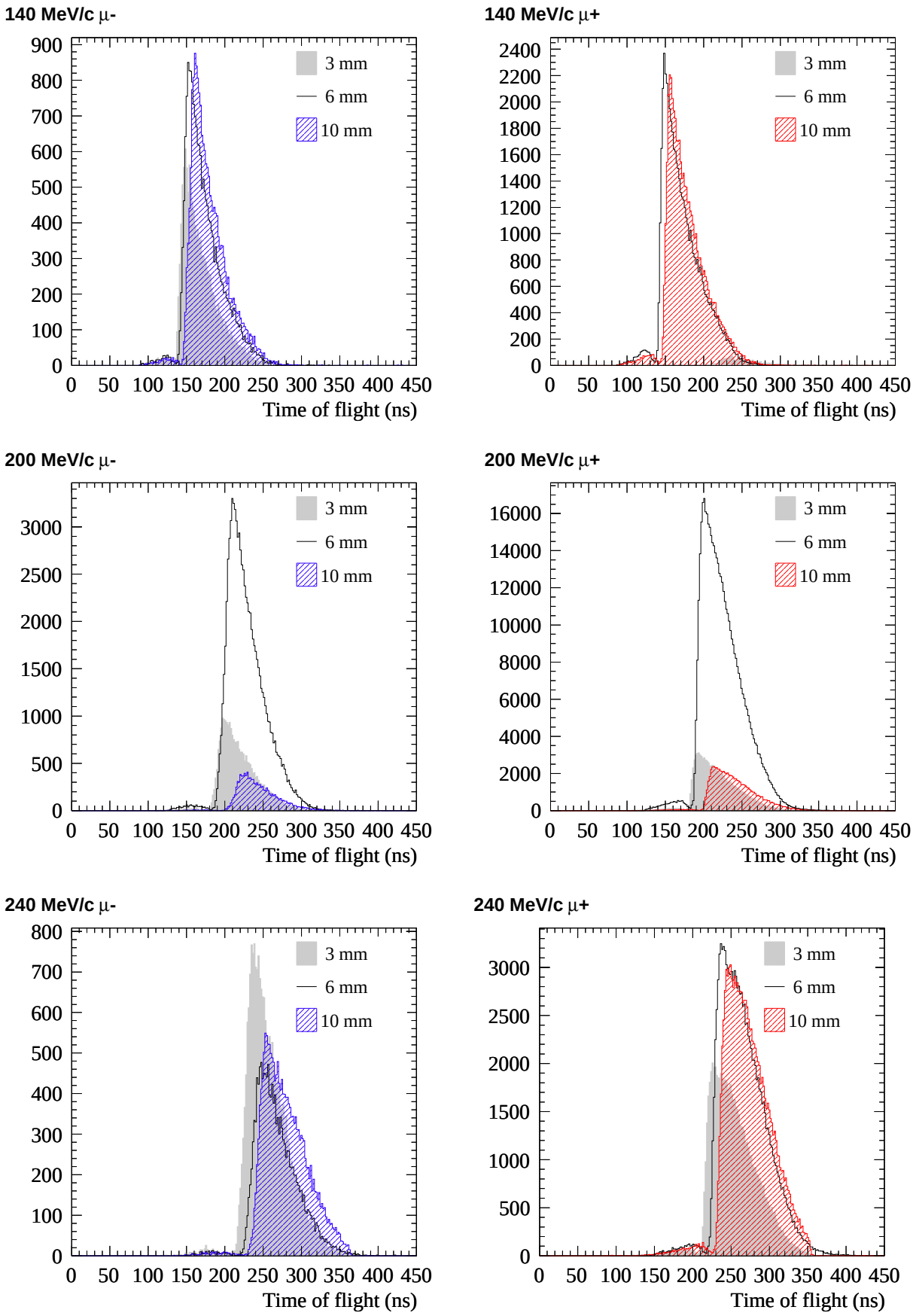

Figure 5.13: Momentum spectra for all the Step I re-scaled TURTLE beams.

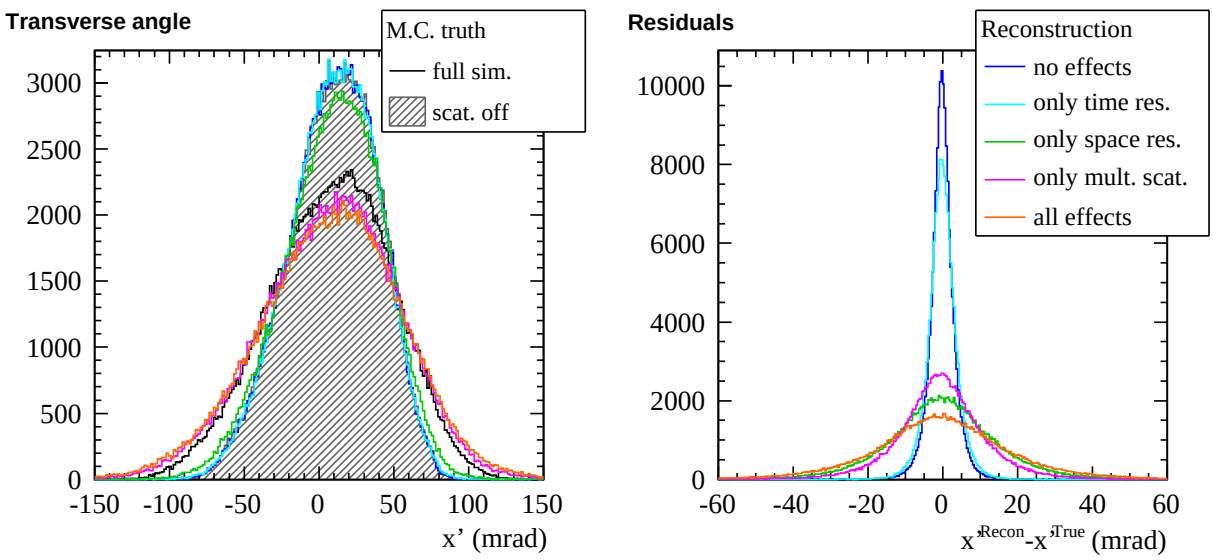

Figure 5.14: Reconstructed and true x'_1 in the simulations described in Table 5.1. The corresponding measurement biases and resolutions are recorded in Table 5.5. With multiple scattering off, $\langle x' \rangle = 10.16$ mrad, with an RMS of 29.77 mrad. In the full simulation, $\langle x' \rangle = 7.98$ mrad, with an increased RMS of 40.73 mrad.

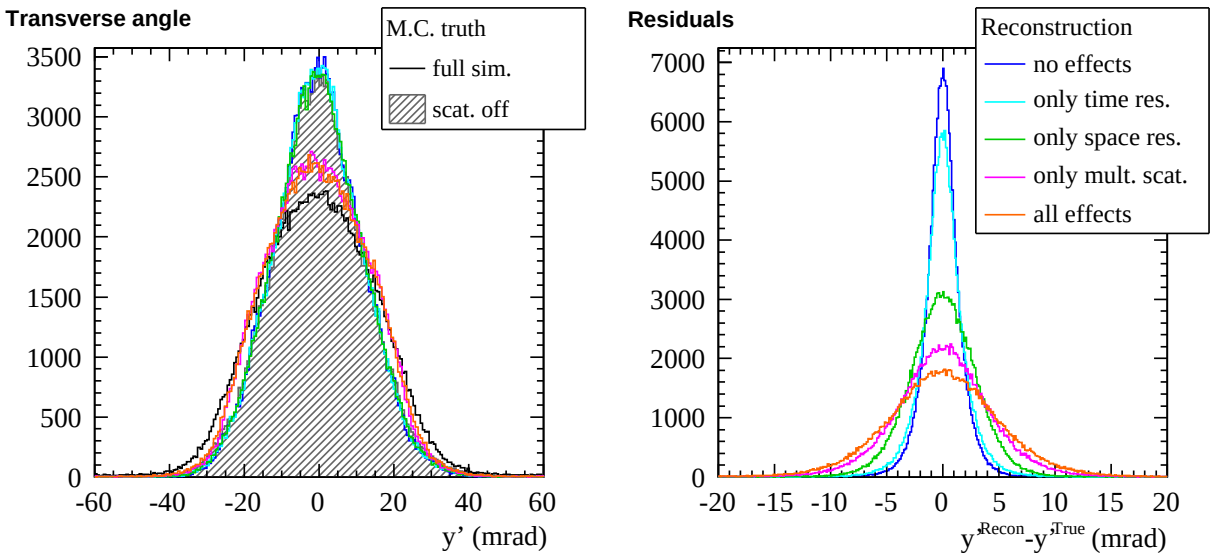

Figure 5.15: Reconstructed and true y'_1 in the simulations described in Table 5.1. The corresponding measurement biases and resolutions are recorded in Table 5.5. With multiple scattering off, $\langle y' \rangle = -0.12$ mrad, with an RMS of 12.38 mrad. In the full simulation, $\langle y' \rangle = -0.27$ mrad, with an increased RMS of 15.21 mrad.

x' and y' (mrad)	no effects	only t res.	only x res.	only M.S.	all effects
Mean bias on x'	-0.15	-0.12	-0.14	-0.45	-0.40
RMS error on x'	3.66	4.25	14.70	12.19	18.12
Mean bias on y'	0.01	0.01	0.01	0.02	0.02
RMS error on y'	1.65	2.02	3.00	4.26	5.05

Table 5.5: A table showing the bias and RMS error of each of the reconstructions of x' and y' shown in Figure 5.14 and Figure 5.15.

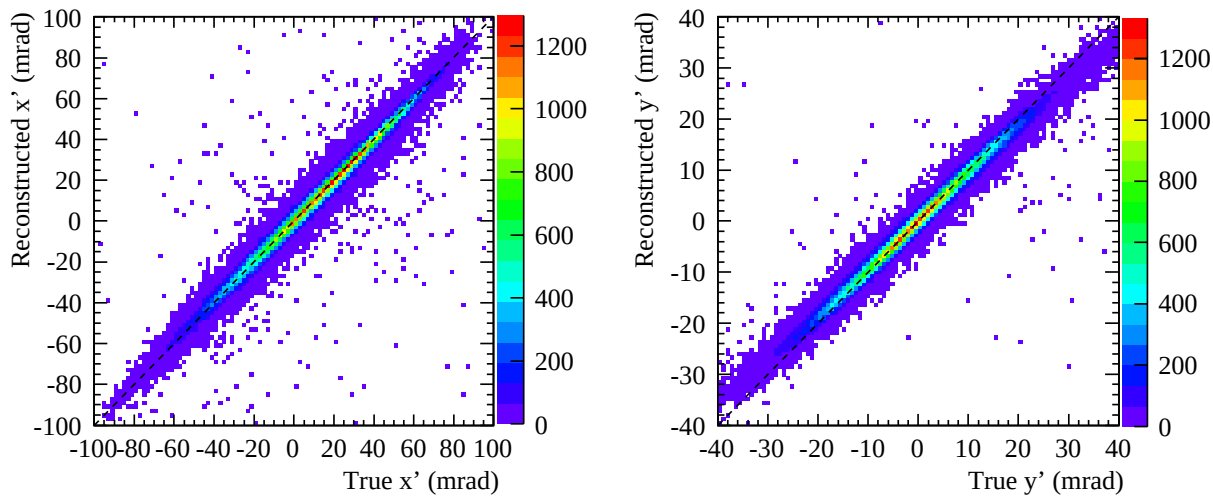

Figure 5.16: A scatter plot showing the correlation between true and reconstructed x' and y' at TOF1. Multiple scattering is off and the detectors are perfect.

models TOF0 and TOF1 as having perfect time and position resolution and reconstructs muon trajectories in a simulation with multiple scattering deactivated. Given the symmetry of the beam x' and y' are unsurprisingly reconstructed with negligible bias. The intrinsic resolution of the algorithm – illustrated by the width of the dark blue distribution in Figures 5.14 and 5.15 – is 12% and 14% of the RMS of the distributions in the two planes (the shaded distributions) for this particular optical configuration.

The correlation between the true and reconstructed angles is shown in Figure 5.16. Agreement is good in both planes however there is a suggestion that the distributions are not precisely aligned with the dashed lines indicating perfect correlation and $|y'|$ in particular is visibly reconstructed with a slightly small value.

Figure 5.17 illustrates that this effect is caused by nonlinearities in the beam transport which cannot be modelled using transfer matrices. The blue profile is the error profile of reconstructed angle from a separate Monte Carlo where the OPERA quadrupole field map has been replaced with a perfect top hat gradient profile: the reconstruction algorithm was therefore simplified to also use the top hat model transfer matrices in Section 5.1.1. These errors are significantly smaller than those corresponding to the double hyperbolic tangent model of the simulation with realistic fringe fields. Nonlinear effects are most pronounced in the sparsely populated high amplitude regions of trace space where the fringe fields diverge from the central gradient profile and the paraxial approximation is less valid.

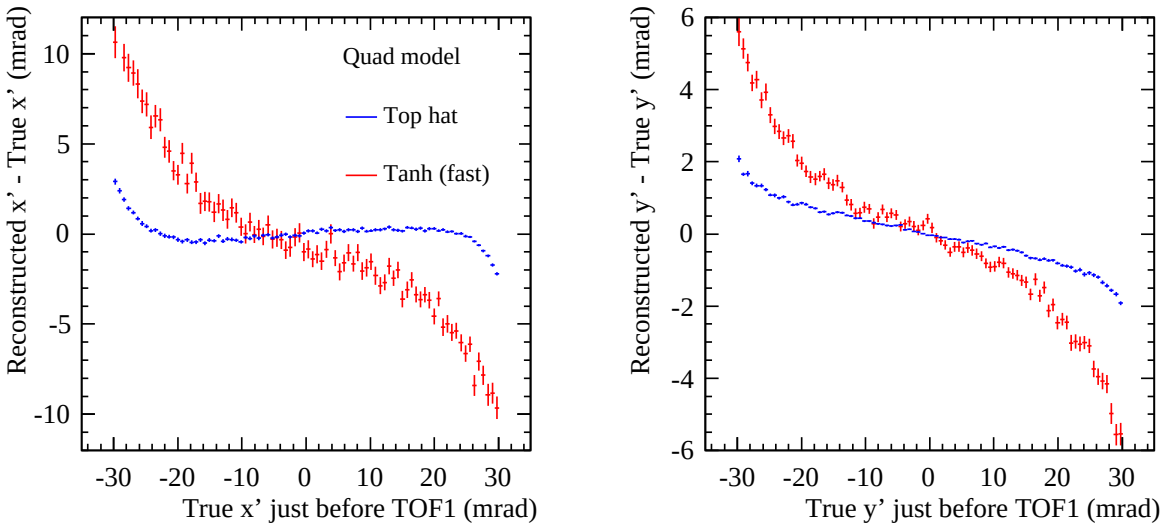

Figure 5.17: The error profile of x' and y' in the 'no effects' reconstruction of the Monte Carlo study described in Section 5.2.2. The standard reconstruction is the curve labelled 'Tanh (fast)', a reference to the use of the double hyperbolic tangent used to model the quadrupole fringe fields in the calculation of $\mathbf{M}_x$ and $\mathbf{M}_y$, sped up by the use of a top hat model in the estimation of path length. The lower magnitude error profiles which would result from quadrupoles with a perfect top hat gradient profile are also plotted to illustrate that nonlinear effects in the standard reconstruction are dominated by the effect of the fringe fields.

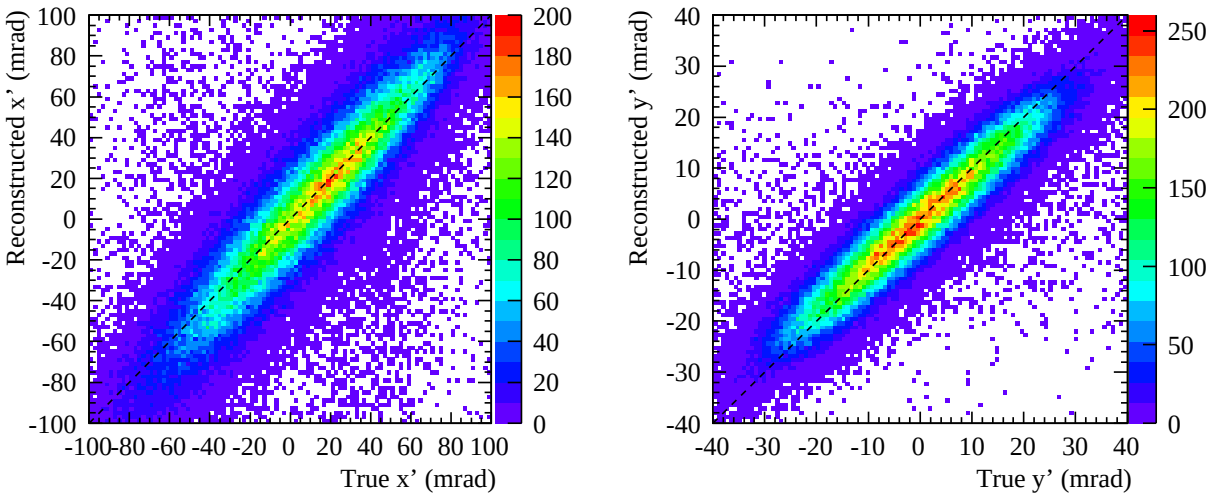

Figure 5.18: A scatter plot showing the correlation between true and reconstructed x' and y' at TOF1. Multiple scattering is on and the detectors measure t, x, and y with realistic resolutions.

By contrast to the reconstruction of p_z, Table 5.5 shows that the total error on x' and y' is dominated by position resolution and the stochastic effect of multiple scattering. Figure 5.18 shows the correlation between the true and reconstructed angles for the full simulation. The spread is now quite broad and the effect of the nonlinearities is clearly visible in the variation in the gradient of the correlation as amplitude increases. Nevertheless, the reconstruction provides a useful measurement of transverse momentum at TOF1, particularly considering that the detectors were not intended for this purpose.

5.3.2 Comparison between data and simulation

The effects discussed in the previous section may be disregarded in the comparison of data and Monte Carlo by comparing reconstructed resolution smeared Monte Carlo simulations with reconstructed data in Figure 5.20 and Figure 5.19. The similarity in the shape and widths of the distributions is very encouraging.

An offset is quite visible in the mean of reconstructed x' in data and simulation. This matches a similar effect in mean x at TOF1 in Figure 4.9. This may be the result of the TOF being displaced between the data taking period and the calibration or an error in the placement of the detectors or magnets in the Monte Carlo.

The striking feature that some y' distributions are reconstructed with a narrower RMS width than simulation truth is a result of the nonlinearities illustrated in Figure 5.17.

5.4 Conclusion

Underestimating path length via the approximation $s \approx L$ biases TOF momentum measurements by $\sim$ 5 MeV/c. This chapter demonstrates a practical method which reduces measurement bias to a fraction of a MeV/c. An iterative reconstruction algorithm has been developed to eliminate the systematic bias by tracking the muon through the quadrupole fields between the detectors. It is applied to particles individually, and does not depend on tuning by Monte Carlo simulations. The resolution is of order 3 MeV/c and dominated by the 70 ps time of flight resolution of the detectors. The algorithm has been applied to the Step I re-scaled TURTLE data sets and good agreement with Monte Carlo is observed.

The measurement may also in future complement that made by the upstream spectrometer. Although for $p_\perp > 70$ MeV/c the trackers measure longitudinal momentum with $\sigma_{p_z} <$ 2 MeV/c, below transverse momenta of 5 MeV/c near where the distribution will be peaked, the tracker measurement error on longitudinal momentum increases to 6 MeV/c [49].

The algorithm also allows a measurement of the transverse angles x' and y' at TOF1. Encouraging agreement between data and reconstructed resolution smeared Monte Carlo simulations is observed. These measurements are used to characterize the transverse phase space of the beams in Chapter 6.

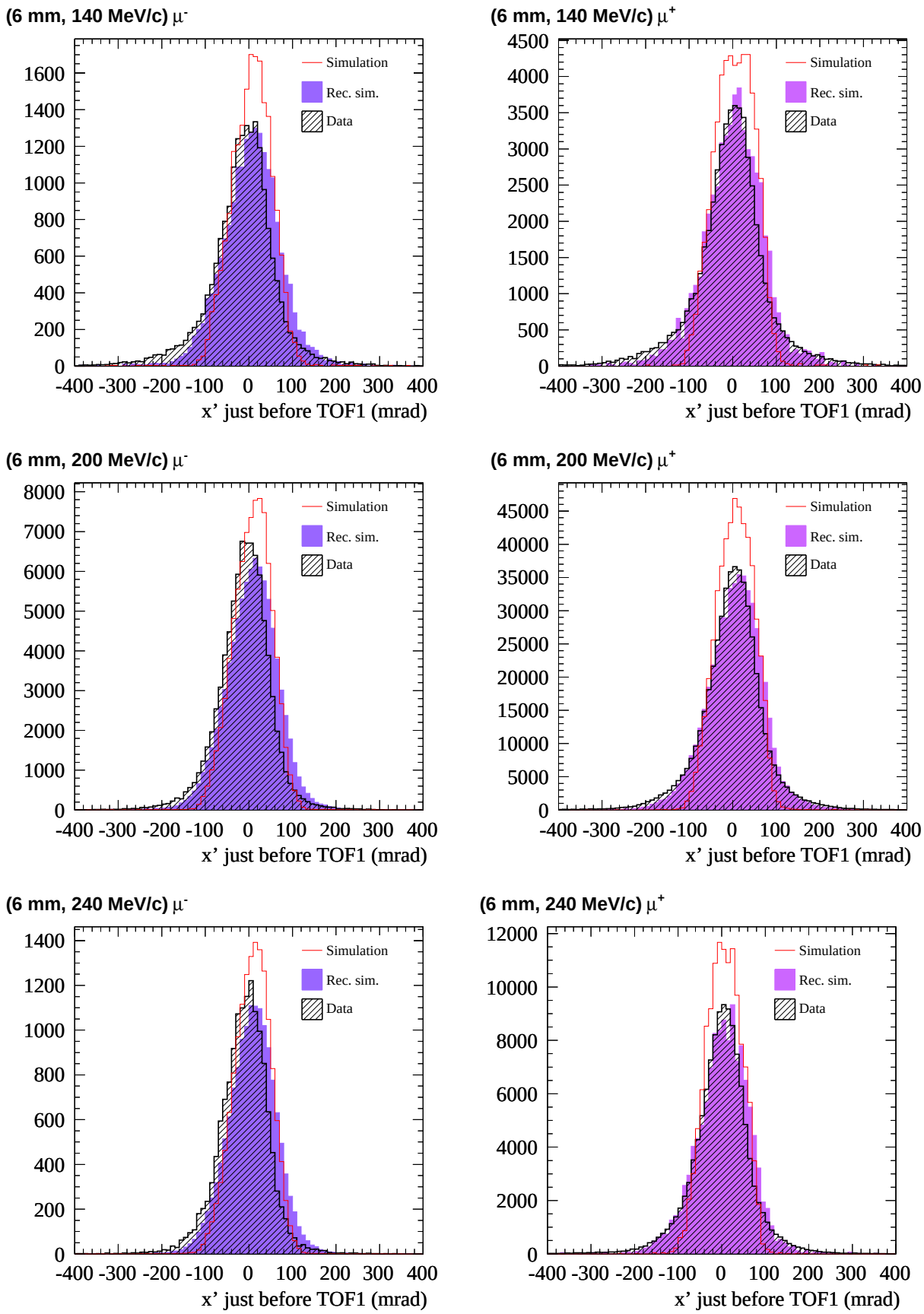

Figure 5.19: Comparison between measurements of x' in data and simulation.

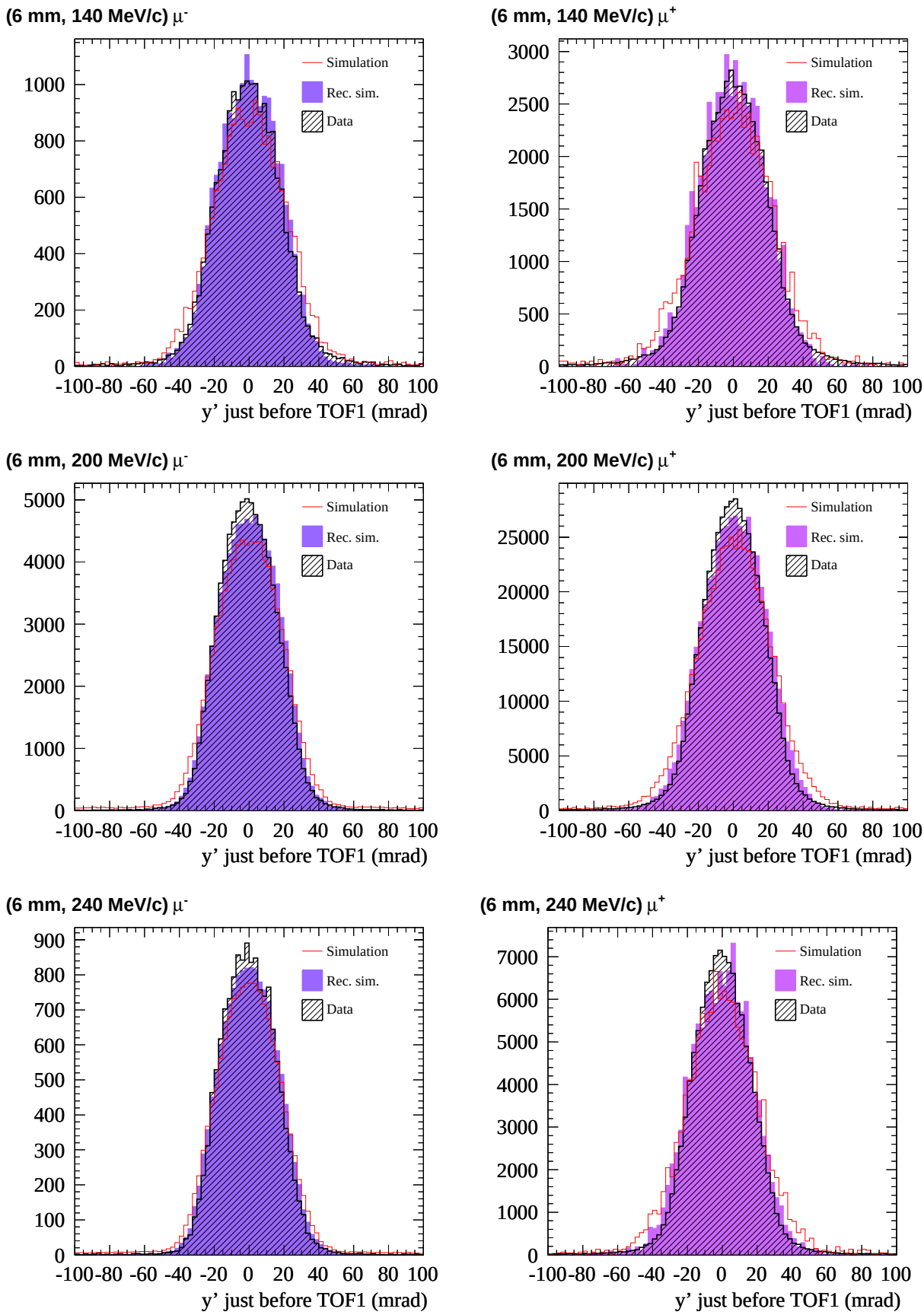

Figure 5.20: Comparison between measurements of y' in data and Monte Carlo.

Chapter 6

Distributions in transverse trace space at TOF1

The iterative reconstruction algorithm developed in Chapter 5 is used to characterize the Step I re-scaled TURTLE beams in horizontal and vertical trace space at TOF1. After taking into account the effect of detector resolution, good agreement is found with Monte Carlo.

The iterative reconstruction algorithm described in Chapter 5 corrects a path length bias on p_z by reconstructing the trace space vector (u, u') of each muon at TOF0 and tracking it through quadrupole triplet Q7-Q8-Q9 to (v, v') at TOF1. In each plane u is measured directly by TOF0 in the manner described in Chapter 3 and u' is deduced from v using Equation 5.6. Once p_z has been measured the process is reversed to obtain v' from u. In this way the direct mapping of points in trace space at TOF0 to points in trace space at TOF1 is used to reconstruct individual muon trajectories at the end of the Step I beam line.

The horizontal and vertical trace space distributions of the simulated base line μ^- beam[1] are plotted in Figure 6.1. The beam fills the detector in both planes but its angular distribution is approximately three times wider in horizontal trace space than in vertical trace space.

As these distributions are numerous it is useful to parameterize them. In Chapter 2 the emittance and Twiss parameters were introduced in both two-dimensional trace space and four-dimension phase space as complementary ways of parameterizing beam distributions. The latter parameterization is a particularly concise way to summarize the properties of beams in solenoidal focusing channels. It is inappropriate here however, as it assumes that the probability distribution functions of the beams are cylindrically symmetric. In this chapter the beams are characterized in horizontal and vertical trace space at TOF1.

As discussed in Section 2.1.1, the orientation of a distribution in horizontal or vertical trace space is parameterized by the Twiss parameters α, β and γ:

$$\alpha = -\frac{\sigma_{vv'}}{\epsilon}, \qquad \beta = \frac{\sigma_{vv}}{\epsilon}, \qquad \gamma = \frac{\sigma_{v'v'}}{\epsilon} \tag{6.1}$$

[1] The base line beam is designed to have a nominal normalized emittance $\epsilon_{\mathrm{N}} = 6$ mm upstream of the first absorber and a nominal mean momentum $p_z = 200$ MeV/c in the centre of each absorber. Chapter 2 explains the design and measurement of optical configurations of an emittance-momentum matrix of beams.

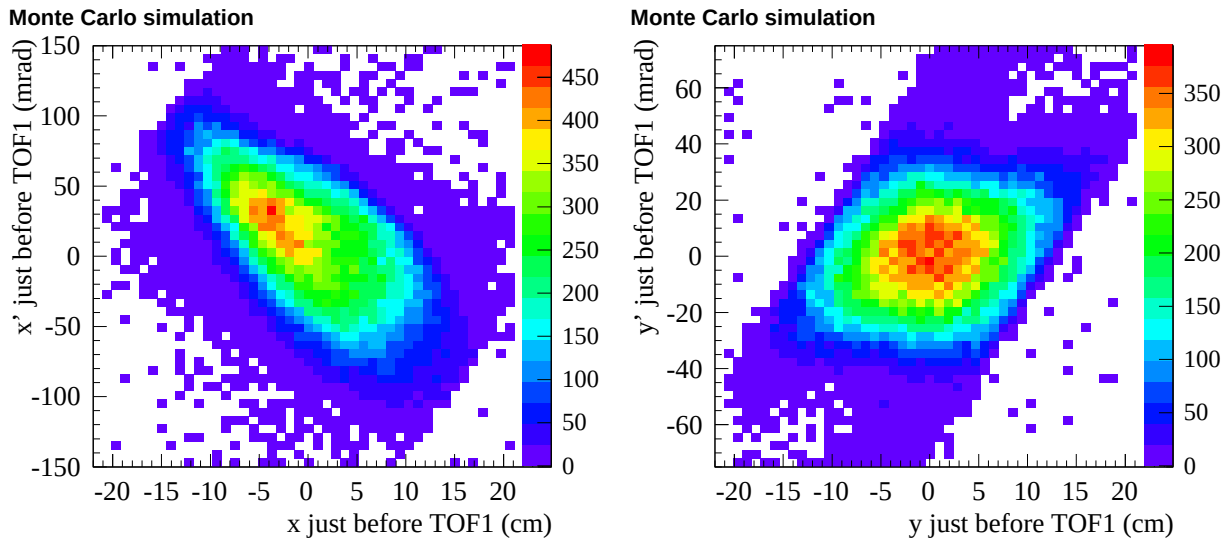

Figure 6.1: Unsmeared simulated transverse trace space distributions of the base line (6 mm, 200 MeV/c) μ^- beam at TOF1.

where $\gamma = (1+\alpha^2)/\beta$ and ϵ is the emittance:

$$\epsilon = \sqrt{\sigma_{vv}\sigma_{v'v'} - (\sigma_{vv'})^2}. \tag{6.2}$$

The emittance describes the area occupied by the beam in trace space.

Calculated separately in the horizontal and vertical plane, α, β and ϵ are a useful way to characterize the beam distribution. The disadvantage of this parameterization is that it does not take account of dispersion,which can be significant in wide-p_z spectrum beams such as those used by MICE. The dispersion in the base line beam simulation is shown in Figure 6.2. Although the total conserved volume in phase space has not increased by the separation of components of different p_z, dispersion does register an increased emittance in the trace emittance ϵ defined here[2]. Nevertheless, it is not obvious how to model the nonlinear dispersion in Figure 6.2 in a covariance matrix and the trace space parameterization has the virtue of simplicity.

As the matching conditions in MICE are expressed in terms of the normalized emittance and transverse betatron function it is worth relating them to trace space variables here. For a cylindrically symmetric beam let $\epsilon = \epsilon_x = \epsilon_y$ and $\beta = \beta_x = \beta_y$. In the phase space parameterization described in Section 2.1.3 the normalized emittance is therefore $\epsilon_{\mathrm{N}} = (p_z/m_\mu)\epsilon$ and the transverse betatron function is simply $\beta_\perp = \beta$. It is useful therefore to plot β_x and β_y to gauge the extent to which the MICE beams are not cylindrically symmetric. Chapter 7 investigates whether an asymmetry $\beta_x \neq \beta_y$ will be a problem for MICE; until then it may be useful to bear in mind the monochromatic approximations:

$$\epsilon_{\mathrm{N}} = \frac{p_z}{m_\mu}\sqrt{\epsilon_x\epsilon_y}$$

[2] It is contentious whether this increase will be reflected in the normalized emittance in the upstream spectrometer solenoid.

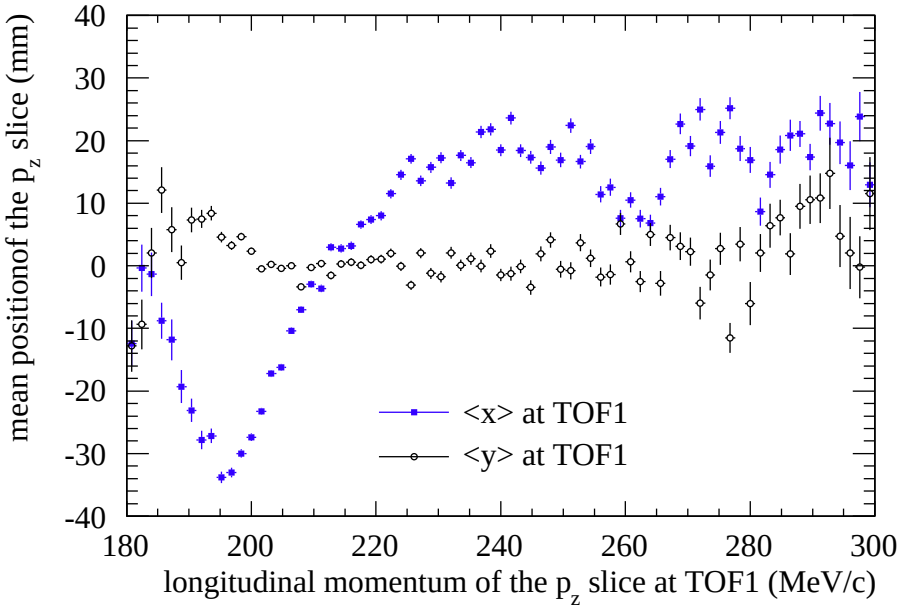

Figure 6.2: Dispersion in a simulation of the base line μ^- beam.

and:

$$\beta_\perp = \tfrac{1}{2}\left(\sqrt{\frac{\epsilon_x}{\epsilon_y}}\beta_x + \sqrt{\frac{\epsilon_y}{\epsilon_x}}\beta_y\right).$$

6.1 Resolution bias on optical parameters

The (x, x') and (y, y') distributions of the base line beam in the Step I data are plotted in Figure 6.3. They have been reconstructed using the iterative algorithm described in Chapter 5. While the areas occupied in trace space in simulation and data are similar to those in the corresponding Monte Carlo truth distribution in Figure 6.1, it is difficult to make a comparison as the data distribution is convoluted with the resolution function of the reconstruction algorithm.

The transverse angle is reconstructed using Equation 5.6, parameterized as:

$$v' = A(p_z)u + B(p_z)v, \tag{6.3}$$

where u and v are the transverse positions measured by TOF0 and TOF1 in either the horizontal or the vertical plane. A and B vary with p_z as they are a function of elements of the transfer matrix between TOF0 and TOF1. The coefficients A and B for the base line optical configuration are illustrated in Figure 5.5.

The previous chapter showed that the error on the v' caused by the timing resolution of the detectors is negligible compared to that caused by their position resolution. This is true because, although $A(p_z)$ and $B(p_z)$ vary significantly over the momentum spectrum of the beams, they are approximately constant over the momentum resolution of the reconstruction

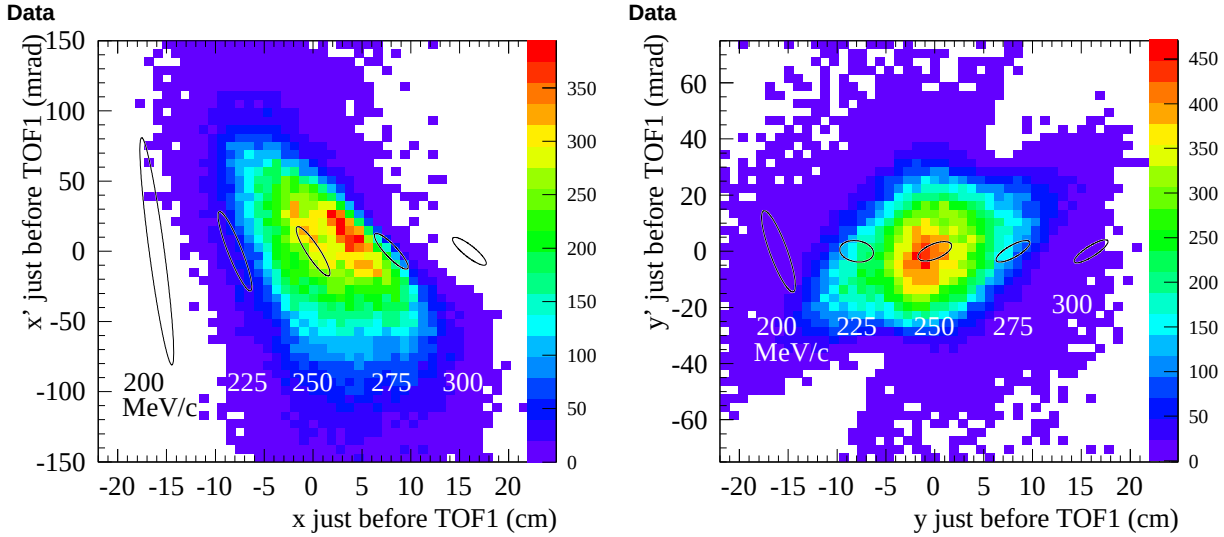

Figure 6.3: The transverse trace space of the base line (6 mm, 200 MeV/c) μ^- beam at TOF1. The trace space vectors have been reconstructed from TDC and ADC hits in the Step I TOF0 and TOF1 data using the algorithm described in Chapter 5. 1σ error ellipses have been superimposed and labelled by their corresponding p_z. They are displaced for clarity; the size and orientation of the error ellipse are invariant in trace space.

algorithm. It follows that the resolution (or error) matrix $\mathbf{R}$ is given by:

$$\mathbf{R}(p_z) = \begin{pmatrix} r_{vv} & r_{vv'} \\ & r_{v'v'} \end{pmatrix} = \begin{pmatrix} r_{vv} & Br_{vv} \\ & A^2 r_{uu} + B^2 r_{vv} \end{pmatrix}, \tag{6.4}$$

where r_{uu} and r_{vv} are the squares of the position resolutions of TOF0 and TOF1[3]. The error is correlated for $B \neq 0$ and varies as a function of p_z. Note the value of pursuing the timing-based position measurement in Chapter 3 despite the small improvement in resolution: the unpredictable and asymmetric error distributions of the quantized slab based method (illustrated in Figure 3.15) would lead to a highly convoluted measurement of the trace space distributions.

By contrast the Gaussian error originating from jitter in the signal from the photo-multipliers may be visualized by picturing an error ellipse $(v, v')^{\mathrm{T}}\mathbf{R}^{-1}(v, v') = \Delta\chi^2$ around the position of every muon in trace space. When $\Delta\chi^2 = \chi^2 - \chi^2_{\mathrm{min}} = 2.30$ (the 1σ ellipse) there is a 68.28% probability [8] that a particle with that true trace space vector will be reconstructed by the algorithm within this region.

The simulated momentum spectrum of the base line beam was illustrated in Figure 5.3. 1σ error ellipses for $\mathbf{R}$ have been been drawn to scale in Figure 6.3 for a selection of momenta in this range and displaced for clarity: as a result of the approximate linearity of beam transport between TOF0 and TOF1 the ellipses are invariant throughout trace space. Although the resolution in v remains constant the increased focusing strength leads to larger errors on v' at low momenta and the variation of the total phase advance alters the correlation of the error distribution. Qualitatively one can see how these errors could plausibly be convoluted

[3] r is used rather than the more conventional σ to distinguish the resolution of a variable from its covariance in trace space.

with the simulated distributions to give the observed data distributions.

Similar distributions exist for all the Step I beams and are too numerous to include here. In the following sections their properties are summarized through measurements of emittance and the Twiss parameters. The following section focuses on the effect of detector resolution on measurements of these statistical parameters.

6.1.1 The effect of detector resolution on emittance measurements

Let the relationship between a measurement of a particle's position in trace space (m, m'), its true position (v, v') and the error on the sampled trace space vector of a particular muon (δ, δ') be simply:

$$(m, m') = (v, v') + (\delta, \delta'),$$

where (δ, δ') is sampled from a bivariate Gaussian distribution with covariance matrix $\mathbf{R}(p_z)$. It follows from the definition of covariance that:

$$\sigma_{m_i m_j} = \sigma_{v_i v_j} + \sigma_{\delta_i \delta_j} + \sigma_{v_i \delta_j} + \sigma_{\delta_i v_j},$$

where i and j label the element of the two-dimensional trace space vector. This may be rewritten in matrix form as:

$$\mathbf{M} = \mathbf{\Sigma} + \mathbf{R} + \mathbf{C} + \mathbf{C}^{\mathrm{T}} \tag{6.5}$$

where $\mathbf{R}(p_z)$ is the familiar resolution matrix and $\mathbf{C}$ accounts for the effect of errors being correlated to trace space parameters as in Figure 5.17. If $\mathbf{R}$ and $\mathbf{C}$ are known one may estimate the true emittance and Twiss parameters from the measured covariance matrix $\mathbf{M}$ by solving Equation 6.5 for $\mathbf{\Sigma}$. While $\mathbf{R}$ has the effect of inflating the emittance, the effect of $\mathbf{C}$ is difficult to predict reliably and is typically calculated using a Monte Carlo study.

To study the effect of resolution bias a simulation of the base line beam was performed in which the model of multiple scattering was deactivated. As $\mathbf{R}$ varies with p_z the beam was divided into 20 equally populated momentum bites. The horizontal and vertical emittance $\sqrt{\det \mathbf{\Sigma}}$ of each slice is plotted in Figure 6.4. Statistical errors are also drawn: they are derived in Appendix C.

The estimate obtained from the covariance matrix of the raw measurements $\sqrt{\det \mathbf{M}}$ and the corrected estimate $\sqrt{\det\left(\mathbf{M} - \mathbf{R}(p_0)\right)}$ are also plotted for each slice, where p_0 is the mean momentum of the muons in the slice. The correction is largest at low momenta where the focusing is strongest. Figure 6.3 suggests that the low-p_z bias is larger in horizontal trace space because the error on v' is a larger fraction of its RMS spread. The agreement between the corrected estimate and the true emittance shows that $\mathbf{C}$ is negligible.

6.1.2 The effect of multiple scattering

The reconstruction of trajectory angles at TOF0 and TOF1 relies on the mapping $(v, v') = \mathbf{M}(p_z) \cdot (u, u')$: Equation 5.6 demonstrates that the relationship can be rearranged to map the measured positions (u, v) to unique values of the transverse angles (u', v').

This principle is undermined by the stochastic effect of multiple scattering between TOF0

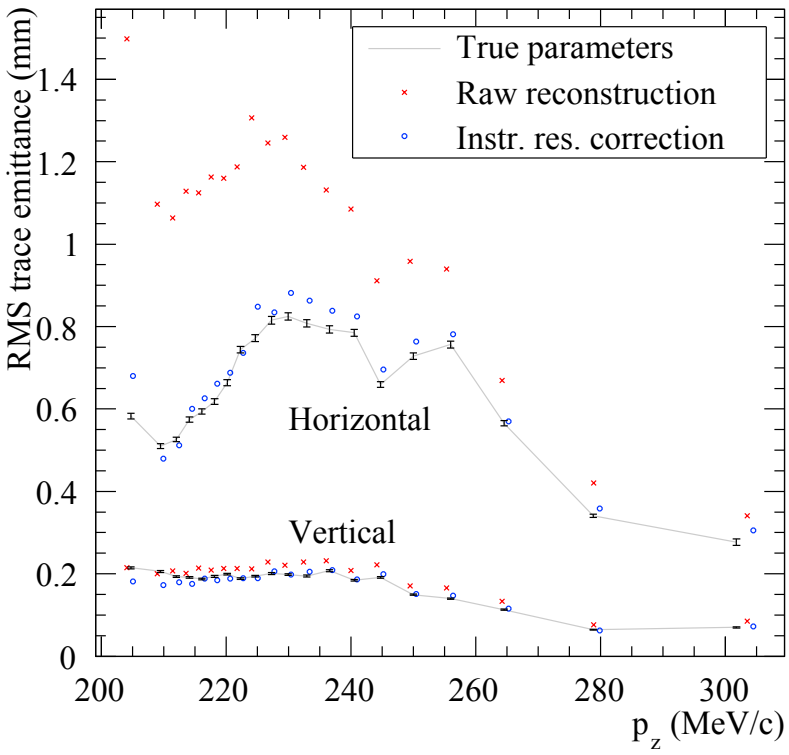

Figure 6.4: The true, measured and corrected 2D RMS trace emittance of equally populated momentum-slices of a simulation of the base line (6 mm, 200 MeV/c) μ^- beam. The analysis was carried out independently in horizontal and vertical trace space at TOF1. The multiple scattering model was deactivated in the Monte Carlo (cf. Section 5.2.2) in order to investigate the effect of detector resolution on the measurement.

and TOF1. If one knows (u, u') and p_z one can only estimate the most likely vector (v, v') within some probability distribution in trace space. More pertinently to the reconstruction algorithm, the value of u which maps to the true v' in the absence of stochastic processes will in general be different to the true u of the muon at TOF0. Therefore multiple scattering effectively contributes to the error on u.

The uncertainty on u can be estimated by summing the variances in u caused by multiple scattering in each longitudinal slice δz between the detectors. The angular variance introduced by multiple scattering in a thickness δz of material is approximately $\delta\theta^2 = (13.6\text{ MeV})^2/(\beta cp)^2 \delta z/X_0$ [8]. Consider the propagation of a pencil beam impinging from positive z on the slice. Equation 5.2 may be rearranged such that the covariance of the pencil beam at TOF0 is given by:

$$\mathbf{\Sigma}_0 = \mathbf{M}^{-1}\mathbf{\Sigma}_{\text{slice}}\left(\mathbf{M}^{-1}\right)^{\text{T}},$$

where $\mathbf{M}(z)$ is the transfer matrix from TOF0 to z. A short calculation yields:

$$\mathbf{\Sigma}_0 = \begin{pmatrix} M_{22} & -M_{12} \\ -M_{21} & M_{11} \end{pmatrix} \begin{pmatrix} 0 & 0 \\ 0 & \delta\theta^2 \end{pmatrix} \begin{pmatrix} M_{22} & -M_{21} \\ -M_{12} & M_{11} \end{pmatrix} = \begin{pmatrix} M_{12}^2\delta\theta^2 & -M_{11}M_{12}\delta\theta^2 \\ -M_{11}M_{12}\delta\theta^2 & M_{11}^2\delta\theta^2 \end{pmatrix}.$$

Therefore the uncertainty on u due to multiple scattering in δz is given by the square root of the variance $\delta\sigma_{uu}^{\text{scat}} = M_{12}^2\delta\theta^2$. The total uncertainty due to multiple scattering can be estimated by integrating the variance:

$$\sigma_{uu}^{\text{scat}} = \int_{z_0}^{z_1} M_{11}^2(z)\mathrm{d}\theta^2 = \int_{z_0}^{z_1} \left(\frac{13.6\text{ MeV}}{\beta cp}\right)^2 M_{11}^2(z)\frac{\mathrm{d}z}{X_0}.$$

Figure 6.5 illustrates the performance of the bias correction in a full simulation of the base line beam including multiple scattering. Note that multiple scattering in the channel is a significant effect: the simulated beams have approximately twice the emittance compared to Figure 6.4. The resolution bias on the horizontal emittance has increased in proportion, again increasing the emittance of the low-p_z slices by almost a factor two. Nevertheless a raw reconstruction of the measured covariance is again a reasonably unbiased estimate of the true vertical emittance.

The magnitude of the increase in emittance suggests that applying the correction for instrumental resolution alone will be insufficient: the figure shows that this correction indeed only accounts for half the bias. Therefore $\sigma_{uu}^{\text{M.S.}}$ has been calculated for the base line beam and added to the instrumental position resolution variance σ_{uu} in Equation 6.4. The resulting correction is also illustrated in the figure. The new corrected ϵ_x is not perfect it is but of the right order of magnitude; however the correction degrades the estimate of ϵ_y by a factor of up to a half for $p_z < 260$ MeV/c. This is due the effect of correlations and nonlinearities which have not been modelled. Indeed in Figure 5.17 the raw estimate is smaller than the true emittance in the low-p_z slices as they have a greater proportion of high amplitude particles. The effect is not noticeable in horizontal trace space because it is cancelled out by resolution bias.

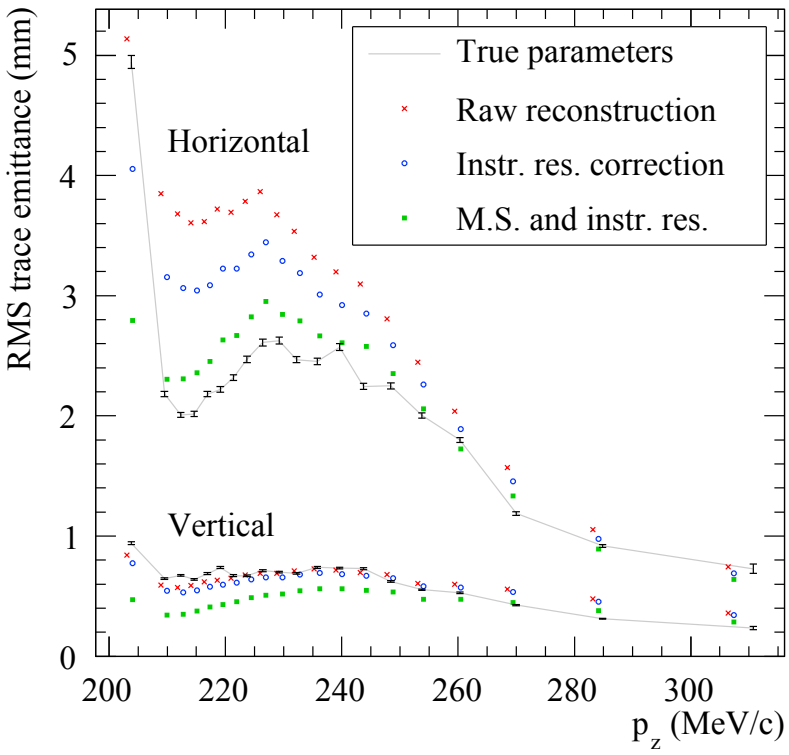

Figure 6.5: The true, measured and corrected 2D RMS trace emittance of equally populated momentum-slices of a full simulation of the base line (6 mm, 200 MeV/c) μ^- beam (cf. Section 5.2.2). The analysis was carried out independently in horizontal and vertical trace space at TOF1. The corrections for bias due to detector resolution alone and due to detector resolution *and* multiple scattering are both plotted.

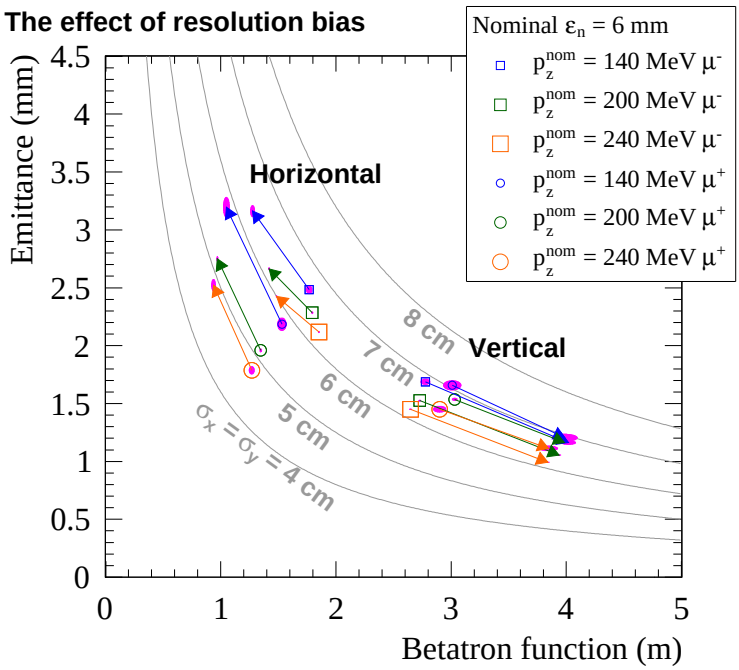

Figure 6.6: The betatron function and RMS trace emittance for the Monte Carlo simulations of the $\epsilon_N = 6$ mm beams described in Section 4.3. True (ϵ_x, β_x) and (ϵ_y, β_y) at TOF1 and values from covariance matrices of trace space vectors of reconstructed resolution smeared simulation truth times are plotted with statistical error ellipses. The arrows point from the true to reconstruction values. The beams are labelled with design values of their 4D normalized emittance after the diffuser, and the momentum in the absorber centres (ϵ_n/mm, p_z/MeV/c).

6.1.3 Resolution bias in (β, ϵ)-space

The previous two sections demonstrated that resolution bias on emittance measurements is a significant feature in horizontal but not vertical trace space and that it is caused by position resolution and multiple scattering in approximately equal measure. Furthermore it is not possible to derive a simple and transparent correction. Therefore no correction is made in this thesis.

In this section reconstructed resolution smeared simulations are used to quantify the bias and the discussion is broadened to include measurements of the betatron function as well as the emittance. The betatron function is an interesting quantity as it is the quantity which must be matched to boundary conditions in the upstream spectrometer (cf. Section 2.3.2).

The effect of resolution bias on measurements of the emittance and betatron function is illustrated in Figure 6.6. (β_x, ϵ_x) and (β_y, ϵ_y) are plotted for each of the full simulations of the $\epsilon_N = 6$ mm beams described in Section 4.3: arrows point from the true emittance $\sqrt{\det \mathbf{\Sigma}}$ to the value reconstructed from resolution smeared times and positions $\sqrt{\det \mathbf{M}}$, illustrating the bias arising from position resolution and multiple scattering. Statistical error ellipses are drawn for each point according to the calculations in Appendix C.

Despite emerging from the decay solenoid with a cylindrically symmetric distribution, the horizontal and vertical trace space of the beams occupy different regions in (β, ϵ)-space. This is potentially problematic for MICE as simulations of muon cooling channels - and indeed the

transverse trace space parameterization of phase space itself - assume cylindrical symmetry. Care is therefore required when interpreting the Step I results.

The horizontal emittance is larger than the vertical emittance because of the dispersion introduced in the beam at dipole 2: different momentum slices in the wide p_z-spectrum of the MICE beam emerge from the dipole at different angles to the design orbit. This effect can be cancelled by subsequent magnets and is therefore typically removed in standard accelerator calculations by modifying the simple formula $\epsilon_x = \sqrt{\sigma_{xx}\sigma_{x'x'} - \sigma_{xx'}^2}$ [37]. Such a correction is not applied here because there are no subsequent magnets before the upstream spectrometer solenoid in which horizontal and vertical trace space will be mixed. The spread in phase space caused by dipole 2 is therefore preserved in MICE and reflected in the normalized emittance in the cooling channel.

Consider finally the resolution bias vectors in Figure 6.6. The effect is consistent with Figure 6.5 in approximately conserving ϵ_y, while revealing a hidden increase in β_y. Interestingly the bias moves parallel to the contours of constant RMS beam size $\sqrt{\beta\epsilon}$, but in opposite directions. As $\sigma_{v'v'} = (1+\alpha^2)\epsilon/\beta$, $\alpha = 0$ contours with constant $\sigma_{v'v'}$ could be drawn on the plot as straight lines $\epsilon = \sigma_{v'v'}\beta$. The approximate constancy of the beam size reflects the fact that position is measured directly: larger errors are expected in the measurement of beam parameters relating to angles.

The trend is therefore that the resolution bias increases the apparent angular divergence in horizontal trace space and decreases it in vertical trace space. This is reflected by Figure 5.19 and Figure 5.20. This effect is believed to be the result of a balance between resolution bias and nonlinearities in the beam transport which are not modelled in the reconstruction (cf. Figure 5.17). The former dominates in horizontal trace space and the latter dominates in vertical trace space.

6.2 Comparison between data and simulation

The Step I MICE beams are designed to reach the upstream spectrometer with a matrix of emittances and momenta while fulfilling the matching conditions specified in Section 2.3.2. Neither the diffuser nor the upstream spectrometer was present during Step I; In the spectrometer it would have been simple to measure ϵ_{N}, $\langle p_z \rangle$, $\beta_\perp$ and $\alpha_\perp$ and directly test whether the design criteria had been met.

The beams have therefore been characterized at TOF1 instead of the spectrometer. Simulating the passage of the measured muon trajectories from TOF1 to the spectrometer is the subject of Chapter 7. This section follows the simpler approach of directly comparing the reconstructed optical parameters at TOF1 with Monte Carlo simulations.

The previous section showed that detector resolution and multiple scattering cause a significant bias on measurements of the emittance and Twiss parameters which it is not trivial to correct. Therefore in this section reconstructed data are compared with reconstructed resolution smeared simulations. The simulations described in Section 4.3 were designed for this purpose. The error distributions measured in Chapter 3 were applied to the positions and times that electrons, muons and pions hit the mid-planes of TOF0 and TOF1 and the iterative reconstruction algorithm described in Chapter 5 was used to produce the reconstructed

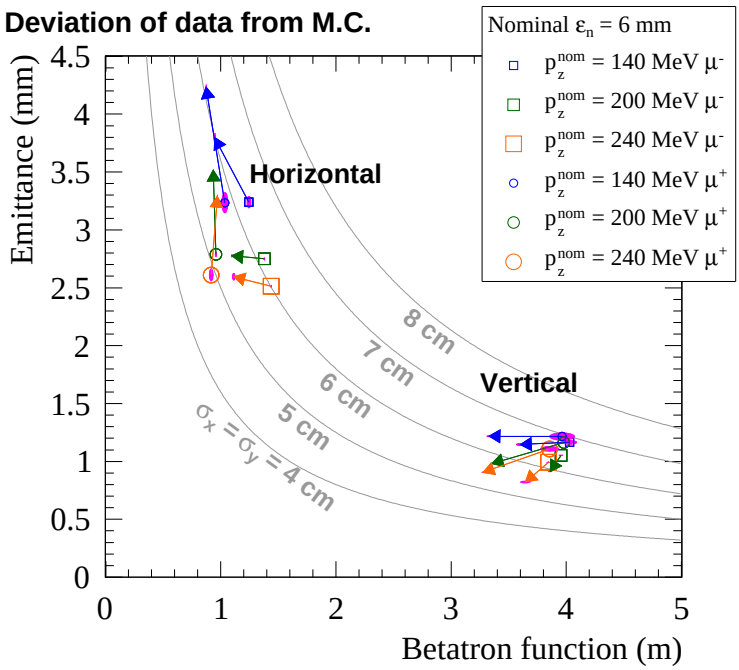

Figure 6.7: A comparison between the measured and simulated horizontal and vertical beam parameters of the $\epsilon_N = 6$ mm re-scaled TURTLE beams. To ensure a fair comparison the effect of detector resolution was modelled and the parameters obtained using the same reconstruction software. The arrows point from reconstructed resolution smeared simulation to reconstructed data. The error ellipses represent the statistical error on the measurements.

resolution smeared data sets used in this chapter. Precisely the same software routines were used in the analysis of data and of these Monte Carlo simulations.

The emittance and Twiss parameters in horizontal and vertical trace space have been calculated from the covariance matrices of the raw measurements in both the measured and simulated data sets and are plotted in Figure 6.7. The differences between (β_x, ϵ_x) and (β_y, ϵ_y) in data and reconstructed resolution smeared simulation are illustrated by arrows.

The comparison cannot be said to be good as the (β, ϵ) deviation vectors are often longer than the distance separating beam measurements and are longer than the width of the statistical error distributions. Note that in both planes there is a systematic trend for reconstructed data to have a greater angular divergence $\sigma_{v'v'}$ than the reconstructed simulation (cf. Section 6.1.3). Note also that the disagreement between data and simulation is worse for the μ^+ beams than for the μ^- beams. These effects are investigated in the following sections.

6.2.1 The trace space distribution of the base line beam

Reconstructed trace space distributions of the Step I base line (6 mm, 200 MeV/c) μ^- beam have already been shown in Figure 6.3. They are plotted again next to distributions of their corresponding reconstructed resolution smeared Monte Carlo simulation in Figure 6.8. The qualitative agreement is significantly better than with the distribution of true simulated trace space vectors in Figure 6.1.

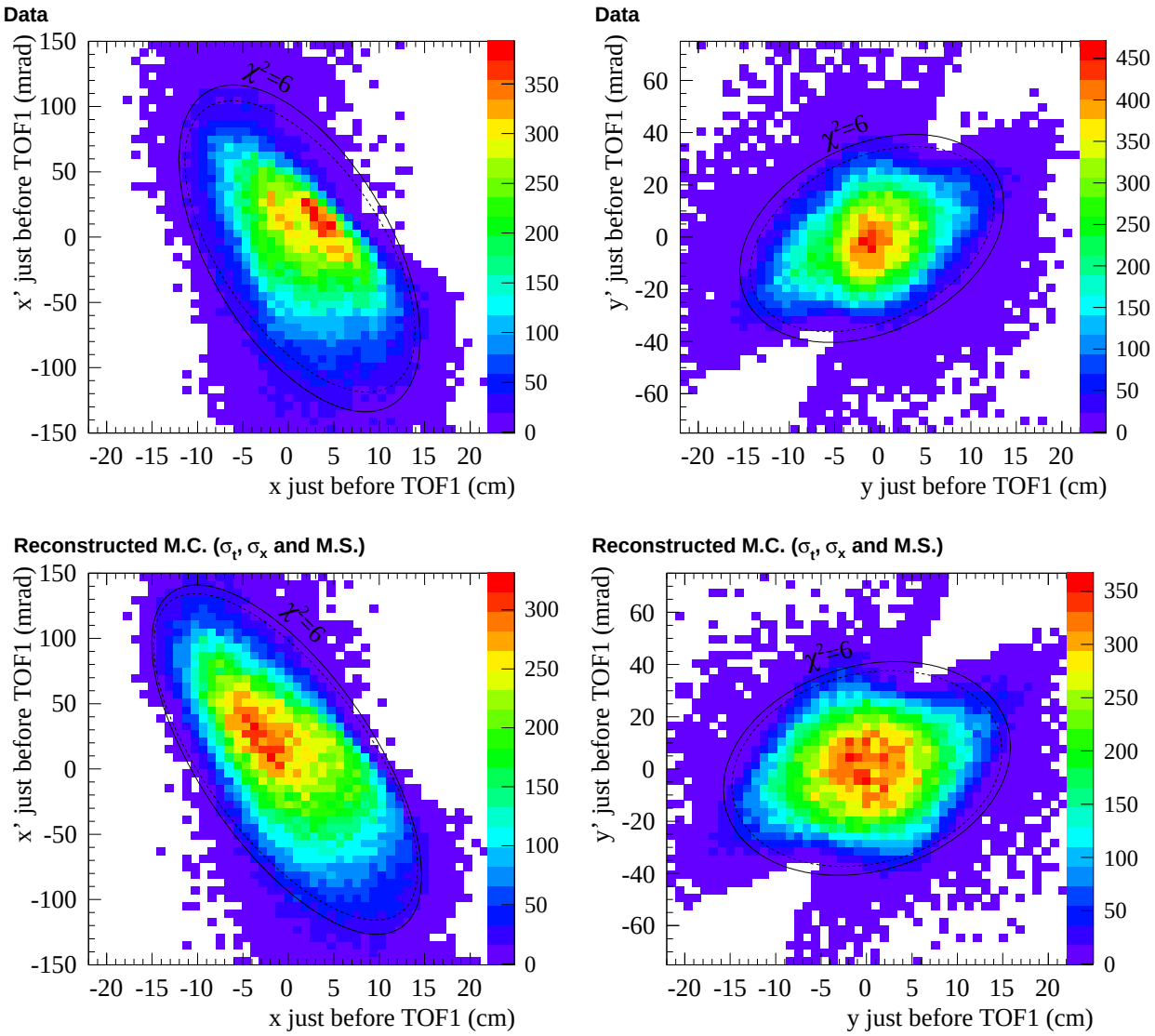

Figure 6.8: Horizontal and vertical trace space distributions of the base line (6 mm, 200 MeV/c) μ^- beam in reconstructed data and reconstructed resolution smeared simulation. The $\chi^2 = 6$ (95% confidence in the Gaussian approximation) ellipse has been calculated from the raw covariance matrix of the distribution and drawn as a solid ellipse: it is treated as a cut in the analysis. The dashed ellipse is the $\chi^2 = 6$ contour after the cut.

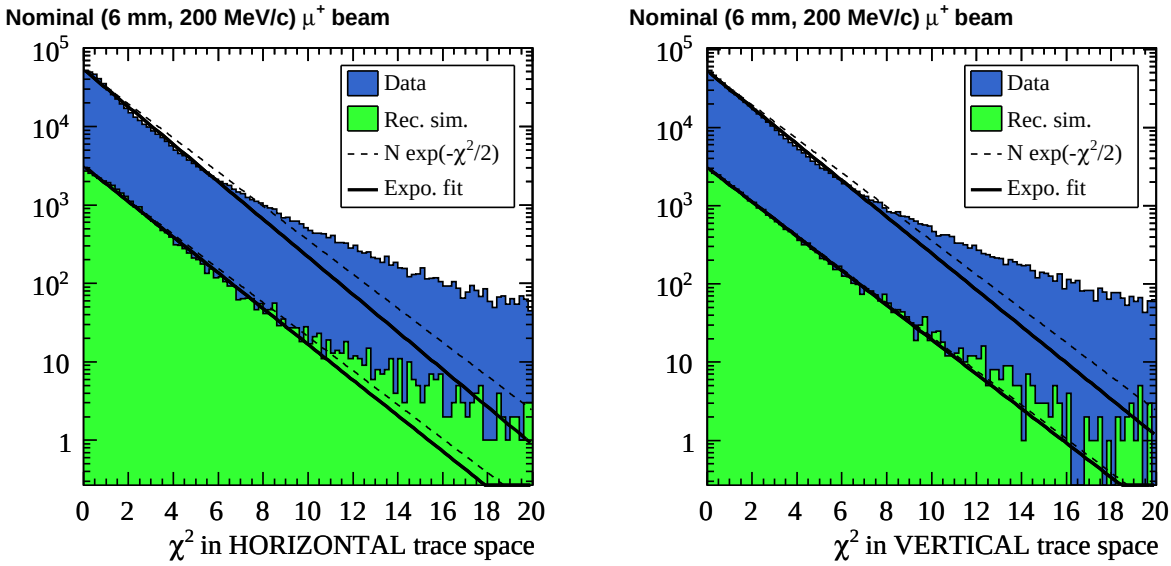

Figure 6.9: χ^2 distributions for the (6 mm, 200 MeV/c) μ^+ beam in data and simulation. The core of the beam is Gaussian to a good approximation up to $\chi^2 = 6$ (95%).

Both the measured and simulated beams have striking high amplitude features which do not appear to be found in the core distributions, such as the resemblance of the outlying regions of the vertical trace space distributions to butterfly wings. Whilst it is encouraging that the Monte Carlo reproduces these features they have a significant impact on the measured optical parameters as the emittance is proportional to the mean amplitude. High amplitude features can also be problematic when comparing data and Monte Carlo as they can be difficult to model and are most likely to be affected by nonlinear effects. These regions of phase space are also the least likely to be transported into the acceptance of the cooling channel and are likely to contain the greatest fraction of misidentified pions and coincidences.

Inspection of Equation 2.2 shows that the relationship between amplitude and $\chi^2 \equiv (x, x')^{\mathrm{T}} \boldsymbol{\Sigma}^{-1} (x, x')$ is $A = \frac{1}{2}\chi^2$. Therefore in order to compare these high amplitude features histograms of χ^2 in data and simulation are plotted in Figure 6.9.

In a Gaussian beam the amplitude follows a χ^2 distribution with two degrees of freedom. This distribution has been normalized to the size of the measured and simulated data sets and drawn on the figure. Long tails cause both distributions to deviate from this. An exponential function with free parameters has also been fitted to each of the four distributions independently. The distributions rise above this fit at $\chi^2 \approx 6$.

The $\chi^2 = 6$ contour is drawn on each of the trace space distributions in Figure 6.8 for reference. It appears by eye to roughly delineate the region with strong high amplitude features not found in the core of the distributions. For a Gaussian beam it encloses 95% of the distribution. Assuming the horizontal and vertical distributions are independent the fraction of particles with $\chi^2 < 6$ in both planes is $\sim 90\%$.

Visually, and from the gradient of the free fit, we see that the tails in the χ^2 distributions in Figure 6.9 are longer in data than in simulation. The difference could be due to deficiencies in the Monte Carlo simulation's treatment of high amplitude particles or noise in the data. As these effects are not understood a $\chi^2 = 6$ cut has been applied (blindly) to the other data

sets.

Before examining the results it is important to note that particular care is required when applying a χ^2 cut in a measurement of emittance. A cut on χ^2 is a direct cut on amplitude $A_{\text{cut}} = \frac{1}{2}\langle A\rangle \chi^2_{\text{cut}}$ and reduces the mean amplitude to:

$$\langle A\rangle_{\text{cut}} = \frac{\int_0^{A_{\text{cut}}} Ae^{-A/\langle A\rangle}\mathrm{d}A}{\int_0^{A_{\text{cut}}} e^{-A/\langle A\rangle}\mathrm{d}A}.$$

As $\epsilon = \langle A\rangle/2$ the estimated emittance of a Gaussian beam is therefore reduced by a factor:

$$\frac{\langle A\rangle_{\text{cut}}}{\langle A\rangle} = \frac{\int_0^{\chi^2_{\text{cut}}}(\chi^2/2)e^{-\chi^2/2}\mathrm{d}\chi^2}{\int_0^{\chi^2_{\text{cut}}} e^{-\chi^2/2}\mathrm{d}\chi^2} = 1 - \frac{\chi^2_{\text{cut}}/2}{e^{\chi^2_{\text{cut}}/2} - 1}.$$

For $\chi^2_{\text{cut}} = 6$ the estimated emittance will therefore be reduced by a factor $\epsilon_{\text{cut}}/\epsilon = \langle A\rangle_{\text{cut}}/\langle A\rangle = 0.84$. The estimate of the betatron function will only change if there is an internal correlation between amplitude and the Twiss parameters. Such a correlation cannot be represented by this parameterization.

This correction is not applied to the results as the distributions are clearly not Gaussian. It is provided to quantify extent of the bias being introduced on the measured emittance. As the real beams have longer tails than a Gaussian distribution, the bias will in fact be larger.

6.2.2 The effect of a χ^2 cut on simulated beam measurements

The effect of the cut on the reconstructed emittance and betatron functions of the resolution smeared Monte Carlo simulations is illustrated in Figure 6.10, which should be compared with Figure 6.6 (without the cuts). The emittance reduction is greater than the Gaussian estimate as expected. The change is more noticeable in horizontal trace space because it is fractional and $\epsilon_x > \epsilon_y$. No change is visible in the betatron functions.

The effect of the χ^2 cut on the comparison between reconstructed data and reconstructed resolution smeared simulation is shown in Figure 6.11. Much better agreement between data and Monte Carlo is observed now that outliers have been removed. In the horizontal plane the discrepancy vectors are shorter and point in different directions. In the vertical plane the scatter in the direction of the discrepancy vectors has been resolved into a systematic difference which requires further investigation. The agreement is reasonably good between reconstructed simulation and data.

α_x and α_y are also plotted now, as otherwise the correlation of the distribution is unconstrained. Both α and β govern the subsequent evolution of the betratron function and decide whether the beam will be matched in MICE. Reasonably good agreement between reconstructed simulation and data is observed here too.

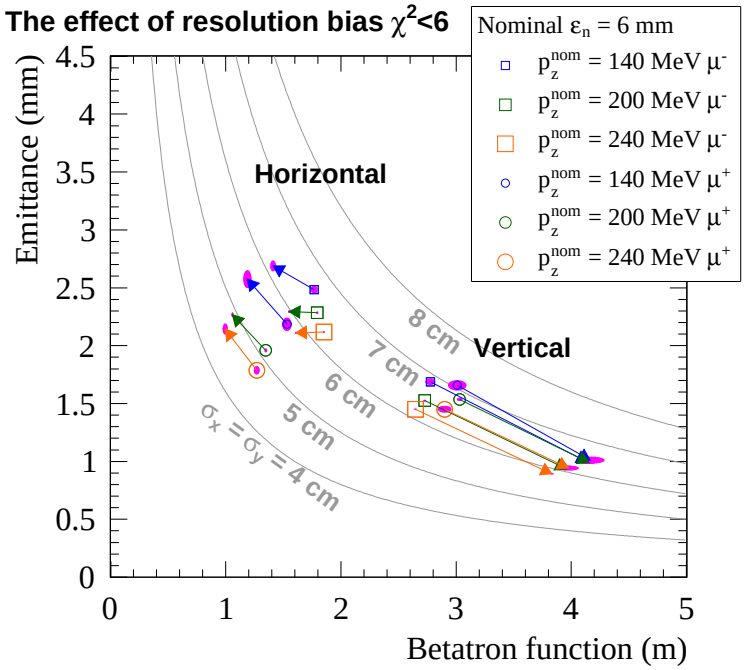

Figure 6.10: The effect of resolution and reconstruction of measurements of (β_x, ϵ_x) and (β_y, ϵ_y) for the $\epsilon_N = 6$ mm beam simulations after a cut at $\chi^2 = 6$. Figure 6.6 shows the same analysis with no cut. The arrows point from simulation truth to reconstructed resolution smeared simulation.

6.3 Measurement of the emittance of the Step I beams

Figure 6.12 shows results for all beams but with no simulations. The amplitude cut has been applied. The curious arrangement of the points (β_y, α_y) and the correlation of nominal emittance with betatron function is not understood.

The trace space parameterization used in this chapter is valuable for it's simplicity, however it does not reflect correlations with momentum. Figure D.2 and Figure D.3 in Appendix D provide greater detail on the dependence of ϵ, β and α on p_z of the re-scaled TURTLE beams.

6.4 Summary

Measurement errors are moderately significant in the reconstruction of trace space optical parameters with TOF0 and TOF1. Outliers are not well described in the simulation, but there is reasonably good agreement between reconstructed simulation and data for the inner 90% of the beam (after a $\chi^2 < 6$ cut in both planes). In the light of this agreement the next chapter proceeds to study the performance of the base line beam in a simulation of the final experimental configuration of MICE, and test whether it is suitable for cooling.

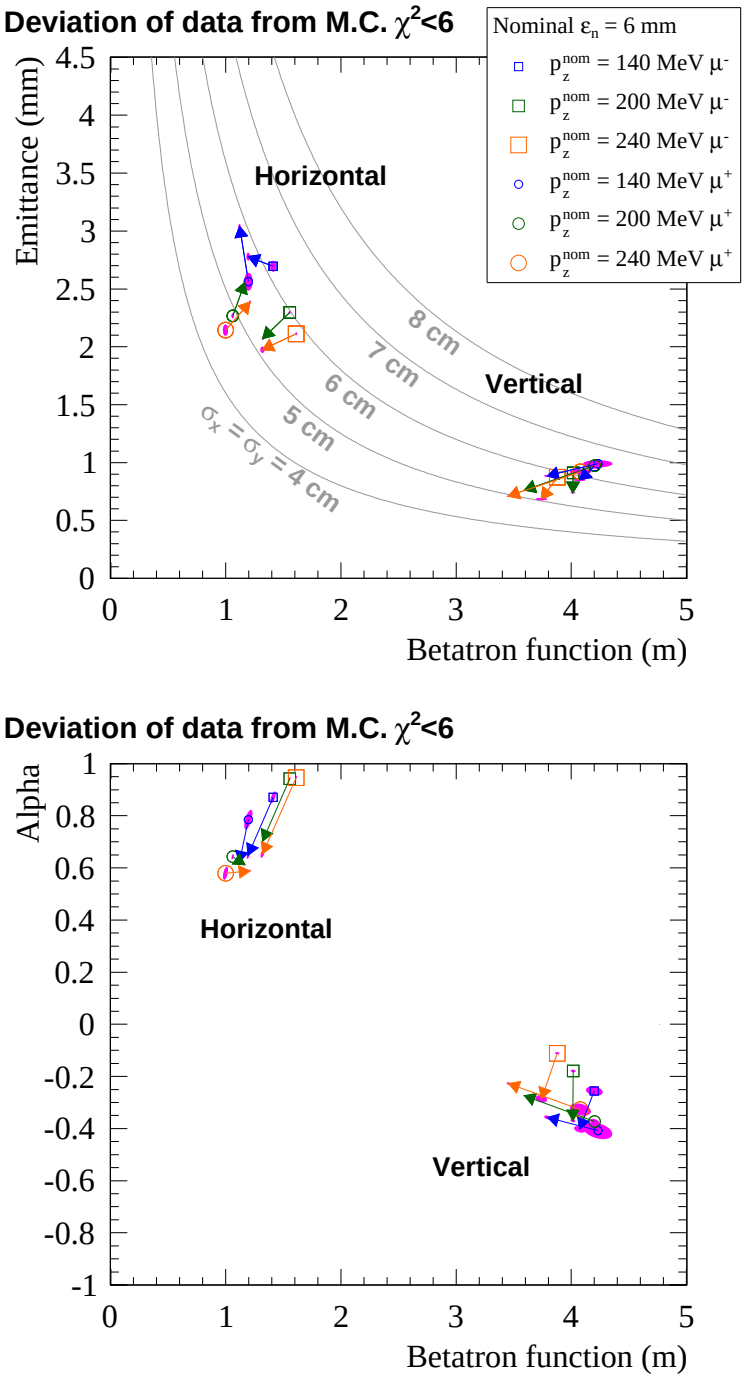

Figure 6.11: (β, ϵ) and (β, α) of reconstructed data and the reconstructed resolution smeared $\epsilon_{\mathrm{N}} = 6$ mm beam simulations calculated after a cut at $\chi^2 = 6$. The arrows point from reconstructed simulation to data.

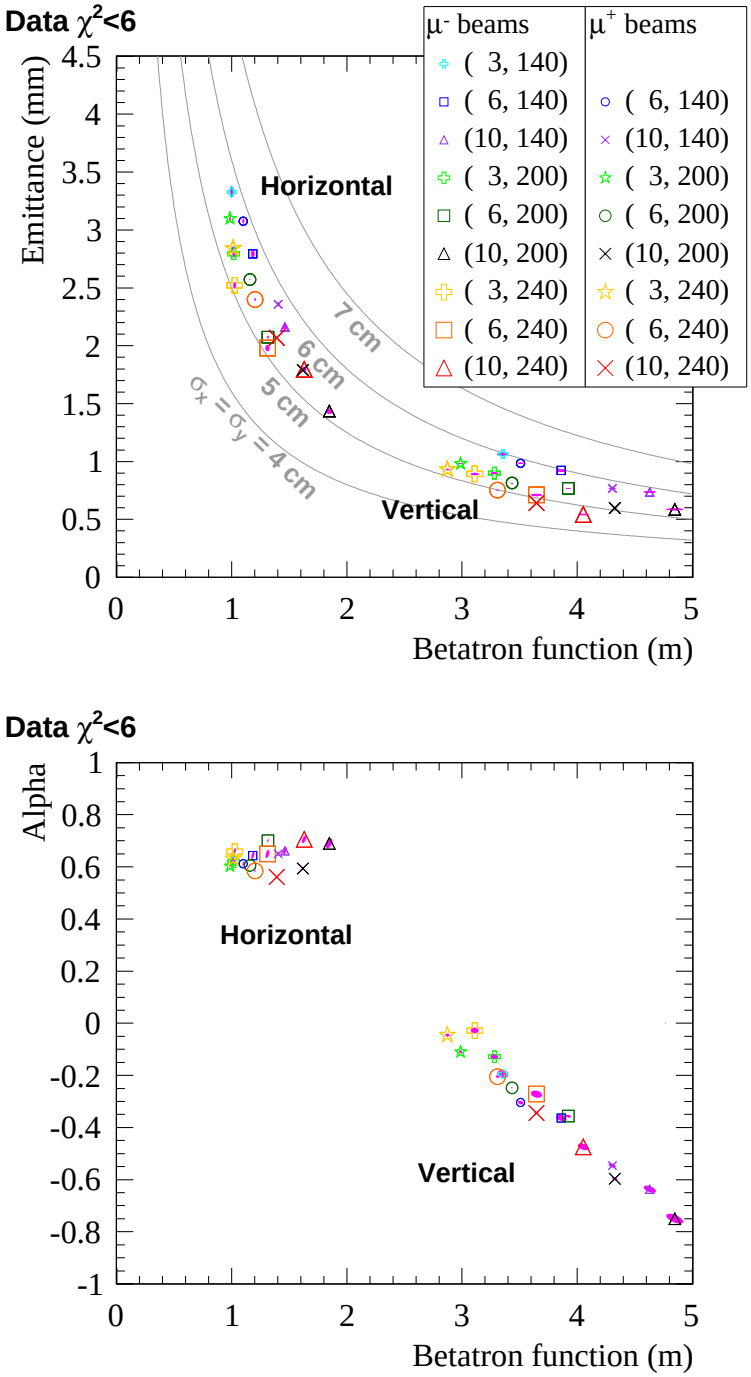

Figure 6.12: (β, ϵ) and (β, α) of the re-scaled TURTLE emittance-momentum matrix beams measured in Step I of the MICE experiment. A $\chi^2 = 6$ cut (95% in the Gaussian approximation) has been applied to remove the effect of high amplitude outliers as they are difficult to model and have a disproportionate effect on estimated statistical parameters.

Chapter 7

Simulation of a measured beam in the MICE cooling channel

The trajectories of muons measured in the Step I base line beam are passed through a simulation of the final MICE configuration. The beam is found to be suitable for demonstrating muon cooling, although some fine tuning of the cooling channel optics will eventually be required.

A direct way to test whether the Step I beams are suitable for an ionization cooling demonstration is to simulate a sample of muons passing from TOF1 through the MICE cooling channel. In this chapter real muons with phase space vectors measured in the base line (nominal) $\epsilon_{\mathrm{N}} = 6$ mm and $p_z = 200$ MeV/c μ^+ beam are injected into a G4MICE simulation of Step VI, starting just before TOF1 [67]. For simplicity eleven monochromatic slices of width 1 MeV/c were selected at intervals of 10 MeV/c between $p_z = 200$ MeV/c and 300 MeV/c. The cooling channel is as described in Section 2.2.

The mean energy and momentum profiles and the betatron function of the simulated monochromatic beams are plotted for the momentum slices $p_z = 210$ MeV/c, 220 MeV/c, 230 MeV/c, 240 MeV/c and 250 MeV/c in Figure 7.1. These slices have been chosen as they are well populated (cf. the p_z distribution in Figure 5.13) and they are clustered around the nominal momentum of 200 MeV/c in the absorber. In the figures the orange lines denote the centres of the three absorbers. The p_z-slice which best fits this criterion is therefore seen to have p_z between 230 MeV/c and 240 MeV/c before TOF1.

The dashed blue lines denote the centres of the eight RF cavities. Energy loss in the cavity windows is just visible. The reference particle in each case is defined to be a zero amplitude muon with the p_z of the slice in question. This particle is used to phase each of the eight cavities such that a zero amplitude muon will experience the maximum accelerating voltage as it passes through the centre of each cavity. Muons with nonzero amplitude are focused by the solenoidal fields and arrive in the cavities fractionally off the peak phase. Note that while the design muon (dashed in the energy-momentum profiles) is fully re-accelerated after energy loss in the absorbers, the mean energy and momentum are not fully re-accelerated after the absorbers. An increasing spread in time is inevitable in channels which rely on peak acceleration[1].

The magnet currents and positions are the same as in the note by Apollonio and Witte [60]. The axial field profile is shown in Figure 7.2. The design betatron function is conventionally

[1] Due to power and cost limitations MICE will run 'on crest'.

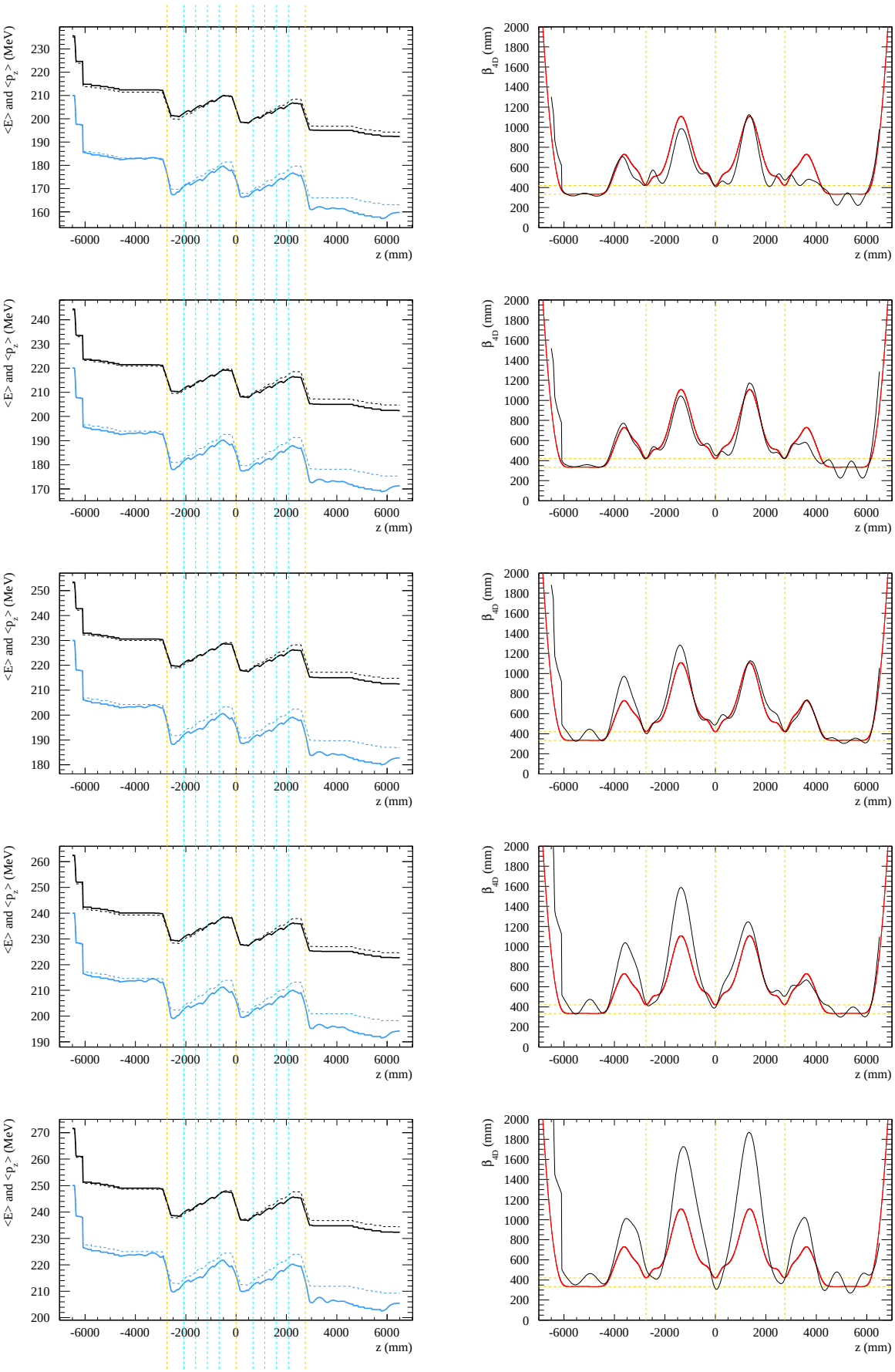

Figure 7.1: From top to bottom: the mean enegy and momentum profile and the measured betatron function of monochromatic slices of the base line μ^+ beam with $p_z = 210$, 220, 230, 240 and 250 MeV/c immediately upstream of TOF1. They are defined by their initial $\langle p_z \rangle$ upstream of TOF1 at $z = -6.5$ m in the figure. The diffuser is at $z = -6.2$ m. The yellow dashed lines indicate the positions of the absorber centres and the dashed blue lines indicate the centre of the RF cavities. The red curve is the design betatron function.

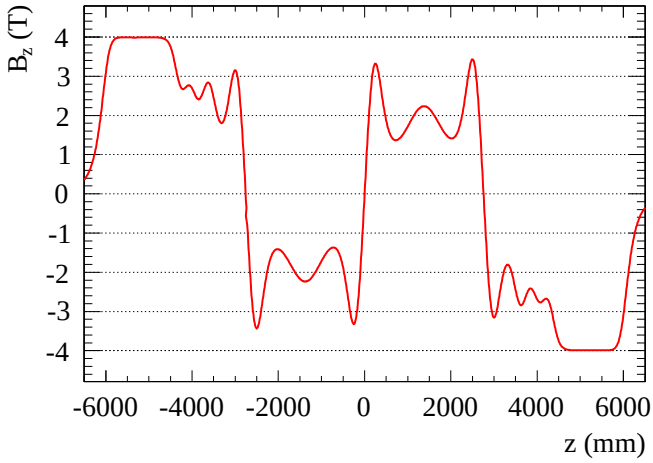

Figure 7.2: The longitudinal magnetic field in Step VI. The constant field region at $z = \pm 5$ m is inside the upstream and downstream spectrometer solenoids. A matched beam will have a constant betatron function in this region.

taken to be the solution to the envelope equation (Equation 2.7) with the focusing strength $\kappa(z)$ calculated using this field profile and a constant $p_z = 200$ MeV/c. This is plotted as a red line in each of the betatron function profiles in Figure 7.1. The boundary conditions are the matching conditions specified in Section 2.3.2; Apollonio and Witte's optimization of the matching coil currents ensures that these are equivalent to the requirement for a focus in the absorbers at $\beta_\perp = 42$ cm.

A potential difficulty emerges when one comes to measure the betatron function. The definitions in the covariance matrix (Equation 2.8) and the envelope equation both assume cylindrical symmetry, but Chapter 6 has demonstrated that there is a marked asymmetry between the horizontal and vertical trace spaces of the MICE beams. However, to be compatible with Penn's definition [39], in Figure 7.1 the betatron function is taken to be:

$$\beta_\perp \equiv \frac{p_z}{m_\mu c \epsilon_{\mathrm{N}}} \left(\frac{\sigma_{xx} + \sigma_{yy}}{2} \right)$$

where the emittance has the standard definition $\epsilon_{\mathrm{N}} = \sqrt[4]{\mathbf{\Sigma}_\perp}/m_\mu$.

The simulated betatron functions of these slices behave encouragingly well, most importantly having minima at approximately the right $\beta_\perp$ in each absorber. The only unsatisfactory curve in the figure is the 250 MeV/c case where $\beta_\perp$ rises high in the RF cavities, leading to scraping. The situation deteriorates further for higher p_z slices, but this is to be anticipated as the neutrino factory channel itself has a limited p_z acceptance.

The test for this beam, however, is whether it obeys the matching criteria in the constant field region of the upstream tracker. Unlike the other elements of the re-scaled TURTLE optical configuration, the base line (6 mm, 200 MeV/c) beam is specifically designed to be matched with $\beta_\perp = 333$ mm and $\beta'_\perp = 0$ in the uniform field region of the upstream tracker at $z = -5$ m. While the 210 MeV/c and 220 MeV/c slices obey the matching conditions quite well, the beams nearer to achieving the nominal absorber p_z arrive in the spectrometer with $\beta_\perp > 333$ mm and $\alpha_\perp > 0$. To match these slices one must tune the initial beam to

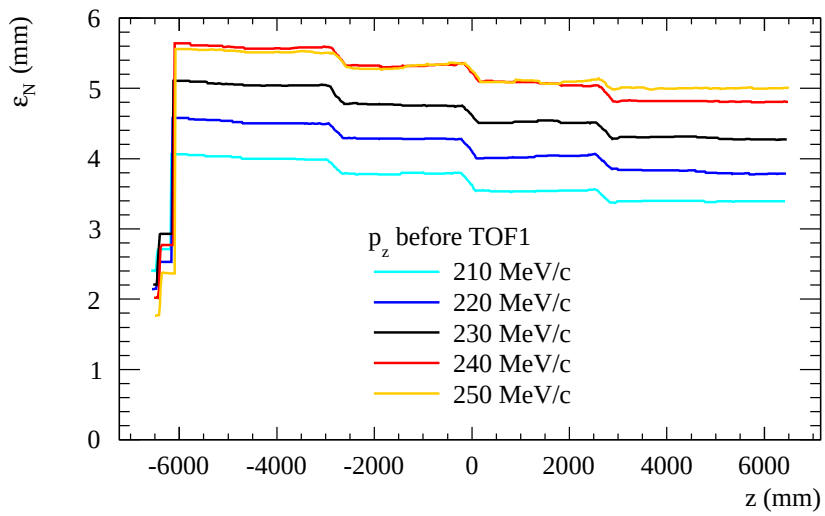

Figure 7.3: Simulated evolution of 1 MeV/c wide p_z slices of the measured beams.

change the initial conditions, and possibly increase the thickness of the diffuser ($z = -6.2$ m) so it causes a greater reduction in $\beta_\perp$.

In reality of course, all the slices will contribute to the same beam. Eventually the task of tuning magnet currents and the diffuser to create matched beams will need to be undertaken. This thesis provides tools and measurements to begin that process.

The final, and most important parameter to investigate, is the emittance, shown in Figure 7.3. Each of the well matched beams is cooled by about 16% in the absorbers as expected and, though the mis-match in the 250 MeV/c slice hinders cooling, it does not cause nonlinear emittance growth: the base line beam therefore appears to perform remarkably well for a first attempt at matching a beam into MICE. It is hoped that within the next two to three years MICE will have demonstrated ionization cooling.

Appendix A

The Step I data sets

Step 1 of the MICE experiment was devoted to testing the newly installed muon beam line at the ISIS proton synchrotron, and demonstrating that it can generate beams with a range of emittances and momenta, which will be matched in the upstream spectrometer. This appendix defines data sets for matched beams with certain optical parameters, and sets of runs where magnet currents are tuned around those of the base line designs.

In order to demonstrate cooling over a range of emittances and momenta, the beam line must generate several matched beams with different optical parameters. The beam line is designed to create nine base line beams. These are the combinations of transverse normalized emittance ϵ_{N} = (3 mm, 6 mm, 10 mm) upstream of the first liquid hydrogen absorber, and mean momentum $\langle p_z \rangle$ = (140 MeV/c, 200 MeV/c, 240 MeV/c) in the centre of each absorber [52]. This is achieved by varying the dipole currents, and inflating the emittance in various thicknesses of material in a diffuser inside the upstream spectrometer. The beam is matched into the cooling channel lattice by varying the quadrupole currents.

In this appendix, experimental runs with the same magnet currents are collated so that the largest possible data sets may be analysed in a consistent way [73]. Every run from the 2010 Step 1 data taking campaign after quadrupole 3 was fixed is considered. Magnet currents were required to be consistent to better than 1%, and must not have been labelled as unsuitable for analysis. The appendix should be read with reference to Chapter 2 and in particular Table 2.3 which shows the currents in each of the magnets corresponding to the data sets defined here. Table A.1 shows current to field conversions used by Tilley and Apollonio when designing these optical configurations.

Magnet	Conversion	Limits
Quadrupoles 1–3	I [A] $= 96\, g$ [T/m]	$g_0^{\max} = 2.086$ T/m
Dipoles 1 and 2	I [A] $= 39.59\,(B_y$ [T]$)^3$ $-55.998\,(B_y$ [T]$)^2 + 256.914\, B_y$ [T]	D1: $B_y^{\max} = 1.65$ T D2: $B_y^{\max} = 0.84$ T
Decay solenoid	I [A] $= 174.0\, B_z$ [T]	$B_z^{\max} = 5$ T
Quadrupoles 4–9	I [A] $= 174.09\, g$ [T/m]	$g_0^{\max}$ is 2.30 T/m

Table A.1: Conversions between current and field for the beam line magnets.

Diffuser ϵ_N	Absorber p_z	Experimental runs
3 mm	140 MeV/c	2263–2264, 2300
	200 MeV/c	2266–2268, 2299
	240 MeV/c	2259, 2260–2262, 2290–2293, 2296–2298, 2306, 2325
6 mm	140 MeV/c	2271, 2302, 2526
	200 MeV/c	2175–2176, 2187, 2190, 2199–2200, 2204–2211, 2238–2239, 2241, 2243–2245, 2253–2256, 2272–2276, 2286–2287, 2289, 2303, 2323, 2498–2502, 2514, 2525
	240 MeV/c	2269–2270, 2531–2532
10 mm	140 MeV/c	2246–2247, 2278–2279
	200 MeV/c	2257–2258, 2283–2285
	240 MeV/c	2250–2251, 2280–2282, 2305, 2324, 2339

Table A.2: μ^- base line emittance-momentum matrix element data sets with magnet currents from the re-scaled TURTLE optical designs.

Diffuser ϵ_N	Absorber p_z	Experimental runs
3 mm	140 MeV/c	2461
	200 MeV/c	2401–2403
	240 MeV/c	2384, 2386, 2463
6 mm	140 MeV/c	2453, 2455–2457, 2459–2460
	200 MeV/c	2396, 2398, 2423, 2444, 2446, 2462, 2466, 2482, 2534, 2538–2539, 2553–2558, 2561–2562, 2616, 2702, 2714–2715, 2726, 2734–2741, 2743, 2767, 2803, 2846, 2873–2884, 2887–2891, 2893–2895
	240 MeV/c	2387–2388, 2464
10 mm	140 MeV/c	2447–2448
	200 MeV/c	2424
	240 MeV/c	2389–2390, 2392, 2535

Table A.3: μ^+ base line emittance-momentum matrix element data sets with magnet currents from the re-scaled TURTLE optical designs.

A.1 The re-scaled TURTLE data sets

The re-scaled TURTLE optical configurations are based on a (6 mm, 200 MeV/c) design created by Kevin Tilley. The magnet currents have been re-scaled by p_z/p_{z0} to generate the other elements, as the focusing strength in quadrupoles scales as $1/p_z$, and the radius of curvature in dipoles scales as p_z. Base line data sets with μ^- and μ^+ are shown in Table A.2 and Table A.3.

On a number of occasions, the currents in certain beam line magnets were varied around the nominal values of the optical design of a re-scaled TURTLE emittance-momentum matrix element. Table A.4 shows data sets related to scanning the currents in the quadrupoles 7, 8, and 9 individually, and as a triplet around the base line currents for the (6 mm, 200 MeV/c) matrix element's optical design with positively charged particles. Table A.5 shows data sets for scans of each of the quadrupole triplets and the decay solenoid around the base line currents for the (6 mm, 200 MeV/c) with negatively charged particles. Table A.6 shows

Δf (%)	Q7	Q8	Q9	Q789
−40				2441
−30				2439
−20				2438
−15	2497	2491	2481	2472
−10	2496	2489	2476	2437, 2470
−5	2492	2484	2474	2443, 2468
0	2482	2482	2482	2444, 2466
+5	2493	2486	2473	2442, 2467
+10	2494	2487–2488	2475	2433, 2469
+15	2495	2490	2483	2471
+20				2434
+30				2435
+40				2436

Table A.4: Data sets for scans of the current in quadrupoles 7, 8, and 9, individually and collectively, around the base line design for the (6 mm, 200 MeV/c) re-scaled TURTLE μ^+ matrix element. In each case the base line current I_0 is transformed as $I = (1 + \Delta f)I_0$.

data sets for scans of each of the quadrupole triplets around the base line currents for the (3 mm, 240 MeV/c) with negatively charged particles. Although not a scan around a matrix element, Table A.7 shows data sets for a scan of the current in dipole 1 with a beam predominantly composed of pions.

A.2 The genetic algorithm data sets

Genetic algorithm optical configurations were subsequently created by Marco Apollonio using a genetic algorithm which employed G4Beamline simulations. Not all matrix elements have yet been designed using this method. Base line emittance-momentum matrix data sets with μ^- and μ^+ are shown in Table A.8 and Table A.9.

Δf (%)	Q123	Decay Solenoid	Q456	Q789
−50			2222	2229
−40			2221	2230
−30			2215	2231
−20			2216–2217	2232
−15	2181–2182	2198		
−10	2177	2192	2218	2233
−5	2186			
0	2175–2176, 2187, 2190	2197	2204–2211, 2223, 2238–2239	2223, 2238–2239
+5	2185			
+10	2178–2179	2199–2200	2214	2228
+15	2180	2196	2235	
+20	2183	2191	2213	2227
+25	2184	2195		
+30		2193	2212	2226
+40			2220	2225
+50			2219	
+75			2237	2234

Table A.5: Data sets for scans of the current in the three quadrupole triplets collectively, and the decay solenoid, around the base line design for the (6 mm, 200 MeV/c) re-scaled TURTLE μ^- matrix element. In each case the base line current I_0 is transformed as $I = (1 + \Delta f)I_0$.

Δf (%)	Q123	Q456	Q789
−20	2309, 2329	2333	2337
−10	2310–2312, 2328	2315–2317, 2332	2336
0	2306, 2325	2306, 2325	2306, 2325
+10	2308, 2327	2314, 2331	2335
+20	2326, 2338	2313, 2330	2334

Table A.6: Data sets for scans of the current in the three quadrupole triplets collectively, around the base line design for the (3 mm, 240 MeV/c) re-scaled TURTLE μ^- matrix element. In each case the base line current I_0 is transformed as $I = (1 + \Delta f)I_0$.

Δf (%)	Dipole 1
−20	2751
−10	2750
−5	2755
0	2745, 2756
+5	2752–2753
+10	2746
+15	2747
+20	2748
+30	2749

Table A.7: Data sets for a scan of the current in dipole 1, for an optical design which predominantly transports π^+. During this scan there was no current in quadrupoles 7, 8, and 9. In each case the base line current I_0 is transformed as $I = (1 + \Delta f)I_0$.

Diffuser ϵ_N	Absorber p_z	Numbers of experimental runs with the correct optics
3 mm	140 MeV/c	
	200 MeV/c	
	240 MeV/c	
6 mm	140 MeV/c	2519–2520
	200 MeV/c	2503, 2505, 2522–2523
	240 MeV/c	2510–2512, 2528–2529
10 mm	140 MeV/c	2515–2518
	200 MeV/c	2507, 2524
	240 MeV/c	

Table A.8: μ^- base line emittance-momentum matrix element data sets with magnet currents from the genetic algorithm optical designs.

Diffuser ϵ_N	Absorber p_z	Numbers of experimental runs with the correct optics
3 mm	140 MeV/c	
	200 MeV/c	
	240 MeV/c	
6 mm	140 MeV/c	
	200 MeV/c	2399, 2432, 2546, 2564, 2601
	240 MeV/c	2477–2478
10 mm	140 MeV/c	2449, 2451–2452
	200 MeV/c	2431
	240 MeV/c	2393–2395, 2537

Table A.9: μ^+ base line emittance-momentum matrix element data sets with magnet currents from the genetic algorithm optical designs.

Appendix B

Sketch of a fully constrained calibration

Experts at the University of Sofia calibrated TOF0 and TOF1 to measure the time of passage of muons with resolution approaching 50 ps. This chapter describes how the calibration has been extended for postion measurements of resolution ~ 1 cm. If the TOFs are required to measure position in the future it may be beneficial to fully constrain the calibration at the first pass.

This appendix is devoted to sketching a possible method for calculating the relative lengths T_i, B_i, L_i, and R_i of the cables connecting the top, bottom, left and right PMTs of slab i of a TOF station to the DAQ. Cable lengths are calculated in terms of the time delay incurred on measurements. As described in Section 3.2, the TOF calibration in G4MICE version 2.4 only constrains the $2n$ constants $T_i + B_i$ and $L_i + R_i$, allowing measurements of t [67]. If known, the remaining $2n$ degrees of freedom allow an unbiased measurement of x and y. n is the number of slabs per plane of a detector.

As illustrated in Figure 3.3, the calibration is complicated because the PMTs of each detector are connected to two TDC boards with clocks which are not synchronized. The trigger time could have been recorded by either board. In each TOF, however, the left and top (and right and bottom) PMTs are connected to the same TDC board. The situation is illustrated in more detail in Figure B.1.

When a particle passes through the intersection between horizontal slab i and vertical slab j, the times in the DAQ from the left and top PMTs are:

$$t_{\mathrm{L}i} = t + L_i + \frac{l + x}{c_{\mathrm{eff}}} \tag{B.1}$$

$$t_{\mathrm{T}j} = t + T_j + \frac{l - y}{c_{\mathrm{eff}}} \tag{B.2}$$

These equations are simple, because on the same TDC board the clock is the same. The subtracting is meaningful because unlike the alternative combination, both times are measured on synchronized clocks.

A measurement m_{ij} of the difference $L_i - T_j$ may be made by subtracting Equation B.1 from

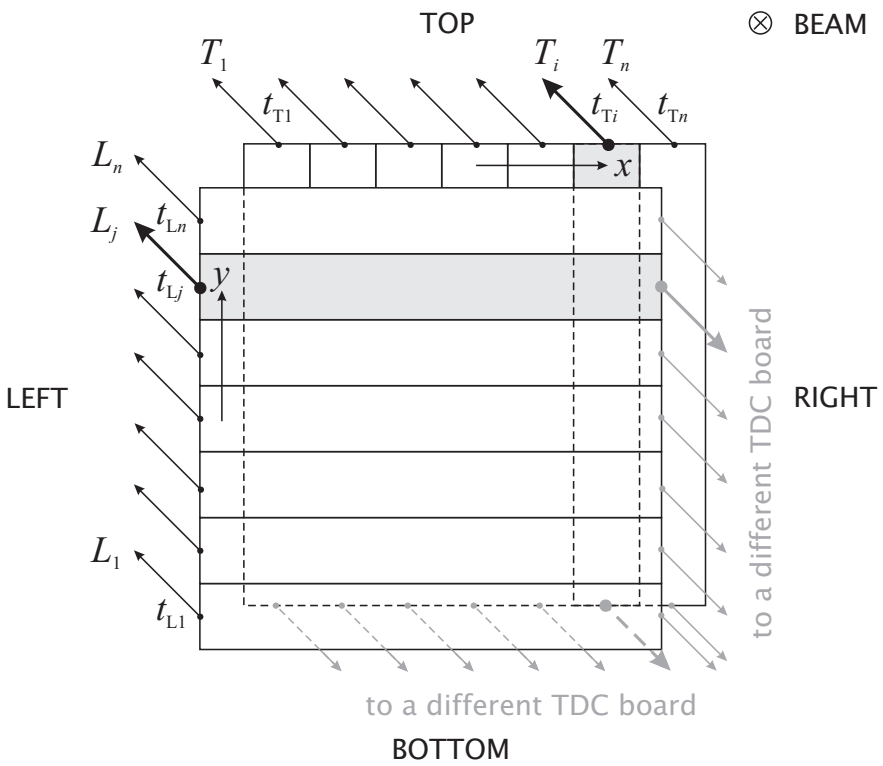

Figure B.1: Diagram of the TOF cable calibration constants.

Equation B.2:

$$m_{ij} = t_{\mathrm{L}i} - t_{\mathrm{T}j} - \frac{x+y}{c_{\mathrm{eff}}}$$

N_{ij} particles passing through pixel (i,j) allow m_{ij} to estimate $L_i - T_j$ with resolution

$$\sigma_m = \sqrt{2\sigma_{\mathrm{PMT}}^2 + 2\left(a/\sqrt{12}c_{\mathrm{eff}}\right)^2}.$$

The two terms are due to the effect of electronic jitter, and the physical size of the pixel respectively. The mean $\langle m_{ij}\rangle$ threfore measures $L_i - T_j$ with resolution $\sigma_{ij} = \sigma_m/\sqrt{N_{ij}}$.

We wish to make estimates of the $2n$ cable delays $\vec{L} \equiv (L_1, \ldots, L_n)$, and $\vec{T} \equiv (T_1, \ldots, T_n)$, using the n^2 $\hat{m}_{ij}$. Therefore construct and maximize $2n$ χ^2:

$$\chi^2_{L_i} = \sum_j \frac{[m_{ij} - (L_i - T_j)]^2}{\sigma_{ij}^2}; \ \frac{\partial \chi^2_{L_i}}{\partial L_i} \equiv 0 \Leftrightarrow \sum_j \frac{m_{ij} - (L_i - T_j)}{\sigma_{ij}^2} = 0$$

$$\chi^2_{T_j} = \sum_i \frac{[m_{ij} - (L_i - T_j)]^2}{\sigma_{ij}^2}; \ \frac{\partial \chi^2_{T_j}}{\partial T_j} \equiv 0 \Leftrightarrow \sum_i \frac{m_{ij} - (L_i - T_j)}{\sigma_{ij}^2} = 0.$$

Defining the weights matrix $w_{ij} \equiv 1/N_{ij}$ and the diagonal matrix $D_{ij} = \sum_k w_{ik}\delta_{ij}$, after some cancellation we may write

$$\begin{pmatrix} \mathbf{D} & \mathbf{w} \\ \mathbf{w}^{\mathrm{T}} & \mathbf{D}^{\mathrm{T}} \end{pmatrix} \begin{pmatrix} \vec{L} \\ -\vec{T} \end{pmatrix} = \begin{pmatrix} \sum_k w_{ik} m_{ik} \\ \sum_k w_{kj} m_{kj} \end{pmatrix}$$

Or in a shorter notation

$$\mathbf{W}\vec{\Delta} = \vec{M}\,. \tag{B.3}$$

We are now close to solving for the cable delay corrections $\vec{\Delta}$, but Equation B.3 is over-constrained: $\det W = 0$, and inversion is not possible. The solution is to define a zero correction for a reference PMT and invert a reduced $(2n-1)\times(2n-1)$ matrix $\mathbf{W}_{\mathrm{red}}$ in order to solve the remaining $2n-1$ simultaneous equations:

$$\begin{aligned} L_1 &= 0 \\ \vec{\Delta}_{\mathrm{red}} &= \mathbf{W}_{\mathrm{red}}^{-1}\vec{M}_{\mathrm{red}}. \end{aligned}$$

In this manner, the length of $2n$ cables may be constrained relative to each other. By applying the method to the bottom and right PMTs, the remaining $2n$ can also be constrained. All that remains is to calibrate the two sets of corrections relative to each other using the reference slabs, and the cable length calibration is fully constrained for measuring both time and position.

Appendix C

Statistical error on Twiss parameters

The likelihood function of a Gaussian beam of N particles in two-dimensional trace space is:

$$\begin{aligned} L &= \prod_i^N f(v_i, v_i'|\epsilon, \alpha, \beta) \\ &= \frac{1}{2\pi\epsilon} \exp\left[\sum_i^N -\frac{(v_i, v_i')^{\mathrm{T}} \mathbf{\Sigma}^{-1} (v_i, v_i')}{2}\right] \end{aligned}$$

where $f(v, v'|\epsilon, \alpha, \beta)$ is the probability distribution function of the beam and ϵ, α and β are the emittance and Twiss parameters defined in Section 2.1.1. The log-likelihood $\mathcal{L} = -\ln L$ may be written:

$$\mathcal{L} = N \ln 2\pi + N \ln \epsilon + \frac{\gamma \sum_i^N v_i^2 + 2\alpha \sum_i^N v_i v_i' + \beta \sum_i^N (v_i')^2}{2\epsilon}.$$

The well known definitions of the parameters $\vec{\zeta} = (\epsilon, \alpha, \beta)$ are obtained by solving the equations $\partial\mathcal{L}/\partial\zeta_i = 0$; the statistical error matrix $\mathbf{E}$ of the parameters is given by:

$$E_{ij}^{-1} = -\frac{\partial^2 \mathcal{L}}{\partial\zeta_i \partial\zeta_j}.$$

After some calculation [48] the error on ϵ is found to be independent of α and β:

$$\sigma_\epsilon = \frac{\epsilon}{\sqrt{N}}.$$

The two-dimensional error matrix of α and β is given by:

$$E_{\alpha\beta} = \begin{pmatrix} (1+\alpha^2)/N & \alpha\beta/N \\ \alpha\beta/N & \beta^2/N \end{pmatrix}.$$

Appendix D

Measurements of the Step I data sets

It is important to note that the trace space parameterization neglects the p_z correlations observed in Figure 6.4 and Figure 6.5. The effect is illustrated for momentum slices of the μ^- and μ^+ re-scaled TURTLE beams in Figure D.2 and Figure D.3 respectively. The legend for the plots is Figure D.1.

The optical parameters graphed in Figure 6.12 are recorded in Table D.1.

The analyses may be reproduced using the G4MICE `Step1Ensemble`, `Step1Reconstruction` and `Step1Optics` applications [67]. These applications use the key reconstruction classes `Step1BeamLine`, `Step1Tracking` and `Step1Iteration`.

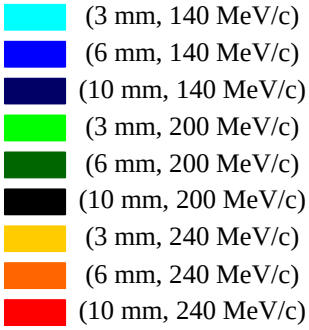

Figure D.1: Legend for the emittance-momentum matrix beam plots in Figure D.2 and Figure D.3.

	ϵ_n (mm)	p_z (MeV/c)	$\langle p_z \rangle$ (MeV/c)	σ_{pz} (MeV/c)	ϵ_x (mm)	β_x (m)	α_x	D_x (cm)	ϵ_y (mm)	β_y (m)	α_y
μ^- beams	3	140	170.8	24.5	4.39	0.84	0.56	14.9	1.64	2.54	-0.13
		200	223.1	25.2	3.58	0.87	0.57	16.8	1.26	2.76	-0.12
		240	261.9	26.5	3.15	0.90	0.60	16.7	1.15	2.81	-0.06
	6	140	174.8	24.7	3.80	0.95	0.58	13.8	1.47	2.85	-0.22
		200	230.9	25.6	2.78	1.09	0.64	13.7	1.07	3.33	-0.29
		240	270.8	28.3	2.60	1.11	0.59	17.1	0.95	3.19	-0.23
	10	140	181.2	24.9	3.01	1.17	0.61	12.7	1.18	3.47	-0.39
		200	245.0	27.0	1.98	1.50	0.64	15.1	0.78	4.38	-0.63
		240	281.9	31.0	2.42	1.34	0.65	14.0	0.76	3.62	-0.35
μ^+ beams	3	200	222.0	28.6	4.08	0.82	0.52	18.1	1.54	2.26	-0.08
		240	260.0	30.4	3.75	0.85	0.53	18.9	1.40	2.26	-0.05
	6	140	173.9	26.3	4.24	0.87	0.54	15.4	1.62	2.54	-0.16
		200	227.1	28.0	3.52	0.93	0.53	18.8	1.23	2.73	-0.17
		240	268.0	31.0	3.29	0.97	0.50	20.0	1.13	2.67	-0.13
	10	140	179.7	26.2	3.37	1.07	0.57	14.9	1.29	3.10	-0.30
		200	239.6	30.0	2.61	1.23	0.52	18.5	0.94	3.40	-0.38
		240	274.2	31.7	2.91	1.09	0.48	20.2	0.95	3.05	-0.22

Table D.1: Measured beam properties of the Step I re-scaled TURTLE beams. The reconstruction algorithm is described in Chapter 5. The data sets are defined in Appendix A.

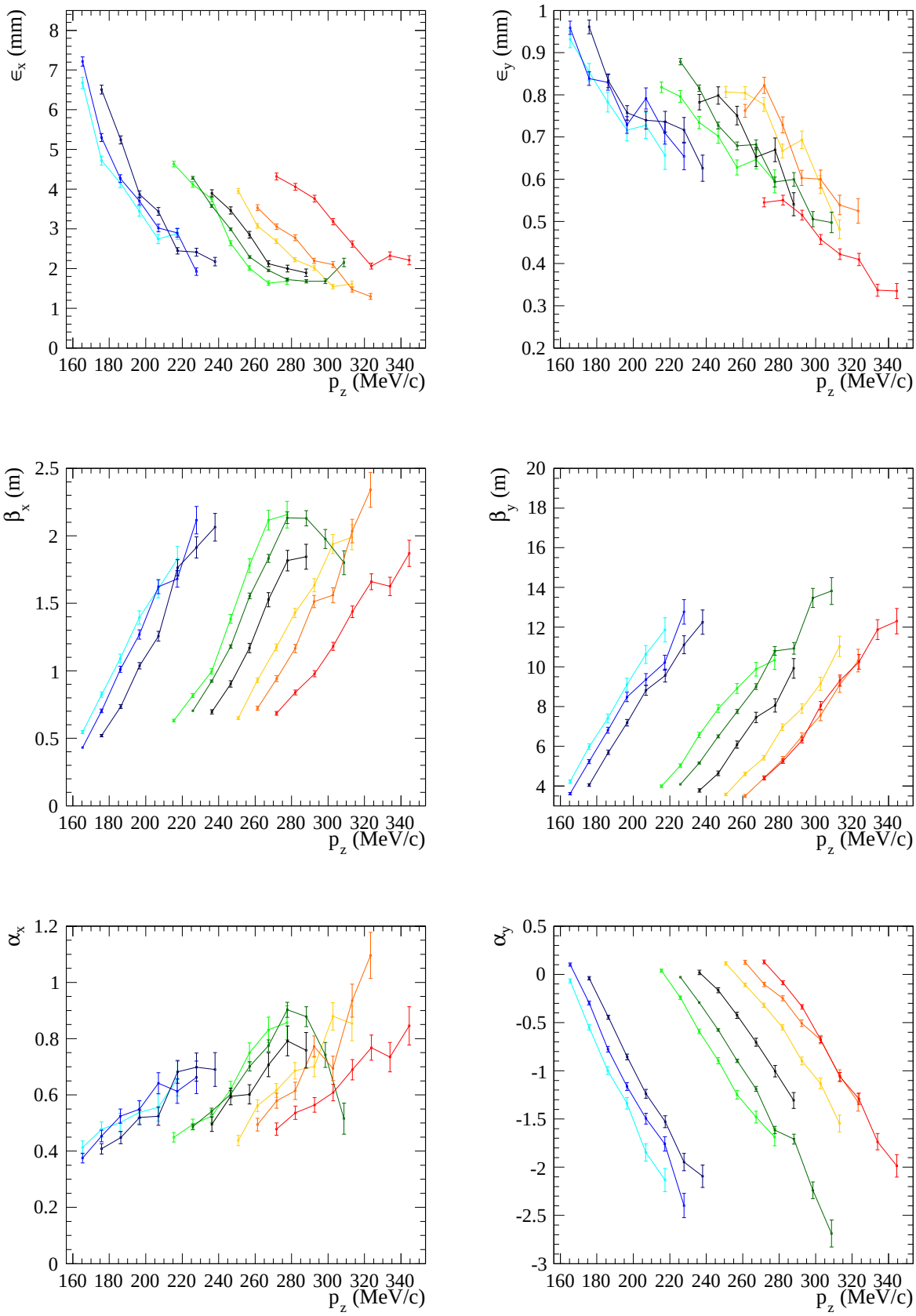

Figure D.2: ϵ, β and α (deduced from the measured covariance matrix) as a function of p_z for the Step I re-scaled TURTLE μ^- beams. Figure D.1 is the legend.

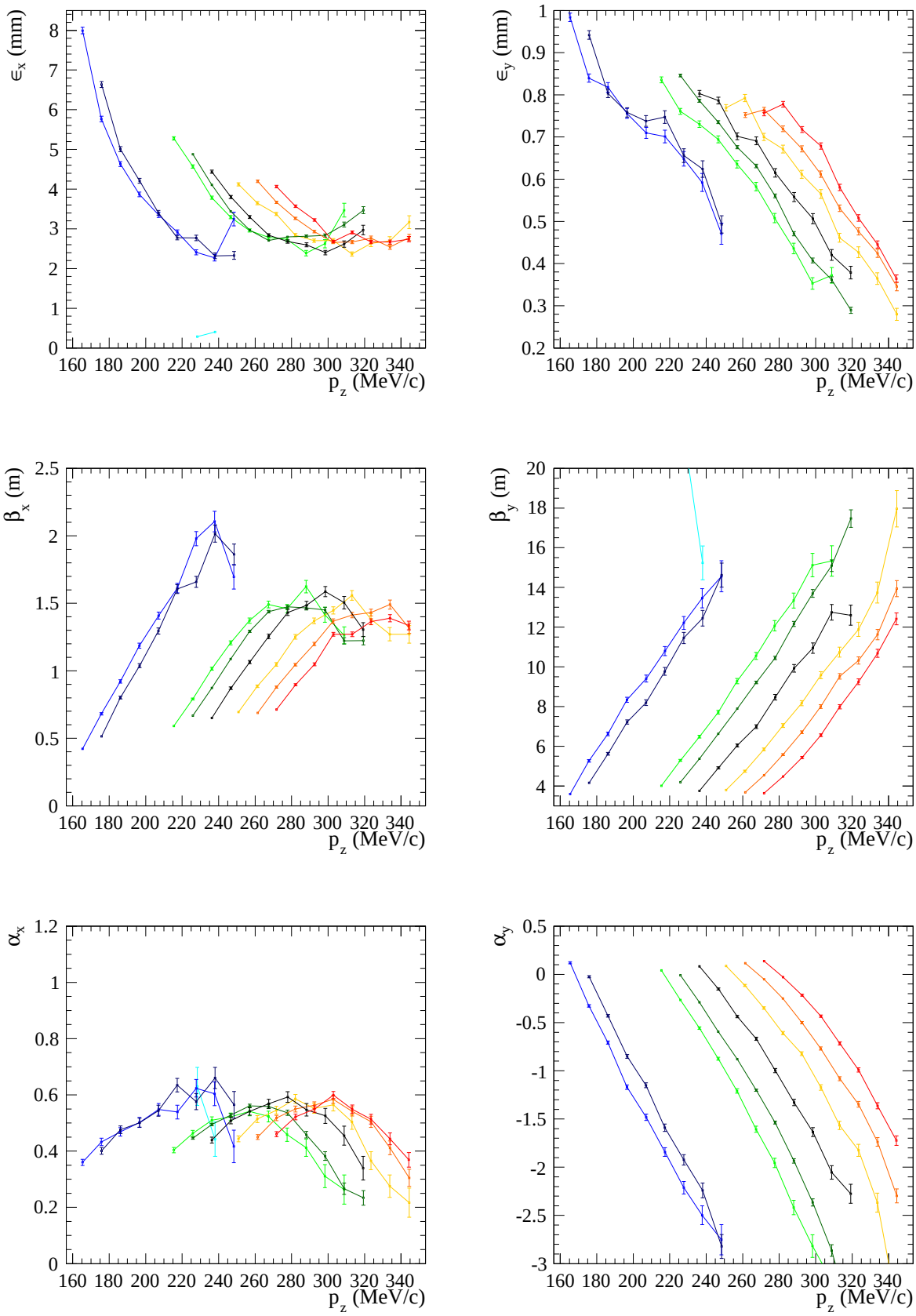

Figure D.3: ϵ, β and α (deduced from the measured covariance matrix) as a function of p_z for the Step I re-scaled TURTLE μ^+ beams. Figure D.1 is the legend.

Bibliography

[1] B. Aharmim et al. Independent measurement of the total active ^{8}B solar neutrino flux using an array of ^{3}He proportional counters at the Sudbury Neutrino Observatory. *Phys. Rev. Lett.*, 101(11):111301, September 2008.

[2] J. Hosaka et al. Three flavor neutrino oscillation analysis of atmospheric neutrinos in super-kamiokande. *Phys. Rev. D*, 74(3):032002, August 2006.

[3] M. Apollonio et al. Search for neutrino oscillations on a long base-line at the CHOOZ nuclear power station. *The European Physical Journal C - Particles and Fields*, 27:331–374, 2003.

[4] K. Abe et al. Indication of electron neutrino appearance from an accelerator-produced off-axis muon neutrino beam. *Preprint submitted to Physical Review Letters*, 2011.

[5] P. Adamson et al. Improved search for muon-neutrino to electron-neutrino oscillations in MINOS. *Preprint submitted to Physical Review Letters*, 2011.

[6] A. D. Sakharov. Violation of CP invariance, C asymmetry, and baryon asymmetry of the universe. *JETP Lett.*, 5:24, 1967.

[7] W Buchmüller, R. D. Peccei, and T. Yanagida. Leptogenesis as the origin of matter. *Annu. Rev. Nucl. Part. Sci.*, 55:311–355, 2005.

[8] K. Nakamura et al. The review of particle physics. *J. Phys. G.*, G37, 2010.

[9] D. N. Spergel et al. Wilkinson Microwave Anisotropy Probe (WMAP) three year results: implications for cosmology. *Astrophys. J. Supp.*, 170:377, 2007.

[10] The Super-Kamiokande Collaboration. Evidence for oscillation of atmospheric neutrinos. *Phys. Rev. Lett.*, 81:1562–1567, 1998.

[11] B. Pontecorvo. Mesonium and anti-mesonium. *Sov. Phys. JETP 6*, 6:429, 1957.

[12] Z. Maki, M. Nakagawa, and S. Sakata. Remarks on the unified model of elementary particles. *Prog. Theor. Phys.*, 28:870, 1962.

[13] P. Adamson et al. Measurement of Neutrino Oscillations with the MINOS detectors in the NuMI beam. *Phys. Rev. Lett.*, 101(13):131802, 2008.

[14] D. H. Perkins. *Introduction to High Energy Physics.* Cambridge University Press, April 2000.

[15] L. Wolfenstein. Neutrino oscillations in matter. *Phys. Rev. D*, 17:2369–2374, May 1978.

[16] S. Mikheyev and A. Smirnov. Resonant amplification of neutrino oscillations in matter and solar-neutrino spectroscopy. *Il Nuovo Cimento C*, 9:17–26, 1986.

[17] S. Abe et al. Precision measurement of neutrino oscillation parameters with KamLAND. *Phys. Rev. Lett.*, 100(22):221803, 2008.

[18] S. Antusch, J. Kersten, M. Lindner, and M. Ratz. Running neutrino masses, mixings and CP phases: analytical results and phenomenological consequences. *Nuclear Physics B*, 674(1-2):401 – 433, 2003.

[19] E. D. Church, K. Eitel, G. B. Mills, and M. Steidl. Statistical analysis of different $\bar{\nu}_\mu \to \bar{\nu}_e$ searches. *Phys. Rev. D*, 66(1):013001, June 2002.

[20] P. Adamson et al. First direct observation of muon antineutrino disappearance. *Phys. Rev. Lett.*, 107(2):021801, July 2011.

[21] P. Novella et al. Double Chooz: Searching for θ_{13} with reactor neutrinos. arXiv:1105.6079v1 [hep-ex], May 2011.

[22] W. Wang et al. The hunt for θ_{13} at the Daya Bay nuclear power plant. arXiv:0910.4605v1 [hep-ex], October 2009.

[23] W. Wang et al. RENO: An experiment for neutrino oscillation parameter θ_{13} using reactor neutrinos at Yonggwang. arXiv:1003.1391v1 [hep-ex], March 2010.

[24] N. Agafonova et al. Observation of a first candidate event in the opera experiment in the cngs beam. *Physics Letters B*, 691(3):138 – 145, 2010.

[25] T. Adam et al. Measurement of the neutrino velocity with the OPERA detector in the CNGS beam. *arXiv:1109.4897*, 2011.

[26] R. D'Inverno. *Introducing Einstein's relativity.* Clarendon Press, 1992.

[27] A. Bandyopadhyay et al. Physics at a future neutrino factory and super-beam facility. *Reports on Progress in Physics*, 72(10):106201, 2009.

[28] T. Kobayashi. Indication of electron neutrino appearance in the T2K experiment and its long-term implications, 2011. CERN colloquium.

[29] P. Huber and W. Winter. Neutrino factories and the "magic" baseline. *Phys. Rev. D*, 68:037301, Aug 2003.

[30] S. Ozaki, R. Palmer, M. Zisman, and J. Gallardo. Feasibility Study-II of a muon-based neutrino source. Technical Report 52623, BNL, 2001.

[31] G. K. O'Neill. Storage-ring synchrotron: Device for high-energy physics research. *Phys. Rev.*, 102:1418–1419, 1956.

[32] G. I. Budker. Accelerators and colliding beams (in Russian). In *7th International Conference on High-Energy Accelerators, Yerevan, USSR*, 1969.

[33] S. Wojcicki et al. Project X and the science of the intensity frontier. A white paper based on the Project X Physics Workshop, Fermilab, November 2009.

[34] Muon Accelerator Program. R&D proposal for the National Muon Accelerator Program. Technical Report FERMILAB-TM-2459-APC, Fermilab, 2010.

[35] V. I. Arnold. *Mathematical Methods of Classical Mechanics*. Springer-Verlag, 1978.

[36] E. T. Jaynes. *Probability Theory : The Logic of Science*. Cambridge University Press, April 2003.

[37] J. B. Rosenzweig. *Fundamentals of beam physics*. Oxford University Press, 2003.

[38] H. Wiedemann. *Particle Accelerator Physics*. Springer-Verlag, 1993.

[39] G. Penn. Beam envelope equations in a solenoidal field, 2000. Muon Collider note 71.

[40] A. J. Dragt, F. Neri, and G. Ragarajan. General moment invariants for linear Hamiltonian systems. *Phys. Rev. A*, 45(4):2572–2585, 1992.

[41] J. S. Berg, S. A. Bogacz, S. Caspi, J. Cobb, R. C. Fernow, J. C. Gallardo, S. Kahn, H. Kirk, D. Neuffer, R. Palmer, K. Paul, H. Witte, and M. Zisman. Cost-effective design for a Neutrino Factory. *Phys. Rev. ST Accel. Beams*, 9(1):011001, January 2006.

[42] R. B. Palmer. Muon colliders, 2008. HEPAP P5, Brookhaven National Laboratory.

[43] C. M. Ankenbrandt et al. Status of muon collider research and development and future plans. *Phys. Rev. ST Accel. Beams*, 2(8):081001, August 1999.

[44] J. H. Cobb. 'Initial' cooling - muon cooling for a Neutrino Factory, October 2007. Topical workshop on The Neutrino Factory and Muon Collider, the physics and the R&D programmes, The Cosener's House, Abingdon, UK.

[45] S. Q. Yang, W. Lau, R. S. Senanayake, H. Witte, M. A. Green, and Y. Ivanyushenkov. Progress on the focus coil for the MICE channel. `http://mice.iit.edu`, 2005. MICE note 125.

[46] J. H. Cobb. Ferromagnetic projectiles in MICE and the possible desirability of bullet proofing the solenoid apertures. `http://mice.iit.edu`, 2008. MICE note 213.

[47] C. Rogers and M. Ellis. High precision measurement of muon emittance reduction in MICE. `http://mice.iit.edu/`. MICE note 122.

[48] J. H. Cobb. Statistical errors on emittance measurements. `http://mice.iit.edu/`. MICE note 268.

[49] A. Khan et al. MICE scintillating fibre tracker prototype. `http://mice.iit.edu/`. MICE note 90.

[50] A. Blondel. An International Muon Ionization Cooling Experiment: Goals and preliminary design. Historical document on goals and preliminary design, August 2001.

[51] The MICE Collaboration. The MICE schedule. `http://mice.iit.edu/MICE-schedule-July-2011.pdf`, July 2011.

[52] M. Apollonio and M. A. Rayner. The MICE muon beam line optimization and emittance generation. In *Proceedings of the International Particle Accelerator Conference*. Kyoto, April 2010.

[53] M. Apollonio and J. H. Cobb. Optimal size for the MICE diffuser. `http://mice.iit.edu/`. MICE note 176.

[54] V. Blackmore, J. H. Cobb, M. Dawson, J. Tacon, and M. Tacon. Particle tracking and beam matching through the new variable thickness MICE diffuser. In *Proceedings of PAC11, New York, United States of America*, 2011.

[55] M. Hills and A. Nichols. MICE essential beamline geometry. `http://mice.iit.edu`, 2009. MICE note 242.

[56] C. Booth, P. Hodgson, and P. J. Smith. MICE target operation and monitoring. In *Proceedings of IPAC10, Kyoto, Japan*, 2010.

[57] C. Booth, P. Hodgson, P. J. Smith, and J. Tarrant. MICE target hardware. In *Proceedings of IPAC10, Kyoto, Japan*, 2010.

[58] A. Dobbs et al. The mice muon beam: Status and progress. In *Proceedings of the International Particle Accelerator Conference*. Kyoto, April 2010.

[59] A. Dobbs. *Particle Rate and Host Accelerator Beam Loss on the MICE Experiment*. PhD thesis, Imperial College London, 2011.

[60] M. Apollonio and H. Witte. Optimizing the MICE matching coil currents for the production spectrometer solenoids. `http://mice.iit.edu`, 2006. MICE note 153.

[61] M. Apollonio. Pion-muon beam line magic table. `http://mice.iit.edu/bl/`.

[62] T. Roberts. A Swiss army knife for Geant4, optimized for simulating beam lines. `http://www.muonsinc.com/tiki-index.php`.

[63] W. Spensley and J. S. Graulich. Survey inspection report of the Step 1 MICE beam line. Private communication. The survey was performed out on the 11th and 12th September 2010.

[64] M. A. Rayner. The performance of the MICE muon beam line. In *Proceedings of the 12th International Workshop on Neutrino Factories, Superbeams, and Beta Beams*. Tata Institute for Fundamental Research, Mumbai, October 2010.

[65] R. Bertoni, A. Blondel, M. Bonesini, G. Cecchet, A. de Bari, J. S. Graulich, Y. Karadzhov, M. A. Rayner, I. Rusinov, R. Tsenov, S. Terzo, and V. Verguilov. The design and commissioning of the MICE upstream time-of-flight system. *Nuclear Instruments and Methods in Physics Research*, A615, 2010.

[66] M. Bonesini. The construction and laboratory tests for the MICE TOF0/1 detectors. `http://mice.iit.edu/`. MICE note 241.

[67] The MICE Collaboration. G4MICE. `http://mice.iit.edu/software/software.html`. The MICE project's tracking, detector reconstruction and accelerator physics analysis framework.

[68] S. Agostinell et al. Geant4: a simulation toolkit. *Nucl. Inst. Meth. A*, 506(3):250 – 303, 2003.

[69] Y. Karadzhov, M. Bonesini, J. S. Graulich, and R. Tsenov. TOF detectors time calibration. `http://mice.iit.edu/`. MICE note 251.

[70] R. Bertoni, M. Bogomilov, M. Bonesini, A. de Bari, G. Cecchet, Y. Karadzhov, D. Orestano, F. Pastore, L. Tortora, and R. Tsenov. Analysis of PID detectors (TOF and KL) performances in the MICE 2010 run. `http://mice.iit.edu/`. MICE note 337.

[71] The MICE Collaboration. *The MICE Technical Reference Document*.

[72] M. A. Rayner. Step 1 emittance-momentum matrix data sets. `http://mice.iit.edu/`. MICE note 325.

[73] The MICE Collaboration. Run conditions summary spreadsheet. `http://mice.iit.edu/mico/`, August 2010.

[74] V. Palladino et al. Practical information to operate MICE TOF0. `http://mice.iit.edu/mico/manuals/`, 2008.

[75] V. Palladino et al. Practical information to operate MICE TOF1. `http://mice.iit.edu/mico/manuals/`, 2008.

[76] Saint Gobain Crystals. BC-418, BC-420, BC-422 premium plastic scintillator data sheet. `http://www.detectors.saint-gobain.com/`.

[77] Saint Gobain Crystals. BC-400, BC-404, BC-408, BC-412, BC-416 premium plastic scintillator data sheet. `http://www.detectors.saint-gobain.com/`.

[78] J. H. Cobb. Private communication.

[79] M. A. Rayner and J. H. Cobb. Momentum measurement by the upstream Time of Flight detectors. `http://mice.iit.edu/`. MICE note 317.

[80] A. Bross. Private communication.

[81] Vector Fields Limited, 24 Bankside, Kidlington, Oxford, OX5 1JE, UK. *Opera-3d reference manual*.

[82] A. J. Dragt. Numerical third-order transfer map for solenoid. *Nucl. Inst. Meth. A*, 298:441–459, 1990.

[83] A. J. Dragt et al. Lie algebraic treatment of linear and nonlinear beam dynamics. *Annu. Rev. Nucl. Part. Sci.*, 38:455–496, 1988.

[84] M. A. Rayner. Presentation of latest results. `http://mice.iit.edu/`. Presentation at the 30th collaboration meeting of the MICE experiment, July 2011, Oxford.